

Luminescence properties of ZnO and ZnO:Eu³⁺ nanostructures and thin films

by

Emad Hasabeldaim Hadi Hasabeldaim

(MSc)

A thesis submitted in fulfilment of the requirements for the degree of

PHILOSOPHIAE DOCTOR

in the

Faculty of Natural and Agricultural Sciences

Department of Physics

at the

University of the Free State

Republic of South Africa

Promoter: Prof. H. C. Swart

Co-Promoter: Prof. O.M. Ntwaeaborwa

Co-Promoter: Prof. R.E. Kroon

October 2019

What is being neglected, has never been understood.

Acknowledgement

This work cannot be complete without thanking and acknowledging the following individuals and institutions: I would like to express my deepest appreciation and gratitude to

- My promoter Prof H.C. Swart for his professional supervision, suggestions and guidance throughout this work, for giving me the opportunity to join his research group (advanced luminescence materials).
- My co-promoter Prof O.M. Ntwaeaborwa for his guidance and professional supervision throughout this thesis.
- My co-promoter, Prof R.E. Kroon for his assistance in PL measurements, fruitful suggestions and discussions.
- Prof E. Coetsee for helping me with XPS measurements and her comments and suggestions.
- Dr. M.M. Duvenhage for the TOF-SIMS measurements.
- Mr. Edward Lee of the Centre of Microscopy UFS for his assistance with SEM measurements.
- Mr. Lucas Erasmus for helping me with the pulsed laser deposition system.
- Mr. Anthonie Fourie for taking care of the chemicals.
- Friends and colleagues (staff and students) in the Department of Physics at the University of the Free State for their positive and impactful attitude, and wonderful time we spent together.
- My parents, brother and sister for their endless love, support and encouragements that helped me to pursue my dreams and made me who I am today.
- Special thanks and gratitude to my wife Rajaa for her love, support, and encouragements along the way, for her patience and perseverance waiting for me at home to complete my degree in a foreign country.
- National Research Foundation (NRF), South Africa Chair initiative (SARCHI) chair and the cluster program of the University of the Free State for providing measurement facilities.
- For my sponsors African Laser Centre (ALC) and the rental pool programme of the National Laser Centre (NLC) who made it possible to me to come through this stage, for their financial support for three year including bursary and workshops.

Abstract

Eu³⁺ doped ZnO thin films and ZnO nanorods were successfully prepared by using different techniques. Successful incorporation of Eu³⁺ ions in the ZnO matrix and preferred orientation along the c-axis for the films and the nanorods were achieved. The structure, morphology, luminescence and stability of the samples under electron beam irradiation were investigated.

Firstly: Low Eu³⁺ concentration (0.4, 0.6, 0.8, and 1 mol%) doped ZnO thin films were successfully prepared using the *spin coating* technique. The preferred orientation of the films was reduced with increasing Eu³⁺ content. The average particle sizes and the optical band gap of the films decreased with increasing Eu³⁺ concentration. The films were excited at 325 nm and 464 nm using a xenon lamp. Upon excitation at 325 nm, the films exhibited band to band emission at ~378 nm and a broad deep level emission due to defects, with a small peak associated with characteristic Eu³⁺ emission at 614 nm that protruded from the broad band deep level emission. Upon excitation at 464 nm the characteristic Eu³⁺ emission features were observed and their intensity increased with increasing Eu³⁺ content until 0.6 mol% of Eu³⁺ and was then quenched. Multipole-multipole interaction, defects created due to the differences in ionic radii and charge states of Eu³⁺ and Zn²⁺ were found to contribute to luminescence quenching. Judd-Ofelt intensity parameters and asymmetry ratio analysis revealed the dependence of the Eu³⁺ emission intensity on the local environment around the Eu³⁺ ions in the host.

Secondly: ZnO thin films doped with higher Eu³⁺ concentration up to 4 mol% were also successfully prepared using a sol-gel *spin coating* technique. X-ray photoelectron spectroscopy (XPS) confirmed the presence of Zn atoms in their doubly ionized state (Zn²⁺), while Eu atoms were found to be present in their divalent (Eu²⁺) and trivalent (Eu³⁺) states. Excitation spectra showed a broad band near 288 nm which was attributed to the charge transfer between O to Eu³⁺. For the excitation at 464 nm, the doped samples exhibited only the characteristic emissions of Eu³⁺ which were attributed to the ⁵D₀-⁷F_J (J = 0, 1, 2, 3, 4) transitions, respectively. The Eu³⁺ emission intensity increased with increasing Eu³⁺ concentration up to 3 mol% and was then quenched. Cathodoluminescence (CL) spectra showed only the Eu³⁺ characteristic emission similar to PL excited at 464 nm. Judd-Ofelt intensity indicated strong covalence of Eu-O bond and higher asymmetry in the vicinity of the Eu³⁺ ions. The optimum sample (3 mol%) was degraded in vacuum under electron beam irradiation for 160 C/cm² (about 22 h). The CL intensity showed a slight decrease at the initial electron dose at ~ 30 C/cm² and then stabilized at further electron dosages. XPS analysis confirmed the formation of defects as a

result of electron beam irradiation. Slight changes of the surface morphology and roughness were observed from the degraded area.

Thirdly: Eu^{3+} (3 mol%) doped ZnO thin films were deposited by *pulsed laser deposition* (PLD) at different oxygen partial pressures (vacuum, 5.9×10^{-2} Torr, 8×10^{-2} Torr and 10×10^{-2} Torr). The 002 X-ray diffraction (XRD) peak of the thin film initially increased with an increase in the oxygen partial pressure, but then slightly decreased. The film thickness, roughness and emission intensity also followed the same trend. The films' morphology improved as a function of increasing oxygen pressure. When excited by a He-Cd laser at 325 nm, the film deposited in vacuum exhibited an intense UV emission at ~ 379 nm, broad-weak deep level emission in the region from 450 nm to 700 nm, as well as a small peak associated with the characteristic emission of the $4f - 4f$ transitions of Eu^{3+} at 616 nm standing out from the deep levels emission for the films deposited in oxygen partial pressure. When the Eu^{3+} ions were selectively excited at 464 nm, only the characteristic emission of the $4f - 4f$ transitions of Eu^{3+} were observed at 536 nm, 578 nm, 595 nm, 616 nm, 656 nm and 707 nm corresponding to the ${}^5\text{D}_1 - {}^7\text{F}_0$, ${}^5\text{D}_0 - {}^7\text{F}_J$ ($J = 0, 1, 2, 3$ and 4) transitions. When excited at 288 nm, the film deposited in vacuum only exhibited a broad peak centred at 585 nm which was due to the ZnO deep defect levels. The O to Eu^{3+} charge transfer band near 288 nm was observed for the films deposited in oxygen, and its intensity increased with increasing oxygen pressure. The samples prepared in oxygen exhibited characteristic emission of Eu^{3+} with an increase in intensity for increasing oxygen partial pressure. No CL was observed for the sample prepared in vacuum, whereas only the characteristic emission of Eu^{3+} was detected for the films obtained in oxygen partial pressure. Current-voltage measurements of the p-type Si/ZnO: Eu^{3+} junctions showed a diode-like behaviour with turn on voltage of about 10 V.

Fourthly: For Eu^{3+} doped ZnO ($\text{ZnO}:\text{Eu}^{3+}$) thin films deposited by PLD, the oxygen working atmosphere, deposition time and target-substrate distance were optimized to achieve the best luminescence and morphology properties. The surface and luminescence stability of the film under electron beam irradiation was also studied. The CL intensity of the Eu^{3+} dominant peak at 616 nm increased slightly during the initial stage of electron irradiation, after which it stabilized. XPS high resolution spectra of the O 1s peak confirmed the creation of new defects during electron beam irradiation. Atomic force microscopy images revealed that the particle sizes increased slightly during irradiation (degradation). Colour rendering and purity of the CL spectra were slightly changed during degradation.

Fifthly: Preferentially c-axis oriented ZnO nanorods were grown on a ZnO seed layer spin coated on a crystalline silicon substrate. A low temperature aqueous chemical growth method using the chemical bath deposition (CBD) technique was used to grow the ZnO nanorods. The samples were annealed at 700 °C in a reducing atmosphere (H₂/Ar) with a relative ratio of 5%:95% for different times (20, 30 and 50 min). XRD analysis revealed that the crystallite sizes increased with increasing annealing time up to 30 min and then decreased for longer annealing time. Scanning electron microscope images showed a successful growth of the vertically-aligned ZnO nanorods which were approximately 500 nm in length and 50 nm in diameter. The diameter of the nanorods increased with increasing annealing time up to 30 min and then decreased when the annealing time was increased further. PL measurements confirmed that the un-annealed sample exhibited two distinct emissions, namely the band to band emission around 378 nm and a broad orange emission centred at 600 nm which was due to the oxygen related defects. The annealed samples exhibited only a broad green emission centred at 500 nm and their intensities increased with annealing time. The highest intensity was recorded for the sample annealed for 30 min and the intensity decreased for further annealing time. The deconvoluted PL peak of the green emission indicated that three different kinds of defects were responsible for the emission at 500 nm. The decay measurements indicated that the green emission (500 nm) had an average lifetime of 11.58 μs. The quantum yield of the sample annealed for 30 min was measured using an integrating sphere at a wavelength of 325 nm and it was found to be 43%.

The surface state, chemical and luminescence stability of the sample with higher luminescence intensity were investigated under electron beam irradiation. Auger electron spectroscopy, XPS and secondary electron microscopy (SEM) were used. The CL intensity was monitored concurrently with the Auger peak-to-peak heights using the same electron beam. The degradation experiment was performed in vacuum and in an oxygen ambient. According to the AES spectra, all the principal elements (zinc and oxygen) were detected as well as carbon, which was removed at the initial stage of electron beam irradiation. No chemical change was observed during electron beam irradiation. In vacuum, the CL intensity decreased to almost half of its initial intensity after 100 C/cm² electron dose and then stabilized. In the oxygen atmosphere, the CL intensity also decreased initially up to a dose of ~10 C/cm² and thereafter recovered to about 90% of its original intensity and stabilized after a dose of ~100 C/cm². No difference in the chemical state of Zn was observed with XPS for the original and degraded samples. Only a small change in the defect contribution part of the O peak was observed. SEM

images for the original and degraded samples showed that the electron beam irradiation induced surface changes in the morphology of the ZnO nanorods.

These results suggest that the ZnO nanorods and ZnO:Eu³⁺ thin films are promising green and red materials for optoelectronic devices such as light emitting diodes (LEDs) and flat panel displays (FPDs) among others.

Table of contents

Acknowledgement	I
Abstract	II
Table of contents	VI
Chapter 1	1
Introduction.....	1
1.1 Overview.....	1
1.2 Motivation.....	3
1.3 Research aim.....	3
1.4 Research Objectives.....	3
1.5. Thesis organization	4
Chapter 2	7
Background and theory	7
2.1. Luminescence and luminescent material	7
2.1.1. Zinc oxide (ZnO)	8
2.1.2. Crystal structure of ZnO	9
2.1.3. Native point defects of ZnO.....	10
2.1.4. Physical properties and parameters of ZnO in a hexagonal wurtzite structure	11
2.1.5. Lanthanide ions (Ln^{3+})	12
2.1.6. Europium ions ($\text{Eu}^{3+/2+}$)	16
2.2. Energy transfer.....	16
2.3. Charge transfer.....	18
2.4. Concentration quenching	19
2.5. Applications of luminescent materials.....	19
2.3. References.....	20
Chapter 3	24
Experimental techniques.....	24
3.1. Thin film preparation	24
3.1.1. Pulsed laser deposition (PLD).....	24
3.1.2. Spin coating technique	29
3.1.3. Chemical bath deposition (CBD).....	31
3.2. Characterization Techniques.....	32

3.2.1. X-ray diffraction (XRD)	32
3.2.2. Scanning electron microscopy (SEM)	33
3.2.3. Atomic force microscopy	35
3.2.4. X-ray photoelectron spectroscopy (XPS).....	36
3.2.5. Time-of-flight secondary ion mass spectrometry (ToF-SIMS).....	37
3.2.6. Auger electron spectroscopy (AES).....	38
3.2.8. Cathodoluminescence spectroscopy (CL).....	41
3.2.9. UV-Vis spectroscopy	42
3.3. References.....	43
Chapter 4	47
Structural, optical and photoluminescence properties of Eu doped ZnO thin films prepared by spin coating.....	47
4.1. Introduction.....	47
4.2. Experimental details.....	48
4.2.1. Preparation	48
4.2.2. Characterization	49
4.3. Results and discussion	49
4.3.1. Structural and morphological analysis	49
4.3.2. Transmittance and band gap analysis (UV–Vis spectroscopy).....	55
4.3.3. Photoluminescence analysis.....	55
4.3.4. Judd-Ofelt analysis.....	61
4.4. Conclusion	63
4.5. References.....	64
Chapter 5	69
Photoluminescence and cathodoluminescence of spin coated ZnO films with different concentration of Eu ³⁺ ions	69
5.1. Introduction.....	69
5.2. Experimental methods	70
5.2.1. Preparation	70
5.2.2. Characterization	71
5.3. Results and discussion	72
5.3.1. Structure and morphology.....	72
5.3.2. Transmittance and band gap analysis (UV–vis spectroscopy).....	82
5.3.3. Photoluminescence analysis.....	83
5.3.4. Judd-Ofelt analysis.....	86
5.3.5. Cathodoluminescence and degradation analysis.....	88

5.4. Conclusion	92
5.5. References.....	93
Chapter 6	98
Luminescence properties of Eu doped ZnO PLD thin films: the effect of oxygen partial pressure	98
6.1. Introduction.....	98
6.2. Experimental methods	99
6.2.1. Pellet preparation and thin film deposition	99
6.3. Result and discussion	100
6.3.1. Structural and morphological analysis	100
6.3.2. Chemical analysis	105
6.3.3. Luminescence analysis.....	109
6.3.4. Current-voltage measurements	114
6.4. Conclusion	115
6.5. References.....	116
Chapter 7	121
Pulsed laser deposition of a ZnO:Eu ³⁺ thin film: study of the luminescence and surface state under electron beam irradiation	121
7.1. Introduction.....	121
7.2. Experimental procedures.....	122
7.3. Result and discussions	124
7.3.1. Structure and morphology analysis.....	124
7.3.2. Luminescence analysis.....	133
7.4. Conclusion	136
7.5. References.....	137
Chapter 8	142
Enhanced green luminescence from ZnO nanorods.....	142
8.1. Introduction.....	142
8.2. Experimental	143
8.2.1. Deposition of ZnO seed layer	143
8.2.2. Growth of the ZnO nanorods	143
8.2.3. Characterization	144
8.3. Results and discussion	144
8.3.1. Structure and morphology.....	144
8.3.2. XPS analysis	148
8.3.3. Photoluminescence analysis.....	152
8.4. Conclusions.....	157

8.5. References.....	157
Chapter 9	160
Cathodoluminescence degradation study of the green luminescence of ZnO nanorods	160
9.1. Introduction.....	160
9.2. Experimental	161
9.3. Results and discussions.....	162
9.4. Conclusion	172
9.5. References.....	173
Chapter 10	176
Summary and future work	176
10.1. Summary.....	176
10.2. Future work.....	178
Appendix	179
Publications	179
Presentations at national and international conferences/workshops	180

Chapter 1

Introduction

1.1 Overview

Luminescence phenomenon and technology has a very long history that can be traced back to the first observation of the naturally occurring luminescence in glow worms, fireflies, seashells, aurora borealis, luminescent wood, rotting fish and meat, etc. [1]. In the 17th century, the first luminescent material (Barite or BaSO₄) was discovered from the fired BaS, and is still known to be an important host material for different luminescent applications [2]. Since then, luminescence has become an imperative scientific research area. Over the years, better understanding of mechanisms of luminescence has been established and has led to the discovery of new materials with different properties. The results have directly been reflected in novel applications of illumination in our day-to-day life [3]. These applications include light bulbs (fluorescent lamps), cathode ray tube (CRTs), flat panel displays (FPDs) and light emitting diodes (LEDs) [4]. Luminescent materials can be used in different forms such as powders or thin films and nanostructures or bulk in the above mentioned applications. Thin films and nanostructure technology evolved as a result of demand for highly efficient devices with better resolution, electrical and luminescence properties and lower power consumption [5]. Thin films are the deposition of small amounts of a material on a substrate to form a layer with thickness in the range of nanometres to one micron. Nanostructures form during deposition of a small fraction of a material in ordered arrays and shapes (nanorods, nanotubes, etc.) with sizes ranging from few nanometres to a micron. Thin film technology exceeds its counterpart powder in many important properties including better crystallinity, finite particle size with uniform distribution, good material to substrate adhesion, thermal and chemical stability. On the other hand, nanostructures have their own advantages over powder and thin films, particularly, high surface to volume ratio which enables high efficiency photovoltaic and LED devices [6].

Luminescent materials can be classified into two groups based on their band gap: semiconductors with wide band gaps ranging from 2 to 4 eV, and insulators with larger band gaps above 5 eV. The choice of the luminescent material is merely depending on the type of application and the design in which the material will be used.

Wide band gap semiconductors such as ZnO, TiO₂, Ga₂O₃, SiC, GaN, etc. are very important luminescent materials in different optoelectronic devices [7]. They possess relatively large band gaps compared to the conventional semiconductors such as silicon (Si), germanium (Ge)

and gallium arsenide (GaAs) [8]. Wide band gap materials have shown the ability to overtake the conventional small band gap materials in producing high-temperature, frequency, power and efficiency semiconductor-based devices [9]. Moreover, they are capable of emitting light across a wide range of the electromagnetic spectrum from ultraviolet (UV) to the near infrared (NIR) region, as well as their ability to accommodate incorporated luminescent activators/dopants such as rare earth (RE) ions. Furthermore, they possess additional unique properties such as high saturation current, chemical stability, low thermally generated current and high thermal conductivity [10]. Many wide band gap materials are available with different crystal structures and lattice constants, which is beneficial when heterostructure epitaxial growth is necessary. ZnO is a divalent metal oxide semiconductor that can be used in a wide range of optoelectronic applications. It has been realized as a potential wide band gap (3.37 eV at room temperature) semiconductor with excellent properties that can fulfil the need of today's technology. ZnO surpasses the commercially available wide band gap semiconductors such as gallium nitride (GaN) in many aspects including: its large exciton binding energy (60 meV) at room temperature which could account for an efficient radiative recombination and lower threshold voltage of lasing emission [11], its compatibility for wet etching which is useful during fabrication, patterning and miniaturization processes [12] and its chemical and mechanical stability [13]. Due to the (0001) polar surface of the ZnO crystal, it can be grown in different nanostructure forms such as nanorods, nanotubes, nanocombs, etc. [14]. Nevertheless, ZnO is abundant in nature which makes it an eco-friendly material, as well as easy to synthesis via different chemical and deposition methods in different forms (powder, thin film and nanostructures). ZnO has shown the ability to accommodate different lanthanide (Ln^{3+}) ions in a wide concentration range (0.2 – 7.0 mol %) without changing the crystal phase [15, 16, 17].

RE^{3+} ion doped ZnO thin films have drawn considerable attention over the last few decades [17] due to their potential to provide finely tuned colours from the blue to the infra-red region [18, 19]. Among these, europium (Eu^{3+}) is an important dopant ion in ZnO to prepare red light emitting materials (in powder or thin film form) for different optoelectronic applications such as field emission displays (FEDs) and LEDs [19].

To ensure a long term operation and stable luminescence efficiency of any material, chemical and surface stability of luminescent materials are inevitable characteristics that must be taken into consideration. Prolonged electron beam irradiation combined with Auger electron spectroscopy (AES), cathodoluminescence (CL), scanning electron microscopy (SEM), atomic

force microscopy (AFM) and X-ray photoelectron spectroscopy (XPS) are useful tools to study materials' stability.

1.2 Motivation

ZnO contains native defects which are responsible for the optical and electrical properties of the film. ZnO is well-known by its green luminescence which is thought to originate from its native oxygen vacancies (V_o) [20]. However, the exact origin is yet to be fully understood. Taking advantage of ZnO nanostructure forms, which provide high surface to volume ratio, highly luminous green emission can be achieved from ZnO nanorods.

Over the past few years, intensive research has been done in order to achieve an efficient and bright red emission from Eu^{3+} doped ZnO thin films. However, it is still a challenge to achieve dazzling red emission. This is due to the difficulties of achieving an efficient energy transfer from the ZnO to the Eu^{3+} ion (see chapter 4). The deposition techniques play an important role in manipulating the film's properties by varying the growth parameters, via which energy transfer may be maximized. Different techniques (pulsed laser deposition (PLD) and spin coating techniques) were used to grow Eu^{3+} doped ZnO thin films with different Eu concentrations. The stability of Zn doped ZnO powders and thin films, which emit a green luminescence around 500 nm were examined under electron beam irradiation and they were found to be generally stable under prolonged electron bombardment. Therefore, it is imperative to study the luminescence, chemical and surface stabilities of Eu^{3+} doped ZnO under electron beam irradiation and also study the effect of electron beam irradiation on the surface state, morphology and the green luminescence of ZnO nanorods.

1.3 Research aim

To study the fundamental properties (e.g. structure, chemical and surface stability, particle morphology, optical and luminescent properties) of undoped and Eu^{3+} doped ZnO nanostructures and thin film forms.

1.4 Research Objectives

The objectives of this study are:

1. Preparation of different concentration of Eu^{3+} doped ZnO thin films by using spin coating and PLD techniques.
2. Study the structure, morphology and the luminescence properties of the films.
3. Study the surface, chemical and the luminescence stability of the films under prolonged electron beam irradiation.

4. Preparation of ZnO nanorods and optimizing the green luminescence from the nanorods.
5. Study the surface, chemical and the luminescence stability of the green emission of the nanorods under electron beam irradiation.

1.5. Thesis organization

This thesis is divided into ten chapters, each chapter focusing on a particular aspect: Chapter 1 is the Introduction, giving an overview and motivation about this work, followed by the research objectives. Chapter 2 (Background) is devoted to luminescent materials and luminescence phenomena, basic properties of ZnO as a host and lanthanide ions, the energy transfer concept and some of the luminescent material applications. Chapter 3 (Techniques) describes the working principles underlying the deposition and characterization techniques that were used in this study. Chapter 4 provides analysis on the Structural, optical and photoluminescence properties of Eu doped ZnO thin films prepared by spin coating technique. Chapter 5 addresses the Photoluminescence and cathodoluminescence of spin coated ZnO films doped with 0.4 mol% of Eu^{3+} . Chapter 6 is devoted to the Luminescence properties of Eu doped ZnO PLD thin films: the effect of oxygen partial pressure. Chapter 7 focuses on the study of Pulsed laser deposition of a ZnO:Eu³⁺ thin film: study of the luminescence and surface state under electron beam irradiation. Chapter 8 is about the Enhanced green luminescence from ZnO nanorods. Chapter 9 is on the Cathodoluminescence degradation of the green luminescence of ZnO nanorods. Chapter 10 gives the summary of the thesis results and suggestions for future work. The last part of the thesis provides a list of publications resulting from this work and the conferences/workshops presentations.

1.5. References

- [1] K. V. R. Murthy and H. S. Virk, Luminescence Phenomena: An Introduction, *Defect and Diffusion Forum*, **347** (2014) 1-34. doi:10.4028/www.scientific.net/DDF.347.1.
- [2] W. M. Yen, S. Shionoga and H. Yamamoto, Phosphor handbook, Boca Raton, Florida, United States: CRC press, 2018.
- [3] R. C. Ronda, Luminescence: from theory to applications, Hoboken, New Jersey, United States: John Wiley & Sons, 2007.
- [4] A. Kitai, Luminescent Materials and Applications, Hoboken, New Jersey, United States: John Wiley & Sons, 2008.

- [5] Y. Tang, Modern Technologies for Creating Nanostructures in Thin-Film Solar Cells, *Modern Technologies for Creating the Thin-film Systems and Coatings*, London, United Kingdom: IntechOpen, 2017. p. 345. <http://dx.doi.org/10.5772/64611>.
- [6] I. Tiginyanu, P. Topala and V. Ursaki, Nanostructures and Thin Films for Multifunctional Applications: Technology, Properties and Devices, New York City, United States: Editura Springer, 2016.
- [7] F. Roccaforte, P. Fiorenza, G. Greco, R. L. Nigro, F. Giannazzo, F. Iucolano and M. Saggio, Emerging trends in wide band gap semiconductors (SiC and GaN) technology for power devices, *Microelectron. Eng.* **187** (2018) 66-77. <https://doi.org/10.1016/j.mee.2017.11.021>.
- [8] H. Jin, L. Qin, L. Zhang, X. Zeng and R. Yang, Review of wide band-gap semiconductors technology, *MATEC Web of Conf.* **40** (2016) 01006. <http://dx.doi.org/10.1051/mateconf/20164001006>.
- [9] D. Garrido-Diez and I. Baraia, Review of Wide Bandgap Materials and their Impact in New Power Devices, In *IEEE International Workshop of Electronics, Control, Measurement, Signals and their Application to Mechatronics (ECMSM)*, 2017, pp 1-6.
- [10] K. F. Brennan and P. P. Ruden, Topics in High Field Transport in Semiconductors, Singapore: World Scientific, vol **22** 2001.
- [11] M. Soosen Samuel, Lekshmi Bose and K. C. George, Optical properties of ZnO nanoparticles, *SB Academic Review*, **XVI (1)** (2009) 57-65. ISSN: 0973-7464.
- [12] T. Zhang, L. Sun, D. Han, Y. Wang and R. Han, Surface Uniform Wet Etching of ZnO Films and influence of oxygen annealing on etching properties, In *6th IEEE International Conference on Nano/Micro Engineered and Molecular Systems*, Kaohsiung, Taiwan (2011) 626-629. [doi:10.1109/nems.2011.6017433](https://doi.org/10.1109/nems.2011.6017433).
- [13] G. Wisz, I. Virt, P. Sagan, P. Potera and R. Yavorskyi, Structural, Optical and Electrical Properties of ZnO layers produced by pulsed laser deposition method, *Nanoscale Res. Lett.* **12** (2012) 253. DOI: 10.1186/s11671-017-2033-9.
- [14] X. Liu, X. Wu, H. Cao and R. P. Chang, Growth mechanism and properties of ZnO nanorods synthesized by plasma-enhanced chemical vapor deposition, *J. Appl. Phys.* **95** (2004) 3141. [doi: 10.1063/1.1646440](https://doi.org/10.1063/1.1646440).

- [15] N. Babayevska, I. Iatsunskyi, P. Florczak, M. Jarek, B. Peplińska and S. Jurga, Enhanced photodegradation activity of ZnO:Eu³⁺ and ZnO:Eu³⁺@Au 3D hierarchical structure, *J Rare Earth*, In press, 2019.
- [16] N. S. Singh, S. D. Singh and S. D. Meetei, Structural and photoluminescence properties of terbium-doped zinc oxide nanoparticles, *Chin. Phys. B* **23** (2014) 058104. doi:10.1088/1674-1056/23/5/058104.
- [17] V. Kumar, O. M. Ntwaeaborwa, T. Soga, V. Dutta and H. C. Swart, Rare Earth Doped Zinc Oxide Nanophosphor Powder: A Future Material for Solid State Lighting and Solar Cells, *ACS Photonics* **4** (2017) 2613-2637. DOI: 10.1021/acsp Photonics.7b00777.
- [18] A. Manikandan, E. Manikandan, B. Meenatchi, S. Vadivel, S. K. Jaganathan, R. Ladchumananandasivam, M. Henini, M. Maaza and J. S. Aanand, Rare earth element (REE) lanthanum doped zinc oxide (La: ZnO)nanomaterials: Synthesis structural optical and antibacterial studies, *J. Alloys Compd* **723** (2017) 1155-1161. <http://dx.doi.org/10.1016/j.jallcom.2017.06.336>.
- [19] D. and Y. K. Agrawal, Rare Earth-Doped Zinc Oxide Nanostructures: A Review, *Rev. Nanosci. Nanotechnol.* **5** (2016) 1-27. doi:10.1166/rnn.2016.1071.
- [20] Y. Gong, T. Andelman, G. F. Neumark, S. O'Brien and I. L. Kuskovsky, Origin of defect-related green emission from ZnO nanoparticles: effect of surface modification, *Nanoscale Res Lett.* **2** (2007) 297–302. doi: 10.1007/s11671-007-9064-6.

Chapter 2

Background and theory

This chapter is devoted to explaining the basic concepts of luminescence processes, luminescent materials and their applications.

2.1. Luminescence and luminescent material

Luminescence phenomena have been observed since the earliest ancient history of mankind. Some examples of the naturally occurring luminescence are the luminescence from glow worm, wood, rotting fish, meat, aurora borealis, etc [1].

Luminescence is a physical phenomenon that refers to the emission of light from a substance (luminescent material) when it is exposed to an external energy source [2]. When external excitation energy is absorbed by the luminescent material, an electron from the ground state will be promoted to the excited state. The electron does not stay permanently in the excited state. On its return to the ground state, energy may be released radiatively (in the form of light) with a certain wavelength depending on the electronic configuration of that material's molecules or atoms [1]. There are different types of luminescence depending on the excitation source that was used. Luminescence obtained when the sample is excited by a photon, is called photoluminescence, when the excitation source was an electron it is called cathodoluminescence and in the case of electric field it is called electroluminescence, etc. Luminescence is divided into two categories, namely fluorescent and phosphorescent depending on the emission rate or lifetime after the excitation source has ceased. The fast emission rate of about 10^8 s^{-1} with a lifetime near 10 ns is called fluorescent, which originates from singlet state transitions. In the phosphorescent case, the excited electron has the same electron spin as the second electron which remained in the ground state electron (triplet state), hence a transition of the excited electron back to the ground state is forbidden unless it undergoes internal spin conversion, e.g. by means of interaction with lattice vibrational energy states. Therefore, phosphorescence lifetime is relatively longer than fluorescence and it is in the order of magnitude of 10^{-4} to 10 s, or may be longer in the case of afterglow in which the emission life time can persist up to hours or days. Fig. 2. 1 illustrates the basic concept of luminescence process.

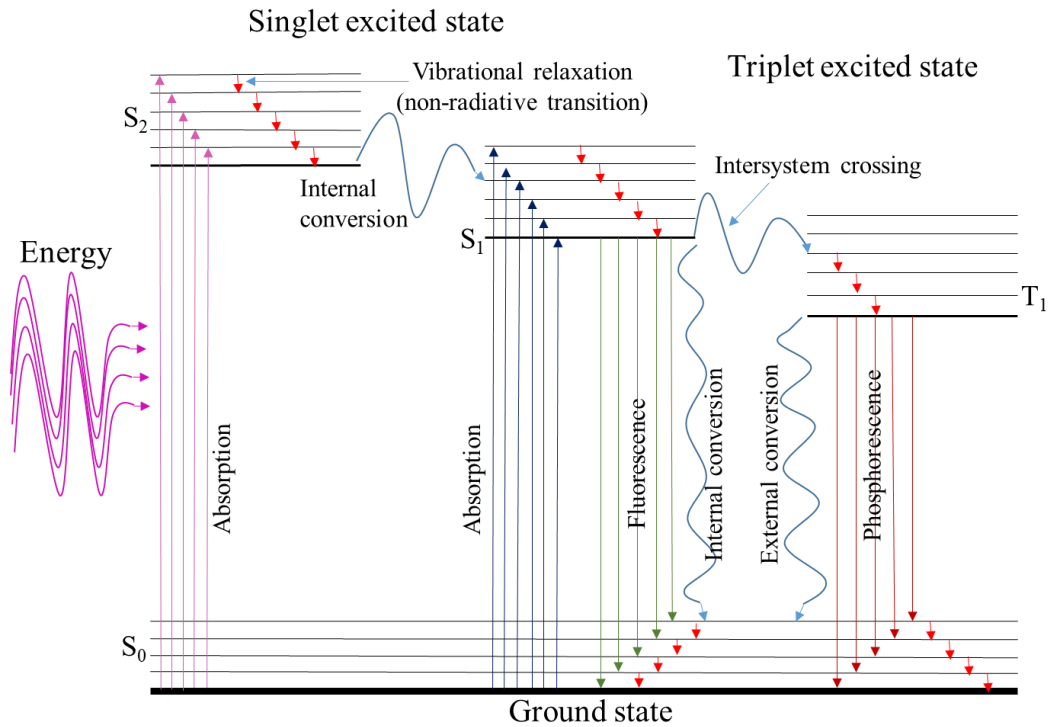


Fig. 2.1. Part of the Jablonski's diagram which explains the concept of luminescence phenomenon [3].

Luminescent materials usually consist of two components, namely the host and activators (dopants). The host material is crucial to control the dopant distribution and keeps them at optimized distances to circumvent rapid non-radiative processes. The activators are small amounts of foreign atoms or ions incorporated in the host lattice to create luminescent centres (energy levels) that can be excited and emit the desired luminescence [4]. Dopants are usually lanthanide or other metal ions depending on the required emission. In some instances, such as wide band gap semiconductors, dopants may not be needed because the host has self-luminescent centres [5] (native defects or excitonic recombination) that emit light in the ultraviolet to the visible regions. For example; ZnO exhibit UV emission at about 380 nm which is due to the free exciton recombination, and bright green emission at about 500 nm which has been attributed to native oxygen vacancy (V_o) defect. In this study ZnO was used as a host and europium (Eu^{3+}) ions as dopant (activator).

2.1.1. Zinc oxide (ZnO)

ZnO is an inorganic compound that occurs naturally as a mineral zincite or is chemically synthesized. It was discovered in 1810 in Franklin (New Jersey, USA) by Bruce [6]. Since then it has been considered the most important compound of zinc minerals and it is being used in a wide range of applications. It is an abundant material in nature which made it cost-effective in

the large-scale of production. ZnO is a wide band gap (3.37 eV) semiconductor with large exciton binding energy (60 meV) at room temperature which makes it a suitable material for use in a variety of electronic and optoelectronic devices such as: light emitting diodes (LEDs) and flat panel displays (FPDs). ZnO is a superior wide band gap semiconductor because of its excellent properties including: good chemical stability, resistance to damage when confronted with high energy radiation, high electron mobility, excellent transparency, high resistance to thermal quenching and the ease of preparation. ZnO can be grown in different forms of nanostructures including nanorods, nanotubes, nanocomb, nanowalls, nanoflowers, nanobelts, nanorings, nanocages, nanosprings and nanohelices.

2.1.2. Crystal structure of ZnO

ZnO crystallizes in three different structures, namely the hexagonal wurtzite, zinc blende and rock salt structures [7]. In the rock salt structure, each Zn or O atom is surrounded by six nearest neighbours, unlike in the wurtzite and zinc blende structures for which each Zn or O atoms are surrounded by four nearest neighbours. The ionicity of the zinc blende ZnO is lower compared to that of wurtzite structure which leads to lower carrier scattering and high doping efficiencies (the ability to accommodate foreign impurities effectively). However, the preparation of zinc blende is very difficult and can be grown only by epitaxial growth on a cubic crystal substrate. The cubic rock salt structure can only be present at very high pressure (about 10 GPa) and it is not stable. ZnO prefers to crystallize in the hexagonal wurtzite structure with a symmetry point group $6mm$ and space group $P63mc$ at ambient conditions. Fig. 2.2 depicts the hexagonal wurtzite structure of ZnO. In the wurtzite structure, each zinc ion is surrounded by four oxygen ions which are arranged in a tetrahedral coordination, and alternatively each oxygen ion is surrounded by four zinc ions that are tetrahedrally coordinated along the c-axis [8]. The tetrahedral arrangement of the zinc and oxygen ions gives rise to a non-centrosymmetric crystal structure of ZnO, consisting of two sub-lattices of zinc and oxygen atoms penetrating each other to form a hexagonal close packed structure. The two zinc and oxygen sub-lattices are displaced with respect to each other by $3/8$ of the lattice parameter along the c-axis. The non-centrosymmetric structure is the reason behind the piezoelectric properties of ZnO, and plays a crucial role during the crystal growth. The wurtzite structure of ZnO has two polar face terminations amongst which are the Zn and oxygen terminations on the (0001) and (000 $\bar{1}$) planes, respectively, as well as another two non-polar terminations that contain an equal number of Zn and O atoms on the (1120) and (1010) planes [7]. The polar surfaces occurred due to their sudden termination by their outermost cations or anions in the case of Zn or O

terminated polar surfaces, respectively. The construction of the polar surfaces is due to the interactions of the cations (Zn) and anions (O) on the surface, and it depends on the polar charges distribution. The construction arrangements relax at the minimum electrostatic energy. This is the main reason behind the growth of ZnO in various nanostructure forms as well as the spontaneous polarization that is observed in ZnO.

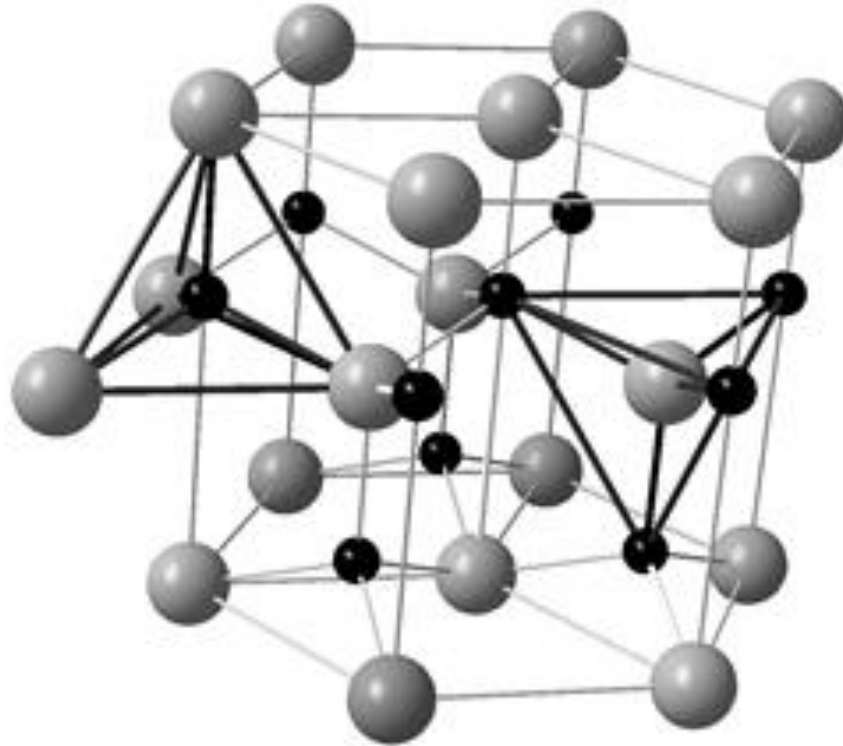


Fig. 2. 2. Hexagonal wurtzite structure of ZnO crystal [9].

2.1.3. Native point defects of ZnO

Due to imperfection of the crystal structure of ZnO, point defects always form during the crystal growth and they play a vital role on optical and electrical properties of ZnO. These defects are oxygen vacancies (V_o), oxygen interstitials (O_i), zinc vacancies (V_{Zn}), zinc interstitials (Zn_i), zinc antisites (Zn_o) and oxygen antisites (O_{Zn}) [10, 11]. Several theoretical and computational approaches have been implemented to understand their configurations, electronic structures and formation energies. Some of these methods are the ball-stick model, molecular orbital theory and density functional theory (DFT) [12, 13]. Generally, zinc and oxygen antisite defects have very high formation energies and they are not expected to occur at near equilibrium conditions, even in zinc or oxygen-rich environments, respectively [14]. Oxygen vacancies are the most studied defects in ZnO because of their low formation energies amongst donor defects. They can be formed in three types, including neutral, single and double ionized oxygen vacancies, and they have been thought to be the origin of the green luminescence at

about 500 nm observed in ZnO [15]. Zinc vacancies are acceptor defects located above the valence band maximum. They occur in three charges state resembling the oxygen vacancies case. Zinc interstitials are shallow donor defects with high formation energies that decreases with decreasing Fermi level to the valence band. They are stable at 2+ charge states and located below the conduction band minimum. Oxygen interstitials are double acceptor defects with relatively high formation energy and are favoured to form in oxygen-rich environments [16, 17]. Moreover, hydrogen impurities are also present in ZnO and have been associated with the formation of donor-like states of two types namely interstitials and substitutional hydrogen to oxygen atoms. Hydrogen atoms play a significant role in the electrical and optical properties of ZnO, as they can act as non-radiative centres which eventually reduces the luminescence intensity of ZnO [18, 19, 20]. The above mentioned defects create energy levels within the ZnO band gap, and they give emissions across the visible region along with the free exciton recombination ultraviolet at about 380 nm. Fig. 2.3 illustrate the suggested energy levels created due to the ZnO native defects and emission corresponding these energy levels.

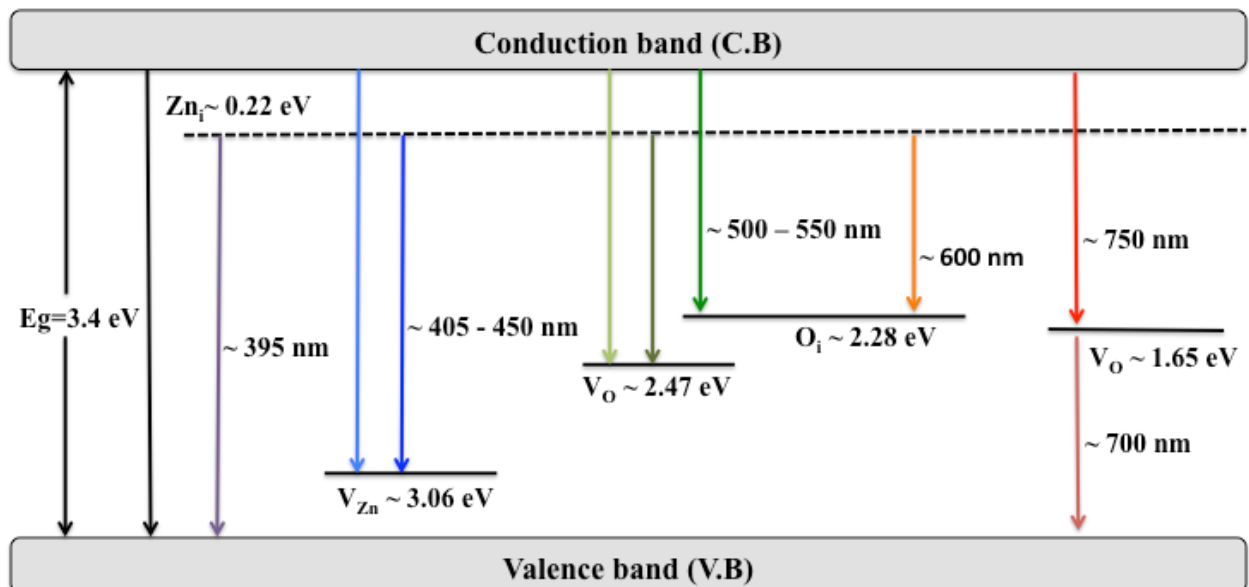


Fig. 2. 3. Schematic band diagram of ZnO deep level emissions (DLE), based on the full potential linear muffin-tin orbital method and other reported data [21].

2.1.4. Physical properties and parameters of ZnO in a hexagonal wurtzite structure

ZnO is naturally n-type semiconductor, while preparing p-type ZnO is proven to be difficult, although some groups reported p-type ZnO but it is not stable. Due to the non-centrosymmetric crystal structure, ZnO is a piezoelectrical material and suitable for many mechano-electrical transducer devices. The physical parameters of the hexagonal wurtzite ZnO are summarized in Table 2.1. The hole mobility and its effective mass are not asserted yet.

Table 2. 1. Physical properties of the ZnO in the wurtzite structure [9]

Lattice constant a_0	0.32495 nm
Lattice constant c_0	0.52069 nm
a_0/c_0	1.602 nm (1.633 nm for the ideal hexagonal)
Density	5.606 g/cm ³
Melting point	1975 °C
Boiling point	2360 °C
Thermal conductivity	0.6, 0.13, 1-1.2
Linear expansion coefficient (/°C)	a_0 : 6.5×10^{-6} , c_0 : 3.0×10^{-6}
Static dielectric constant	8.656
Energy band gap (direct)	3.44 eV at lower than room temperature and 3.37 eV at room temperature
Exciton binding energy	60 meV
Refractive index	2.008, 2.029
Intrinsic carrier concentration	$< 10^6 \text{ cm}^{-3}$ (max n-type doping $> 10^{20} \text{ cm}^{-3}$ electrons; max p-type doping $< 10^{17} \text{ cm}^{-3}$)
Electron effective mass	0.24
Electron hole mobility at 300 K for the low n-type conductivity	200 cm ² /Vs
Hole effective mass	0.59
Hole hall mobility at 300 K for low p-type conductivity	5.50 cm ² /Vs
Bulk hardness, H (GPa)	5.0 ± 0.1

2.1.5. Lanthanide ions (Ln^{3+})

Lanthanides are the 15 metallic chemical elements situated in the f-block of the periodic table, and they have atomic number of 57 to 71 from lanthanum to lutetium, respectively [22]. The trivalent form of lanthanide ions is the common and abundant form that is generally found in nature. These elements have special electronic configurations which distinguish them from the other metal elements. The partially filled 4f orbit of Ln^{3+} plays a profound role in their optical and magnetic properties. The general electronic configuration of lanthanides is $4f^n 5d^1 6s^2$, where n represents the number of electrons from 0 to 14 occupying the f-orbital. The trivalent state of lanthanides (Ln^{3+}) with electronic configuration $4f^n$ is the most stable oxidation state

especially in water [22]. The number of configurations within the 4f orbital is given by $[14!/n!(14-n)!]$, where each configuration has a particular energy level. The 4f orbitals are shielded by the filled 5s and 5p electron orbits. Therefore, they are less affected by the crystal field and the surrounding ligands. Hence, 4f-4f electron transitions are reasonably narrow lines in the excitation and absorption spectra [23]. According to the selection rules of electron transitions, 4f-4f electron transitions are forbidden via the electric dipole. However, they are allowed via the magnetic dipole moment or electric quadrupole. Electric dipole transition can take place with a very low probability. Although 4f-4f electron transitions are theoretically forbidden, introducing Ln^{3+} into a host crystal can increase the probability of such transitions. This is due to the interaction of the 4f electron wave functions with other wave functions of opposite parities of the host which form intra 4f-4f transitions. However, emission resulting from such transitions is weak and narrow.

Despite the small effect of the crystal field and the ligands on the 4f-4f transitions, it can split the energy levels which accounts for the final emission spectrum. The split caused by the crystal field (Stark splitting) is usually smaller than the separation due to spin-orbit coupling. Therefore, the emission and excitation spectra of Ln^{3+} in a host look similar to that of the free Ln^{3+} ion [24]. Fig. 2.5 illustrates the 4f transitions split due to the spin-orbit and crystal field interactions.

The Hamiltonian for a free Ln^{3+} ion can be written as [25]

$$H_F = \frac{\hbar^2}{2m} \sum_{i=1}^N \nabla_i^2 - \sum_{i=1}^N \frac{Ze^2}{r_i} + \sum_{i<j}^N \frac{Ze^2}{r_{ij}} + \sum_{i=1}^N \xi(r_i)(s_i \cdot l_i) \quad (2.1)$$

where the first term is the sum of kinetic energies of all 4f ion electrons, the second term represents the potential energies of all electrons in the nucleus field, the third term expresses the potential of the repulsive Coulomb interaction between electron pairs and the fourth term expresses the coupling between the spin angular momentum and the orbital angular momentum (spin – orbit interaction). When a free lanthanide ion introduced into a host lattice, the crystal field of that host will exert a force on the free Ln^{3+} ion, which finally perturbs the $2s + {}^1L_J$ states of the 4f levels and result in additional splitting (Stark splitting). Therefore, a new term of the crystal field can be added to the equation (2.1) and the perturbed Hamiltonian of a free ion can be written as

$$H = H_F + V_{CF} \quad (2.2)$$

where V_{CF} represents the Hamiltonian of the perturbation due to the crystal field around the Ln^{3+} ion. Stark splitting caused by the crystal field (V_{CF}) is smaller than the spin-orbit splitting (Fig. 2.4).

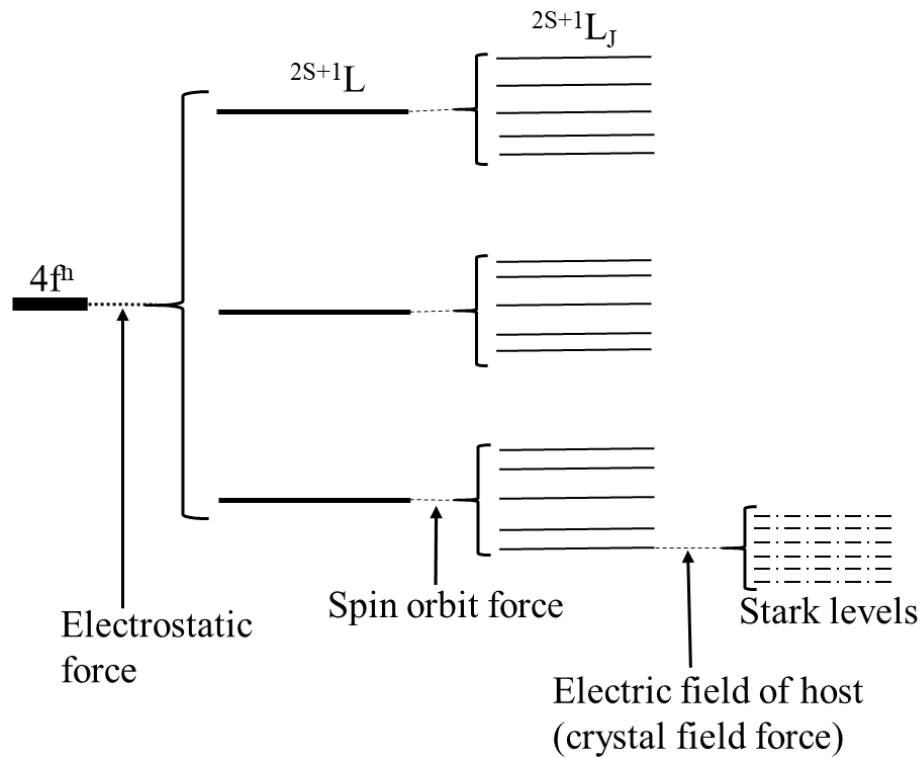


Fig. 2.4. Splitting of the $4f^n$ electronic configuration of Ln^{3+} ions due to atomic and crystal field [24].

The well-known Dieke diagram (Fig. 2.5) illustrates the energy levels of the 4f electrons of Ln^{3+} ions. The thickness of the line that represent the energy level, depicts the extent to which the energy level split due to the crystal field.

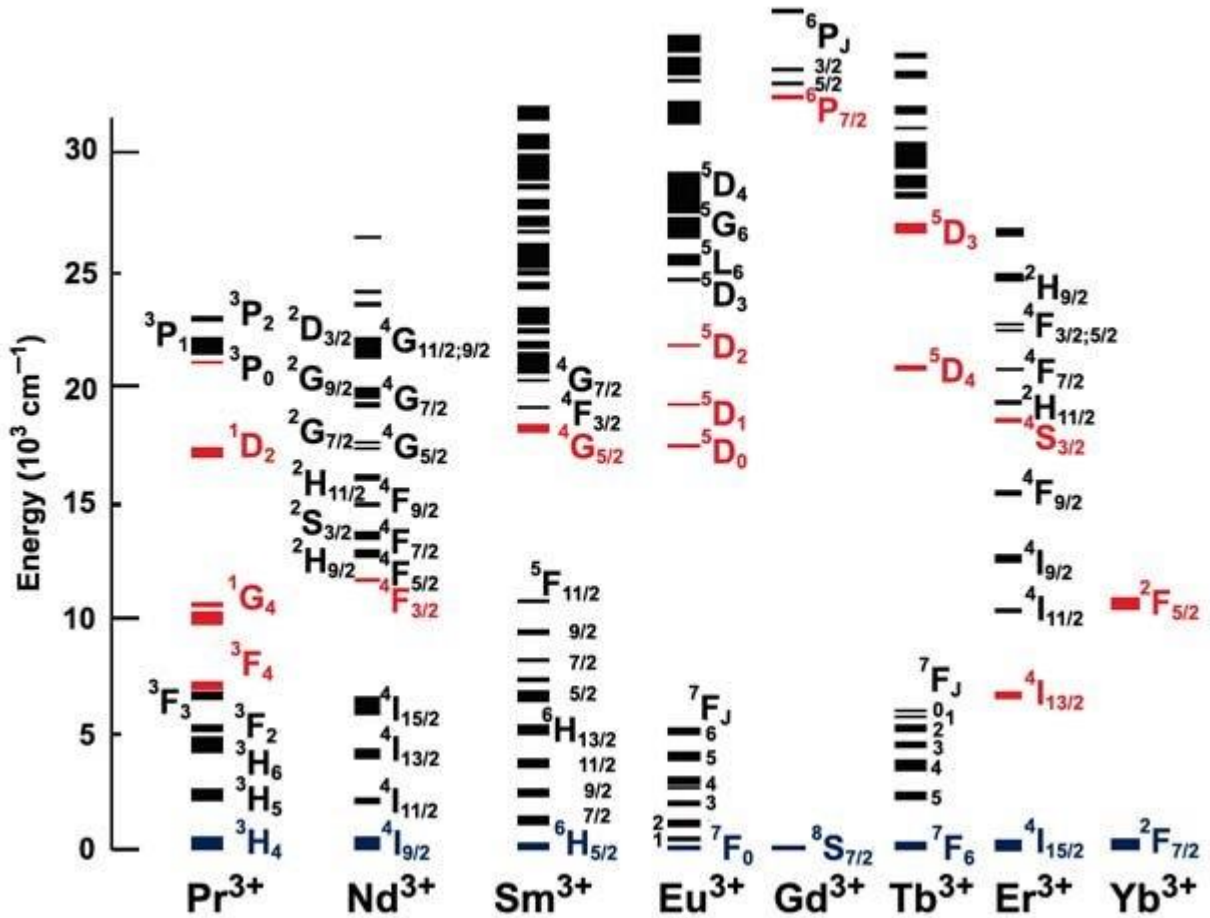


Fig. 2.5. Dieke diagram [22]

Apart from 4f-4f transitions which give weak emissions, 4f-5d transitions are allowed and have the potential to yield high intensity. The 5d orbital is greatly affected by the crystal field and the surrounding anion ligands compared to the spin-orbit interaction. Therefore the split of the 5d energy levels depends on the site symmetry of the Ln^{3+} ion in the lattice. The interaction between 5d energy level and the anion ligand of the crystal results in shifting of the 5d energy levels to lower energy levels and the bonding strength of 4f-5d result in a broad absorption band [26].

Charge transfer can also take place, where a 2p electron of the crystal anion will be transferred to the 4f orbital of the Ln^{3+} ion. This type of transfer is allowed and produces an intense broad absorption band [27]. Charge transfer can take place from the lanthanide dopant, host ions or defects. An efficient charge transfer from ZnO lattice defects to the Eu^{3+} ion is one of the proposed ways to improve the emission of Eu^{3+} ion incorporated in ZnO lattice, which is part of this study.

2.1.6. Europium ions ($\text{Eu}^{3//2+}$)

The Eu ion is one of the most studied lanthanide ions during the past decades. This because of their importance in optoelectronic applications [28]. The divalent Eu^{2+} ion gives emission from the $4f5d-4f^7$ transition, which depends on the crystal field. Therefore, it can be tuned for various wavelengths (from red to blue) in different hosts [29]. The trivalent Eu^{3+} ions with electronic configuration of $4f^75s^25p^6$ give narrow emission that dominate the red region. In this work we dealt with Eu^{3+} ion for red luminescence materials. Fig. 2.6 (a) depicts the absorption and emission spectra of Eu^{3+} incorporated in ZnO and (b) the corresponding energy levels of the emission and absorption. The broad band at ~ 288 nm of the excitation spectrum is due to the charge transfer between $\text{Eu}^{3+} - \text{O}^{2-}$.

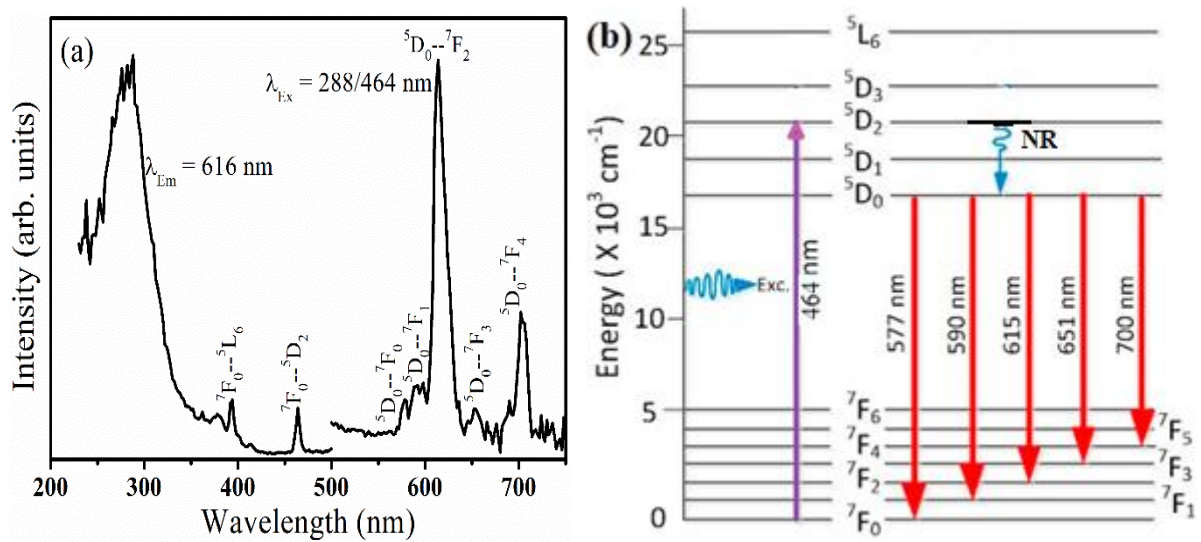


Fig. 2.6. (a) Excitation and emission spectra of Eu^{3+} ions doped ZnO thin film, and (b) Energy levels diagram of Eu^{3+} ion [30].

2.2. Energy transfer

As it is well-known that the $4f - 4f$ electrons of the lanthanide ions are well-shielded by the $5s$ and $5p$ outer most orbits. Based on the selection parity rule, the $4f - 4f$ electric dipole transitions are forbidden. Therefore, they exhibit very weak absorption efficiency. When a lanthanide ion is introduced into the asymmetric solid host, the probability of these transitions slightly increases and hence the absorption efficiency of the intra-configurational $4f$ transition increases. However, the corresponding emission remains narrow and weak [31]. Therefore, an energy transfer from different excited centres to the activator centres (Ln^{3+} ions) is needed to enhance the emission intensity of the activators. Generally, energy transfer occurs when an excited centre (S^*) transfers its excitation energy to an activator centre (A) during the returning

of the excited electron to its ground state. The following analogy is used to explain the energy transfer from sensitizer to activator.



The excited centre (S^*) is then called sensitizer and A is the activator. The sensitizer can be intentionally added impurities, crystal defects or lanthanide ions. S represents the emission of the excited centre (S^*). A^* represents the excited state of the sensitized activator which can decay radiatively or non-radiatively. In case of non-radiative decay of the A^* , the activator will be called quencher of the S emission. Most of the used sensitizers are metals (Bi^{3+} , Pb^{2+} , etc.) which is due to their strong optical absorption in the ultraviolet region [32, 33], which is attributed to the parity allowed $s^2 \rightarrow sp$ transition; the case may be applied to the energy transfer from crystal anion defects (as sensitizer) to activator in the case of metal oxide hosts. Fig. 2.7 depicts the energy levels of sensitizer and activator centres separated in a solid host by a certain distance R.

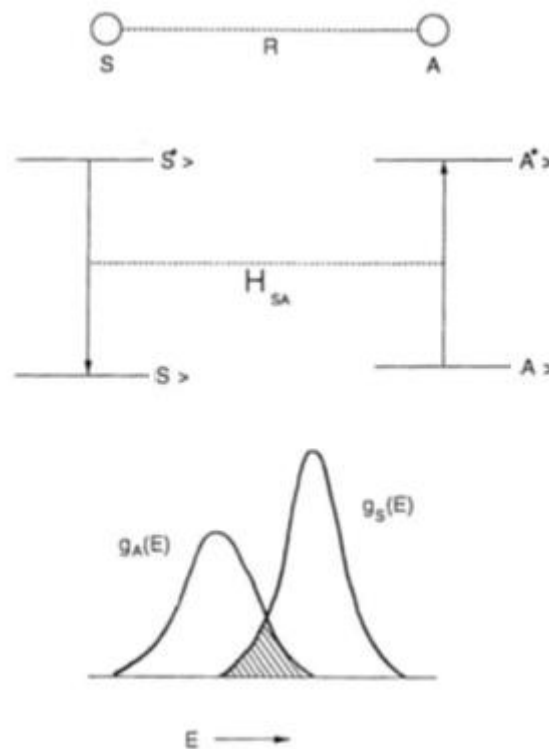


Fig. 2.7. Energy transfer between the S and A centers separated at distance R (top). The energy levels of S and A as well as their interaction H_{SA} are given in the middle. The spectral overlap is demonstrated at the bottom [34].

For the energy transfer to take place; the energy difference between the sensitizer (S^*) and the activator A must be equal (resonant transfer), as well as the distance (R) must be short enough

to allow interaction between (S^*) and A. The interaction can occur either via an exchange interaction (in case of overlap between the wave functions of the two centres), or via an electric or magnetic multipolar interaction [35]. The resonant transfer can be verified by the spectral overlap of S emission and A absorption. The transfer probability is given by the Dexter expression [36]

$$P_{SA} = \frac{2\pi}{\hbar} |\langle S, A^* | H_{SA} | S^*, A \rangle|^2 \int g_s(E) g_A(E) dE \quad (2.4)$$

where H_{SA} represents the interaction Hamiltonian, $g_s(E)$ and $g_A(E)$ are the normalized shape functions of the S emission and A absorption, respectively. The integral reflects that energy conservation is essential. From the equation, the transfer probability diminishes with reduction in overlap. Overlap between the wave function of S^* and A is required for the exchange interaction, and the dependence of the transfer rate on R distance is exponential. The transfer rate dependence on the distance R for electric dipole - dipole, dipole - quadrupole interaction, is given by R^n where $n = 6, 8, 10$. An important parameter is being driven when the transfer rate (P_{SA}) is equal to the emission rate of the sensitizer (P_S). This parameter is called the critical distance (R_c) which play a significant role in the energy transfer process. If $R > R_c$, the radiative emission from S^* centre dominates, whereas if $R \leq R_c$, energy transfer from S^* to A dominates.

2.3. Charge transfer

In this case, the optical transition is due to the chemical bonding between two different ions (anions and cations) [37]. An electron from the 2p orbital of a neighbouring anion (e.g. oxygen in oxides) is transferred to another cation in the host or to the 4f orbit of lanthanide ions. Excitation of this kind strongly alter the charge distribution of the optical centre which subsequently causes considerable change to the chemical bonding state. This state of charge transfer results in a strong and broad absorption spectrum. Some examples of the systems that involve charge transfer are CaWO_4 and MgWO_4 . CaWO_4 has been used for decades to detect X-rays. This compound shows luminescence that originates from charge transfer between W and O in the WO_4 group. The MgWO_4 compound is used in early generation of blue emission for fluorescent lamps. Its blue emission originates from energy transfer from oxygen ions to empty d-levels of the tungsten ion. In this type of luminescent materials, no intentional dopants are needed and therefore they are called self-activated luminescent materials. A modern example of charge transfer is the transfer from oxygen ions of oxide crystals to the 4f orbit of the Eu^{3+} ion incorporated in the host. The result of this charge transfer exhibits a broad

absorption spectrum centred at ~ 236 up to 304 nm depending on the host properties [38], as well as characteristic emission of 4f – 4f transitions of Eu^{3+} . Fig 2.6 (a) shows charge transfer spectra of Eu^{3+} doped ZnO thin film.

2.4. Concentration quenching

The concentration quenching phenomenon is always observed in lanthanide (Ln^{3+}) ion doped materials, where the luminescence efficiency decreases at a certain Ln^{3+} ion concentration, usually at high concentration. This phenomenon is closely associated to the distance R between Ln^{3+} ions. When the distance R between the radiative centres is short enough (about 10 \AA), energy transfer between the same centres (Ln^{3+} ions) can occur and then energy migration will take place. This process shifts the excitation energy far from where it occur, and hence the excitation energy will be transferred to a site where non-radiative occurs (quencher or killer site) [39]. Although the fact that 4f electrons of Ln^{3+} are well-shielded and their radiative rate is weak, the spectral overlap can be great [39]. Therefore, energy transfer between Ln^{3+} ions can easily surpass the radiative rate.

2.5. Applications of luminescent materials

Luminescent materials are basically transducers which convert energy from one form to another such as electric field to light (electroluminescence) or vice versa (photovoltaic), electron kinetic energy to light (cathodoluminescence), photon with short wavelength to another with long wavelength (down conversion) or vice versa (up conversion), etc. Therefore, they are used in a wide range of lighting applications including: fluorescent lamps, light emitting diodes (LEDs), flat panel displays (FPDs), solar cells, etc. The choice of the luminescent material properties depends mainly on the device nature (design, operation principle and the device output) that the material will be used in. In this section, examples of today's technologies and devices that use luminescent materials are given, as illustrated in Fig. 2.8.

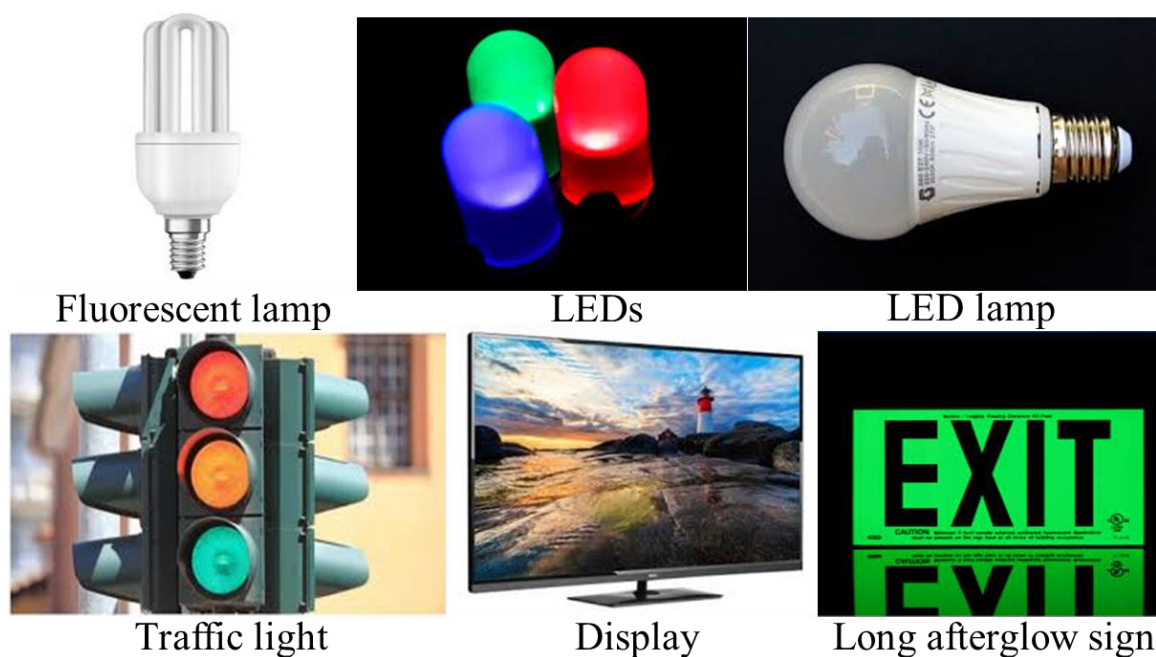


Fig. 2.8. Some applications of luminescent materials.

2.3. References

- [1] K. V. R. Murthy and H. S. Virk, Luminescence Phenomena: An Introduction, *Defect and Diffusion Forum* **347** (2014) 1-34. doi:10.4028/www.scientific.net/DDF.347.1.
- [2] X. Huang, S. Han, W. Huang and X. Liu, Enhancing solar cell efficiency: the search for luminescent material as spectral converters, *Chem. Soc. Rev.* **42** (2013) 173. doi: 10.1039/c2cs35288e, 2013.
- [3] Bernard Valeur, *Molecular Fluorescence Principles and Applications*, New York: Wiley-VCH, 2001.
- [4] H. Wen and F. Wang, Lanthanide-Doped Nanoparticles: Synthesis, Property, and Application, *In Nanocrystalline Materials*, Amsterdam, Netherlands: Elsevier, 2014, pp. 121-160. <https://doi.org/10.1016/B978-0-12-407796-6.00004-X>.
- [5] J. Zhou, F. Huang, J. Xu, H. Chen and Y. Wang, Luminescence study of a self-activated and rareearth activated $\text{Sr}_3\text{La}(\text{VO}_4)_3$ phosphor potentially applicable in W-LEDs, *J. Mater. Chem. C* **3** (2015) 3023-3028. doi: 10.1039/c4tc02783c.
- [6] D. S. Ginley and J. D. Perkins, *Handbook of Transparent Conductors*, Boston, MA: Springer, 2011.

- [7] V. A. Coleman and C. Jagadish, Basic Properties and Applications of ZnO, *In Zinc oxide bulk, thin films and nanostructures*, Amsterdam, Netherlands: Elsevier Science Ltd, 2006, pp. 1-20.
- [8] P. J. P. Espitia, N. D. F. F. Soares, J. S. dos Reis Coimbra, N. J. de Andrade, R. S. Cruz and E. A. A. Medeiros, Zinc Oxide Nanoparticles: Synthesis, Antimicrobial Activity and Food Packaging Applications, *Food Bioprocess Technol* **5** (2012) 1447–1464. doi 10.1007/s11947-012-0797-6.
- [9] T. Hanada, Basic Properties of ZnO, GaN, and Related Materials, *In Oxide and nitride semiconductors*, Berlin, Heidelberg: Springer, 2009, pp. 1-19. doi:10.1007/978-3-540-88847-5_1.
- [10] F. A. Selim, M. H. Weber, D. Solodovnikov and K. G. Lynn, Nature of Native Defects in ZnO, *Phys. Rev. Lett* **99** (2007) 085502. doi:10.1103/PhysRevLett.99.085502.
- [11] M. D. McCluskey and S. J. Jokela, Defects in ZnO, *J. Appl. Phys.* **106** (2009) 071101-071114. doi: 10.1063/1.3216464.
- [12] F. Oba, M. Choi, A. Togo and I. Tanaka, Point defects in ZnO: an approach from first principles, *Sci Technol Adv Mater.* **12** (2011) 034302. doi: 10.1088/1468-6996/12/3/034302.
- [13] W. Mackrodt, R. Stewart, J. Campbell and I. Hillier, The calculated defect structure of ZnO, *J. Phys. Colloq.* **41** (1980) C6-64-C6-67. DOI : 10.1051/jphyscol:1980617.
- [14] A. Janotti and C. G. Van de Walle, Native point defects in ZnO, *Phys. Rev. B* **76** (2007) 165202. <https://doi.org/10.1103/PhysRevB.76.165202>.
- [15] F. Oba, S. R. Nishitani, S. Isotani and H. Adachi, Energetics of native defects in ZnO, *J. Appl. Phys.* **90** (2001) 824 - 828. <https://doi.org/10.1063/1.1380994>.
- [16] A. Janotti and C. G. Van de Walle, Fundamentals of zinc oxide as a semiconductor, *Rep. Prog. Phys.* **72** (2009) 126501 - 126530. doi:10.1088/0034-4885/72/12/126501.
- [17] A. M. Gsies, J. P. Goss, P. R. Briddon, R. M. Al-habashi, K. M. Etmimi, K. A. Marghani, Native point defects in ZnO, *Int. J. Math. Comput. Phys. Elec. Comput. Eng.* **8(1)** (2014) 127-132.
- [18] J. Bang and K. J. Chang, Atomic Structure and Diffusion of Hydrogen in ZnO, *J. Korean Phys. Soc.* **55** (2009) 98 -102. DOI: 10.3938/jkps.55.98.

- [19] A. B. Usseinov, E. A. Kotomin, Yu. F. Zhukovskii, J. Purans, A. V. Sorokin and A. T. Akilbekov, Atomic and electronic structure of hydrogen on ZnO (1-100) surface: ab initio hybrid calculations, *In IOP Conf. Series: Materials Science and Engineering*, **49** (2013) 012054.
- [20] A. B. Usseinov, E. A. Kotomin, A. T. Akilbekov, Yu. F. Zhukovskii and J. Purans, Hydrogen adsorption on the ZnO (1-100) surface: ab initio hybrid density functional linear combination of atomic orbitals calculations, *Phys. Scr.* **89** (2014) 045801- 045808. doi: 10.1088/0031-8949/89/04/045801.
- [21] N. H. Alvi, K. ul Hasan, O. Nur, M. Willander, The origin of the red emission in n-ZnO nanotubes/p-GaN white light emitting diodes, *Nanoscale Res. Lett* **6.1** (2011) 130, doi: 10.1186/1556-276X-6-130.
- [22] J. C. G. Bu' Nzli, Benefiting from the Unique Properties of Lanthanide Ions, *Acc. Chem. Res.* **39** (2006) 53-61. doi:10.1021/ar0400894.
- [23] G. Blasse, The physics of new luminescent materials, *Mater. Chem. Phys* **16** (1987) 201-236. doi:10.1016/0254-0584(87)90100-3.
- [24] P. C. de Sousa Filho, J. F. Lima and O. A. Serra, From Lighting to Photoprotection: Fundamentals and Applications of Rare Earth Materials, *J. Braz. Chem. Soc.* **26** (2015) 2471-2495. <http://dx.doi.org/10.5935/0103-5053.20150328>.
- [25] E. U. Condon and G. H. Shortley, The theory of atomic spectra, Cambridge, United Kingdom: Cambridge University Press, 1951.
- [26] X. Qin, X. Liu, W. Huang, M. Bettinelli and X. Liu, Lanthanide-Activated Phosphors Based on 4f-5d Optical Transitions: Theoretical and experimental aspects, *Chem. Rev.* **117** (2017) 4488–4527. doi: 10.1021/acs.chemrev.6b00691.
- [27] A. H. Krumpel, P. Boutinaud, E. van der Kolk and P. Dorenbos, Charge transfer transitions in the transition metal oxides $ABO_4:Ln^{3+}$ and $APO_4:Ln^{3+}$ (A=La, Gd, Y, Lu, Sc; B=V, Nb, Ta; Ln^{1/4}lanthanide), *J. Lumin.* **130** (2010) 1357–1365. doi:10.1016/j.jlumin.2010.02.035.
- [28] P. Dorenbos, Valence Stability of Lanthanide Ions in Inorganic Compounds, *Chem. Mater.* **17** (2005) 6452-6456. <https://doi.org/10.1021/cm051456o>.
- [29] N. Higashiyama, Y. Izumi and G. Adachi, Fluorescence properties of europium(II) and other divalent metal ion doubly-doped poly(methacrylate containing 15crown-5

- structure) complexes, *Inorganica Chim. Acta* **207** (1993) 233-240, doi:10.1016/s0020-1693(00)90715-1.
- [30] E. H. H. Hasabeldaim, O. M. Ntwaeaborwa, R. E. Kroon, E. Coetsee and H. C. Swart, Photoluminescence and cathodoluminescence of spin coated ZnO films with different concentration of Eu^{3+} ions, *Vacuum* **169** (2019) 108889. <https://doi.org/10.1016/j.vacuum.2019.108889>.
- [31] J. H. Van Vleck, The puzzle of rare-earth spectra in solids, *J. Phys. Chem.* **41** (1937) 67-80, <https://doi.org/10.1021/j150379a006>.
- [32] V. Babin, K. D. Oskam, P. Vergeer, A. Meijerink, The role of Pb^{2+} as a sensitizer for Gd^{3+} - Eu^{3+} downconversion couple in fluorides, *Radiat. Meas* **38** (2004) 767 – 770, doi:10.1016/j.radmeas.2003.12.015.
- [33] A. A. Setlur, A. M. Srivastava, The nature of Bi^{3+} luminescence in garnet hosts, *Opt. Mater* **29** (2006) 410–415, doi:10.1016/j.optmat.2005.09.076.
- [34] B. D'Artolo, Energy Transfer Processes in condensed matter, Berlin, Germany: Springer Science & Business Media, 2012.
- [35] D'Artolo and Baldassare, energy transfer process in condensed matter, Berlin, Germany: Springer Science & Business Media, **114** 2012.
- [36] S. Bai, P. Zhang, P. Antoniou, S. S. Skourtis, D. N. Beratan, Quantum interferences among Dexter energy transfer pathways, *Faraday Discuss.* **216** (2019) 301-318, doi:10.1039/C9FD00007K.
- [37] J. Ulstrup, Charge Transfer Processes in condensed media, Berlin, Germany: Springer Science & Business Media, 2012.
- [38] X. Liu, L. Li, H. M. Noh, B. K. Moon, B. C. Choi and J. H. Jeong, Chemical bond properties and charge transfer bands of O^{2-} - Eu^{3+} , O^{2-} - Mo^{6+} and O^{2-} - W^{6+} in Eu^{3+} -doped garnet hosts $\text{Ln}_3\text{M}_5\text{O}_{12}$ and ABO_4 molybdate and tungstate phosphors, *Dalton Trans.* **43** (2014) 8814. DOI: 10.1039/c4dt00674g.
- [39] D. L. Dexter and J. H. Schulman, Theory of Concentration Quenching in Inorganic Phosphors, *J. Chem. Phys.* **22** (1954) 1063 -1070. doi: 10.1063/1.1740265.

Chapter 3

Experimental techniques

This chapter is divided into two main sections: section 3.1 is devoted to explaining the basic theory, principles and operation of the thin film preparation techniques, as well as the dynamics of the formation of the thin film. Section 3.2 is devoted to the basic principles underlying the characterization techniques.

3.1. Thin film preparation

In this section a brief description of the pulsed laser deposition (PLD), spin coating technique and chemical bath deposition (CBD) is given.

3.1.1. Pulsed laser deposition (PLD)

PLD is a physical vapour deposition technique that solely depends on interaction of light with matter [1], in which high energy focused light (laser) strikes a solid surface that vaporises and condenses on a substrate to form a thin film. The experimental setup of the PLD is quite simple as illustrated in Fig. 3.1. In the typical process, a solid material (target) and a substrate are held opposite to each other with a certain distance in a vacuum chamber. A laser beam is directed onto the target surface through a quartz window, while the target is usually rotated and rastered concurrently to avoid laser-pinning effects on the target surface. Once the laser beam strikes the target surface, a vapour/ plasma plume of the target material is generated in a cone shape toward the substrate. The plasma plume axis is normal to the target surface [2]. The plasma plume reaches the substrate surface and then nucleates, condenses and forms the film [3]. Although the PLD set up is simple, the physical processes taking place during vaporization of the target material, formation of the plasma plume and condensation of the ejected material (plasma plume) on to the substrate (deposition) are very complicated. These physical processes are divided into three levels including: ablation of the target material, expansion of the ejected particle (plasma plume formation) and condensation of the ejected particles on the substrate [4].

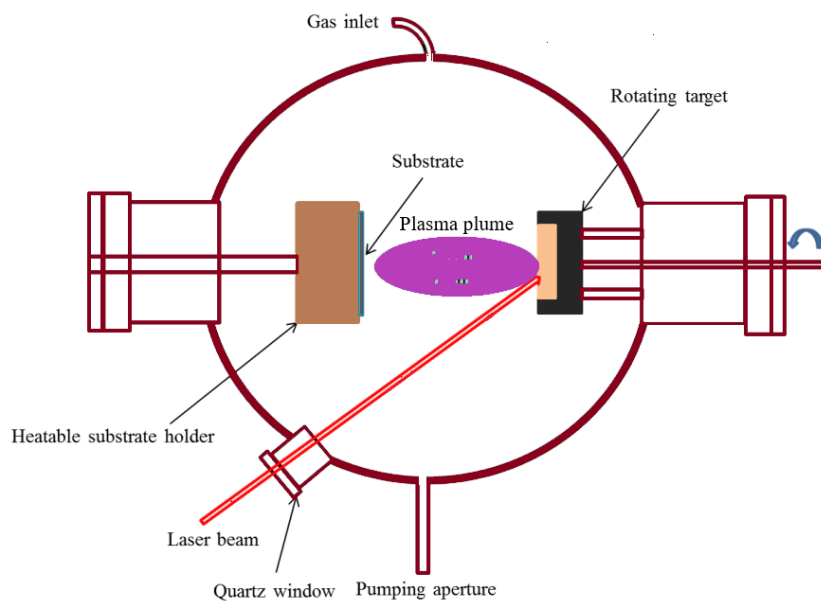


Fig. 3.1. Schematic diagram of a PLD setup.

3.1.1.1. Ablation

Ablation is the removal of material from the target surface when the laser beam interacts with the target material. Ablation may occur via vaporization, chipping or any other erosive processes. There are many mechanisms by which the laser beam interacts with the target materials such as photo-thermal, photo-chemical and hydro-dynamical ablation processes [3].

Photo-thermal ablation

This process takes place when the laser energy is absorbed as heat by the material. Before the chemical bonds of the material are broken, the absorbed energy heats the target to a very high temperature reaching to the material boiling/vaporization point, and then leads to the vaporization of the target material [5].

Photo-chemical ablation

This process occurs when the laser energy is absorbed directly by the electronic bands of the material, leading to instant breaking of the bonds and subsequent evaporation.

Hydro-dynamical ablation

This process causes the target surface to melt and to form small droplets, the ejected particles are ablated in a liquid form. This process leads to the formation of bulk material, particulates or droplets on the film surface, and they can be identified by their unique spherical shape [6]. The interaction between the laser and the target depends on the laser energy and wavelength as well as the band gap of the target material. Other parameters of the laser beam, compactness and rigidity of the target material may also influence this process.

3.1.1.2. Expansion of the plasma plume (ablated particles)

This process takes place immediately after the ablation occurred, the plasma plume expands toward the substrate usually in a cone shape with a direction normal to the target surface. The plume may consist of ions, atoms, molecules and clusters. The expansion of the plume depends on the surrounding gas pressure. The plume particles interact with the gas molecules through collisions, which reduce the kinetic energy of the plume particles. The plume expansion takes the shape of a $\cos^n(\theta)$ function, where the higher order of n results from the higher laser energy and low gas pressure, which leads to a more directional plume. The visible light of the plume is due to the fluorescence of the target material. Fig. 3.2 shows the effect of different O₂ pressures on the plume shape as reported by T. Haugan et al [7]

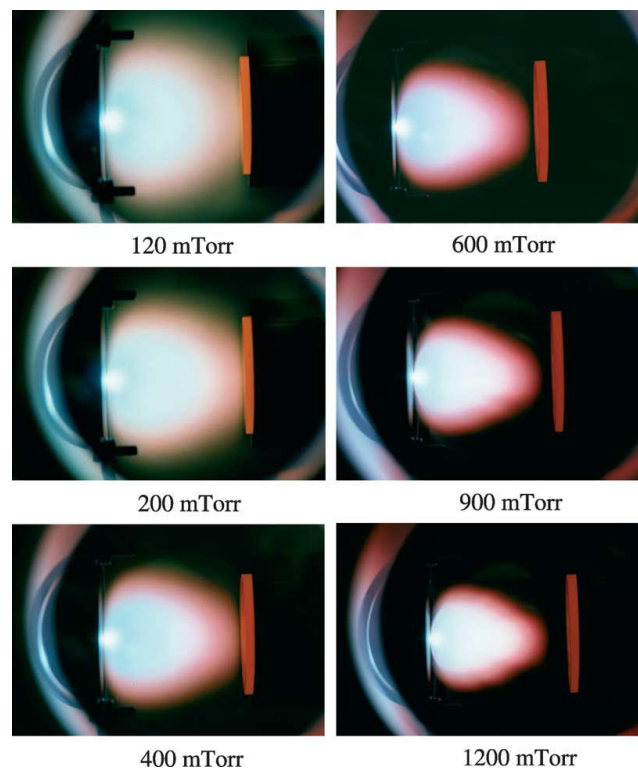


Fig. 3.2. Photographic images of a $\text{YBa}_2\text{Cu}_3\text{O}_{7-\delta}$ plume ablated at different O₂ pressures [7].

3.1.1.3. Deposition of the film

Different theoretical and experimental studies were performed to understand the process of the deposition of the ablated material on the substrate. Generally, the deposition takes place through nucleation and growth processes. The step-by-step model is still the best way to explain the film formation process [8]:

1. The ejected species of the plume reach the substrate, lose their velocity components by impacting on the substrate and then get adsorbed on the substrate surface. This takes place if the incident energy is not too high.

2. Due to the thermal disequilibrium between the adsorbed species and the substrate surface, the adsorbed species interact with themselves and form bigger clusters/nuclei.
3. The clusters are thermodynamically unstable. Therefore, this stage depends on the deposition parameters (maybe substrate temperature). If the deposition parameters are suitable to offset the instability of the clusters/nuclei, the adsorbed species (clusters) collide with each other and grow in size until reaching the critical size and become thermodynamically stable. This stage is called nucleation.
4. Formation of islands. In this stage the nuclei with critical sizes grow in number and again in size until they reach a saturation nucleation density. At this point the growth rate is much higher than the first nucleation growth.
5. Coalescence of the islands. In this stage the formed islands coalesce and agglomerate together in an attempt to reduce the substrate surface area.
6. Film formation: During this stage the grown larger islands stick together and form a discontinuous film with unfilled areas like channels and holes. As the islands continue to grow and stick together, channels and holes are filled and the film becomes completely continuous.

These growth processes are dependent on the thermodynamic parameters of PLD deposition such as substrate surface, temperature, gas pressure, laser energy, etc.

The step-by-step model of the film growth processes is illustrated in Fig. 3.3 and can be summarized as follows [9];

- a. Volmer-Weber step (island type).
- b. Frank-van der Merwe step (layer type).
- c. Stranski-Krastanov step (mixed type).

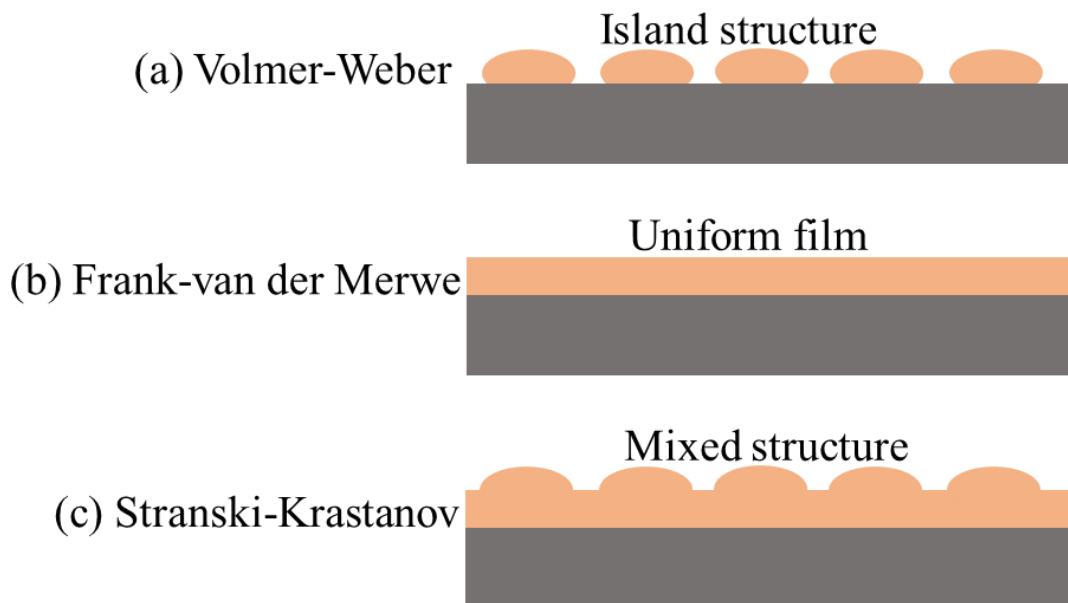


Fig. 3.3. Three stages of the step-by-step growth model of a PLD thin film [10].

3.1.1.4. Advantages of pulsed laser deposition (PLD)

PLD has its own advantages [11] over the other deposition techniques such as chemical vapour deposition (CVD), spin coating, electron beam evaporation, radio frequency, etc. These advantages include:

- 1- Simplicity: the experimental setup and procedures of PLD are simple.
- 2- Versatility: PLD offers a number of parameters to vary by which a fine control of the film properties can be obtained. These parameters are: laser wavelength, energy, frequency and fluence, vacuum, different types of gas and their pressure, substrate temperature and the distance of the substrate from the target.
- 3- Use of reactive gases: PLD offers an option of using reactive gases such as oxygen during deposition, by which a fine control of the optical and electrical properties of oxide material films can be obtained. And hence, post annealing process may not be needed.
- 4- Deposition at room temperature: Highly crystalline films can be deposited at room temperature, which gives opportunity to use flexible substrates.
- 5- In-situ deposition: different materials can be deposited from multiple targets without opening the PLD chamber and contaminate the film. This offer the possibility to achieve high quality and high performance devices.
- 6- Materials saving: only a small amount of the target material is used for the film deposition.

- 7- The ability to realize stoichiometric transfer of ablated material from multiple targets for many materials is readily possible.

3.1.1.5. Disadvantages and limitations of PLD

Despite the excellent advantages of PLD, there are still two main limitations that hold it back from being used in a wide range of commercial fields [11]. These limitations are:

1. Particulates: the presence of micron and sub-micron particles on the film surface and inside the film negatively affect the quality of the film. The origin of these particulates is associated with the laser beam-target material interaction. There are some research that has shown the possibility of eliminating these particulates by using two laser beams with different angles of incident.
2. Difficult to scale-up on a large wafer: achieving a uniform film on a large area is challenging. This is due to the directional and small diameter of the plume (ejected particles) nature, i.e. only an area of about 1 cm² can be deposited uniformly. Research has shown that this issue can be overcome by simultaneously rotating the substrate as well as rastering the laser beam over a large diameter area on the rotated target.

3.1.2. Spin coating technique

Spin coating is a popular deposition technique that has been used for decades in the field of microelectronics fabrication. The deposition mechanism of coating is dependent on the centripetal force that is induced on a spun substrate, and finally causes the solution to spread off toward the substrate edges leaving a thin layer of a material [12]. In a typical spin coating experiment, a solution containing the required precursors of the film material is needed. For example, zinc acetate dehydrate is needed for ZnO thin films. The precursors are dissolved in solvents such as organics (Ethanol) to form the solution, and stabilizers such as (monoethanolamide MEA) are also required to avoid precipitation of the precursor's ions. The solution can be prepared by different chemical methods in different forms such as sol-gel [13], suspension or colloid solutions. For the coating (casting) process, a substrate is held on the spin coater chuck by using a vacuum pump, the stock solution is dispensed (dropped) on the substrate surface until it is covered by the solution. The substrate then spun for a required time to fling off the solution. Preheating to a relatively low temperature is needed to evaporate the unwanted chemicals such as the organic solvent, and finally a thin layer of the thin film material is left [14]. This process can be repeated many times to achieve the required thickness. The resulting film is mostly amorphous, therefore post annealing treatment is required to obtain the crystalline phase of the film. Fig. 3.4 illustrates the spin coating process.

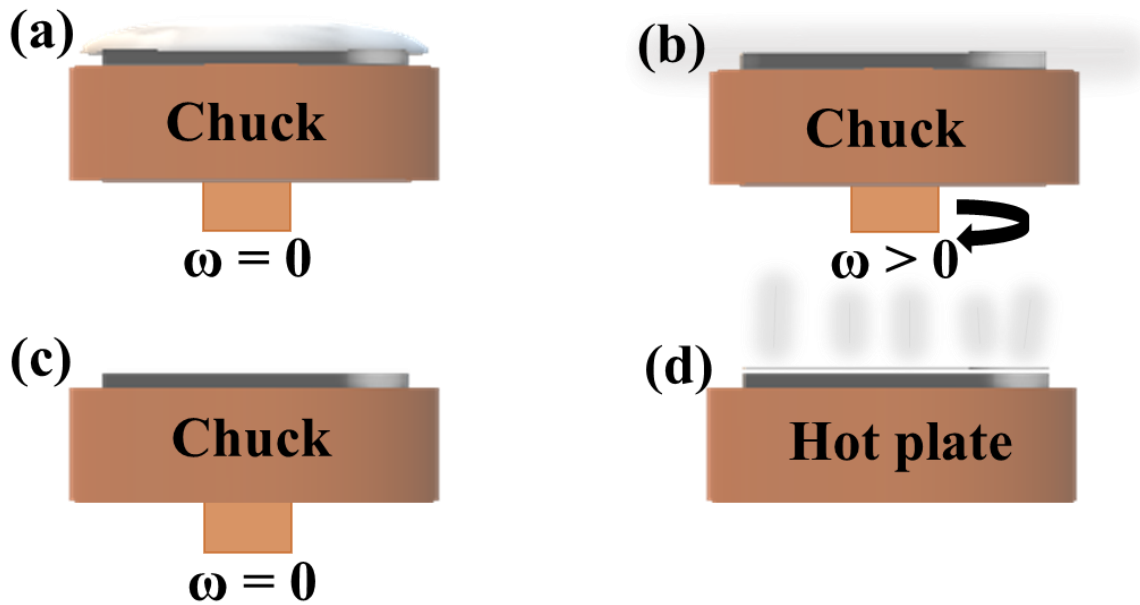


Fig. 3.4. Schematic diagram of the spin coating technique and process [15].

There are several parameters that can be varied in the spin coating process to control the final physical properties of the thin film. These parameters can be divided into three categories:

1. Solution parameters which include the solution type (sol-gel, suspension, colloid solutions), molarity and chemicals ratio.
2. Machine parameters including time of spinning, speed of the spinning and acceleration toward the final speed.
3. The surrounding environment parameters including humidity, dust particles, air speed and noise created by the user (operator). However, these parameters have less effect on the film properties [15].

3.1.2.1. Advantages and disadvantages [12]

The spin coating technique holds several advantages over the other deposition techniques, these advantages can be summarized as follow:

- a- Simplicity and cost-effective technique [13].
- b- Uniform and homogeneous films over a large substrate area can easily be deposited.
- c- Low crystallization temperature.
- d- Less time period is needed for the coating process.

As any other deposition technique, spin coating technique also has its own disadvantages such as:

1. Wastages of materials, only about 2% to 5% of the solution will be used.
2. The spinning rate efficiency decreases with increasing the substrate size.

A SPEN 150 spin coater from Semiconductor Production System at the University of the Free State was used in this study.

3.1.3. Chemical bath deposition (CBD)

CBD is a deposition technique that uses an aqueous chemical growth (ACG) method to produce ZnO nanostructured films (nanorods). ACG was first described by Vayssieres et al. [16]. In the CBD deposition process, an equimolar ratio of zinc nitrate hexa-hydrate ($\text{Zn}(\text{NO}_3)_2 \cdot 6\text{H}_2\text{O}$) and hexa-methylene-tetra mine (HMT, $\text{C}_6\text{H}_{12}\text{N}_4$) solution with molarity usually ranging from 0.01 to 0.1 can be used. The stock solution is kept in a beaker, which is inserted in a chemical bath with growth temperature ranging from 50 °C to 100 °C. A substrate is immersed in the solution with a particular angle and then the growth continues for a few hours (2 – 5 h). In this work the substrate was placed with a growth face downward to the bottom of the solution. Different materials such as Cu_2O , TiO_2 , etc. can be grown in their different nanostructured forms using CBD. Fig. 3.5 shows a similar CBD setup that was used in this study.

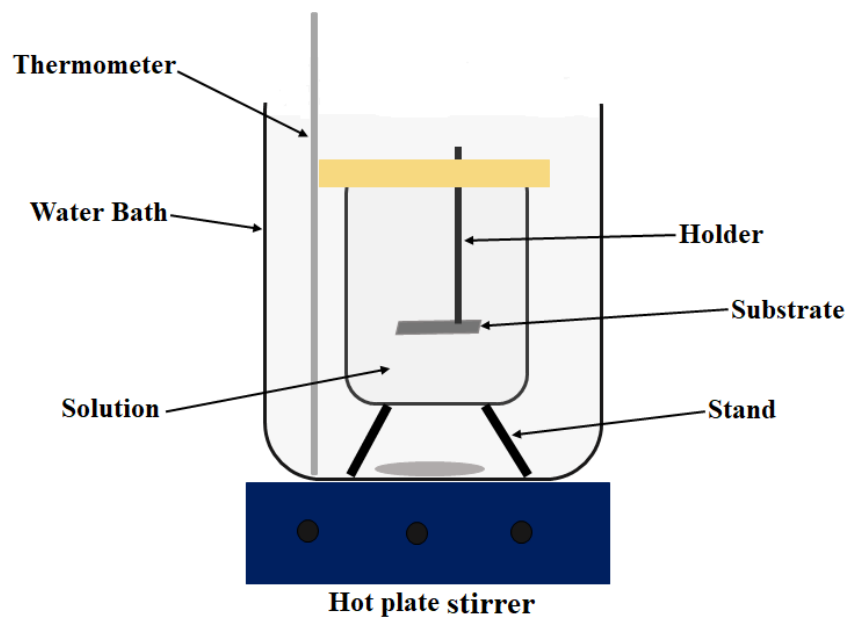
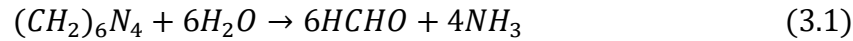


Fig. 3.5. CBD experimental setup.

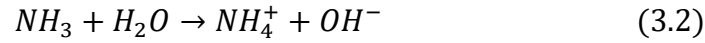
3.1.3.1. Mechanisms underlying the growth processes in CBD

The basic principle behind the ACG and CBD process is merely relying on the chemical reaction and equilibrium of the reactants and the solvent, as well as the nature of the substrate. The principle is similar to precipitation reactions which are based on the relative solubility of the products. Precipitation takes place when the ionic products of reactants exceed the solubility product, re-dissolution of the produced solid phase occurs when the ionic product is less than the solubility product. The reaction temperature, type of the solvent and particle size are significant factors affecting the solubility product. For the growth of ZnO nanorods by CBD

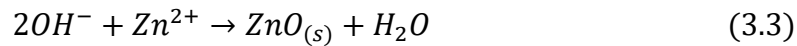
the following reactions will take place. Firstly, HMT reacts with water and produces ammonia according to the following reaction:



The produced ammonia reacts again with water and dissociates into ammonium and hydroxide ions:



The hydroxide ions react with Zn ions and forms solid insoluble ZnO nanorod crystals on the substrate surface:



Cleaning by deionized water after the growth is necessary to remove unwanted material. Direct growth of ZnO nanorods on a bare substrate using CBD produces ZnO nanorods with less density and poor rod alignment. Therefore, it is crucial to deposit a thin ZnO seed layer on the substrate [17] using another technique such as spin coating, PLD, etc. The CBD technique offers different parameters that can be varied in order to control the film structure and its properties. These parameters are growth temperature, solution concentration, reactants ratio and time of growth.

This technique (CBD) has many advantages over the other deposition techniques. These advantages are:

- 1- Simplicity and low-cost deposition technique.
- 2- Low-temperature growth.
- 3- Achieving high quality nanostructured film over a large area of a substrate is possible.
- 4- Post-annealing treatment is mostly not required to achieve crystalline film.

Despite the aforementioned advantages of the CBD, wastage is one of the main disadvantages associated with this technique.

3.2. Characterization Techniques

This section is devoted to the basic principles underlying the characterization techniques employed in this study:

3.2.1. X-ray diffraction (XRD)

X-ray diffraction (XRD) is a well-established non-destructive technique that has been widely used in industries and research areas to study the structure of a wide range of materials [18]. The basic operation principle of XRD is accounted to Bragg's law. Since the discovery of X-ray in 1895, a new way of realizing a material phase structure became available. In 1913 W. H and W. L. Bragg realised that the reflected X-rays from a crystalline material gave a different

pattern than that reflected from a liquid. Bragg concluded that the path difference between two X-rays reflected from two successive lattice planes is $2d\sin\theta$ which gave birth to Bragg's law as formulated below [19]:

$$n\lambda = 2d\sin\theta \quad (3.4)$$

where n represent the order of reflection and it is integer number, λ is the wavelength of the X-ray beam, d is the distances between the lattice planes, and θ represent the angle of X-ray incidence. Fig. 3.6 illustrate the Bragg reflection from a crystalline solid with interplanar distance d .

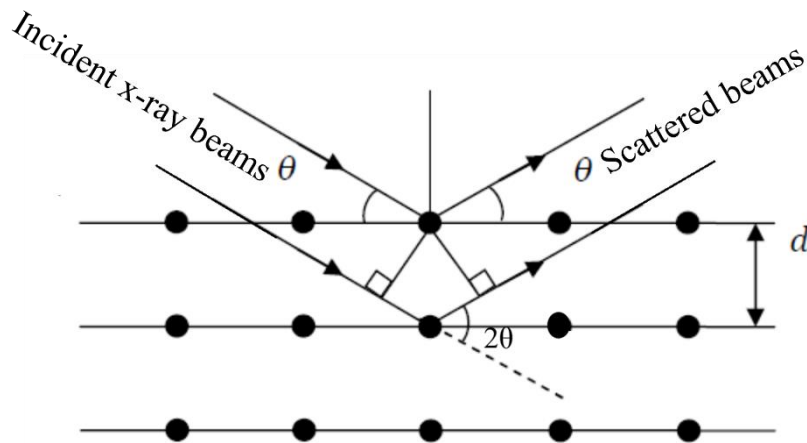


Fig. 3.6. Bragg's reflection diagram (from crystalline lattice planes with interplanar distance d)

Interatomic distances in solid materials are approximately 1 \AA , therefore the X-ray wavelength must be very close to this distance for the reflection to occur from consecutive lattice planes. A Bruker D8 Advance diffractometer with Cu $K\alpha$ radiation having wavelength (λ) about 1.54184 \AA was used in this study.

3.2.2. Scanning electron microscopy (SEM)

Scanning electron microscopy (SEM) is an analytical technique that has been used in various scientific and industrial fields to study materials' morphology and topography. The scientific phenomenon that SEM is based on is interaction between high energy incident electrons and a sample. When a high energy electron impinges on a sample surface, various emission/particles, including secondary electrons, backscattering electrons, Auger electrons, photons and X-rays, are emitted. The most important particles for the formation of SEM images are the secondary and backscattering electrons. Secondary electrons are emitted due to the inelastic scattering of the primary electrons by the sample's atoms. The secondary electrons gain the lost energy from the primary electrons and will be emitted with kinetic energy less than 100 eV . The kinetic

energy of many emitted secondary electrons is different depending on the atomic structure and composition of the specimen. Hence, secondary electrons carry information about the topography contrast of the specimen. Backscattered electrons are the reflected primary electron by the mean of elastic scattering, their lost energy is very close to the energy of the primary electrons. The kinetic energy differs for each backscattered electron depending on their position reflected from, angle of scattering and atomic number of the atom caused the scattering. Backscattered electrons give information about the specimen morphology contrast. Therefore, the kinetic energies of the both secondary and backscattered electrons are the key factor for the formation of SEM images. A scintillation detector is usually used to measure the energy differences between these electrons, and send a necessary electric or photonic signal to produce a final SEM image. In a typical SEM instrument, an energetic electron beam is focused on a sample surface using different magnetic lenses, and then scanned over a given area, similar to that of a traditional cathode-ray tube to form an image. The ideal environment of a SEM measurement is usually a vacuum atmosphere of about 5×10^{-5} bar. Fig. 3.7 illustrates the basic components of a SEM instrument as well as the emitted particles during the measurement. A JEOL JSM-7800 SEM with electron beam working voltage at ~ 5 kV was utilized in this work for the SEM images and morphology studies.

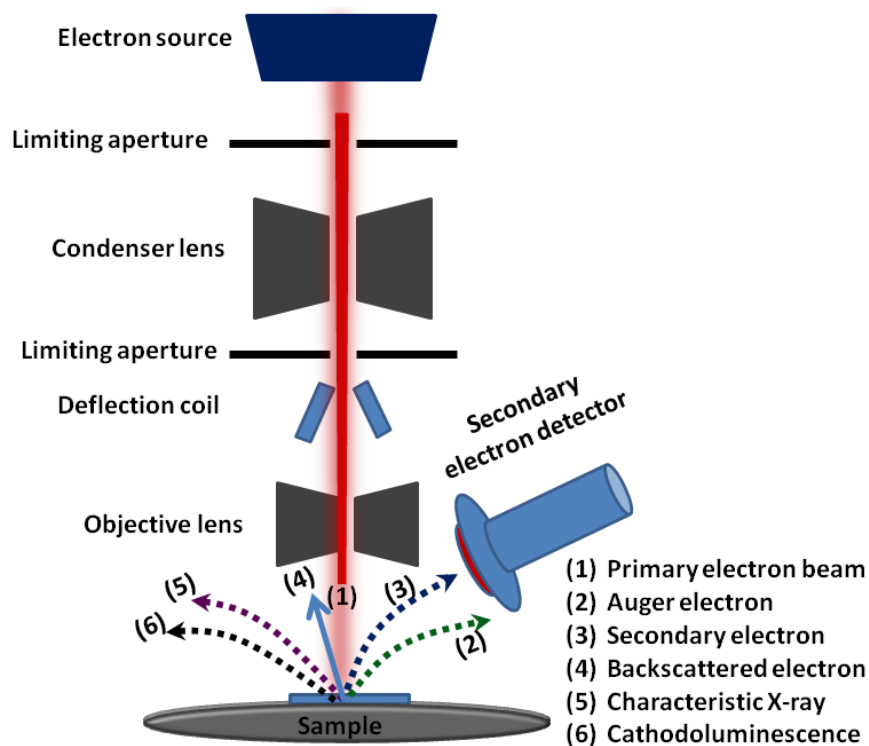


Fig. 3.7. Schematic diagram of a SEM experimental setup, and the types of emitted electrons and photons during the electron beam-specimen interaction [20].

3.2.3. Atomic force microscopy

Atomic force microscopy (AFM) is a high resolution scanning probe microscope (SPM) that has been used in research and industries for studying materials' surface profiles at nanoscale levels, as well as in the study of atoms manipulation. Van der Waal's force of atoms/molecules on a material surface is the critical phenomenon behind the AFM operation. When a small tip with tip diameter size of about 10 nm is subjected on to a material surface, they will interact through Van der Waal's forces and the tip experience either attraction or repulsion, depending on the atoms/molecules polarities of the material and the tip. The operation principle of AFM is schematically diagrammed in Fig. 3.8. A sample is held on a piezoelectric crystal, small tip attached on a cantilever subjected over the sample, a focused laser beam is shone at the back of the cantilever and reflected to a quadrants photodetector. When the sample is scanned on an X and Y axis, the cantilever bends up and down following the same pattern of the sample surface profile at nanoscale level, and then the laser beam will be deflected from one quarter to another of the photodiode. A signal will be sent from the photodiode to an amplifier and a controller unit and then to a computer for processing and displaying as an image. The results can be processed in two and three dimensional images using commercial PC based AFM software.

The cantilever obeys Hooke's law for small bending distances [21]. The Van der Waal's force can be determined from the following equation:

$$F = - KZ \quad (3.5)$$

where F is Van der Waal's force, K is spring constant (stiffness of the cantilever) and Z is the displaced distance of the cantilever deflection.

AFM scanning measurements can be performed in three different modes [22]:

1. Contact mode where the tip makes a soft physical contact with the sample surface, in this case repulsive force is dominant.
2. Non-contact mode where the tip is positioned at a suitable distance from the sample surface; in this case the attraction force is dominant.
3. Tapping mode where both short and long range forces are operating.

The choice of the operation mode critically depends on the sample and the tip properties.

A Shimadzu SPM-9600 AFM at the University of the Free State, Department of Physics was used to obtain two and three dimensional images in this study.

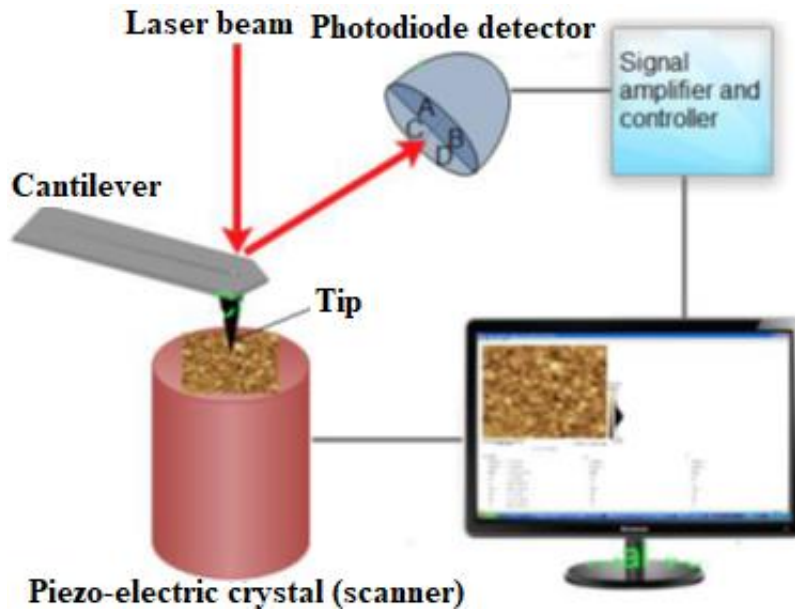


Fig. 3.8. Schematic diagram of an AFM system.

3.2.4. X-ray photoelectron spectroscopy (XPS)

X-ray photoelectron spectroscopy (XPS), also known as electron spectroscopy for chemical analysis (ESCA), is a sophisticated analytical technique widely used to study the chemical state and composition of materials. The fundamental principle of XPS lies in the photoelectric effect. When a material is bombarded with a high energy photon (such as a monochromatic Al K_{α} X-ray with photon energy of about 1486.6 eV), a core electron from K level will be ejected into vacuum as depicted in Fig. 3.9.

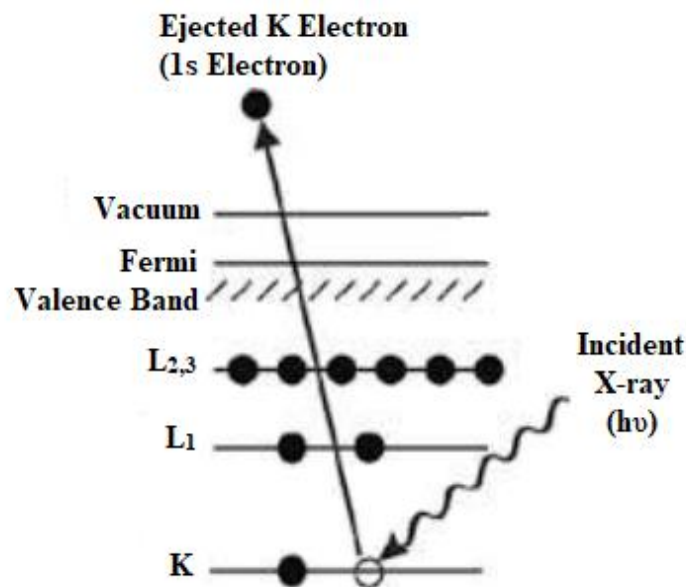


Fig. 3.9. Schematic diagram represents the photoelectric effect.

The key factor determining XPS measurements and analysis is the binding energy of the ejected electron. The binding energy of the electron is unique for each element depending on its atomic properties and configuration. The binding energy of the electron of a particular element is slightly affected by the chemical environment in the vicinity of this atom: the binding energy shifts to higher energy when the atom is in an oxidative environment and vice versa. Therefore, the binding energy of a measured electron can be calculated as follows [23]:

$$E_B = h\nu - KE - \Phi \quad (3.6)$$

where E_B and KE are the binding and kinetic energy of the ejected electron and Φ represents the work function of the measured sample. To ensure a reliable XPS measurement, the sample and energy analyser (detector) must be grounded together by aligning their Fermi levels. Due to the weak energy of the ejected electron and the sensitivity of the sample surface to the adsorbed gases, ultra-high vacuum (UHV) at about 7.5×10^{-7} to 7.5×10^{-9} Torr is required for obtaining a useful spectrum.

Depth profile measurement to determine the elemental distribution and the chemical composition of the sample across the thickness is also possible. In this case, an Ar^+ ion gun will be used to sputter the sample meanwhile the system collects XPS data. Thus, the thickness can also be roughly measured for a thin film by taking the sputtering rate into account.

In this study, A PHI 5000 Versa probe-scanning ESCA microprobe from the Department of Physics facilities at the University of the Free State was utilized for the XPS measurements.

3.2.5. Time-of-flight secondary ion mass spectrometry (ToF-SIMS)

ToF-SIMS is a sophisticated sensitive analytical technique, capable of determining elemental, compositional, chemical and molecular information about a measured solid sample (organic or inorganic). Fig. 3.10. represents the diagram of the basic principles underlying the ToF-SIMS measurement process [24, 25]. The solid sample is struck by a pulsed primary ions beam (usually Bi, Cs or Ga), secondary ions and ion clusters are ejected from the sample surface and then accelerated into a field-free drift path region. The accelerated ions or ion clusters will then be reflected back to a multi-channel plate detector, they will be measured based on their time of flight, where ions and ion clusters with different masses travel at different velocities and then arrive at different times. Mass to charge ratio of the ejected secondary ions or ion clusters is essential in the ToF-SIMS measurement process as can be deduced from the following equation [26]

$$\frac{m}{z} = 2U_0 \left(\frac{t}{L}\right)^2 \quad (3.7)$$

where m represents the mass of the secondary ion, z its charge, t its time of flight, L is the effective length of the mass spectrometer, and U_0 is the accelerating voltage which was kept at ± 2000 volts during measurements. A negative potential is usually favoured for positive species and vice versa.

Depth profile and 3D images are possible in ToF-SIMS measurements, by sputtering the sample surface by either oxygen (O^+) or cesium (Cs^+) active ion sources. Whereas bismuth (Bi) was used as the primary ion source.

A ToF-SIMS instrument from ION-TOF that forms part of the Physics facilities at the University of the Free State was used in this study.

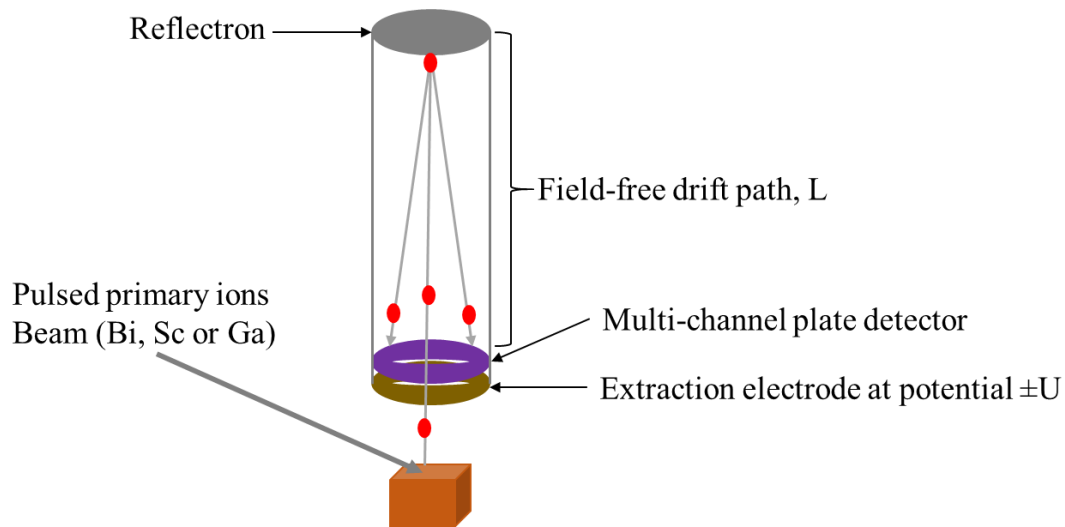


Fig. 3.10. Schematic diagram depicts the principle of ToF-SIMS.

3.2.6. Auger electron spectroscopy (AES)

Auger electron spectroscopy (AES) is a surface analytic technique similar to the XPS technique. The invention of AES came a few years after the discovery of the Auger electron in 1923 by Pierre Auger. Since then, AES became a reliable technique to realize elemental composition and chemical state of materials. Auger observed an electron with kinetic energy independent to the electron beam energy; he thought that this phenomenon came from an ionized atom leaving a hole in the core level K , when an electron from the L_1 level dropped to fill the hole in the K level. Another electron from the $L_{2,3}$ level will be released with the excess energy to conserve energy. Fig. 3.11 depicts the Auger process.

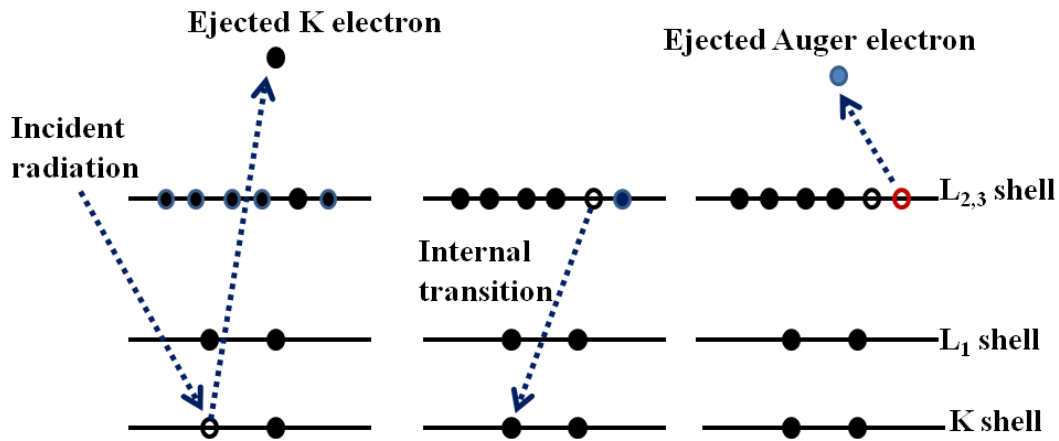


Fig. 3.11. Transitions involved in the ejection of a K L_{2,3} L_{2,3} Auger electron.

When a high energy particle (photons, electrons, etc.) strikes a material surface, an electron from the core level K will be released into vacuum level leaving an ionized and excited atom. An electron from L_{2,3} level has to fill the K level hole through internal transition leaving a hole in its original level which makes an unstable atom, due to the atom's tendency to relaxation to the minimum energy. Auger electrons will leave the L_{2,3} level into vacuum. The kinetic energy of the Auger electron carries valuable information about the chemical state and the type of atom involved in the Auger process. Each element has its own characteristic due to its atomic number, electron configuration and the chemical environment that the atom exist in. The kinetic energy of the Auger electron can be estimated as follow:

$$KE = E_K - E_{L1} - E_{L2,3} - \Phi \quad (3.8)$$

where K, L1 and L2,3 represents the energy levels involved in the Auger process, and Φ represents the work function of the analyser material. This formula did not take into account single and double ionized states transitions. Chung and Jenkins [27, 28] modified this formula by considering the single and double ionized state transition as follow:

$$KE(Z) = E_K(Z) - 0.5[E_{L1}(Z) + E_{L1}(Z+\Delta)] - 0.5[E_{L2,3}(Z) + E_{L2,3}(Z+\Delta)] - \Phi \quad (3.9)$$

where Z represents the number of involved atoms and the Δ term is the energy difference between the final double ionized state and individual ionization of the same levels.

The direct record of an Auger spectrum can be noisy because of the weak characteristic of the Auger electrons within a high background of other emitted particles. In 1968 Harris achieved the retrieved characteristic Auger features by differentiating the direct spectrum with respect to the energy. Fig. 3.12 shows the schematic diagram of an AES instrument.

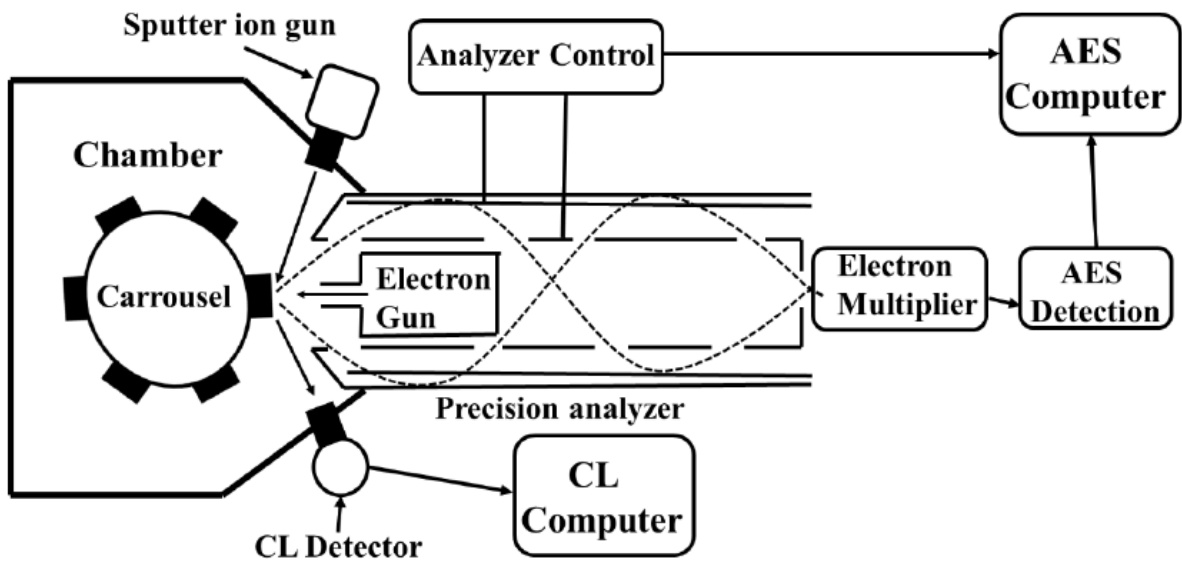


Fig. 3.12. Schematic diagram of AES and CL system.

The PHI model 549 AES at the Department of Physics, University of the Free State was used for the Auger, cathodoluminescence and degradation studies.

3.2.7. Photoluminescence spectroscopy (PL)

Photoluminescence (PL) spectroscopy is an optical analytical technique that utilizes photon energy as an excitation source to excite a material. PL phenomenon is an absorption of light energy (photon) by a material, which causes an electron to be promoted from the ground state to the excited state. The material may emit light when the electron returns to its ground (radiative recombination), or otherwise through a non-radiative recombination (releasing of heat) [29]. PL spectroscopy is able to measure excitation, emission and lifetime of an optically-excited sample. Moreover, other useful information such as band gap, electronic structure, defect levels and chemical environment of the excited material can be obtained from the PL spectra. The standard setup of PL instrument looks similar to the one in Fig. 3.13.

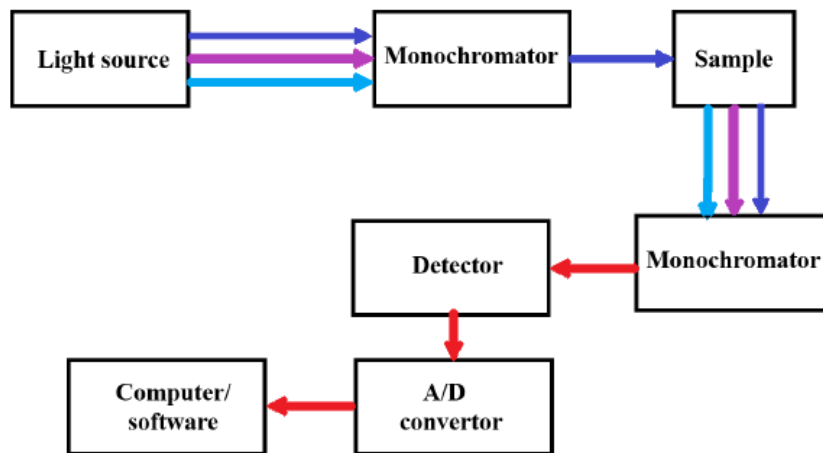


Fig. 3.13. Schematic diagram of the basic setup of a PL system.

Light with different wavelengths is generated from a source (xenon lamp) and then directed to a monochromator which selectively transmit a single wavelength that will be used to excite the sample. Alternatively, a monochromatic excitation source (laser) can be used. The emitted light from the sample is collected using another monochromator and then sent to a detector (PMT or photodiode detector). Finally, the detector converts the emission into an analog electrical signal and then send it to an analog/digital convertor, and then to a computer for processing and displaying the PL spectrum.

PL spectroscopy measurements are divided into two modes:

- 1- steady-state in which the PL information extracted from the emission and excitation spectra.
- 2- time-resolved measurements in which the decay curve is used to extract the information.

In this work, three PL instruments, part of the Department of Physics facilities at the University of the Free State, were used, i.e. Cary Eclipse fluorescence spectrophotometer, 325 nm He-Cd laser combined with a PMT detector instrument, and FLS980 system (Edinburgh Instruments).

3.2.8. Cathodoluminescence spectroscopy (CL)

Cathodoluminescence (CL) is a powerful technique with use in a wide range of investigations including the study of luminescent material properties. CL to some extent looks similar to its counterpart PL where in both cases the luminescence centres are excited and then recombined, followed by emission of light. However, due to the differences of their excitation particles (photons for PL and electrons for CL), their interaction with luminescent materials is different and hence their excitation mechanism is also different. Electrons excite luminescent centres in two ways: direct and indirect excitation [30].

In the direct excitation, the incident electrons directly excite the luminescent centres. In this case, the emission intensity increases with increasing activator concentration and decreases due to the concentration quenching mechanism.

In the indirect excitation, incident electrons generate mobile electron-hole carriers via collisions with lattice ions. These carriers may not recombine directly: they can move through the material and recombine later at luminescent centres (in the case of rare earth ion activators). In this case, other than the luminescent centre concentration, the CL emission intensity depends on many factors including the particle size, penetration depth of the incident electrons, the scattering volume of the incident electrons, etc. During the CL process, luminescent centres may be excited through impact excitation/ionization.

In this work, the electron beam of a PHI model 545 AES system was used to excite the samples, while Ocean optics PC2000 and USB2000+ spectrometers were used to collect the CL spectra. CL degradation spectra could be obtained together with Auger spectra during long exposure times.

3.2.9. UV-Vis spectroscopy

UV-Vis spectroscopy is an optical analytical technique used to study the optical properties (absorptivity) of materials. Absorbance of light by a material is a phenomenon that is dependent on the electronic structure of the tested material [31, 32]. To understand the technical working principle of this technique, it must be remembered that when light falls on a material surface it is either reflected, absorbed or transmitted. Hence, in the UV-Vis, a beam of light passed through a monochromator is split into two beams: one is directed to the system detector and used as a reference and the second sent to the measured sample. The sample absorbs part of the light and reflects or transmits (depending on the chosen measurement mode) the other part of the light and sends it to a processing unit. The reflected or transmitted light from the sample is compared to the reference light and the result is reflectance or transmittance data points. To generate a spectrum over a wide range of wavelengths, the light source must emit light with a wide range of wavelengths, and using a monochromator the source light is monochromatized and then scanned through the selected wavelength range (for example from 800 nm to 200 nm). A deuterium lamp is usually used to generate light with wavelength ranging from 200 nm to 330 nm and a tungsten lamp is used to generate light with wavelength ranging from 300 nm to 3000 nm. In a typical UV-Vis spectroscopy, three types of spectra can be obtained by using different three modes including transmittance, absorbance and reflectance. Fig. 3.14 shows the basic setup of a UV-Vis spectroscope.

An integrating sphere coated with white material that exhibit almost perfect (100%) reflectance in the range from UV to NIR is usually used for diffuse reflectance measurements (DRS), with spectralon used as standard. The integrating sphere collects the reflected light from the standard and the solid sample and send it to the detector.

The optical band gap energy of a measured sample can be calculated from the reflectance or absorption spectra. The well-known Tauc's law formula [33] is used (in case of absorption spectrum);

$$\alpha h\nu = C_1(h\nu - E_g)^m \quad (3.10)$$

where α , $h\nu$, C_1 and E_g represents the absorption coefficient, incident photon energy, a constant and optical band gap energy, respectively. The exponent parameter (m) depends on the

electronic transition involved in the absorption. It has values of $1/2$ and $1/3$ for direct band gap for allowed and forbidden transitions, respectively. For indirect band gap m has values of 2 and 3 for allowed and forbidden transitions, respectively. $(ah\nu)^2$ is plotted vs $h\nu$ and by extrapolating the linear part of the plot and extending straight line to the energy axis, the band gap can be found.

In this study, a Lambda 950 UV-Vis spectrophotometer with wavelength range from near UV to the near IR was used to record the transmittance spectra. The system is part of the Department of Physics facility, University of the Free State.

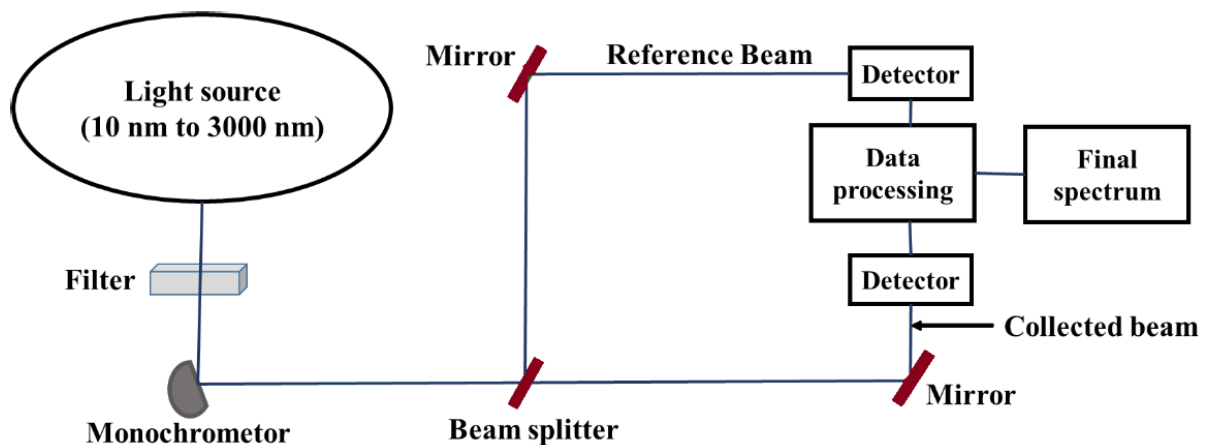


Fig. 3.14. Schematic diagram of a UV-Vis spectroscopy technique.

3.3. References

- [1] M. Stafe, A. Marcu and N. N. Puscas, Pulsed laser ablation of solids: basics, theory and applications, Berlin, Germany: Springer Science & Business Media, 2013.
- [2] R. Eason, Pulsed laser deposition of thin: applications-led growth of functional materials, Hoboken, New Jersey: John Wiley & Sons, 2007.
- [3] S. Logothetidis, Nanostructured materials and their applications, Berlin Heidelberg, Germany: Springer Science & Business Media, 2012.
- [4] E. Morintale, C.Constantinescu and M. Dinescu, Thin films development by pulsed laser-assisted deposition, *Physics AUC* **20** (2010) 43-56, 2010.
- [5] D. B. Chrisey and G. K. Hubler, Pulsed laser deposition of thin films, Lincoln, United States: unl.edu, 1994.
- [6] C. Belouet, Thin film growth by the pulsed laser assisted deposition technique, *Appl. Surf. Sci.* **96** (1996) 630-642. [https://doi.org/10.1016/0169-4332\(95\)00535-8](https://doi.org/10.1016/0169-4332(95)00535-8).

- [7] T.Haugan, P.N. Barnes, L. Brunke, I. Maartense and J. Murphy, Effect of O₂ partial pressure on YBa₂Cu₃O_{7-δ} thin film growth by pulsed laser deposition, *Physica C* **397** (2003) 47–57. doi:10.1016/s0921-4534(03)01088-8.
- [8] K. S. Sree Harsha, Principles of vapor deposition of thin films, Amsterdam, Netherlands: Elsevier , 2005.
- [9] I. N. Mihailescu and A. P. Caricato, Pulsed Laser Ablation Advances and Applications in Nanoparticles and Nanostructuring Thin Films, Boca Raton, Florida, United States: CRC Press, 2018.
- [10] K. Wasa, M. Kitabatake and H. Adachi, Thin Films Material Technology: Sputtering of Compound Materials, Norwich, NY: William Andrew, Inc., 2004.
- [11] C. Popescu, G. Dorcioman and A. C. Popescu, Laser Ablation Applied for Synthesis of Thin Films: Insights into Laser Deposition Methods, *In Applications of Laser Ablation- Thin Film Deposition, Nanomaterial Synthesis and Surface Modification*, IntechOpen, 2016, pp 3-32. <http://dx.doi.org/10.5772/65124>.
- [12] N. Sahu, B. Parija and S. Panigrahi, Fundamental understanding and modeling of spin coating process : A review, *Indian J. Phys.* 83 (2009) 493-502. DOI:10.1007/s12648-009-0009-z.
- [13] N. T. Nguyen, Fabrication technologies, In *Micromixers: fundamentals, design and fabrication*, Norwich, NY: William Andrew, 2011, pp. 113-161. doi:10.1016/b978-1-4377-3520-8.00004-8 .
- [14] M. Aliofkhaezai, Anti-Abrasive Nanocoatings Current and Future Applications, Amsterdam, Netherlands: Elsevier, 2014.
- [15] M. D. Tyona, A theoretical study on spin coating technique, *Adv Mat Res* **2** (2013) 195-208. doi: <http://dx.doi.org/10.12989/amr.2013.2.4.195>.
- [16] L. Vayssieres, K. Keis, S. E. Lindquist and A. Hagfeldt, Purpose-Built Anisotropic Metal Oxide Material: 3D Highly Oriented Microrod Array of ZnO, *J. Phys. Chem. B* **105** (2001) 3350-3352. doi: from <https://pubs.acs.org/doi/10.1021/jp010026s>.
- [17] L. E. Greene, M. Law, D. H. Tan, M. Montano, J. Goldberger, G. Somorjai and P. Yang, General Route to Vertical ZnO Nanowire Arrays Using Textured ZnO Seeds, *Nano Lett* **5** (2005) 1231-1236. DOI:10.1021/nl050788p.

- [18] A. A. Bunaciu, E. G. Udriștioiu and H. Y. Aboul-Enein, X-Ray Diffraction: Instrumentation and Applications, *Crit. Rev. Anal. Chem* 45 (2015) 289–299. doi: 10.1080/10408347.2014.949616.
- [19] A. Clearfield, J. H. Reibenspies and N. Bhuvanesh, Principles and Applications of Powder Diffraction, Hoboken, New Jersey: John Wiley and Sons, Ltd., 2008.
- [20] S. S. Dlamini, Characterization of $Y_3(Al,Ga)_5O_{12}:Ce^{3+}$ phosphor thin films prepared by PLD, Bloemfontein: M.Sc thesis, University of the Free State, 2013.
- [21] A. Y. M. Ahmed, Luminescence properties of $Y_3(Al,Ga)_5O_{12}:Tb$ thin films, Bloemfontein, Ph.D Thesis, University of the Free State, 2014.
- [22] A. Vilalta-Clemente and K. Gloystein, Principles of Atomic Force Microscopy (AFM), Thessaloniki: Physics of Advanced Materials Winter School, Aristotle University of Thessaloniki, 2008.
- [23] M. Inagaki and F. Kang, Materials science and engineering of carbon: characterization, Oxford, United Kingdom: Butterworth-Heinemann, 2016.
- [24] R. J. Cotter, Time-of-Flight Mass Spectrometry, *Journal of the American Society for Mass Spectrometry* 7.1 (1996) 123-124.
- [25] P. Van der Heide, Secondary ion mass spectrometry: an introduction to principles and practices, Hoboken, New Jersey, United States: John Wiley & Sons, 2014.
- [26] S. Fearn, An introduction to time-of-flight secondary ion mass spectrometry (ToF-SIMS) and its application to materials science, Williston, Vermont, United States: Morgan & Claypool Publishers, 2015.
- [27] L. H. Jenkins and M. F. Chung, Auger and other characteristic energies in secondary electron spectra from Al surfaces, *Surf. Sci* 28 (1971) 409-422.
- [28] J. F. Watts and J. Wolstenholme, An Introduction to Surface Analysis by XPS and AES, New York: Wiley-VCH, 2003.
- [29] S. Eaton-Magaña and C. M. Breeding, An introduction to photoluminescence spectroscopy for diamond and its applications in gemology, *Gems & Gemology* 52 (2016) 2-17. <http://dx.doi.org/10.5741/GEMS.52.1.2>.
- [30] L. Ozawa, Cathodoluminescence and photoluminescence: theories and practical applications, Boca Raton, London, New York: CRC Press, 2007.

- [31] H. H. Perkampus, *UV-VIS Spectroscopy and its Applications*, Berlin/Heidelberg, Germany: Springer Science & Business Media, 2013.
- [32] L. Sommer, *Analytical absorption spectrophotometry in the visible and ultraviolet: the principles*, Amsterdam, Netherlands: Elsevier, 2012.
- [33] E. Morales, E. S. Mora and U. Pal, Use of diffuse reflectance spectroscopy for optical characterization of un-supported nanostructures, *Rev. Mex. Fis.* **53** (2017) 18-22.

Chapter 4

Structural, optical and photoluminescence properties of Eu doped ZnO thin films prepared by spin coating

4.1. Introduction

Research on wide band gap semiconductors has gained much attention in the field of optoelectronic materials and their applications. In particular, ZnO is a fascinating metal oxide semiconductor with wide direct band gap of ~ 3.37 eV [1] that can accommodate different luminescent centers. It has a large exciton binding energy (60 meV) which allows efficient exciton emission which is stable even above room temperature [2]. It exhibits low thermal quenching [3], high chemical and thermal stability, good radiation hardness and low growth temperature [4]. ZnO can easily be grown in a single crystal form and becomes transparent across the visible region of the spectrum [5]. ZnO is a low-cost material compared to the GaN which is currently widely used in micro and nano optoelectronic devices, and they have almost similar structure and band gap physics [6, 7], and hence it is an excellent candidate to replace GaN based devices. Furthermore, because of the poor stability and degradation of sulfide-based phosphors under high current density, ZnO may have the potential to replace sulfide-based materials in the optoelectronic field [8]. ZnO is widely used as a green phosphor for vacuum fluorescent devices owing to its bright green emission that originates from its intrinsic defects. Yellow to red luminescence has also been observed from ZnO, but their intensities and chromaticities are insufficient to be used in applications that require an accurate color index [9].

Rare earth (RE) ions, due to their 4f-4f transitions, have the ability to emit sharp emission bands at different wavelengths in the range from ultraviolet to the far infrared region. 4f-4f transitions of RE³⁺ ions are less affected by the surrounding atomic environment due to the electronic shield provided by the outermost and completely filled 5s² and 5p⁶ shells. Europium ions (Eu³⁺) have been used extensively in optoelectronic applications due to their well-known red emission around 611 nm. The Eu³⁺ emission lines are found to be strongly dependent on the structural quality and thermal cycling in the case of GaN [10]. Eu³⁺ doped ZnO has a great opportunity to design a new material for red emission that can be used in optoelectronic devices. However, efficient red luminescence from Eu³⁺ incorporated in ZnO is yet to be achieved. Energy transfer between ZnO intrinsic or extrinsic defects to Eu³⁺ ions is one way proposed to improve its luminescence efficiency. Though many drawbacks were found to hinder the efficient energy

transfer to take place including: low solubility of the Eu^{3+} ions in the ZnO host [11], charge transfer level of Eu^{3+} in ZnO is equal or higher than the bottom of the conduction band in ZnO [12], and the excitons decay time of ZnO is much faster than the energy transfer rate of Eu^{3+} [13]. Over the past few years, many studies have reported energy transfer from ZnO to Eu^{3+} ions. Keigo Susuki et al. [14] reported energy transfer from ZnO to Eu^{3+} ions in nanocrystalline films and they found that reduction in particle size and shift of the charge transfer band into the low energy side play a significant role in expediting the energy transfer. Housei Akazawa et al. [15] reported that the crystallinity degradation is the main factor in attenuating the emission intensity. Non-radiative energy dissipation at defect levels is the main factor to determine the quantum yield of the emission, and they found that the band-edge, defect and Eu^{3+} emissions compete with one another and the excitation energy was shared between them. Energy transfer from ZnO defect levels to the Eu^{3+} luminescence levels is a very controversial issue, and it depends on different factors such as the host crystal field, crystallinity, morphology, etc. We believe that more work is needed to understand the energy transfer mechanism from ZnO defect levels to Eu^{3+} ions in order to achieve high-efficiency red luminescence. Peiliang Chen et. al. reported a strong ${}^5\text{D}_0\text{-}{}^7\text{F}_0$ emission around 580 nm from sol-gel Eu doped ZnO thin films prepared by using the spin coating technique. However, the predominantly required emission is the ${}^5\text{D}_0\text{-}{}^7\text{F}_2$ emission around 614 nm that can fulfill the red color index [16].

In this work, Eu^{3+} doped ZnO thin films were prepared by the sol-gel spin coating technique. Their structure, morphology, optical and photoluminescence (PL) properties were studied. The possible energy transfers between ZnO defect levels to the Eu^{3+} ions were also investigated.

4.2. Experimental details

4.2.1. Preparation

Eu^{3+} doped ZnO thin films were prepared by the sol-gel method using the spin coating technique. The analytical reagents, zinc acetate dihydrate $\text{Zn}(\text{CH}_3\text{COO})_2 \cdot 2\text{H}_2\text{O}$, europium acetate hydrate $\text{Eu}(\text{CH}_3\text{COO})_3 \cdot x\text{H}_2\text{O}$ and monoethanolamine (MEA) $\text{C}_2\text{H}_7\text{NO}$ were used as received from Sigma Aldrich without any further purification. High purity ethanol (99.9%) was used as solvent. For the solution preparation, an equimolar ratio of zinc acetate and MEA was used with molarity of 0.2. In a typical preparation process, a suitable amount of zinc acetate and selected molar mass of europium acetate (0.4, 0.6, 0.8 and 1 mol%) were dissolved in ethanol and stirred at room temperature for 20 min. The MEA solution was added drop wise to the zinc acetate solution and stirring was continued for 1 h until a transparent and homogeneous solution was obtained. The solution was aged for 24 h before the coating process. Si (100) and

soda lime glass substrates were cut into pieces of about 2 cm² and then cleaned in an ultrasonic bath in isopropanol, acetone, ethanol and distilled water for 5 min each, and then dried using nitrogen gas, which is clean, dry and inert. For the coating process, the spin coater was set at 2500 rpm/min for 30 s. The substrate was placed on the spin coating chuck and the solution was dropped on the substrate, after which the spinning was performed. The coated substrates were heated to 300 °C for 10 min. The process was repeated 10 times until the required thickness was obtained. Finally, the films were annealed in air at 500 °C for 2 h in a carbolite 1200 furnace ramped at 5 °C/min to improve the film crystallinity. Yang et al. [17] have done a study on the doping site analysis and control of Eu³⁺ in a ZnO:Eu crystal lattice. Eu³⁺ ions separated out of the host lattice at higher temperatures (700 °C) but at the same time, the doping position of the Eu can be completely controlled by controlling the annealing temperature. It appeared from their study that a good choice of annealing temperature to control the symmetrical site position would be between 450 and 550 °C. The majority of Eu³⁺ ions enter into the ZnO lattice and substitute Zn²⁺ for low-temperature annealing. An annealing temperature of 500 °C was therefore chosen. The films were then characterized.

4.2.2. Characterization

An X-ray diffractometer (Bruker D8 Advance) with monochromatic Cu K α ($\lambda = 0.15405$ nm) radiation source was used for the crystal structure measurements. A JEOL secondary electron microscope (SEM) model JSM-7800F was used for the structure assessments. A 325 nm He-Cd laser and a monochromatized xenon lamp (FLS980 spectrophotometer from Edinburgh Instruments) were used as the excitation sources for the PL measurements. All measurements were done at room temperature. The UV–visible spectrometer (Lambda 950 from PerkinElmer) was used to record the transmittance spectra. The surface topography was probed using a Shimadzu SPM – 950 atomic force microscope (AFM). The surface profile was obtained with the commercial software that came with the AFM system.

4.3. Results and discussion

4.3.1. Structural and morphological analysis

Fig. 4.1(a) shows the XRD patterns of thin films of undoped ZnO and ZnO doped with different concentrations of Eu³⁺ (deposited on glass substrates). ZnO is well known by its close packed hexagonal wurtzite structure. The wurtzite structure is the tetrahedral arrangement where each Zn²⁺ ion is surrounded by four O²⁻ ions or vice versa. The lowest surface energy for the wurtzite structure of ZnO is on the (002) plane [18]. Therefore, the un-doped film has a preferred orientation along the *c*-axis that is perpendicular to the (002) plane. No extra peaks associated

with zinc hydroxide or any other incidental impurities were detected. This indicated that the pure phase of ZnO wurtzite structure was crystallized. No peaks related to the Eu_2O_3 phase were observed, which indicated that Eu^{3+} ions successfully substituted Zn^{2+} ions in the ZnO host. Since XRD pointed to the successful substitution of Eu^{3+} into Zn^{2+} , the presence of Eu^{2+} is possible along with Eu^{3+} (Eu^{2+} may represent the Eu^{3+} that substituted Zn^{2+}) [19]. Adding Eu^{3+} to the ZnO host caused other peaks corresponding to the 100 and 101 planes to develop. This indicated that the films preferred orientation had changed. In Fig. 4.1(b), the 002 peak's intensity slightly decreased at the Eu^{3+} concentration of 0.4 and 0.6 mol% and substantially decreased at higher Eu^{3+} concentrations (0.8 and 1.0 mol%). It is clear that incorporation of Eu^{3+} ions with bigger ionic radius (90 pm) to the ZnO host with smaller zinc ionic radius (74 pm) deteriorated the film's crystallinity. The well-known Scherrer equation and Miller indices were used to calculate the crystallite size and the lattice parameters, respectively. The results are shown in table 1. The lattice parameter (c), interplanar spacing (d) of the (002) planes and the crystallite size (D) did not systematically change with incorporation of Eu. This may be explained by the occupation of the Eu^{3+} ions of zinc or oxygen sites of the host crystal or interstitial sites, or the creation of different defects in the lattice. The fact that strain broadening also contributed to the XRD peak widths means that the crystallite sizes in Table 4.1 represent only a lower bound of possible values.

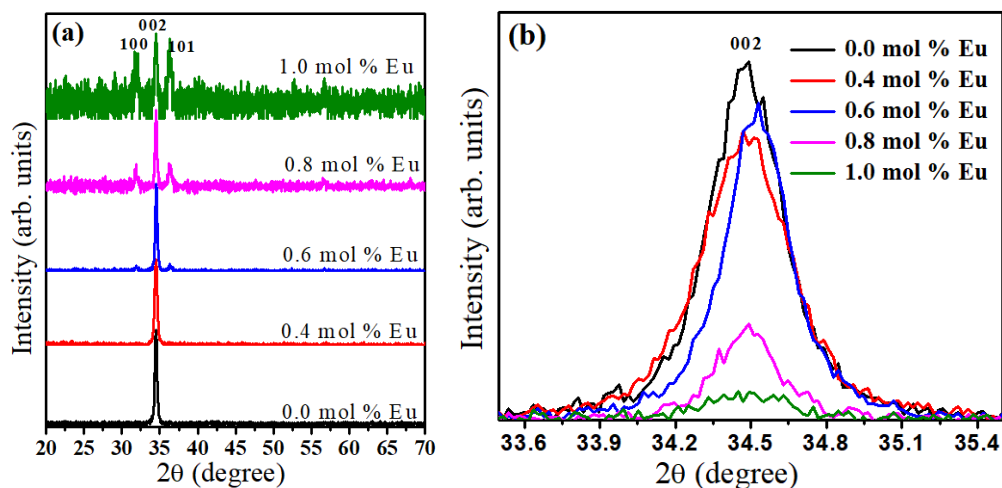


Fig. 4.1. (a) XRD patterns of Eu^{3+} doped ZnO films (b) magnified region of the 002 peak.

Table 4.1. Crystal parameters of the undoped and Eu^{3+} doped ZnO sol-gel thin films.

sample	c (nm)	d (nm)	Crystallite size D (nm)	FWHM (degree)
Un-doped	0.5132	0.2566	24 ± 1	0.3514
0.4 mol% Eu^{3+}	0.5132	0.2566	19 ± 1	0.4313
0.6 mol% Eu^{3+}	0.5117	0.2559	29 ± 1	0.2911
0.8 mol% Eu^{3+}	0.5115	0.2558	27 ± 1	0.3113
1.0 mol% Eu^{3+}	0.5139	0.2570	21 ± 1	0.4039

Fig. 4.2 shows the SEM images and corresponding cross-sections of the films with different Eu^{3+} content deposited on silicon (100) substrates. The films were all continuous, smooth and comprised of tiny randomly distributed nanoparticles. The nanoparticle sizes appeared to decrease with increasing the Eu contents, in agreement with an earlier report by Dai et al. [20]. The thicknesses of all the films were almost equal, i.e. approximately 160 nm. Increasing the Eu^{3+} concentration had little effect on either the morphology and thickness of the films.

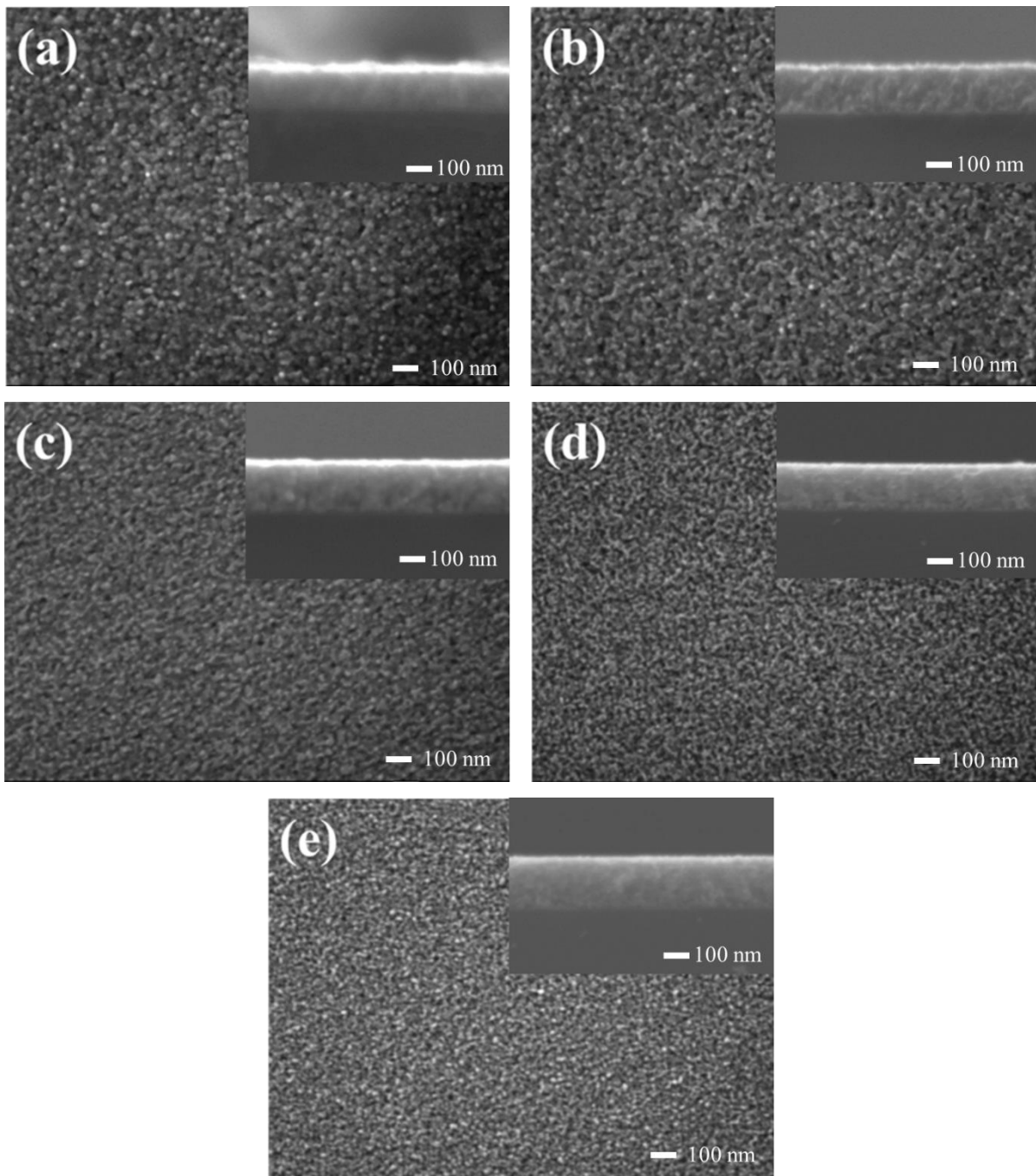


Fig. 4.2. SEM images of (a) un-doped, (b) 0.4 mol%, (c) 0.6 mol% (d) 0.8 mol% and (e) 1 mol% Eu^{3+} doped ZnO films (the insets are the corresponding cross-sections of the films).

AFM was used to examine the topography of the films deposited on the silicon substrate, and the results are shown in Fig. 4.3. The average particle sizes were calculated and plotted as shown in the corresponding histograms. The average particle size was found to slightly decrease as the Eu^{3+} content increased. The values were estimated as 88 nm, 87 nm, 83 nm, 80 nm and 78 nm for the undoped, 0.4 mol%, 0.6 mol%, 0.8 mol% and 1 mol% Eu^{3+} doped ZnO films, respectively. It was reported in the past that the particle size decreased with an increase

in the Eu^{3+} concentration and this was ascribed to the presence of the Eu in the ZnO lattice which perturbed the crystal growth [20]. When Eu^{3+} replaces the Zn^{2+} , charge compensation must also take place via extra Zn^{2+} and O^{2-} ions or vacancies. The inconsistency between the crystallite size calculated from XRD and the grain sizes estimated from AFM is due to the fact that AFM measures the coalesced grains whereas Sherrer's equation measure the defect-free crystallite size [21]. The statistical theory of a Gaussian distribution asperity predicted that the ratio between the root mean square roughness (Rq) and the average roughness (Ra) for a surface must be about 1.25, while the experimental results estimated by the theory revealed that the value must be around 1.31 [22]. The values obtained from our films (Table 4.2) were very close to the theoretical and the experimental values. These results indicate that our films have an excellent and even distribution of grains on the surface.

Table 4.2. Roughness parameters of the undoped and Eu^{3+} doped ZnO sol-gel thin films.

Eu^{3+} doping (mol%)	Rq (nm)	Ra (nm)	Rq/Ra
0.0	2.84 ± 0.1	2.23 ± 0.1	1.27
0.4	2.96 ± 0.1	2.35 ± 0.1	1.26
0.6	1.55 ± 0.1	1.22 ± 0.1	1.27
0.8	1.73 ± 0.1	1.37 ± 0.1	1.26
1.0	1.58 ± 0.1	1.26 ± 0.1	1.25

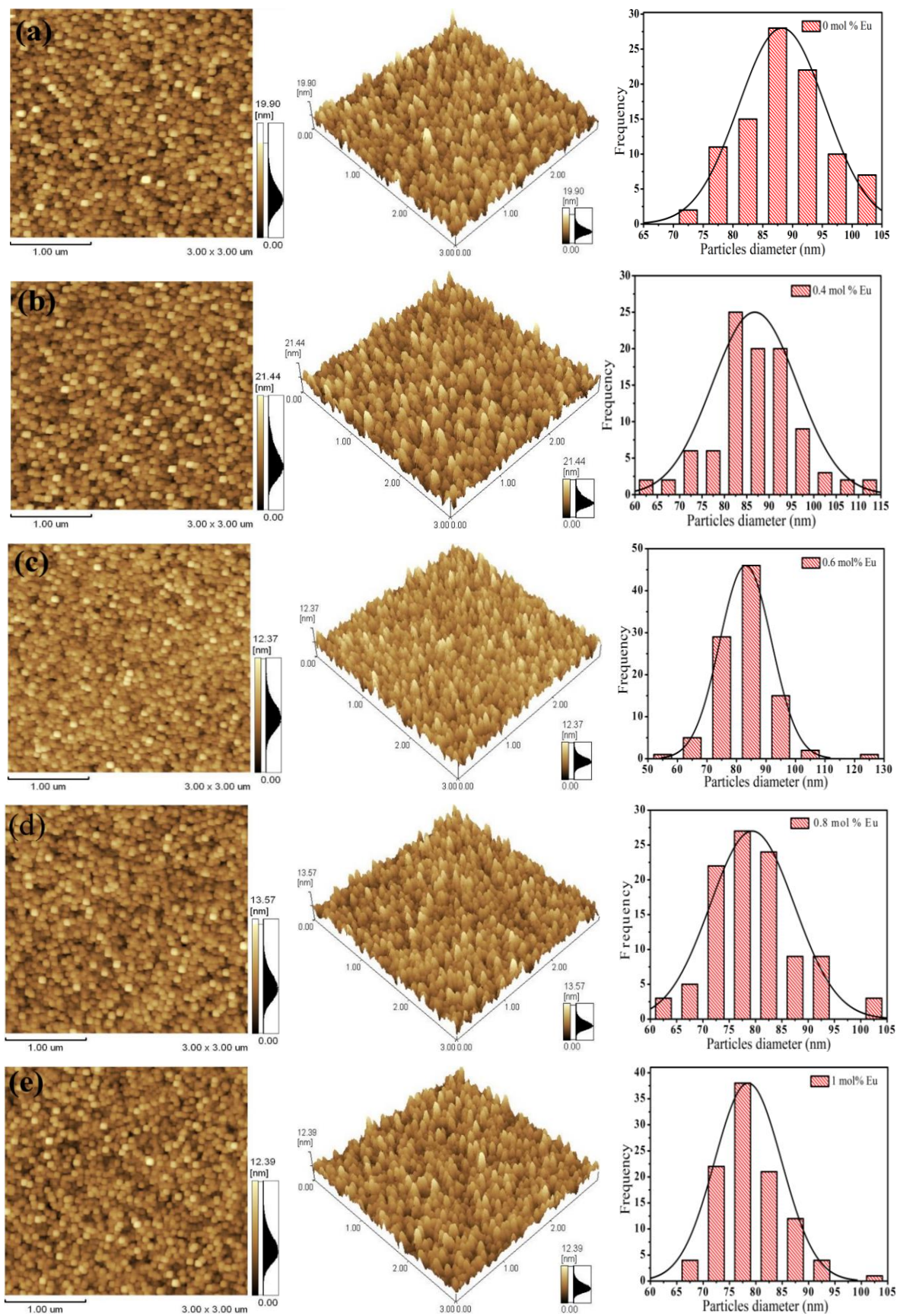


Fig. 4.3. 2D and 3D AFM micrograph and the corresponding particle size distributions of (a) undoped, (b) 0.4 mol%, (c) 0.6 mol% (d) 0.8 mol% and (e) 1 mol% Eu^{3+} doped ZnO films.

4.3.2. Transmittance and band gap analysis (UV-Vis spectroscopy)

The transmittance spectra of Eu^{3+} doped ZnO thin films (deposited on glass substrate) in the wavelength range from 300 to 800 nm are shown in Fig. 4.4(a). All the films exhibited an average transmittance of about 80% in the visible region and a steep absorption increase around 385 nm which is assigned to the optical band gap absorption (band to band transition) of ZnO. The transmission of the films was slightly affected by the Eu^{3+} doping, while there was no systematic decrease or increase due to the Eu^{3+} concentration.

The photon energy ($h\nu$, where h is Planck's constant and ν represents the frequency) is related to the transmittance spectra which determines the absorption coefficient (α) via Tauc's formula [23]. $(\alpha h\nu)^2$ was plotted against $h\nu$ as displayed in Fig. 4.4(b), indicating that ZnO formed a direct band gap. The optical direct band gap was estimated by the extrapolation of the linear part of the plot. The optical band gap was found to slightly decrease from 3.31 eV, 3.30 eV, 3.272 eV, 3.27 eV - 3.26 eV as the Eu^{3+} concentration increased from 0, 0.4, 0.6, 0.8 - 1 mol%, respectively. Adding donor or acceptor impurities into a semiconductor creates energy levels near the conduction or the valance band edges. Increasing the dopant concentration increases the density of these energy states and as a result a continuum of states will be formed [24]. Therefore, the band gap decreased with increasing Eu^{3+} concentration.

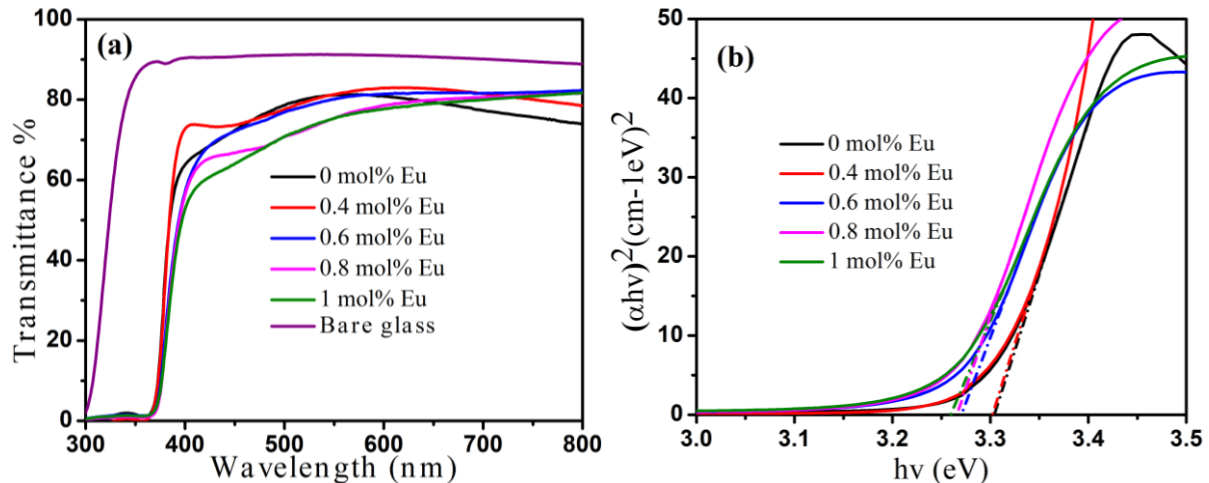


Fig. 4.4. (a) Transmittance spectra and (b) Tauc plot of un-doped and Eu^{3+} doped ZnO thin films.

4.3.3. Photoluminescence analysis

Fig. 4.5 depicts the PL spectra of (a) the undoped and (b) Eu^{3+} doped ZnO films (deposited on silicon substrates) excited at 325 nm by using a He-Cd laser. The undoped film exhibits two distinct luminescence emissions; the ultraviolet emission around 3.28 eV (378 nm) and the deep level emission across the visible region. The well-known ultraviolet emission of ZnO is

due to the free exciton recombination [25]. Since the visible emission showed a broad peak, a Gaussian fit was used to determine the multiple constituent emission peaks. At least four defect-related emissions were found at 3.15 eV (394 nm), 2.4 eV (516 nm), 2.0 eV (611 nm) and 1.7 eV (734 nm). The visible emission of ZnO originated from different defect states within the band gap, such as oxygen vacancies (V_o), oxygen interstitials (O_i), zinc vacancies (V_{Zn}) and zinc interstitials (Zn_i). The most unambiguous arguments are: the ~ 3.15 eV band is due to the recombination of the shallow trapped electrons at the Zn_i site that is very close to the conduction band, associated with the deeply trapped hole in the V_{Zn} site [26]. The bands around 2.4 eV and 2.0 eV are due to the singly and doubly ionized oxygen vacancies, respectively [27, 28], and the red emission centered at 1.7 eV is due to the oxygen interstitial O_i defects [24]. The UV emission at ~ 378 nm increased with increasing the Eu^{3+} contents, reaching its maximum for the film with 0.6 mol% and then decreased for higher Eu^{3+} content (0.8 and 1.0 mol%). This can be ascribed to the concentration quenching effect, or the enhancement of the crystallinity and subsequent deterioration with increasing the Eu^{3+} concentration as seen in XRD analysis (Fig. 4.1(b)), as the result of incorporating Eu^{3+} ions with bigger ionic radii than Zn ions into the ZnO matrix. Enhancement of the crystallinity reduces the defects and increases the free exciton density and thus the UV emission increase. When a trivalent Rare Earth ion (Eu^{3+}) substitute Zn^{2+} ion in ZnO lattice, there will be two possible kinds of defects can be created, either creating donor centres or promoting zinc vacancies in the neighborhoods due to the charge compensation [29]. Therefore, the characteristic emission of ZnO intrinsic defects and the free exciton emissions undergoes changes such as: increase or decrease in their intensities and slight shift in their positions. In our case, the broad emission centred at ~ 516 nm has increased until 0.6 mol% of Eu^{3+} and then decreased for 0.8 and 1.0 mol% of Eu^{3+} . Since we agreed that the emission at ~ 516 nm is due to the oxygen vacancies, incorporation of 0.4 and 0.6 mol% of Eu^{3+} maybe created donors centres at the oxygen vacancies side, whereas at 0.8 and 1.0 mol% of Eu^{3+} zinc vacancies maybe promoted. These can also explain the changes that are observed on the sample with 1 mol% of Eu^{3+} . The broad defect peak centred at ~ 611 nm was reduced for the films with different Eu^{3+} content. Less intense peaks corresponding to the 4f - 4f transitions of Eu^{3+} appeared around 614 nm for the film with 0.6 mol% of Eu^{3+} . The reduction of the broad peak at ~ 611 nm of the ZnO defects for the doped samples could indicate that different possible mechanisms took place such as: the competition between the defects emission and the Eu^{3+} emission, some excited charge carriers transfer their energy to the Eu^{3+} ions rather than being trapped at the defects. Therefore, some characteristic emissions from Eu^{3+} ions were observed and the deep level defect emission at ~ 611 nm

decreased, and maybe the reduction of the defects due to the incorporation of the Eu^{3+} lead to a decrease in the defect emission. (Fig. 4.5(b and c) for comparison). The 4f-4f characteristic emission at ~ 614 nm was only observed for the sample with 0.6 mol% of Eu^{3+} and did not appear for the other samples. This may be explained by two reasons: one is that the 0.6 mol% sample is the optimum sample and exhibit higher 4f-4f intensity which is able to produce the defects emission of ZnO; the second is that 0.6 mol% contain lower defect concentration and therefore the 4f-4f emission was able to compete with lower defect emission intensity. For the other samples, the defect concentration was high and their originated emission was also high enough to suppress the 4f-4f emission of Eu^{3+} . The Commission Internationale de l' éclairage (CIE) chromaticity coordinates of Eu^{3+} doped ZnO films excited at 325 nm were calculated and given in Table 4.3. The corresponding CIE X–Y chromaticity coordinates are shown in Fig. 4.5(d). A possible energy diagram of Eu^{3+} doped ZnO is given in Fig. 4.5 (e). The normal electron excitation from the VB to the CB and then the de-excitation via the exciton and defect levels form the UV band-to-band and broad visible defect emission peaks. With the incorporation of the Eu^{3+} some of these traps are non-radiatively or inefficiently transferred to the Eu^{3+} energy levels leading to the low intensity 4f-4f emission.

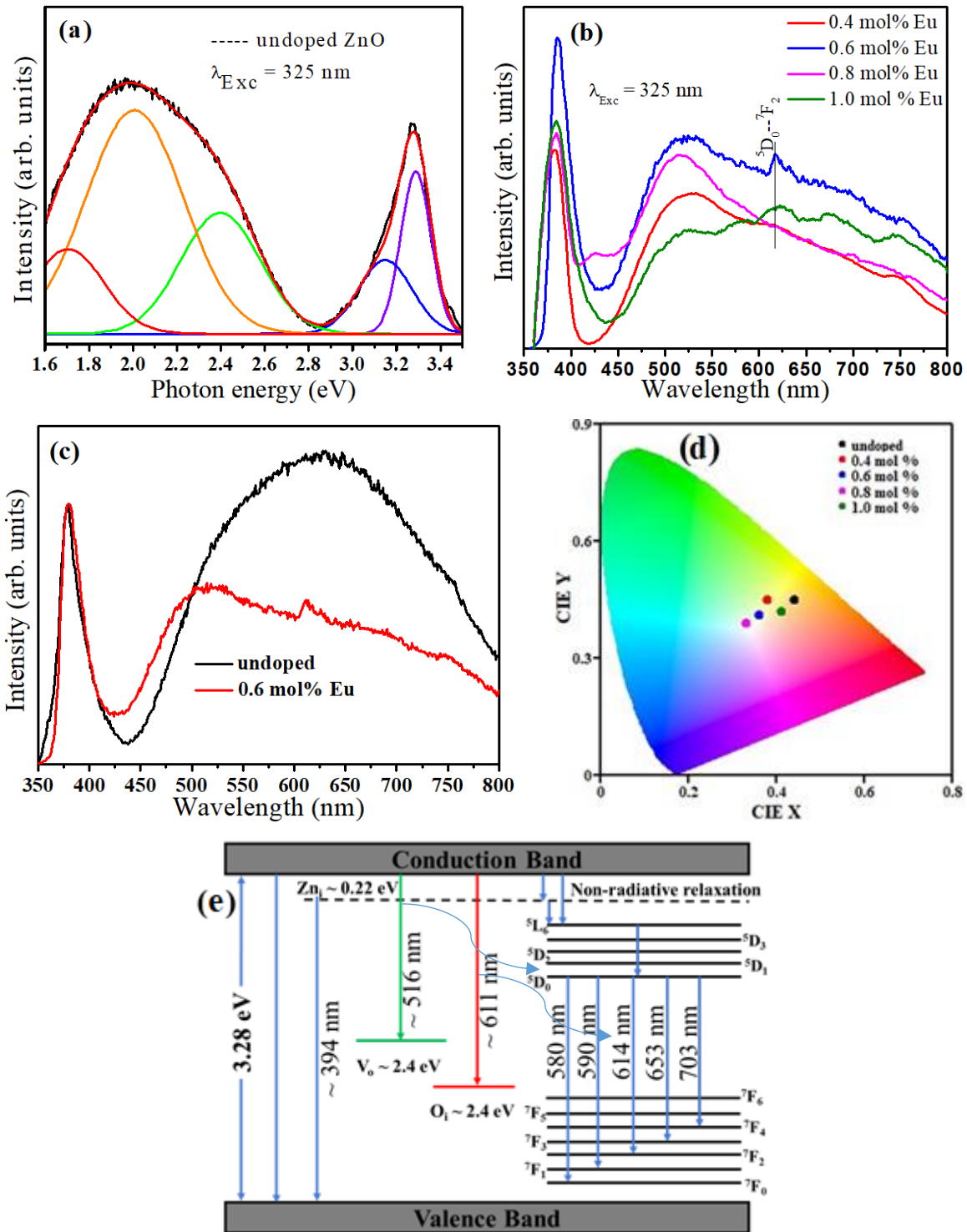


Fig. 4.5. Photoluminescence spectra of (a) deconvoluted PL peak of un-doped ZnO (b) different concentration of Eu^{3+} doped ZnO, (c) normalized PL intensity of the undoped and 0.6 mol% Eu doped ZnO, (d) CIE diagram of the undoped and Eu^{3+} doped ZnO films (excited at 325 nm using He-Cd laser) and (e) proposed diagram of Eu^{3+} doped ZnO films.

Fig. 4.6 displays the room temperature (a) excitation and (b) emission spectra of the Eu^{3+} doped ZnO films (deposited on silicon substrates) when excited using a monochromatized xenon lamp

as excitation source. The excitation spectra were recorded while monitoring the emission wavelength at 614 nm. The spectra showed sharp lines at 464 nm and weak lines at 392 nm which are characteristic of Eu^{3+} ions. The peak at 464 nm is attributed to the ${}^7\text{F}_0 - {}^5\text{D}_2$ transition and the small peak at 392 nm is attributed to the ${}^7\text{F}_0 - {}^5\text{L}_6$ transition as indicated in Fig. 4.6(a). The broad excitation band between 250 and 380 nm is associated with the ZnO host excitation region and showed that energy transfer from the ZnO to the Eu^{3+} ions occurred. The emission spectra (excited at 464 nm to target the Eu^{3+} ions without exciting the ZnO) showed the characteristic emission of the 4f – 4f transitions of the Eu^{3+} ions. The maximum intensity emission at 614 nm was assigned to the ${}^5\text{D}_0 - {}^7\text{F}_2$ transition, while the weak emissions at 590 nm, 653 nm and 703 nm were ascribed to the ${}^5\text{D}_0 - {}^7\text{F}_1$, ${}^5\text{D}_0 - {}^7\text{F}_2$ and ${}^5\text{D}_0 - {}^7\text{F}_4$ transitions, respectively [11, 30]. The emission arising from the ${}^5\text{D}_0 - {}^7\text{F}_1$ transition has been associated with the magnetic dipole, while the emission that arises from the ${}^5\text{D}_0 - {}^7\text{F}_2$ transition is ascribed to the electric dipole. Their intensity depends on the Eu^{3+} ion symmetry in the ZnO host. The ${}^5\text{D}_0 - {}^7\text{F}_1$ transition emission is more intense when Eu^{3+} ions occupy a site with inversion symmetry, while the ${}^5\text{D}_0 - {}^7\text{F}_2$ transition emission becomes intense when Eu^{3+} ions occupy a site without inversion symmetry. Since the emission arising from the ${}^5\text{D}_0 - {}^7\text{F}_2$ transition was the most intense emission and stronger than the ${}^5\text{D}_0 - {}^7\text{F}_1$ transition emission, this indicated that the Eu^{3+} ions occupied sites without inversion symmetry [31, 32], which is consistent with the Zn^{2+} lattice sites. The Eu^{3+} emission intensity initially increased with increasing Eu^{3+} concentration. The highest intensity was recorded from the sample containing 0.6 mol% of Eu^{3+} , after which the intensity decreased as demonstrated in Fig. 4.6(d). This was due to concentration quenching, which has been explained by different models, including energy transfer between rare earth ions caused by exchange or multipole-multipole interactions [33]. When the average distance between luminescent centers is decreased sufficiently, non-radiative energy transfer will become favorable; when the activator ions reaching their critical concentration, increasing the concentration of ions results in activator—activator coupling which enhances the migration of the excitation energy to their quenching centers [34]. The critical distance between the activator (Eu^{3+}) ions can determine whether the quenching is due to the ion exchange or multipole-multipole interactions. Multipole-multipole interaction mechanisms of energy transfer take place only if the critical distance between the activator ions is greater than 0.5 nm while the exchange interaction mechanism take place if the critical distance is less than 0.5 nm [35]. The following equation (4.1) was used to calculate the critical distance:

$$r = \left(\frac{M}{\rho C N_A} \right)^{\frac{1}{3}} \quad (4.1)$$

where r is the critical distance between the ions, M represents the molecular weight of ZnO (81.38 g/mol), ρ is the host (ZnO) density (5.606 g/cm³), C represents the Eu³⁺ ions concentration corresponding to the highest emission intensity (0.6 mol%) and N_A is Avogadro's number (6.023 x 10²³ mol⁻¹). The critical distance (r) was calculated to be 1.6 nm, which is much larger than 0.5 nm, suggesting that multipole-multipole interaction was responsible for the quenching mechanism. Otherwise, the quenching may be due to the created defects caused by the large size difference and valence difference of Eu³⁺ and Zn²⁺.

The Commission Internationale de l'éclairage (CIE) chromaticity coordinates of Eu³⁺ doped ZnO films excited at 464 nm, shown in Fig. 4.6(c), are compared to those excited at 325 nm in Table 4.3. It can be seen that the color coordinates of the film are dependent on the Eu³⁺ concentration. The CIE coordinate of the sample with 0.4 mol% of Eu³⁺ content excited at 464 nm was shifted to the yellow region. This is due to the broad peak around 500 nm - 575 nm which did not appear on the other samples. Since the spectra region (500 nm - 750 nm) was not sufficient to measure the CIE coordinates, and the samples excited at 464 nm which restrict the measurement region. Therefore, the CIE data obtained from the 464 nm excitation are approximations.

Table 4.3. Colour coordinates (X, Y) and color correlated temperature (CCT) of the samples excited at 325 nm and 464 nm.

Excitation wavelength	325 nm			464 nm		
	Sample	X	Y	CCT (K)	X	Y
Undoped	0.44	0.45	3280	-	-	-
0.4 mol% Eu ³⁺	0.38	0.45	4383	0.45	0.53	3567
0.6 mol% Eu ³⁺	0.36	0.41	4711	0.53	0.46	2271
0.8 mol% Eu ³⁺	0.33	0.39	5445	0.54	0.44	2070
1.0 mol% Eu ³⁺	0.41	0.42	3612	0.53	0.46	2271

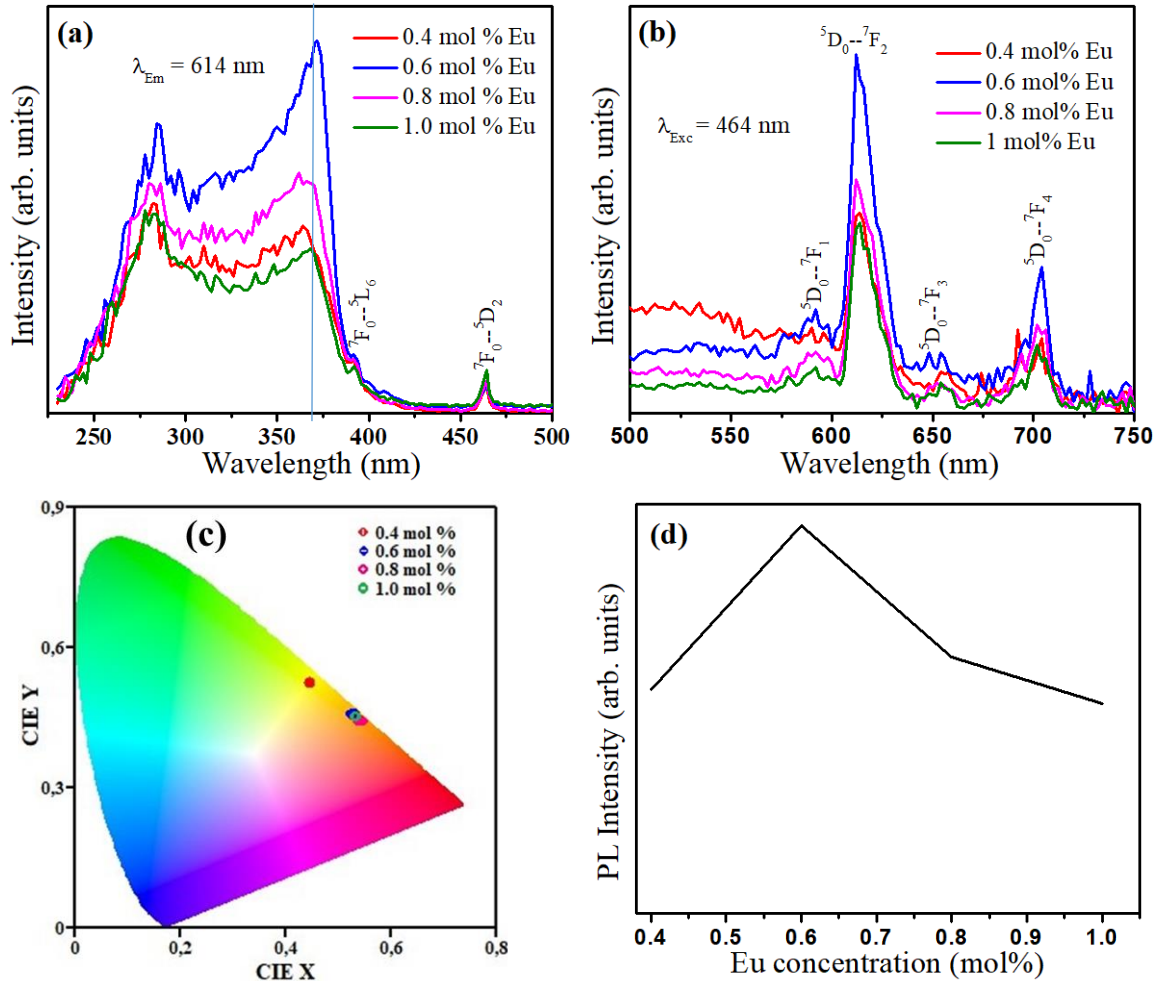


Fig. 4.6. PL (a) excitation and (b) emission spectra (excited at 464 nm) (c) CIE (X, Y) coordinate diagram showing chromaticity points of ZnO:Eu³⁺ with different concentration of Eu³⁺ (d) PL intensity as a function of Eu³⁺ concentration.

The vast change in emission spectrum when these samples are excited at 325 nm (Fig. 4.5(b)) or 464 nm (Fig. 4.6(b)) may also have a potential application to gauge the UV content of an excitation light source from the emission colour i.e. as a simple visible UV sensor.

4.3.4. Judd-Ofelt analysis

Judd-Ofelt analysis is a useful theoretical framework to explain the local environment of Eu³⁺ ions in the host material [36, 38]. The electric dipole (⁵D₀-⁷F₂ transition) intensity is sensitive to the chemical ligands around the Eu³⁺ ions and its intensity increases with an increase in the site asymmetry of Eu³⁺. Meanwhile, the magnetic dipole (⁵D₀-⁷F₁ transition) intensity is insensitive to the surrounding environment. Therefore, the asymmetry ratio (R) of the Eu³⁺ in the host can be determined from the ratio between the electric dipole intensity to the magnetic dipole intensity [19] and gives information on the site symmetry. The asymmetry ratio increased to its highest value for the 0.6 mol % of Eu³⁺ doped sample, after which it slightly

decreased. Generally, the asymmetry ratio values obtained for these samples are relatively high. This indicates the strong covalent nature of the Eu-O bonds and significant asymmetry around the Eu³⁺ ions in the host [39, 40].

Judd-Ofelt intensity parameters Ω_λ ($\lambda=2, 4$ and 6) provide information about the site symmetry and luminescence behaviour of Eu³⁺ in the ZnO host. Ω_2 is associated with the local environment, symmetry and the covalence of the metal ligand bonds around the activator. Ω_4 is sensitive to the microscopic parameters including: rigidity, viscosity, matrix and dielectric constant [37]. The value of Ω_2 increased to its highest value at 0.6 mol% of Eu³⁺ and then decreased for the higher Eu³⁺ content. This is consistent with the Eu³⁺ emission intensity as a function of Eu³⁺ concentration. This means that higher asymmetry around Eu³⁺ ions is very important to achieve a high intensity. Ω_2 and Ω_4 values are given in Table 4.4. The radiative rate properties were determined from the J-O intensity parameters using:

$$\frac{A_{0-2,4}}{A_{0-1}} = \frac{I_{0-2,4}}{I_{0-1}} \frac{h\nu_{0-1}}{h\nu_{0-2,4}} \quad (4.2)$$

where I_{0-J} represents the integrated emission intensity, $h\nu_{0-J}$ represents the energy corresponding to the transition ${}^5D_0 \rightarrow {}^7F_J$ ($J = 1, 2, 4$), A_{0-1} is the magnetic dipole radiative emission rate and has a value of about 50 s^{-1} [41].

Equation (4.3) is used to estimate the radiative emission rate, which is related to the electric dipole transition.

$$A_{0-2,4} = \frac{64\pi^4(\nu_{0-2,4})^3 e^2}{3hc^2} \frac{1}{4\pi\epsilon_0} \chi \sum_{J=2,4} \Omega_J \langle {}^5D_0 | U^{(J)} | {}^7F_{2,4} \rangle^2 \quad (4.3)$$

where $A_{0-2,4}$ is the radiative emission rate, χ is the Lorentz local field correction factor as a function of index of refraction ($\chi = (n(n^2 + 2)^2)/9$) and the squared reduced matrix element (RME) $\langle {}^5D_0 | U^{(J)} | {}^7F_{2,4} \rangle^2$ ($J=2,4$) has values of 0.0032 and 0.0023 for $J=2$ and $J=4$, respectively [40]. The values of Ω_2 and Ω_4 were found by substituting equation (4.2) in (4.3) and the results shown in Table 4.4. The increase of the Ω_2 value and its decrease at high concentration (1 mol%), indicate the dependency of the Eu³⁺ asymmetry in the host on the activators concentration. The value of Ω_2 is generally less than Ω_4 value, but the case is different in our study. This means that the ${}^5D_0 \rightarrow {}^7F_2$ transition efficiency is lower than the ${}^5D_0 \rightarrow {}^7F_4$ transition efficiency [42]. Our $\Omega_{2,4}$ values trends ($\Omega_2 > \Omega_4$) are comparable with trends reported by R. Raji et al. [38]. Other useful parameters such as transition probabilities, branching ratio and radiative lifetime for the excited states of Eu³⁺ ions were also estimated from the $\Omega_{0-2,4}$ intensity parameters.

The total radiative transition probability (A_R) is given by:

$$A_R = \sum_{J=1,2,4} A_{0-J} \quad (4.4)$$

The radiative life time (τ_{rad}) can be calculated from:

$$\tau_{rad} = \frac{1}{A_R} \quad (4.5)$$

The estimated lifetime values for the samples are given in Table 4.4. The life time values showed opposite dependency to the other intensity parameters such as Ω_2 , Ω_4 and asymmetry, where the higher the other parameters the shorter the lifetime. This indicate that the local environment around Eu^{3+} ions plays a significant role in the Eu^{3+} emission lifetime.

The branching ratio β_{0-J} corresponding to the emission from an excited level to its lower levels and is given by:

$$\beta_{0-J} = \frac{A_{0-J}}{A_T} \quad (4.6)$$

The branching ratio (β_{01} , β_{02} and β_{04}) values of the samples are given in Table 4.4.

Table 4.4. Judd-Ofelt intensity parameters, transition probability (A_τ), radiative life time (τ_{rad}), and branching ratio (β_{01} , β_{02} and β_{04}).

Concentration mol %	J-O intensity parameters		Transitions	$A_{0,2,4}(\text{s}^{-1})$	$A_{0,1}(\text{s}^{-1})$	$A_\tau(\text{s}^{-1})$	$\tau_{rad}(\text{ms})$	$\beta(\%)$	Asymmetry ratio R
	$\Omega_2(\text{pm}^2)$	$\Omega_4(\text{pm}^2)$							
0.4	1.70	1.16	$^5\text{D}_{0-7}\text{F}_1$	-	50	243.17	4.11	20.6	2.554
			$^5\text{D}_{0-7}\text{F}_2$	132.41	-			54.4	
			$^5\text{D}_{0-7}\text{F}_4$	60.76	-			25	
0.6	2.93	1.83	$^5\text{D}_{0-7}\text{F}_1$	-	50	377.49	2.65	13.2	4.477
			$^5\text{D}_{0-7}\text{F}_2$	231.49	-			61.4	
			$^5\text{D}_{0-7}\text{F}_4$	96.00	-			25.4	
0.8	2.71	1.63	$^5\text{D}_{0-7}\text{F}_1$	-	50	350.25	2.86	14.3	4.133
			$^5\text{D}_{0-7}\text{F}_2$	214.31	-			61.2	
			$^5\text{D}_{0-7}\text{F}_4$	85.94	-			24.5	
1.0	2.60	1.63	$^5\text{D}_{0-7}\text{F}_1$	-	50	341.16	2.93	14.7	3.970
			$^5\text{D}_{0-7}\text{F}_2$	205.23	-			60.2	
			$^5\text{D}_{0-7}\text{F}_4$	85.93	-			25.1	

4.4. Conclusion

ZnO thin films with different concentrations of Eu^{3+} ions were successfully deposited on Si (100) and glass substrates by the spin coating technique. The effect of the Eu^{3+} concentration on the structure, optical and PL properties of the films was investigated. Incorporation of the Eu^{3+} ions in the ZnO matrix was confirmed from the XRD and PL data. Deterioration of the film crystallinity and the degree of preferred orientation with increasing the Eu^{3+} concentration

was observed. The particle size and the optical band gap were found to be inversely proportional to the Eu^{3+} concentration. Possible inefficient defect-assisted energy and/or charge transfer were found to take place between deep level defects to Eu^{3+} ions. Upon direct excitation of the Eu^{3+} ions (464 nm), the films emitted only Eu^{3+} characteristic peaks and their intensity increased to its maximum value at 0.6 mol% of Eu^{3+} , where after the intensity was quenched, different mechanism were found to be responsible for the quenching including: crystallinity deterioration, creation or reduction of defects and multipole-multipole interaction between Eu^{3+} ions. Judd-Ofelt intensity parameters (Ω_2 and asymmetry ratio) analysis was performed to determine the local environment around the Eu^{3+} ions. It was found that Eu^{3+} asymmetry in the host played a key role in the PL emission intensity, so that higher asymmetry around the Eu^{3+} ions gave higher PL intensity. The estimated lifetime of the Eu^{3+} emission is inversely proportional to the asymmetry ratio and Ω_2 value. Further work based on these results may lead to an increase in the red emission of Eu-doped ZnO spin coating films. The vast change in emission spectrum when these samples are excited at 325 nm or 464 nm may also have a potential application to gauge the UV content of an excitation light source from the emission colour.

4.5. References

- [1] H. Wang, X. Mo, Z. Chen, S. Li, H. Huang, Y. Liu and G. Fang, Near white electroluminescence from self-supporting ZnO nanocone array based heterojunction light-emitting diodes, *Mater. Res. Express* **2** (2015) 035005. <https://doi.org/10.1088/2053-1591/2/3/035005>.
- [2] A. Janotti and C. G Van de Walle, Fundamentals of zinc oxide as a semiconductor, *Rep. Prog. Phys.* **72** (2009) 126501. <https://doi.org/10.1088/0034-4885/72/12/126501>.
- [3] X. Wen, J.A. Davis, L.V. Dao, P. Hannaford, V.A. Coleman, H.H. Tan, C. Jagadish, K. Koike, S. Sasa, M. Inoue and M. Yano, Thermal quenching of photoluminescence in ZnO/ZnMgO multiple quantum wells following oxygen implantation and rapid thermal annealing, *J. Lumin* **129** (2009) 153. <https://doi.org/10.1016/j.jlumin.2008.09.006>.
- [4] H. D. Sun, T. Makino, and Y. Segawa, Enhancement of exciton binding energies in ZnO/ZnMgO multi quantum wells, *J. Appl. Phys* **91** (2002) 1993. <http://dx.doi.org/10.1063/1.1445280>.
- [5] D. G. Thomas, The exciton spectrum of zinc oxide, *J. Phys. Chem. Solids* **15** (1960) 86-96. [https://doi.org/10.1016/0022-3697\(60\)90104-9](https://doi.org/10.1016/0022-3697(60)90104-9).

- [6] A.B. Djurisi, A.M.C. Ng and X.Y. Chen, ZnO nanostructures for optoelectronics: Material properties and device applications, *Prog Quantum Electronics* **34** (2010) 191-259. <https://doi.org/10.1016/j.pquantelec.2010.04.001>.
- [7] B. Gil, Oscillator strengths of A, B, and C excitons in ZnO films, *Phys. Rev. B* **64** (2001) 201310. <https://doi.org/10.1103/PhysRevB.64.201310>.
- [8] S. M. Ahmed, P. Szymanski, M. A. El-Sayed, Y. Badr and L. M. El-Nadi, The photoluminescence properties of undoped & Eu-doped ZnO thin films grown by RF sputtering on sapphire and silicon substrates, *Appl. Surf. Sci.* **359** (2015) 356. <http://dx.doi.org/doi:10.1016/j.apsusc.2015.10.151>.
- [9] K. D. A. Kumar, S. Valanarasu, A. Kathalingam, V. Ganesh, M. Shkir and S. AlFaify, Effect of solvents on sol-gel spin-coated nanostructured Al-doped ZnO thin films: a film for key optoelectronic applications, *Appl Phys A* **123** (2017) 801. <https://doi.org/10.1007/s0033>.
- [10] W. W. Zhong, D. W. Guan, Y. L. Liu, L. Zhang, Y. P. Liu, Z. G. Li and W. P. Chen, Effect of Annealing on the Structure and Photoluminescence of Eu-Doped ZnO Nanorod Ordered Array Thin Films, *Journal of Nanomaterials* **2012** (2012) 1. [doi:10.1155/2012/263679](https://doi.org/10.1155/2012/263679).
- [11] X. Zeng, J. Yuan and L. Zhang, Synthesis and Photoluminescent Properties of Rare Earth Doped ZnO Hierarchical Microsphere, *J. Phys. Chem. C* **112** (2008) 3503-3508. DOI: [10.1021/jp0768118](https://doi.org/10.1021/jp0768118).
- [12] P. Dorenbosa and E. van der Kolk, Location of lanthanide impurity levels in the III-V semiconductor GaN, *Appl. Phys. Lett.* **89** (2006) 061122. <https://doi.org/10.1063/1.2336716>.
- [13] S. M. Ahmed, P. Szymanski, L. M. El-Nadi and M. A. El-Sayed, Energy-transfer efficiency in Eu-doped ZnO thin films: The effects of oxidative annealing on the dynamics and the intermediate defect states, *ACS Appl. Mater. Interfaces* **6** (2014) 1765-1772. DOI: [10.1021/am404662k](https://doi.org/10.1021/am404662k).
- [14] K. Suzuki, K. Murayama and N. Tanaka, Enhanced luminescence in Eu-doped ZnO nanocrystalline films, *Appl. Phys. Lett.* **107** (2015) 031902. <https://doi.org/10.1063/1.4926986>.

- [15] H. Akazawa and H. Shinojima, Energy transfer and dissipation processes studied using photoluminescence of Eu^{3+} ions doped in epitaxial ZnO films, *Thin Solid Films* **616** (2016) 204–212. DOI: 10.1016/j.tsf.2016.08.029.
- [16] P. Chen, X. Ma and D. Yang, ZnO:Eu thin-films: Sol–gel derivation and strong photoluminescence from 5D0 \rightarrow 7F0 transition of Eu^{3+} ions, *J. Alloys Compd.* **431** (2007) 317–320. <https://doi.org/10.1016/j.jallcom.2006.05.078>.
- [17] L. Yang, H. Zheng, Q. Liu, S. Zhou and W. Zhang, The doping site analysis and control of Eu^{3+} in ZnO:Eu crystal lattice, *J. Lumin* **204** (2018) 189-194. <https://doi.org/10.1016/j.jlumin.2018.08.038>.
- [18] E. Hasabeldaim, O. M. Ntwaeaborwa, R. E. Kroon, David E. Motaung, E. Coetsee and H. C. Swart, Effect of PLD growth atmosphere on the physical properties of ZnO:Zn thin films, *Opt. Mater.* **74** (2017) 76-85. <https://doi.org/10.1016/j.optmat.2017.04.061>.
- [19] V. Kumar, Vijay Kumar, S. Som, M. M. Duvenhage, O. M. Ntwaeaborwa and H. C. Swart, Effect of Eu doping on the photoluminescence properties of ZnO nanophosphors for red emission applications, *Appl. Surf. Sci.* **308** (2014) 419-430. <http://dx.doi.org/10.1016/j.apsusc.2014.04.192>.
- [20] Q. Q. Dai, L. Luo, F. Y. Huang, D. P. Xiong, X. G. Tang and J. Chen, Influence of annealing and Europium-doping on the structure and optical properties of ZnO thin films grown on quartz substrate by magnetron sputtering, *Mater. Sci. Forum*, **687** (2011) 667-672. <https://doi.org/10.4028/www.scientific.net/MSF.687.667>.
- [21] V. V. Khomyak, M. M. Slyotov, I. I. Shteplyuk, G. V. Lashkarev, O. M. Slyotov, P. D. Marianchuk and V. V. Kosolovskiy, Annealing effect on the near-band edge emission of ZnO, *J. Phys. Chem. Solids* **74** (2013) 291-297. <https://doi.org/10.1016/j.jpcs.2012.10.001>.
- [22] D. Raoufi and L. Eftekhari, Crystallography and morphology dependence of In_2O_3 :Sn thin films on deposition rate, *surf coat tech.* **274** (2015) 44-50. <http://dx.doi.org/10.1016/j.surfcoat.2015.04.034>.
- [23] V. Kumar, N. Singh, Vijay Kumar, L. P. Purohit, A. Kapoor, O. M. Ntwaeaborwa, and H. C. Swart, Doped zinc oxide window layers for dye sensitized solar cells, *J. Appl. Phys.* **114** (2013) 134506. <https://doi.org/10.1063/1.4824363>.

- [24] V. Kumar, S. Som, Vijay Kumar, Vinay Kumar, O. M. Ntwaeaborwa, E. Coetsee, H. C. Swart, Tunable and white emission from ZnO:Tb³⁺ nanophosphors for solid state lighting applications, *Chem Eng J.* **255** (2014) 541-552. <https://doi.org/10.1016/j.cej.2014.06.027>.
- [25] D. C. Reynolds, D. C. Look, and B. Jogai, Neutral-donor-bound-exciton complexes in ZnO crystals, *Phys. Rev. B* **57** (1998) 12151. <https://doi.org/10.1103/PhysRevB.57.12151>.
- [26] B. Efafi, M. H. Majles Ara and S. S. Mousavi, Strong blue emission from ZnO nanocrystals synthesized in acetone-based solvent, *J Lumin* **178** (2016) 384-387. <https://doi.org/10.1016/j.jlumin.2016.06.026>.
- [27] E. H. H. Hasabeldaim, O. M. Ntwaeaborwa, R. E. Kroon, E. Coetsee and H. C. Swart, Enhanced green luminescence from ZnO nanorods, *J. Vac. Sci. Technol. B* **37** (2019) 011201-011210. <https://doi.org/10.1116/1.5052543>.
- [28] K. Bandopadhyay and J. Mitra, Zn interstitials and O vacancies responsible for n-type ZnO: what do the emission spectra reveal?, *RSC Adv.* **5** (2015) 23540-23547. DOI: 10.1039/c5ra00355e.
- [29] A. Balakrishna, Trilok K. Pathak, E. Coetsee-Hugo, V. Kumar, R. E. Kroon O. M. Ntwaeaborwa and H. C. Swart, Synthesis, structure and optical studies of ZnO:Eu³⁺,Er³⁺,Yb³⁺ thin films: Enhanced up-conversion emission, *Colloids Surf. A* **540** (2018) 123–135. <https://doi.org/10.1016/j.colsurfa.2017.12.066>.
- [30] B. Han, P. Li, J. Zhang, J. Zhang, Y. Xue, X. Suo, Q. Huang, Y. Feng and H. Shi, First observation of the emission from ⁵D_J (J=1, 2, 3) energy levels of Eu³⁺ in Bi₄O₃(BO₃)(PO₄):Eu³⁺ phosphor, *Mater. Lett.* **158** (2015) 208-210. DOI: 10.1016/j.matlet.2015.06.024.
- [31] P. V. Ramakrishna, D. B. R. K. Murthy and D. L. Sastry, White-light emitting Eu³⁺ co-doped ZnO/Zn₂SiO₄:Mn²⁺ composite microphosphor, *Mol. Biomol. Spectrosc.* **125** (2014) 234-238. <https://doi.org/10.1016/j.saa.2014.01.110>.
- [32] T. T. Van Tran, T. M. Dung Cao, Q. V. Lam and V. H. Le, Emission of Eu³⁺ in SiO₂-ZnO glass and SiO₂-SnO₂ glass-ceramic: correlation between structure and optical properties of Eu³⁺ ions, *J. Non-Cryst. Solids* **459** (2017) 57-62. DOI: 10.1016/j.jnoncrysol.2016.12.040.
- [33] S. Yao, L. Xue and Y. Yan, Properties of Eu³⁺ luminescence in the monoclinic Ba₂MgSi₂O₇, *Ceramics* **55(3)** (2011) 251-255. ISSN: 1804-5847.

- [34] G. S. R. Raju, E. Pavitra, S. K. Hussain, D. Balajib and J. S. Yu, Eu^{3+} ion concentration induced 3D luminescence properties of novel red-emitting $\text{Ba}_4\text{La}_6(\text{SiO}_4)\text{O}:\text{Eu}^{3+}$ oxyapatite phosphors for versatile applications, *J. Mater. Chem.* **4** (2016) 1039. DOI: 10.1039/c5tc03919c.
- [35] O. M. Ntwaeaborwa, S. J. Mofokeng, V. Kumar, R. E. Kroon, Structural, optical and photoluminescence properties of Eu^{3+} doped ZnO nanoparticles, *Spectrochim. Acta A* **182** (2017) 42-49. <https://doi.org/10.1016/j.saa.2017.03.067>.
- [36] B. R. JvuD, Optical Absorption Intensities of Rare-Earth Ions, *Phys. Rev.* **127** (1962) 750-761. <https://doi.org/10.1103/PhysRev.127.750>.
- [37] G. S. Ofelt, Intensities of Crystal Spectra of Rare-Earth Ions, *J. Chem. Phys.* **37** (1962) 511-520. <https://doi.org/10.1063/1.1701366>.
- [38] R. Raji, R. G. Abhilash Kumar, K. G. Gopchandran, Influence of local structure on luminescence dynamics of red emitting $\text{ZnO}:\text{Eu}^{3+}$ nanostructures and its Judd-Ofelt analysis, *J. Lumin.* **205** (2019) 179-189. <https://doi.org/10.1016/j.jlumin.2018.09.002>.
- [39] M. Gökçe, Development of Eu^{3+} doped bismuth germanate glasses for red laser applications, *J. Non-Cryst. Solids* **505** (2019) 272–278. DOI: 10.1016/j.jnoncrysol.2018.11.011.
- [40] M. Gökçea, U. Şentürk, D. K. Uslu, G. Burgaz, Y. Şahin and A. G. Gökçe, Investigation of europium concentration dependence on the luminescent properties of borogermanate glasses, *J. Lumin* **192** (2017) 263–268. <https://doi.org/10.1016/j.jlumin.2017.06.041>.
- [41] N. Rakov, D. F. Amaral, R. B. Guimarães and G. S. Maciel, Spectroscopic analysis of Eu^{3+} -and $\text{Eu}^{3+}:\text{Yb}^{3+}$ -doped yttrium silicate crystalline powders prepared by combustion synthesis, *J. Appl. Phys* **108** (2010) 073501-073506. <http://dx.doi.org/10.1063/1.3489992>.
- [42] F. Wang, B. Yang, J. Zhang, Y. Dai and W. Ma, Highly enhanced luminescence of Tb^{3+} -activated gadolinium oxysulfide phosphor by doping with Zn^{2+} ions, *J. Lumin.* **130** (2010) 473-477. doi:10.1016/j.jlumin.2009.10.016.

Chapter 5

Photoluminescence and cathodoluminescence of spin coated ZnO films with different concentration of Eu^{3+} ions

5.1. Introduction

Rare earth trivalent (RE^{3+}) ions doped wide band gap semiconductors have gained considerable attention in the field of optoelectronic devices [1] because of their potential use in different applications including [2] light emitting diodes (LEDs), flat panel displays (FPDs), plasma display panels (PDPs), fluorescent lamps, etc. RE doped ZnO nanophosphors can be synthesized by different methods and the emitted light can be tuned throughout the visible range [3]. Eu^{3+} doped ZnO presents a great opportunity to achieve intense red emission, owing to the advantage of the 4f-4f transition of Eu^{3+} ions and the excellent properties of ZnO as a host, such as its wide band gap (3.37 eV) at room temperature, large exciton binding energy (60 meV) [4], low thermal quenching effect, high thermal and good chemical stability [5], high electron mobility [6] as well as the availability of different crystal sites that activator ions (RE^{3+}) can occupy [7]. Additionally, ZnO is a low-cost material and easy to produce. These properties made ZnO a good material (host) to replace the relatively expensive gallium nitride (GaN), the short lifetime sulphide based wide band gap semiconductors (ZnS) which are commercially available in the market, and selenides-based semiconductors [8].

Over the past few years, extensive research has been done on Eu^{3+} doped ZnO aiming to harvest an efficient red emission from Eu^{3+} incorporated in ZnO. To achieve this, an efficient energy transfer from ZnO native defects to Eu^{3+} energy levels is highly required [9, 10]. However, the efficient energy transfer from ZnO to Eu^{3+} ions still remains a challenge. This is due to different reasons, including the large ionic radius difference between Eu^{3+} (90 pm) and Zn^{2+} (74 pm) that can lead to self-quenching (which decreases the luminescence efficiency especially for annealing at high temperatures) [11], the energy of the charge transfer level of Eu^{3+} in ZnO which is equal or higher than the bottom of the ZnO conduction band [12] and the exciton decay time of ZnO which is much faster than the lifetime of Eu^{3+} ions [10]. In a previous study the effect of lower Eu^{3+} concentration on the structure, optical and photoluminescence (PL) properties of thin films was investigated up to 1 mol% Eu^{3+} [13]. Although the defect emission was reduced due to the Eu^{3+} doping, the Eu^{3+} characteristic emission contribution to the PL emission during excitation at 325 nm was, however, still very low. It was therefore interesting to also investigate the Eu^{3+} emission for higher Eu^{3+} concentrations in this study.

Different techniques were used to deposit Eu^{3+} doped ZnO thin films in the past using techniques such as pulsed laser deposition, magnetron sputtering, metal organic chemical vapor deposition [14], molecular beam epitaxy, spray pyrolysis, etc. Sol-gel spin coating is a low cost and easy technique that has been used for decades in electronic industries. Therefore, it was used in this work to deposit the Eu^{3+} doped ZnO thin films [15, 16].

Most studies of Eu^{3+} doped ZnO have focused on its PL properties and energy transfer mechanisms. Due to the potential of this material for electron-excited applications such as field emission displays (FEDs) and cathode-ray tubes (CRTs) [17], we have made an attempt to investigate the cathodoluminescence (CL) of the Eu^{3+} doped ZnO thin films. Moreover, the electron beam excitation mechanism is similar to the excitation mechanism in electroluminescence [18], where both can excite the luminescence centres via impact ionization/excitation mechanisms. Therefore, studying the CL of the film may also give a preliminary evaluation of its potential application in electroluminescence.

CL emission is well-known by its high electron-photon conversion efficiency over the PL efficiency, because of the differences in their excitation mechanisms [19]. Therefore, in this work, we have studied the luminescence properties of different concentrations (1 to 4 mol%) of Eu^{3+} doped ZnO thin films fabricated by the spin coating technique. PL of the samples was studied when the films were excited at different wavelengths (direct and indirect excitation). Moreover, due to the necessity of the stability of these materials for optoelectronics applications, the surface state, chemical and luminescence stability of the highest intensity sample was examined in vacuum during prolonged electron beam irradiation.

5.2. Experimental methods

5.2.1. Preparation

Eu doped ZnO thin films were prepared by a sol-gel method by using the spin coating technique. Zinc acetate dihydrate $\text{Zn}(\text{CH}_3\text{COO})_2 \cdot 2\text{H}_2\text{O}$, europium acetate hydrate $\text{Eu}(\text{CH}_3\text{COO})_3 \cdot x\text{H}_2\text{O}$ and monoethanolamine (MEA) $\text{C}_2\text{H}_7\text{NO}$ were used as zinc, europium sources and stabilizer, respectively. High purity ethanol (99.9%) was used as a solvent. All these chemical reagents were used as they were received from Sigma Aldrich without any further purifications. An equimolar ratio of zinc acetate and MEA were dissolved in 40 ml of ethanol with molarity kept at 0.2. Firstly, a suitable amount of zinc acetate and proper amount of europium acetate (0, 1, 2, 3 and 4 mol %) were dissolved in ethanol and stirred for about 30 min at room temperature. Then MEA was added dropwise under stirring, which was continued

for another 2 h until a clear and transparent solution formed. The solution was kept overnight at room temperature without any precipitation observed.

p-type Si (100) and glass substrates were cut into about 2x2 cm² pieces and then cleaned in an ultrasonic bath in isopropanol, acetone, ethanol and distilled water for 5 min each, and then dried by gently blowing nitrogen gas on their surfaces. For the coating process, the spin coater was set at 2500 rpm/min for 30 s. The substrate was held on the spin coating chuck and the solution was dropped on the substrate after which the spinning was started. The coated substrates were heated at 300 °C for 10 min. The coating process was repeated 12 times to obtain the required thickness. Finally, the films were annealed in air at 500 °C for 2 h in a quartz tube furnace ramped at 5 °C/min.

5.2.2. Characterization

X-ray diffraction (XRD) technique was used to characterize the structure of the films, which were obtained using a Bruker D8 Advance system with Cu K α X-rays ($\lambda = 0.154$ nm) generated at a voltage of 40 kV and current of 40 mA. A JEOL JSM-7800F scanning electron microscope (SEM) was used to examine the morphology of the sample, with the electron beam voltage maintained at 10 keV during the measurements. An energy dispersive X-ray spectrometer (EDS) attached to the SEM system was employed for the elemental composition measurements. A Shimadzu SPM-9600 atomic force microscope (AFM) was used to obtain images of the surface topography and the roughness was analyzed using the commercial software that came with the AFM system. A PHI 5000 Versaprobe system was utilized to perform the X-ray photoelectron spectroscopy (XPS) measurements using an Al X-Ray beam (100 μ m, 25 W and 15 kV), while an Ar⁺ ion beam (2 kV and 2 μ A) was rastered over an area of 1 mm x 1 mm to sputter the sample for depth profile measurements at a rate of about 14 nm/min. The binding energy charge correction was done by using the C—C bond at a binding energy of 284.7 eV. Time of flight secondary ion mass spectroscopy (ToF-SIMS) measurements were performed using an IONTOF ToF-SIMS. A pulsed 30 keV Bi⁺ primary ion beam with a target current of 1 pA (30 nA DC) and the analytical field-of-view was 100 x 100 μ m². The analysis was performed in saw tooth rastering mode with 512x512 pixels² with a binning of 4 pixels. For depth profiling, the O⁻ sputter gun operated at 1 kV and ~250 nA were used for both spectroscopy and imaging in the positive mode. The sputter area was 300x300 μ m.

A Lambda 950 UV-visible spectrometer (from Perkin Elmer) was used to measure the transmittance spectra. PL spectra were recorded at room temperature using a PMT detector while the samples were excited by He-Cd laser of wavelength of 325 nm. An Edinburgh

Instruments FLS980 spectrometer equipped with a xenon lamp as an excitation source was utilized to measure the PL emission spectra of the samples at different wavelengths. An Ocean Optics PC2000 spectrometer interfaced with OOI Base32 computer software was used to collect the CL data. The samples were excited by an electron beam with working beam voltage of 2 keV, beam current of 24 μA , current density of 2.12 $\text{mA}\cdot\text{cm}^{-2}$ and beam spot size of about 1.2 mm. The highest CL intensity sample was subjected to electron beam irradiation for about 22 hours and the CL intensity was recorded against the electron beam dose. The CL data collection and the irradiation experiment were done in vacuum at a base pressure of 5×10^{-8} Torr.

5.3. Results and discussion

5.3.1. Structure and morphology

Fig. 5.1 displays the XRD patterns of the undoped and Eu^{3+} doped ZnO thin films. The films have preferred orientation along the (002) plane, which is perpendicular to the c-axis. Two additional small peaks associated with the (100) and (101) planes were detected for the undoped and 1 mol% of Eu^{3+} doped ZnO thin films. Disappearance of these peaks for the films at higher Eu^{3+} concentration (2, 3 and 4 mol%) suggest that the preferred orientation of the films and hence their crystallinity improved at these concentrations. These changes support the successful incorporation of Eu^{3+} ions into Zn^{2+} ions sites and suppressing the self-purification mechanism [20]. The absence of any other peaks associated with europium oxide also indicated that the Eu^{3+} ions successfully substituted the Zn^{2+} ion sites. The major peak of the ZnO (002) plane shifted slightly to lower 2θ angles with increasing Eu^{3+} content up to 2 mol% which signified the expansion in the lattice spacing. This phenomenon is commonly observed when a larger ion substitutes a smaller ion in a host crystal [21, 22]. In our case, the Eu^{3+} ion with ionic radius of 90 pm is larger than the Zn^{2+} ion with ionic radius of 74 pm. Sherrer's equation was used to estimate the crystallite size of the ZnO films with different concentrations of Eu^{3+} ions. The crystallite size was found to decrease from 30 nm to 14 nm with increasing Eu^{3+} contents up to 4 mol% as in Table 1. From Bragg's law and the Miller indices the lattice parameter (c) was calculated from the diffraction angle of the (002) peak and the values were listed in Table 1. Lattice expansion was observed until the concentration of 2 mol% and then contraction at 3 or 4 mol% for the Eu^{3+} doped ZnO thin films. While the lattice expansion can be attributed to the differences in Eu^{3+} and Zn^{2+} ionic radii, the lattice contraction for 3 and 4 mol% Eu doped films can be interpreted as follows: the Eu^{3+} concentration might have exceeded the substitutional solubility limit at such high concentrations, so that Eu^{3+} may

instead occupy interstitial sites - these different mechanisms compete each other and the lattice parameter may be decreased [20].

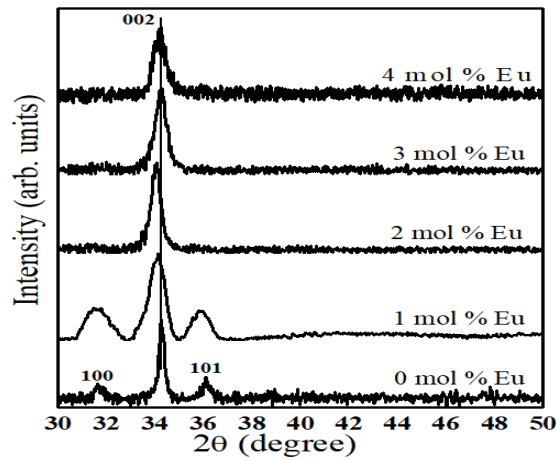


Fig. 5.1. XRD patterns of different contents of Eu^{3+} doped ZnO spin coating films.

Table 5.1. Crystal parameters, crystallite size, roughness and optical band gap for different concentration of Eu^{3+} doped ZnO spin coating thin films.

Sample	Lattice parameter (c) (nm)	Crystallite size (D) (nm)	RMS roughness (nm)	Band gap (eV)
0 mol % Eu^{3+}	0.5230	30 ± 1	3.3 ± 0.1	3.28 ± 0.05
1 mol % Eu^{3+}	0.5259	12 ± 1	1.2 ± 0.1	3.26 ± 0.05
2 mol % Eu^{3+}	0.5264	18 ± 1	0.7 ± 0.1	3.25 ± 0.05
3 mol % Eu^{3+}	0.5235	15 ± 1	0.7 ± 0.1	3.25 ± 0.05
4 mol % Eu^{3+}	0.5242	14 ± 1	0.5 ± 0.1	3.24 ± 0.05

Fig. 5.2 shows the SEM images of the ZnO thin films with different concentrations of Eu^{3+} (on silicon substrates). SEM images confirmed that the sample morphology was slightly affected by the change of the Eu^{3+} concentration. No cracks, voids or exfoliations were observed on all the sample surfaces. The undoped sample showed a homogeneous distribution and tightly packed small grains with an average grain size of less than 80 nm. The Eu^{3+} doped samples showed a more compact grain structure than the undoped sample. These minor modifications may be attributed to the ionic radii differences between Eu^{3+} and Zn^{2+} , causing excess Eu atoms to be aggregated on the grain boundaries due to the low solubility of Eu in the ZnO host. The cross-section images shown as insets confirmed a uniform thickness of the thin films. In order to determine the actual composition of the films with different Eu^{3+} concentration, EDS was performed for the different films and the results are tabulated in Table 5.2. An EDS spectrum

for the sample with 2 mol% of Eu^{3+} is shown in Fig. 5.2(f) as an example. Other than the major elements (Zn, O and Eu), Si from the substrate was detected at 1.8 keV as well as a small peak at ~ 2.5 keV, which is likely due to the atmospheric C on the surface that was also detected. It's worth noting that the oxygen concentrations for the films were almost constant, while the Zn concentration has decreased with an increase in the Eu^{3+} content. This is a good indication for the substitution of Eu^{3+} ions into the Zn ions positions in the ZnO lattice and it is consistent with the XRD results. Keeping the accuracy of EDS concentration calculations in mind this values correlate very well with the actual expected values.

Table 5.2. Elemental composition of the films obtained by EDS.

Samples/ elements	Zn (at%)	O (at%)	Eu (at%)
0 mol%	47.7	52.4	0
1 mol%	46.8	52.4	0.9
2 mol%	45.5	52.5	2.1
3 mol%	45.1	52.4	2.5
4 mol%	44.1	52.5	3.4

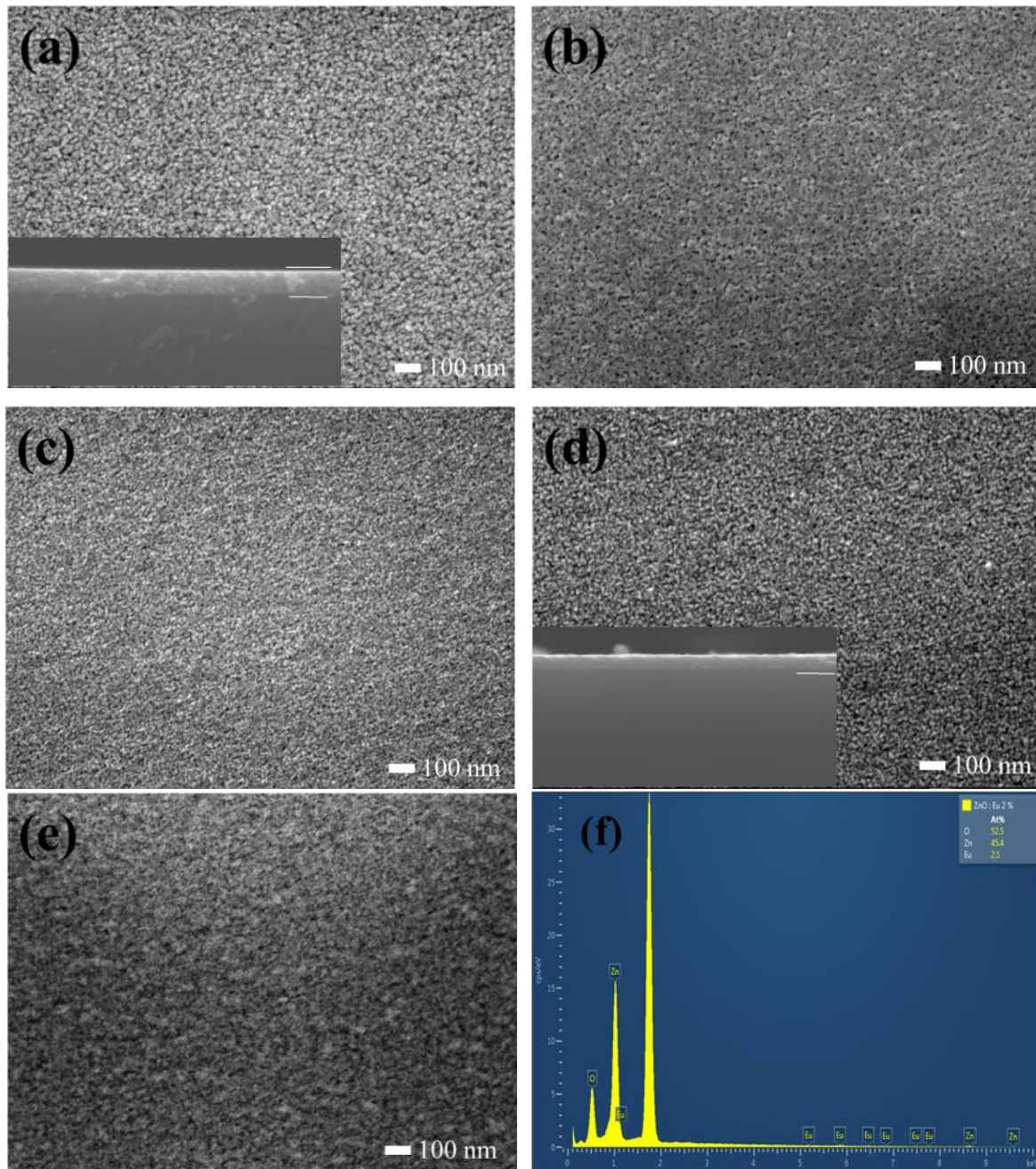


Fig. 5.2. SEM images of ZnO thin films doped with different Eu^{3+} concentrations (a) undoped, (b) 1 mol%, (c) 2 mol%, (d) 3 mol% and (e) 4 mol% and (f) is the EDS spectrum for a sample with 2 mol% of Eu^{3+} . The insets in (a) and (d) show the cross sectional views of these samples.

Fig. 5.3 displays the 3D AFM images of the ZnO films with different Eu^{3+} concentration coated on the silicon substrates. The undoped sample, Fig. 5.3(a), shows evenly distributed particles with pyramids-like shapes at the top of the particles as can be seen in the 3D images. The average particle size estimated from the AFM image was about 76 nm for the undoped sample, and it has decreased with an interval of about 5 nm as the Eu^{3+} content increased from 1, 2, 3 and 4 mol%, see Fig. 5.3 (b), (c), (d) and (e), respectively. The reduction in the particles size

may be attributed to the improvement of the crystal orientation with increasing Eu^{3+} concentration. The root mean square roughness (R_q) has decreased with increasing the Eu^{3+} concentration as shown in Table 5.1. The highest value of the roughness obtained for the undoped film was about 3.3 nm, which has dramatically decreased to 1.2 nm after introducing 1 mol% of Eu^{3+} , and then the roughness continued to slightly decrease for more Eu^{3+} content to 0.7 nm, 0.7 nm and 0.5 nm for the films with 2, 3 and 4 mol% of Eu^{3+} , respectively. The decrease in the film's roughness may be ascribed to the change in the particles' shape and the reduction in the particles' size. When the particles' size decreased, more particles came closer to each other and the boundaries between them will be decreased, thus the roughness may be decreased.

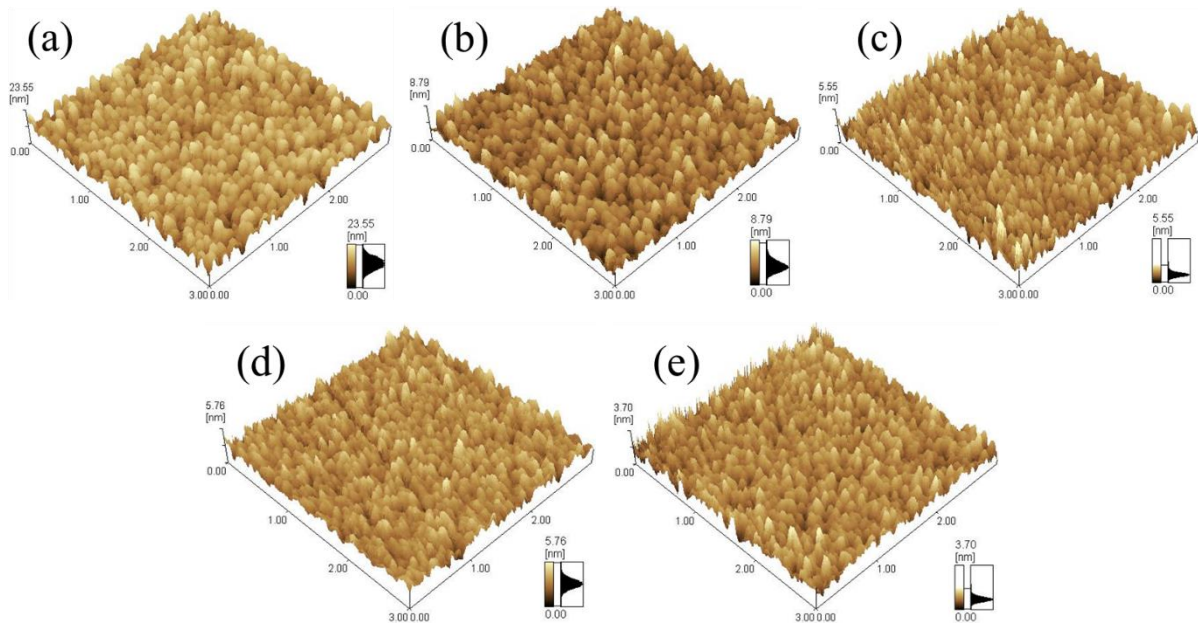


Fig. 5.3. 3D AFM images of ZnO spin coating films with different Eu^{3+} content (a) 0 mol%, (b) 1 mol%, (c) 2 mol%, (d) 3 mol% and (e) 4 mol%.

XPS high-resolution spectra were recorded for the films with different Eu^{3+} concentrations, as well as for the film with 3 mol % of Eu^{3+} after electron beam irradiation (degradation). The results were normalized and are shown in Fig. 5.4. A doublet associated with the Zn 2p core level was detected (Fig. 5.4(a)), with binding energies at 1022.0 eV ($2p_{3/2}$) and 1045.0 eV ($2p_{1/2}$). The binding energy difference was 23 eV which indicated that all Zn atoms were in their fully oxidized divalent state (Zn^{2+}). No metallic zinc with binding energy of 1021.8 eV was detected [23]. XPS high-resolution spectra of the Eu3d level exhibited four peaks in the energy region from 1115 eV to 1180 eV for the samples with different Eu^{3+} concentrations as

well as the sample with 3 mol% of Eu^{3+} that was subjected to electron beam irradiation, Fig. 5.4(b). The dominant peaks at 1135.2 eV and 1165.0 eV correspond to $\text{Eu } 3d_{5/2}$ and $3d_{3/2}$, respectively. The energy difference between these lines was 29.8 eV and indicated the trivalent oxidation state of Eu^{3+} ions in the ZnO matrix, in agreement with oxygen-coordinated Eu ion values as reported in previously [24]. Another two peaks are visible at the lower binding energy side of the Eu^{3+} trivalent peaks and are ascribed to Eu^{2+} divalent ions. The existence of two oxidation state of Eu confirmed that the insertion of Eu occurred in an oxidative environment [25]. Since XRD revealed the formation of phase-pure ZnO for all the samples, divalent Eu components may represent Eu^{3+} ions that replaced Zn^{2+} ions, whereas the trivalent Eu components indicate the Eu^{3+} ions that occupied the interstitial sites. The Eu^{3+} peak increased with respect to the Eu^{2+} peak as the Eu^{3+} concentration increased which can be interpreted as at higher Eu^{3+} concentrations, Eu^{3+} ions tend to occupy the interstitials sides or led to the formation of Eu_2O_3 . The divalent component of the irradiated (degraded) sample had slightly increased after irradiation. Electron beam irradiation may have helped more Eu^{3+} ions to substitute the Zn^{2+} ions sites. Therefore, more defects may be created in the ZnO matrix.

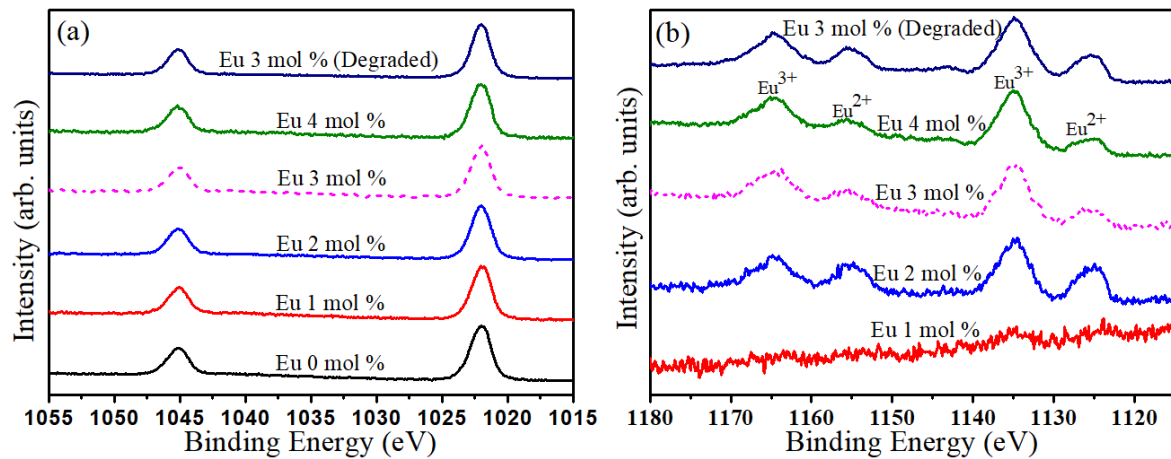


Fig. 5.4. Normalized High-resolution XPS spectra of (a) Zn 2p core levels and (b) Eu^{3+} 3d peaks for the films with different Eu^{3+} concentration and the irradiated sample with Eu^{3+} 3 mol%.

Fig. 5.5 displays XPS high resolution spectra of the O 1s core level for the samples with different Eu^{3+} concentrations and the sample with Eu^{3+} 3 mol% after electron beam irradiation. Gaussian-Lorentz function was used to de-convolute the O 1s peak. Three components were found namely O1, O2 and O3. Kumar et. al. [26] reported that the O1 component is due to oxygen ions (O^{2-}) in the wurtzite structure that are surrounded by its nearest zinc ions in the Zn-O-Zn network, O2 was attributed to the oxygen ions (O^{2-}) associated with oxygen-related

defects and/or Zn-OH groups and O3 is ascribed to the loosely bonded and chemisorbed species on the surface [27]. At least three peaks were detected for the samples with Eu³⁺ 0, 1, 2 and 3 mol%, whereas another small peak associated with Eu₂O₃ was detected at the lower binding energy side for the sample with Eu³⁺ 4 mol%. Since the XRD results did not show any Eu₂O₃ phase, the small Eu₂O₃ peak for the Eu³⁺ 4 mol% doped sample could be in a very small quantity below the XRD detection range. The O2 component for the degraded sample dramatically increased after electron beam irradiation, which confirmed the formation of new defects due to the effect of electron beam irradiation. The details of the de-convoluted O 1s components are shown in Table 5.3.

Table 5.3. Peak position and area of the O1s de-convoluted components.

Sample	Peaks name	Peaks position (eV)	Area %
Eu ³⁺ 0 mol%	O1	530.59	55
	O2	531.76	27
	O3	532.85	18
Eu ³⁺ 1 mol%	O1	530.59	59
	O2	531.76	27
	O3	532.85	14
Eu ³⁺ 2 mol%	O1	530.59	63
	O2	531.76	27
	O3	532.85	10
Eu ³⁺ 3 mol%	O1	530.59	61
	O2	531.76	29
	O3	532.85	10
Eu ³⁺ 4 mol%	O1	530.59	53
	O2	531.76	27
	O3	532.85	18
	Eu ₂ O ₃	529.31	2
Eu ³⁺ 3 mol% (degraded)	O1	530.59	36
	O2	531.76	49
	O3	532.85	15

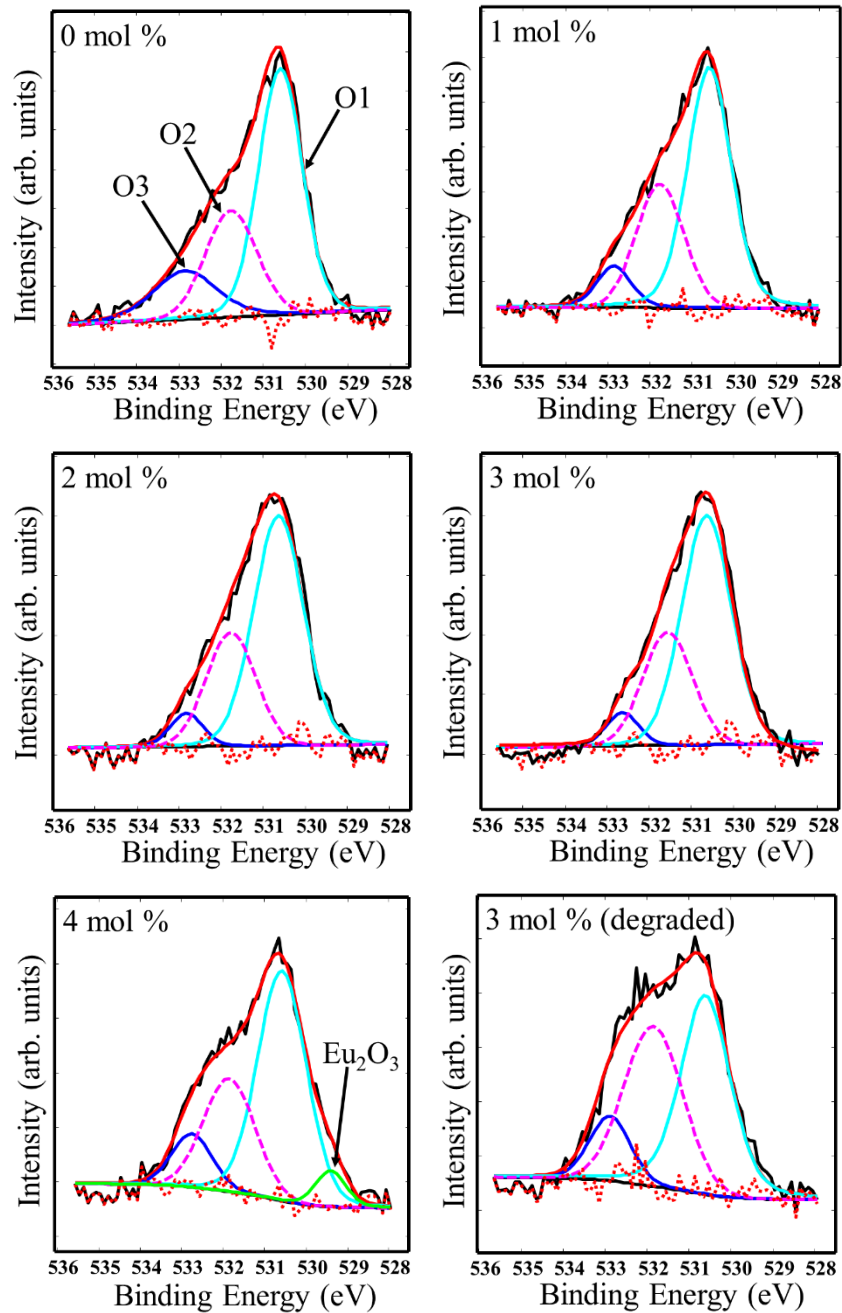


Fig. 5.5. De-convoluted O 1s peak for the films with different Eu^{3+} contents, and the irradiated film with 3 mol% of Eu^{3+} .

XPS depth profile measurements were performed for the different concentrations of Eu^{3+} doped ZnO films as shown in Fig. 5.6. The principal elements (Zn and O) and the dopant (Eu^{3+}) were detected, as well as the C contamination on the surface, which was eliminated just after sputtering started. The atomic concentration of Zn and O were about 55% and 45% for the undoped sample, respectively. The Zn atomic concentration slightly decreased with an increase in the Eu^{3+} content, reaching $\sim 50\%$ for the sample with 4 mol% Eu^{3+} , while the O atomic concentration slightly increased. This suggests that some of the Zn was replaced by the Eu.

Due to the charge compensation needed for Eu^{3+} ions to replace Zn^{2+} more oxygen ions or vacancies are needed, which may be the reason why the O atomic concentration increased with increasing Eu^{3+} content. The thicknesses were estimated to be ~ 184 nm, 147 nm, 161 nm, 170 nm and 204 nm for the undoped and 1 mol%, 2 mol%, 3 mol% and 4 mol% Eu^{3+} doped ZnO thin films, respectively. The sputtering rate, taken as 14 nm/min was calibrated with a SiO_2 standard and furthermore adding the Eu^{3+} dopant into the ZnO host might also affect the sputtering rate of the films. Therefore, the calculated thicknesses represents only a rough but good approximation. Interestingly, the atomic concentration of the Eu^{3+} was slightly higher in the top of the layer of the films (50 nm) compared to the deeper layers for the films with 3 and 4 mol% of Eu^{3+} ions. This may be due to the fact that Eu^{3+} ions with bigger ionic radius than Zn^{2+} ions tend to diffuse to the top layers of the films and occupy the grain boundaries during the spin coating, preheating or annealing processes.

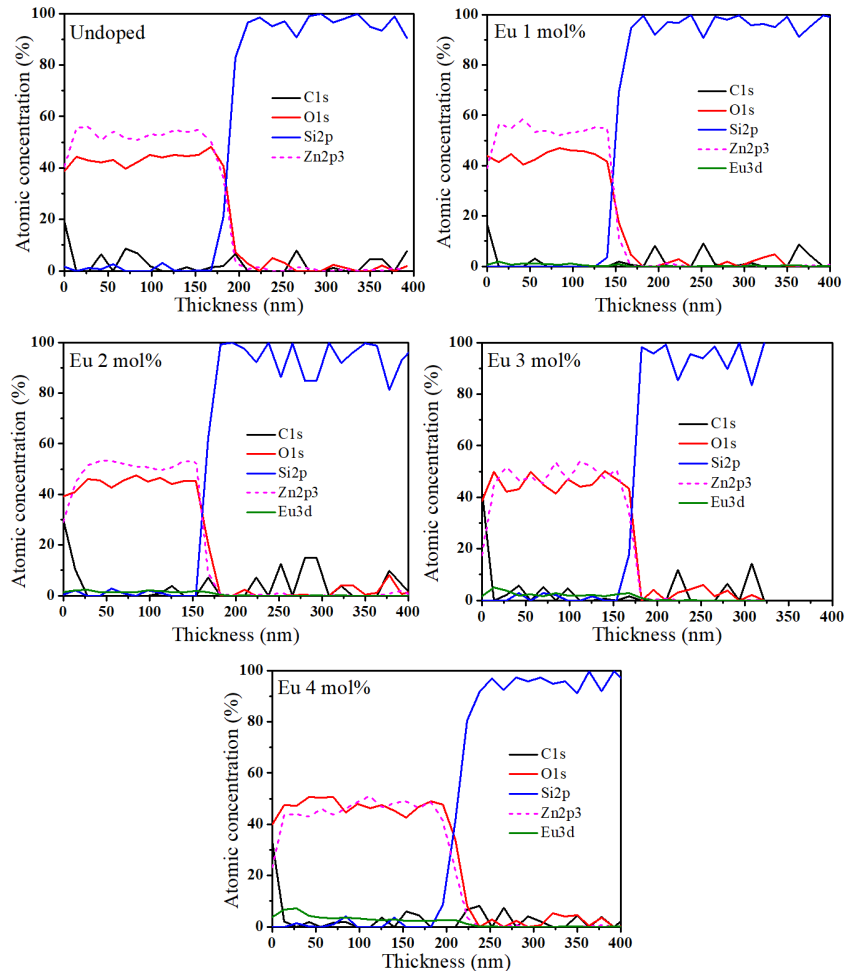


Fig. 5.6. XPS depth profiles for the films with different Eu^{3+} concentrations.

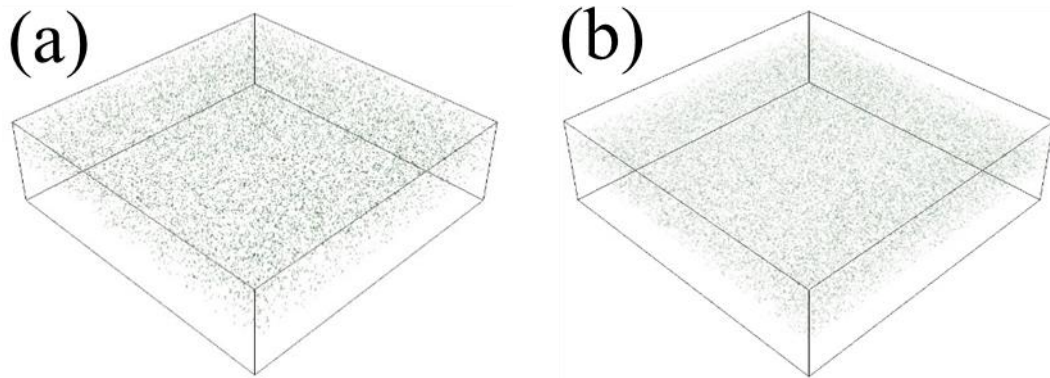


Fig. 5.7. Positive mode ToF SIMS 3D images ($100 \times 100 \mu\text{m}^2$) of the Eu^+ ion distribution in (a) the 3 mol % thin film and (b) the same image after removal of the top layers.

Fig. 5.7 shows the ToF SIMS 3D images ($100 \times 100 \mu\text{m}^2$) of the Eu^+ ion distribution in (a) the 3 mol % thin film and (b) the same image after removal of the top layers. It is clear that the Eu^+ was homogeneously distributed throughout the thin film with a slight enrichment in the top layers (more Eu^+ present) near the surface of the thin film. There was no evidence of agglomeration of Eu of any sort; a clear indication that the Eu was successfully incorporated into the thin films. Doping ZnO homogeneously with 1 mol % Eu^{3+} was also successfully demonstrated in the past by Balakrishna et al. [28]. Fig. 5.8 shows the ToF SIMS depth profile of the 3 mol % Eu^{3+} film indicating the Zn^+ , Si^+ , Eu^+ , Eu^{2+} (EuF^+) and Eu^{3+} (EuO^+) distribution in the film. It must be pointed out that the sensitivity factors for all these ions are different and therefore the big differences in the number of counts, and the EuF^+ was due to adventitious F in the environment during atmospheric exposure. The Eu^{3+} was homogeneously distributed, while the Eu^{2+} was only present in the top few layers. The Eu^+ contribution, which is due to a combination of Eu^{3+} and Eu^{2+} species, was also enriched towards the surface of the thin film. The Eu contribution slightly decreased and the Zn slightly increased deeper into the thin film. The enrichment of Zn and Eu at the Si interface must be interpreted as not real but due to matrix effects due to a native SiO_2 layer on the Si substrate. For a matrix such as Si or Ge, the magnitude of oxygen-induced secondary ion yield enhancement varies with the local oxygen concentration [29].

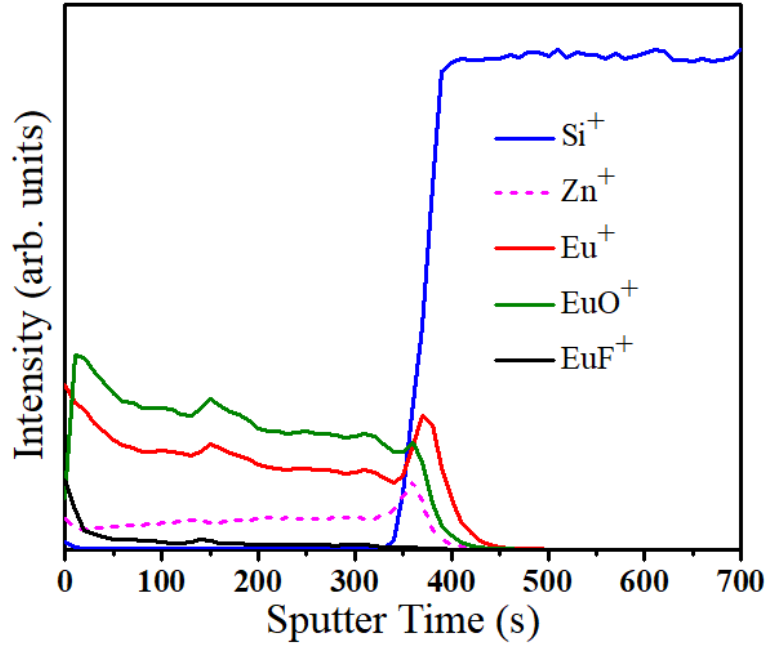


Fig. 5.8. Positive mode ToF SIMS depth profiles indicating the Zn^+ , Si^+ , Eu^+ , Eu^{2+} (EuF^+) and Eu^{3+} (EuO^+) ion distribution in the 3 mol % thin film.

5.3.2. Transmittance and band gap analysis (UV-vis spectroscopy)

Fig. 5.9 illustrates the transmittance spectra of the undoped and Eu^{3+} doped ZnO thin films deposited on glass substrates. The films exhibited a transmittance of about 80 % over the range from 800 nm to about 400 nm below which steep absorption occurred until a wavelength of about 365 nm. The steep absorption is associated with the optical band gap of ZnO (the near band edge along with exciton absorption) [30]. The well-known Tauc's formula was used to extrapolate the band gaps and the plots are shown in Fig. 5.9(b). The band gap values estimated by Tauc's plots were found to slightly decrease from 3.28 eV to 3.24 eV with increasing Eu^{3+} content. Incorporating impurities into a semiconductor host creates energy levels near the conduction band (for donors) or near the valence band (for acceptors). Increasing these impurities will increase these energy levels and thus a continuous density of states will be formed within the band gap, and eventually the band gap will decrease [31]. This may be the reason why the ZnO band gap decreased with increasing Eu^{3+} content. Moreover, other mechanisms may be involved in the decrease of the band gap such as quantum confinement effect as the result of reduction in the crystallite/ particle size as revealed from XRD, SEM and AFM results. Raji et. al. [20] observed widening of the ZnO band gap accompanied with increase in the crystallite size with increasing Eu^{3+} concentrations. They attributed the widening in the band gap to the band gap renormalization effect in the ZnO lattice by the Eu^{3+} ions. In our case, the decrease in the band gap was accompanied by the decrease in the

crystallite and particle size. Similar mechanism as explained by Raji et al [20] although in the opposite direction may be used to explain our observation.

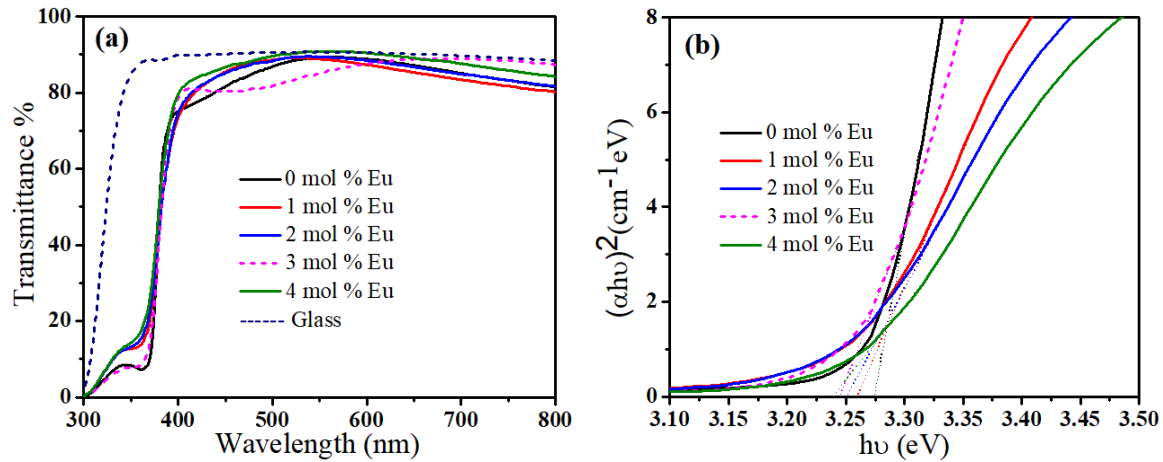


Fig. 5.9. (a) Transmittance spectra and (b) Tauc's plot of un-doped and Eu³⁺ doped ZnO thin films.

5.3.3. Photoluminescence analysis

Fig. 5.10 depicts the PL spectra of the un-doped and Eu³⁺ doped ZnO thin films on silicon substrates excited using a 325 nm He-Cd laser. The undoped film spectrum exhibited a broad range from ultraviolet to visible emission. Therefore, the broad peak was deconvoluted to determine the possible peaks within the main peak, Fig. 5.10(a). At least five peaks were found at ~ 3.3 eV (376 nm), 3.10 eV (400 nm), 2.45 eV (506 nm), 1.87 eV (665 nm) and 1.58 eV (784 nm). The origin of the ultraviolet emission at ~376 nm of ZnO is well-known due to the electron transition from the valence band to the conduction band [32]. The origin of the visible emissions of ZnO is a very controversial issue, although the most acceptable results are that: the blue peak at ~3.10 eV is associated to the shallow electron trapped near the conduction band (zinc interstitial Zn_i) to the zinc vacancies site, the emission at ~2.45 eV is due to the singly or doubly ionized oxygen vacancies (V_o⁺⁺/V_o⁺) [33], while the peaks at ~1.87 and 1.58 eV are commonly attributed to the excess-oxygen related defects such as oxygen interstitials (O_i) and zinc vacancies (V_{Zn}). After incorporation of Eu³⁺ into the ZnO host, the overall PL intensity drastically decreased and the band at ~ 2.45 eV was eliminated. Narrow peaks corresponding to the Eu³⁺ lines protruded around 589 nm, 614 nm and 704 nm. These peaks are associated with the ⁵D₀-⁷F₁, ⁵D₀-⁷F₂ and ⁵D₀-⁷F₄ transitions of the Eu³⁺ intra 4f-4f transitions, respectively. The elimination of the broad peak at ~2.45 eV of the ZnO defects may be attributed to radiative energy transfer between ZnO defects and Eu³⁺. The reduction in the broad peak of ZnO around 1.87 eV could be related to the charge transfer between the oxygen and Eu³⁺ ions. The UV emission at ~376 nm also systematically decreased with increasing the

Eu³⁺ content. Since the decrease was not only in the UV emission, all the ZnO defect-related emission decreased with increasing Eu³⁺ concentration, so we propose that the excitation energy was shared between the band-to-band/exciton emissions, defect transitions and the Eu³⁺ emissions. The surface roughness may have also contributed to the reduction of ZnO emission (UV and defect emissions) after incorporating the Eu³⁺ ions. The rougher surface will have a high surface to volume ratio which may increase the emission intensity of the film. These films roughnesses were drastically decreased after adding the Eu³⁺ contents and kept decreasing with increasing the Eu³⁺ concentration (Table 5.1). That might be why the overall ZnO emission decreased with increasing the Eu³⁺ concentration.

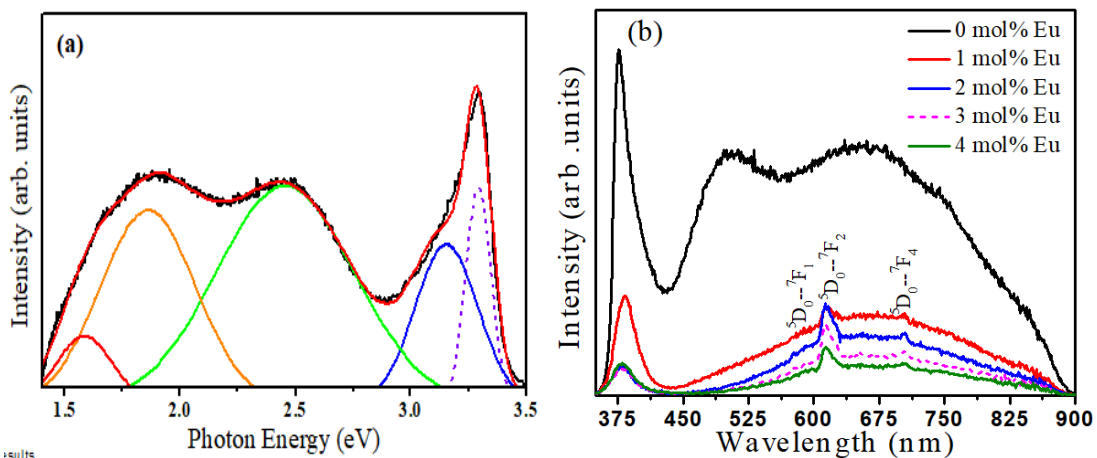


Fig. 5.10. (a) Deconvoluted peak of the PL spectrum of the undoped ZnO thin film and (b) PL spectra of undoped and Eu³⁺ doped ZnO thin films, excited at 325 nm with a He-Cd laser.

Fig. 5.11 displays the PL spectra of the Eu³⁺ doped ZnO films. Fig. 5.11 (a) shows the excitation spectra recorded while monitoring the Eu³⁺ emission at 614 nm and (b) the emission spectra of the films selectively excited for Eu³⁺ absorption band at 464 nm. The excitation spectrum of the undoped sample shows a step absorption around 377 nm which correspond to the ZnO band gap, while the Eu³⁺ doped ZnO samples exhibited sharp lines at 464 nm and 392 nm, which are due to the 4f-4f intrinsic transitions of Eu³⁺ in ZnO. The sharp lines at 464 nm and 392 nm were associated with the ⁷F₀ – ⁵L₆ and ⁷F₀ – ⁵D₂ transitions of Eu³⁺, respectively. The broad absorption peaks centred around 288 nm for the Eu³⁺ doped samples is related to the charge transfer between Eu³⁺ and O²⁻ ions. The emission spectrum of the Eu³⁺ doped ZnO films exhibited the characteristic emissions of Eu³⁺ at 578 nm, 590 nm, 614 nm, 654 nm and 704 nm, which are assigned to ⁵D₀ – ⁷F₀, ⁵D₀ – ⁷F₁, ⁵D₀ – ⁷F₂, ⁵D₀ – ⁷F₃ and ⁵D₀ – ⁷F₄ transitions, respectively. The emission arising from the electric dipole transition (⁵D₀ – ⁷F₂) is higher than the emission from the magnetic dipole transition (⁵D₀ – ⁷F₁), which indicates that the Eu³⁺ ions occupy sites without inversion symmetry. The overall Eu³⁺ emission intensity increased with

increasing Eu^{3+} concentration and the highest intensity was recorded for the sample with 3 mol% of Eu^{3+} , after which the intensity was quenched. There are different mechanisms via which the luminescence of rare earth quenches occurs, including: multipole-multipole interaction, radiation reabsorption and exchange interaction mechanisms of the non-radiative energy transfer. Based on Blasse [34] theory, resonant transfer by exchange interaction or multipole-multipole interaction are responsible for the non-radiative energy transfer of the luminescence. The transfer distance between activators is a critical parameter to determine the quenching mechanism of the luminescence. In case of RE^{3+} activators, if the transfer distance between activators is greater than 5 \AA then the multipole-multipole interaction is the mechanism of the quenching, otherwise exchange interaction is the major mechanism. The following equation was used to estimate the critical transfer distance between Eu^{3+} activators:

$$R_c = 2 \left(\frac{3V}{4\pi C_0 N} \right)^{\frac{1}{3}} \quad (5.1),$$

where, N is the number of Zn ions in the ZnO unit cell (2), V represent the ZnO unit cell volume (47.77 \AA^3) and C_0 the optimum concentration (0.03 mol). The critical transfer distance (R_c) between Eu^{3+} activators was found at about 11.5 \AA , suggesting that the multipole-multipole interaction is the major mechanism responsible for the luminescence quenching. Zeng et al. found that their Eu^{3+} doped ZnO nanosheets exhibited Eu^{3+} characteristic emission protruding the broad yellow emission that was centred around 600 nm when the samples were excited at 325 nm using a xenon lamp. The broad emission around 600 nm was attributed to the O_i transition. Whereas, when the samples were excited at 464 nm, a pure red emission consisted of emission peaks at 577 nm, 589 nm, (612 nm and 619 nm) and 654 nm were observed. These peaks were attributed to the ${}^5\text{D}_0 - {}^7\text{F}_J$ ($J = 0, 1, 2$ and 3) transitions of the $4f-4f$ of Eu^{3+} ions [35].

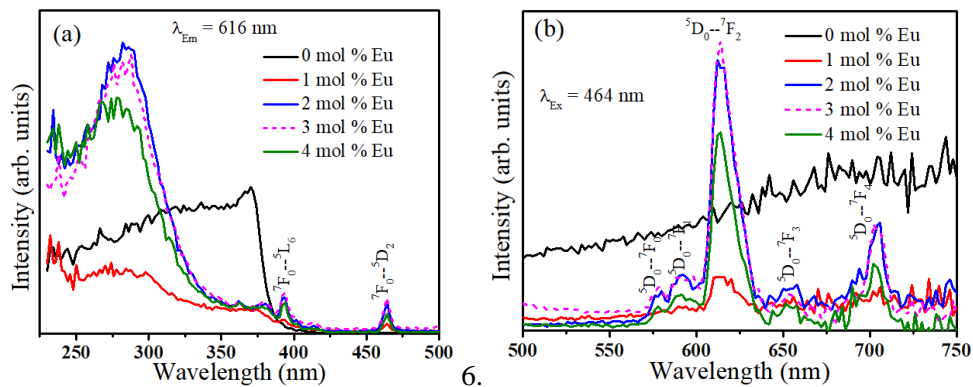


Fig. 5.11. PL (a) excitation monitored while exciting at 614 nm and (b) emission spectra (excited at 464 nm) of $\text{ZnO}:\text{Eu}^{3+}$ with different Eu^{3+} concentrations.

5.3.4. Judd-Ofelt analysis

The local environment of the Eu^{3+} ions in the host and their symmetry are directly related to the characteristic emission of the Eu^{3+} ions. Judd-Ofelt analysis is an important theoretical tool to investigate the Eu^{3+} asymmetry in the host and obtain other important parameters such as the asymmetry ratio, Judd-Ofelt intensity parameters (Ω_2 and Ω_4), spontaneous radiative decay rates (τ_{rad}), total radiative transition rate (A_R), branching ratios ($\beta_{0-1,2,4}$) and stimulated emission cross-sections ($\sigma(\lambda_p)_{0-1,2,4}$) [20]. The electric dipole emission (${}^5\text{D}_0\text{-}{}^7\text{F}_2$) is very sensitive to the local environment and the asymmetry around the Eu^{3+} ions, whereas the magnetic dipole emission (${}^5\text{D}_0\text{-}{}^7\text{F}_1$) is independent of the asymmetry and the local environment of the Eu^{3+} ions. Therefore, the ratio between the integrated intensity of ${}^5\text{D}_0\text{-}{}^7\text{F}_2$ emission to the integrated intensity of ${}^5\text{D}_0\text{-}{}^7\text{F}_1$ is called the asymmetry ratio and is given in Table 5.4. The asymmetry ratio value increased with an increase in the Eu^{3+} concentration up to 3 mol% and then decreased at 4 mol%, implying that the asymmetry ratio also depends on the Eu^{3+} content in the host and has the same trend as the concentration quenching. Intensity parameters Ω_2 and Ω_4 give information about the Eu^{3+} ions polarization and asymmetry behaviour of their ligands. They were estimated from the Judd-Ofelt formulas [20] and the values are given in Table 5.4 and plotted in Fig. 5.12 (a). The Ω_2 value increased with increasing Eu^{3+} concentration until 3 mol% and then decreased at 4 mol%, whereas the Ω_4 value decreased with increasing the Eu^{3+} concentration. The values of Ω_2 are higher than Ω_4 for the samples with 2, 3 and 4 mol%. This indicate that at lower concentration (1 mol%) the Eu^{3+} ions have lower asymmetry and weak covalence bonds, while at higher concentration (2, 3, and 4 mol%) Eu^{3+} ions have strong covalence bonds and high asymmetry in their vicinities. Detailed information about Judd-Ofelt calculations can be found in ref [20]. Other useful parameters such as radiative emission rate (A_{0-J}) total transition probability (A_T), radiative life time (τ_{rad}), branching ratio (β_J), stimulated emission cross-section ($\sigma(\lambda_p)$) can also be obtained from the intensity parameters [20], see Table 5.4. For more elaboration, the variation trend of the stimulated emission cross-sections of the ${}^5\text{D}_0\text{-}{}^7\text{F}_1$ and ${}^5\text{D}_0\text{-}{}^7\text{F}_2$ transitions against Eu^{3+} concentration are shown in Fig. 5.12 (b).

Table 5.4. Judd-Ofelt intensity and radiative parameters.

Concentration mol %	J-O intensity parameters		Transitions	$A_{0,2,4}(S^{-1})$	$A_{0,1}(S^{-1})$	$A_{\lambda}(S^{-1})$	$\tau_{rad}(ms)$	$\beta(\%)$	$\sigma(\lambda_p)(pm^2)$	Asymmetry ratio
	$\Omega_2(pm^2)$	$\Omega_4(pm^2)$								
1	4.55	6.10	$^5D_{0,7}F_1$	-	50	492	2.03	10.1	22.7	4.5
			$^5D_{0,7}F_2$	233	-	-	-	47.5	59.5	
			$^5D_{0,7}F_4$	208	-	-	-	42.4	95.45	
2	5.90	4.13	$^5D_{0,7}F_1$	-	50	493	2.03	10.1	13.8	5.8
			$^5D_{0,7}F_2$	302	-	-	-	61.3	79.0	
			$^5D_{0,7}F_4$	141	-	-	-	28.6	62.3	
3	5.95	3.46	$^5D_{0,7}F_1$	-	50	473	2.11	10.5	13.1	5.9
			$^5D_{0,7}F_2$	305	-	-	-	64.5	83.7	
			$^5D_{0,7}F_4$	118	-	-	-	25.0	60.8	
4	4.70	3.38	$^5D_{0,7}F_1$	-	50	406	2.46	12.3	8.9	4.6
			$^5D_{0,7}F_2$	241	-	-	-	59.3	58.1	
			$^5D_{0,7}F_4$	115	-	-	-	28.4	38.9	

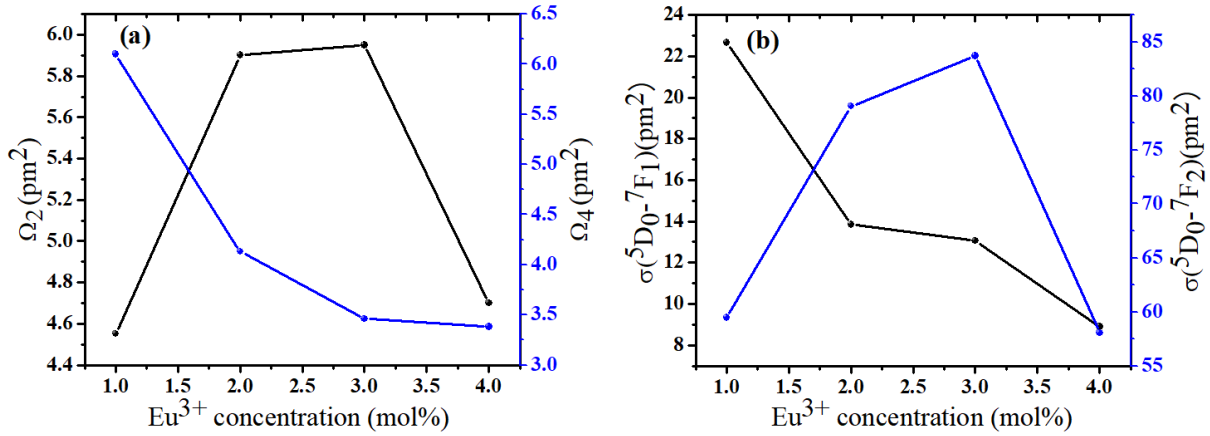


Fig. 5.12. Dependency of the Judd-Ofelt (a) intensity parameters (Ω_2 and Ω_4) and (b) emission cross-sections ($\sigma(\lambda_p)_{0-1,2}$) on the Eu^{3+} concentration.

5.3.5. Cathodoluminescence and degradation analysis

The CL spectra of the Eu^{3+} doped ZnO thin film samples were recorded in vacuum while the samples were excited by using a high energy electron beam (2 keV), Fig. 5.13(a). Only Eu^{3+} characteristic emission was observed at 590 nm, 614 nm, 654 nm and 704 nm which are ascribed to the $^5D_0 - ^7F_J$ ($J = 1, 2, 3, 4$) transitions, respectively. The CL intensity followed the same trends as the PL intensity when excited at 464 nm, where the CL peak intensity increased with increasing Eu^{3+} contents until 3 mol% after which the intensity was quenched. The electron beam energy was orders of magnitude higher than the band gap of ZnO, and therefore ZnO native emissions (band to band and defects emissions) were expected. However, only Eu^{3+} emission was detected. This may be due to the fact that the electron beam excited the luminescence centres through impact excitation/ionization, similar to electroluminescence behavior reported in ref [36]. When a RE^{3+} doped semiconductor host is excited via a photon with energy higher than the band gap, the defect-related emission and RE^{3+} ions emission both could be detected or sometimes at least the defect-related emission was detected, but when they are excited through an electric field (electroluminescence) only RE^{3+} emission was detected [36]. An electron beam has two ways to impact-excite RE^{3+} luminescence centres in the host, either through direct or indirect excitation. In the case of direct excitation, the number of excited Eu^{3+} ions are proportional to the Eu^{3+} concentration, and thus the CL intensity increases with increasing RE ions concentration and quenching may occur due to concentration self-quenching effect. In the case of indirect excitation, the incident electrons generate electron-holes (EHs) by collision with the lattice. These EHs are mobile and do not directly recombine at the lattice sites, but move out of the excited volume and recombine at the RE^{3+} sites. In this case, the number of recombination of the EHs (corresponding to the CL intensity) is dependent

on the particle volume (ϕ^3) and the variation curve of the CL intensity versus the RE ions concentration (C) is not the same as the direct excitation curve [19]. The CL intensity variation for these samples (Fig. 5.13(b)) follows the same trend of the concentration self-quenching of the PL intensity when selectively excited at 464 nm. Therefore, direct excitation may be the major mechanism for the CL spectra. This indicates poor energy transfer from the host excitations to the Eu^{3+} ions and is a limiting factor for the emission intensity.

The photometric characteristics such as colour coordinates (X, Y) and the color correlated temperature (CCT) were assessed using the Commission International de l'Eclairage (CIE) 1931 software. CL spectra and PL spectra excited at 464 nm were used in the CIE software for the calculations. The well-known McCamy method was used to calculate the color correlated temperature (CCT) and the results are shown in Table 5.5. From Fig. 5.13(c), the chromaticity coordinates based on the PL data of the samples were shifted from the orange region to the red region as the Eu^{3+} concentration increased, whereas for the CL spectra the chromaticity coordinate shifted from the purple region to the red region with increasing Eu^{3+} concentration.

Table 5.5. Rendering indexes (X, Y) and the CCT of the samples, based on PL and CL spectra.

Samples	Based on PL spectra excited at 464 nm			Based on CL spectra		
	X	Y	CCT (K)	X	Y	CCT (K)
1 mol% Eu^{3+}	0.54	0.45	2129	0.42	0.34	2687
2 mol% Eu^{3+}	0.63	0.37	1991	0.62	0.35	5514
3 mol% Eu^{3+}	0.59	0.40	1710	0.64	0.35	2434
4 mol% Eu^{3+}	0.63	0.37	1991	0.67	0.34	3181

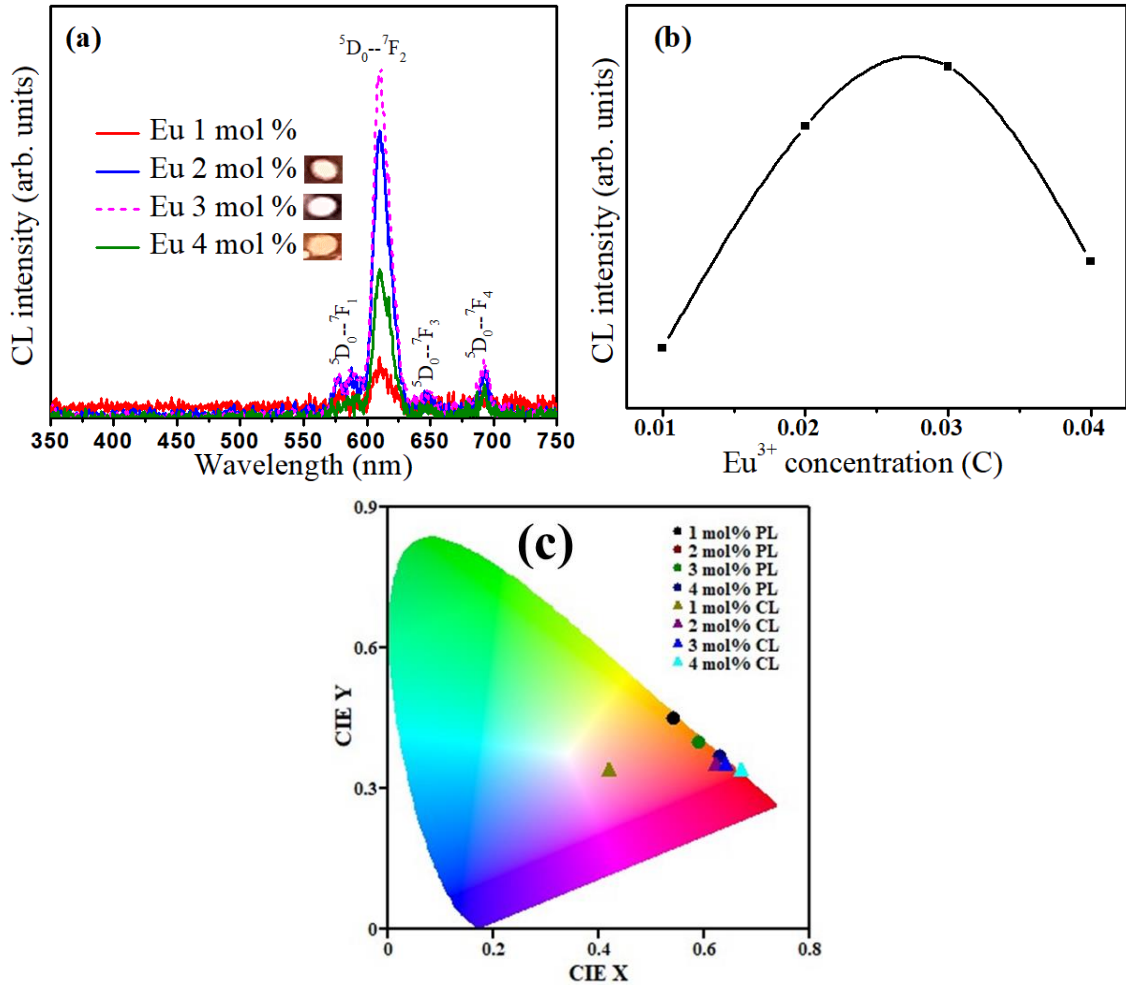


Fig. 5.13. (a) CL spectra of ZnO spin coating films with different Eu^{3+} contents (the insets are the CCD camera photographs of the samples emission), (b) CL intensities of Eu^{3+} line at 614 nm as a function of Eu^{3+} concentration, and (c) CIE color coordinates of the samples based on the PL and CL data.

The highest CL intensity sample (3 mol%) was subjected to electron beam irradiation in vacuum for about 160 C/cm^2 (≈ 22 hours), during which the intensity of the dominant CL emission peak at 614 nm of the Eu^{3+} lines was recorded against the electron dose as shown in Fig. 5.14. The CL intensity of the 614 nm peak has decreased during the initial period of electron dose up to about 30 C/cm^2 and then stabilized. The initial degradation of CL intensity is generally observed for CL degradation of the phosphor materials and was attributed to the formation of an oxide interleaved layer, which inhibits the luminescence and acts as a protective layer that contributes to the further stability of the materials [37]. Coetsee et al. observed a similar decrease in the CL intensity when they degraded $\text{Y}_2\text{SiO}_5:\text{Ce}$ phosphor and they attributed it to the possible formation of a SiO_2 interleaved layer [38]. Swart et al. observed the formation of a non-luminescent ZnO layer which caused the CL degradation of

ZnS:Cu,Al,Au based FED phosphors [39]. Yousif et al. confirmed the presence of AlO_x , YO_x and $\text{Y}(\text{Al,Ga})\text{O}_3$ thin layers on their degraded $\text{Y}_3(\text{Al,Ga})_5\text{O}_{12}:\text{Tb}$ material [40]. In our study, the formation of a non-luminescent ZnO layer may have occurred. Moreover, since XPS results revealed the creation of defects after electron beam irradiation, the initial degradation could be due to the competition between the new-created defects and the Eu^{3+} luminescent centres. It is worthwhile to note that the shape of the CL spectra of the Eu^{3+} emissions remained unchanged as shown in the inset of Fig. 5.14.

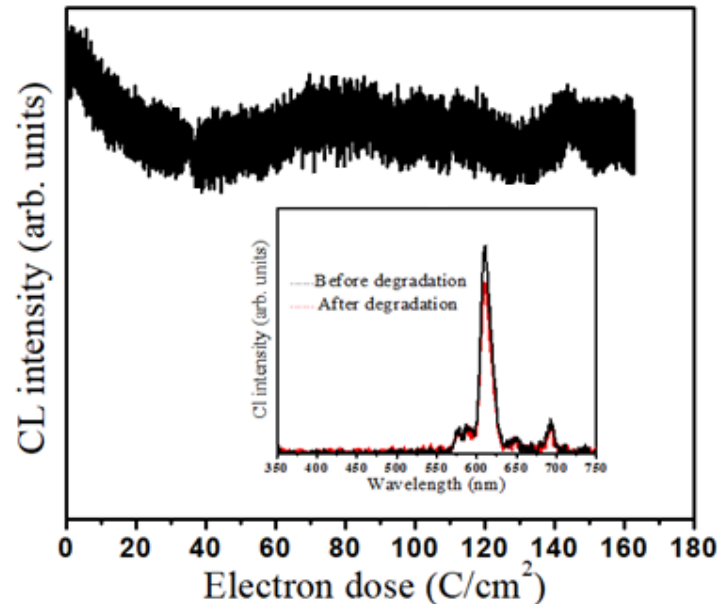


Fig. 5.14. CL intensity of the Eu^{3+} line at 614 nm as a function of electron dose in vacuum base pressure of 3×10^{-8} Torr. The inset shows the CL spectra before and after the irradiation.

Electron beam irradiation can induce heat, electrostatic charging, sputtering, radiolysis and displacement of atoms of the irradiated sample. Consequently, the specimen may undergo damages on the surface, changes in its morphology or creation of defects in the crystal lattice [41]. These changes can severely deteriorate the luminescence efficiency of the materials. Hasabeldaim et al. [42] monitored the morphology changes during the electron irradiation of ZnO nanorods obtained from the chemical bath deposition. They attributed the thinning of the lower half and the growth of the upper half to different reasons including migration and diffusion of the ZnO defects, formation of an interleaved non-luminescent ZnO layer and/or removal of the atomic hydrogen from the ZnO lattice. Hasabeldaim et al. [43] also irradiated an un-doped ZnO thin film for about 24 h. The electron beam induced surface changes (coalition of particles) during prolonged electron beam irradiation. Therefore, the SEM images were recorded at low magnification for the degraded spot and at high magnification for the un-degraded and degraded areas (Fig. 5.15). The effect of the electron beam irradiation on the

sample is clearly visible when the SEM images were captured at low magnification. However, the high magnification SEM images showed no visible modification on the sample morphology. For further analysis, the degraded area in this case was also examined by AFM and is shown in Fig. 5.15. No significant damage/changes were seen on the surface, although the particle boundaries became clearer on the degraded area than the un-degraded area (compare Fig. 5.3(d) the sample before degradation). The root mean square roughness (R_q) has slightly increased after degradation to 0.998 nm, whereas for the un-degraded sample it was 0.647 nm. Based on the XPS results, which showed a creation of defects after irradiation, the creation of the defects can happen through complicated processes such as diffusion of atoms and removal of atoms/ions from the crystal sites. Therefore, reconstruction of crystals/particles must take place to minimize energy in the crystal and hence surface alters [44, 45]. This may explain the minor changes on the irradiated area.

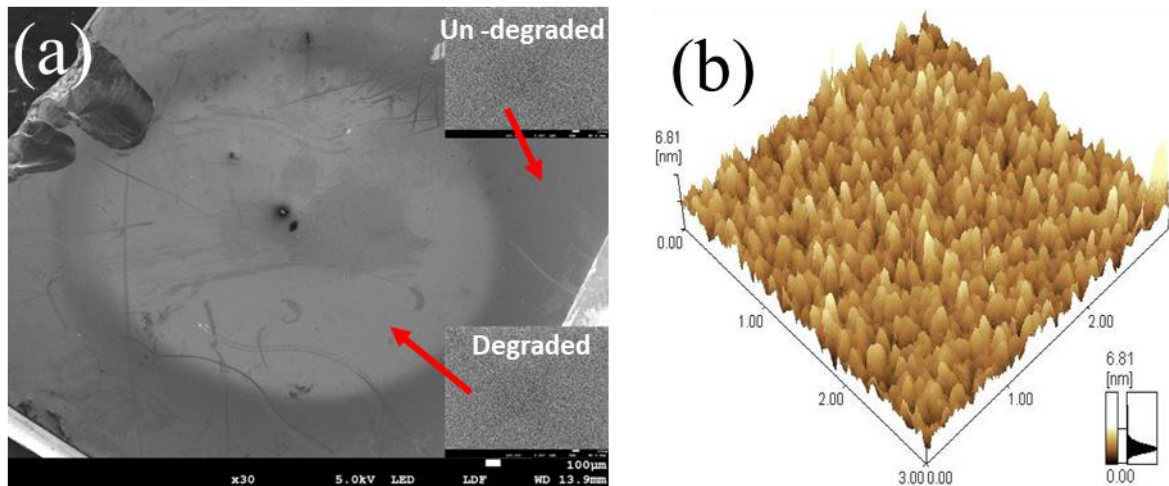


Fig. 5.15. (a) Low magnification SEM image of the degraded spot (the insets are the high magnification SEM images of the un-degraded and degraded area as indicated by red arrows), and (b) 3D AFM image of the ZnO thin film with 3 mol% of Eu^{3+} after electron beam irradiation.

5.4. Conclusion

ZnO doped films with different Eu^{3+} concentration were fabricated by the sol-gel method using the spin coating technique. The surface state, chemical and luminescence stability of the films were studied during prolonged electron beam irradiation. The particle sizes and the band gaps have decreased with an increasing Eu^{3+} content. Although XPS and ToF SIMS indicated some divalent Eu^{2+} on the sample surface, only the characteristic luminescence of Eu^{3+} ions was observed. Multipole-multipole interaction was the major mechanism for the concentration quenching. The maximum intensity sample (3 mol% Eu) was subjected to electron beam

irradiation for about 22 h ($\sim 160 \text{ C/cm}^2$). The CL intensity of the Eu^{3+} emission slightly decreased at the initial stage of electron irradiation after which it has stabilized. XPS measurements revealed the creation of new defects, especially oxygen deficiencies due to the electron beam irradiation. The surface of the electron beam-irradiated area was examined by SEM and AFM, indicating that there were minor changes on the film's surface due to the electron beam irradiation. Therefore, the initial decrease on the CL intensity may be attributed to the creation of the new defects or the change on the surface morphology of the sample. Generally, this film was very stable and promising for optoelectronic applications such as FEDs.

5.5. References

- [1] H.V. S. Pessoni, L. J. Q. Maia, A. Franco Jr, Eu-doped ZnO nanoparticles prepared by the combustion reaction method: Structural, photoluminescence and dielectric characterization, *Mater. Sci. Semicond. Process.* **30** (2015) 135–141.
- [2] Y. Liu, W. Luo, R. Li, G. Liu, M. R. Antonio, X. Chen, Optical Spectroscopy of Eu^{3+} Doped ZnO Nanocrystals, *J. Phys. Chem.* **112** (2008) 686-694.
- [3] V. Kumar, O. M. Ntwaeaborwa, T. Soga, V. Dutta, H.C. Swart, Rare earth doped zinc oxide nanophosphor powder: A future material for solid state lighting and solar cell, *ACS Photonics* **4(11)** (2017) 2613–2637.
- [4] S. López-Romero, M. J. Quiroz-Jiménez, M. H. García, A. Aguilar-Castillo, Bright Red Luminescence and Structural Properties of Eu^{3+} Ion Doped ZnO by Solution Combustion Technique, *World J. of Condens. Matter Phys.* **4** (2014) 227-234.
- [5] J. Petersen, C. Brimont, M. Gallart, O. Crégut, G. Schmerber, P. Gilliot, B. Hönerlage, C. Ulhaq-Bouillet, J. L. Rehspringer, C. Leuvrey, S. Colis, H. Aubriet, C. Becker, D. Ruch, A. Slaoui, A. Dinia, Structural and photoluminescence properties of ZnO thin films prepared by sol-gel process, *J. Appl. Phys* **104** (2008) 113539-2008.
- [6] E. M. Kaidashev, M. Lorenz, H. von Wenckstern, A. Rahm, H. C. Semmelhack, High electron mobility of epitaxial ZnO thin films on c-plane sapphire grown by multistep pulsed-laser deposition, *Appl. Phys. Lett.* **82** (2003) 3901.
- [7] L. Yang, H. Zheng, Q. Liu, S. Zhou, W. Zhang, The doping site analysis and control of Eu^{3+} in ZnO:Eu crystal lattice, *J. Lumin.* **204** (2018) 189–194.
- [8] A. Ishizumi, Y. Taguchi, A. Yamamoto and Y. Kanemitsu, Luminescence properties of ZnO and Eu^{3+} -doped ZnO nanorods, *Thin Solid Films* **486** (2005) 50 – 52.

- [9] K. Suzuki, K. Murayama, N. Tanaka, Enhanced luminescence in Eu-doped ZnO nanocrystalline films, *Appl. Phys. Lett.* **107** (2015) 031902.
- [10] S. M. Ahmed, P. Szymanski, L. M. El-Nadi, M. A. El-Sayed, Energy-Transfer Efficiency in Eu-Doped ZnO Thin Films: The Effects of Oxidative Annealing on the Dynamics and the Intermediate Defect States, *ACS Appl. Mater. Interfaces* **6** (2014) 1765.
- [11] P. P. Pal, J. Manam, Structural and photoluminescence studies of Eu³⁺ doped zinc oxide nanorods prepared by precipitation method, *J. Rare Earth* **31** (2013) 37.
- [12] P. Dorenbos, E. van der Kolk, Location of lanthanide impurity levels in the III-V semiconductor GaN, *Appl. Phys. Lett.* **89** (2006) 061122.
- [13] E. H. H. Hasabeldaim, O. M. Ntwaeaborwa, R. E. Kroon, H. C. Swart, Structural, optical and photoluminescence properties of Eu doped ZnO thin films prepared by spin coating, *J. Mol. Struct.* **1192** (2019) 105-114.
- [14] S. Iwan, J. L. Zhao, S.T. Tan, X.W. Sun, Enhancement of UV photoluminescence in ZnO tubes grown by metal organic chemical vapour deposition (MOCVD), *Vacuum* **155** (2018) 408–411.
- [15] M. Arif, S. Monga, A. Sanger, P. M. Vilarinho, A. Singh, Investigation of structural, optical and vibrational properties of highly oriented ZnO thin film, *Vacuum* **155** (2018) 662–666.
- [16] A. Balakrishna, M. M. Duvenhage, H. C. Swart, Surface and chemical characterization of ZnO:Eu³⁺/Yb³⁺ spin coated thin films using SEM-CL and TOF-SIMS, *Vacuum* **157** (2018) 376–383.
- [17] L. R. Singh, Photoluminescence Studies of ZnO, ZnO:Eu and ZnO:Eu Nanoparticles Covered with Y₂O₃ Matrix, *Mater. Sci. Appl.* **6** (2015) 269-278.
- [18] P. Wellenius, A. Suresh, J. V. Foreman, H. O. Everitt, J. F. Muth, A visible transparent electroluminescent europium doped gallium oxide device, *Mater. Sci. Eng., B* **146** (2008) 252–255.
- [19] L. Ozawa, Cathodoluminescence and photoluminescence: theories and practical applications, CRC Press, Athens, Georgia, 2007.
- [20] R. Raji, R. A. Kumar, K. G. Gopchandran, Influence of local structure on luminescence dynamics of red emitting ZnO:Eu³⁺ nanostructures and its Judd-Ofelt analysis, *J. Lumin.* **205** (2019) 179-189.

- [21] J. Rosowska, J. Kaszewski, B. Witkowski, Ł. Wachnicki, M. Godlewski, The Effect of Synthesis Pressure on Properties of Eu-Doped ZnO Nanopowders Prepared by Microwave Hydrothermal Method, *Proceedings of the 45th International School and Conference on the Physics of Semiconductors*, Jaszowiec, Szczyrk, 2016.
- [22] M. Wang, C. Huang, Z. Huang, W. Guo, J. Huang, H. He, H. Wang, Y. Cao, Q. Liu, J. Liang, Synthesis and photoluminescence of Eu-doped ZnO microrods prepared by hydrothermal method, *Opt. Mater.* **31** (2009) 1502–1505.
- [23] J. F. Moulder, W. F. Strickle, P. E. Sobol, K. D. Bomben, Handbook of X-Ray spectroscopy, ULVAC-PHI, Inc, Chigasaki, 1995.
- [24] E. J. Cho, S. J. Oh, S. Imada, S. Suga, T. Suzuki, T. Kasuya, Origin of the high-binding-energy structure in the 3d core-level spectra of divalent Eu compounds, *Phys. Rev. B* **51** (1995) 10146.
- [25] V. Kumar, Vijay Kumar, S. Som, M. M. Duvenhage, O. M. Ntwaeaborwa, H. C. Swart, Effect of Eu doping on the photoluminescence properties of ZnO nanophosphors for red emission applications, *Appl Surf Sci.* **308** (2014) 419-430.
- [26] V. Kumar, H. C. Swart, O. M. Ntwaeaborwa, R. E. Kroon, J. J. Terblans, S. K. K. Shaat, A. Yousif, M. M. Duvenhage, Origin of the red emission in zinc oxide nanophosphors, *Mater. Lett.* **101** (2013) 57.
- [27] L. Armelao, G. Bottaro, M. Pascolini, M. Sessolo, E. Tondello, M. Bettinelli, A. Speghini, Structure-Luminescence Correlations in Europium-Doped Sol-Gel ZnO Nanopowders, *J. Phys. Chem. C* **112** (2008) 4049-4054.
- [28] A. Balakrishna, T. K. Pathak, E. Coetsee-Hugo, V. Kumar, R. E. Kroon, O. M. Ntwaeaborwa, H. C. Swart, Synthesis, structure and optical studies of ZnO:Eu³⁺, Er³⁺, Yb³⁺ thin films: Enhanced up-conversion emission, *Colloid. Surf. Physicochem. Eng. Asp.* **47** (1) (2018) 521-529.
- [29] G. Gillen, J. M. Phelps, R. W. Nelson, P. Williams, S. M. Hues, Secondary ion yield matrix effects in SIMS depth profiles of Si/Ge multilayers, *Surf. Interface Anal.* **14** (11) (1989) 771-780.
- [30] V. Kumar, N. Singh, Vijay Kumar, L. P. Purohit, A. Kapoor, O. M. Ntwaeaborwa, H. C. Swart, Doped zinc oxide window layers for dye sensitized solar cells, *J. Appl. Phys.* **114** (2013) 134506.

- [31] V. Kumar, S. Som, Vijay Kumar, V. Kumar, O. M. Ntwaeaborwa, E. Coetsee, H. C. Swart, "Tunable and white emission from ZnO:Tb³⁺ nanophosphors for solid state lighting applications," *Chem. Eng. J.* **255** (2014) 541–552.
- [32] V. A. Fonoberov, A. A. Balandin, Origin of ultraviolet photoluminescence in ZnO quantum dots: Confined excitons versus surface-bound impurity exciton complexes, *Appl. Phys. Lett.* **85** (2004) 5971- 5973.
- [33] F. H. Leiter, H. R. Alves, A. Hofstaetter, D. M. Hofmann, B. K. Meyer, The Oxygen Vacancy as the Origin of a Green Emission in Undoped ZnO, *phys. status solidi B* **226** (1) (2001) 4–5 R4-R5.
- [34] G. Blasse, Concentration Quenching of Eu³⁺ Fluorescence, *J. Chem. Phys.* **46** (1967) 2583.
- [35] X. Zeng, J. Yuan, Z. Wang, L. Zhang, Nanosheet-Based Microspheres of Eu³⁺-doped ZnO with Efficient Energy Transfer from ZnO to Eu³⁺ at Room Temperature, *Adv. Mater.* **19** (2007) 4510–4514.
- [36] S. Iwan, S. Bambang, J. L. Zhao, S. T. Tan, H. M. Fan, L. Sun, S. Zhang, H. H. Ryu, X.W. Sun, Green electroluminescence from an n-ZnO: Er/p-Si heterostructured light-emitting diode, *Physica B* **407** (2012) 2721–2724.
- [37] S. S. Pitale, I. M. Nagpure, V. Kumar, O. M. Ntwaeaborwa, J. J. Terblans, H. C. Swart,, Investigations on the low voltage cathodoluminescence stability and surface chemical behaviour using Auger and X-ray photoelectron spectroscopy on LiSrBO₃:Sm³⁺ phosphor, *Mater. Res. Bull.* **46** (2011) 987-994.
- [38] E. Coetsee, H. C. Swart, J. J. Terblans, Cathodoluminescence degradation of Y₂Si O₅: Ce thin films, *J. Vac. Sci. Technol. A* **25** (2007) 1226-1230.
- [39] H. C. Swart, K. T. Hillie, "Degradation of ZnS FED phosphors, *Surf. Interface Anal.* **30** (2000) 383–386.
- [40] A. Yousif, H. C. Swart, O. M. Ntwaeaborwa, Surface state of Y₃(Al,Ga)₅O₁₂:Tb phosphor under electron beam bombardment, *Appl. Surf. Sci.* **258** (2012) 6495–6503.
- [41] Y. Ding, K. C. Pradel, Z. L. Wang, In situ transmission electron microscopy observation of ZnO polar and non-polar surfaces structure evolution under electron beam irradiation, *J. Appl. Phys.* **119** (2016) 015305.

- [42] E. H. H. Hasabeldaim, O. M. Ntwaeaborwa, R. E. Kroon, E. Coetsee, H. C. Swart, Cathodoluminescence degradation study of the green luminescence of ZnO nanorods, *Appl. Surf. Sci.* **484** (2019) 105–111.
- [43] E. Hasabeldaim, O. M. Ntwaeaborwa, R. E. Kroon, V. Craciun, E. Coetsee, H. C. Swart, Surface characterization and cathodoluminescence degradation of ZnO thin films, *Appl. Surf. Sci.* **424** (2017) 412–420.
- [44] B. T. Kelly, *Irradiation Damage to Solids*, Oxford, Pergamon Press, 1966.
- [45] M. R. McCartney, D. J. Smith, Studies of electron irradiation and annealing effects on TiO₂ surfaces in ultrahigh vacuum using high-resolution electron microscopy, *Surf. Sci.* **250** (1991) 169-178.

Chapter 6

Luminescence properties of Eu doped ZnO PLD thin films: the effect of oxygen partial pressure

6.1. Introduction

Eu³⁺ doped ZnO is one of the promising candidates to act as a red luminescent material for optoelectronic applications, such as light emitting diodes (LEDs) and flat panel displays (FPDs). ZnO has excellent properties, particularly its wide band gap (3.37 eV) at room temperature and large exciton binding energy, as well as its low cost of production [1]. The combination of ZnO with the 4f – 4f intrashell transitions of Eu³⁺ ions, which give narrow lines of emission within the red color region [2] provides interesting emission properties. Eu doped ZnO has attracted considerable attention among different research communities. Over the past few years, extensive research has been done to produce efficient red luminescence from Eu³⁺ doped ZnO, but the way has been encumbered by the difficulty of achieving good enough energy or charge transfer in the ZnO:Eu³⁺ system from the ZnO to Eu³⁺ energy levels [3, 4, 5, 6]. Earlier work reported on electroluminescence of Eu³⁺ doped ZnO heterojunctions [7]. Some of these reports showed a visible red emission from the 4f – 4f intrashell transitions of Eu³⁺ incorporated in ZnO as a n-type layer [8, 9]. These results demonstrated that achieving intense red electroluminescence from Eu doped ZnO based heterojunctions is possible regardless of its photoluminescence, which may be due to the different excitation mechanisms.

Another aspect is the preparation method since any technique has its own advantages and disadvantages. Different techniques have been used to prepare Eu³⁺ doped ZnO in the form of powders, thin films and nanostructures (such as nanorods, nanowires, nanocombs, etc.) such as the combustion method, co-precipitation, microemulsion method, sol-gel method, spin coating, radio frequency, electron/ion beam sputtering, chemical bath deposition and chemical vapor deposition [2]. Pulsed laser deposition (PLD) provides different advantages over the above-mentioned techniques, including the versatility, which offers many parameters that can be changed to finely control the final film properties. Obtaining a high quality crystalline thin film at relatively low substrate temperatures is possible and post annealing processes may not be required [10]. Deposition in reactive gases such as oxygen is available [11, 12] and hence post annealing in a reactive atmosphere to activate the luminescence centres may not be needed. Therefore, obtaining high quality thin films with good optical, luminescence and electrical properties is possible. Moreover, PLD offers the possibility of using multiple targets of different materials at the same time, and then in situ deposition of multiple layers is possible.

In our previous work, Eu doped ZnO thin films fabricated by sol-gel method using the spin coating technique, exhibited good luminescence properties and excellent stability under electron beam irradiation [13].

In the present work, Eu doped ZnO thin films were deposited using PLD. The effect of partial pressure of an oxygen reactive atmosphere on the films structure, morphology and luminescence properties was investigated. For achieving electroluminescence, in the case of thin films, rectification is crucial for the junction between substrate and thin film, as well as other conditions such as a transparent conducting film, electron ejection layer, etc. It is therefore important to show that rectification can be obtained and what the effect of the PLD parameters (oxygen atmosphere) would be.

6.2. Experimental methods

6.2.1. Pellet preparation and thin film deposition

For the PLD target pellet preparation, 3 mol% Eu doped ZnO powder was prepared by the combustion method [14]. The Eu content was chosen because it demonstrated a reasonable red emission intensity [15]. The powder was annealed at 950 °C for 2 h in air to improve its stoichiometry [16, 17]. About 12 g of this annealed powder was pressed in a 1-inch disk die using a hydraulic press at 12 Ton, and then taken out from the die and sintered at 950 °C for 8 h in air. The compactness of the pellet particles plays a critical role on the final film morphology and topography, therefore the pellet received further sintering at a higher temperature of 1100 °C for 6 h and then again at 1200 °C for 6 h in air, after which it was ready for laser ablation. It was inserted into a PLD chamber and mounted in a target holder which was rotated at 10 degrees/min to avoid laser-pinning.

A p-type Si (100) substrate was cut into pieces of ~ 3 x 2 cm. They were ultrasonically cleaned using acetone, isopropanol, ethanol and distilled water consecutively for about 5 min each and then nitrogen gas was gently blown on their surfaces for drying purposes. The Si substrate was mounted on the substrate holder in the PLD chamber, with a temperature maintained at 300° C during the ablation process. The target-substrate distance was kept at 5 cm for all the samples. A 266 nm Nd:YAG laser was used for the ablation. The laser energy, time of deposition and the ablated area were fixed at 33 mJ, 60 min and 1.5 mm, respectively. The PLD chamber was pumped down to a vacuum base pressure of ~ 2.6 x 10⁻⁵ Torr for the deposition of the first sample (vacuum). The chamber was then back filled with oxygen to increasing partial pressures of ~ 5.9 x 10⁻² Torr, 8 x 10⁻² Torr and 10 x 10⁻² Torr for the deposition of the other samples, designated as O1, O2 and O3, respectively.

6.2.2. Characterization techniques

A D8 Bruker X-ray diffractometer (XRD) was used for the structural analysis with a 1.5406 nm Cu K α X-ray. A JEOL model JSM-7800F scanning electron microscope (SEM), a Shimadzu atomic force microscopy (AFM) Model SPM-9600, and a PHI 5000 scanning XPS microprobe were used for characterization. Full detail of the characterization techniques can be found in ref [13]. ImageJ software was used to estimate the average particle size from SEM and AFM images. MULTIPACK version 9 software using Gaussian-Lorentz functions was employed to analyze (plot, fit and deconvolute) the spectra to identify the chemical states of the compounds present. The binding energy (BE = 284.6) of the C1s of the graphitic carbon was used as reference to correct the binding energy shift for all detected elements as in ref [18]. For photoluminescence (PL) measurements, a 325 nm He-Cd laser was used as an excitation source above the ZnO band gap, while a photomultiplier tube detector was used to record the sample emission. A FLS980 (Edinburgh Instruments) was employed to excite the samples at different wavelengths using a xenon lamp as an excitation source. The cathodoluminescence (CL) spectra were recorded by an Ocean Optics PC2000 spectrometer, while the samples were under the excitation of an electron beam at a working voltage, beam current and current density of 2 kV, 24 μ A and 2.12 μ A.cm⁻², respectively. The electron beam spot size was about 1.2 mm. The CL measurements were conducted in an ultra-high vacuum using a PHI Auger electron spectroscopy model 545. All the measurements were performed at room temperature. For the current-voltage (IV) measurements, 150 nm thick Al contacts were evaporated on the back side (Si substrate) and the front side (ZnO:Eu films) using electron beam evaporation, after which the devices were annealed at 350 °C in an argon atmosphere. A PVIV test station from Oriol instrument was used for the IV measurements.

6.3. Result and discussion

6.3.1. Structural and morphological analysis

Fig. 6.1 displays the XRD patterns of the Eu doped ZnO thin films deposited in the different atmospheres. The films have the commonly observed (002) orientation along the c-axis of the wurtzite structure of ZnO, which is well-known to be due to the low surface energy along the [002] direction [19, 20]. No peaks associated with Eu₂O₃ were observed, which affirms the substitution of Zn²⁺ by Eu³⁺ ions in the ZnO lattice, or maybe the Eu³⁺ occupied interstitial sites. Comparing the samples grown at oxygen atmospheres to the vacuum sample, the peak position of the 002 reflection shifted to a higher 2 θ angle, which indicated a decrease in the lattice parameter. The 002 peak intensity has increased while the full width at half maxima

(FWHM) decreased until O2 sample, after which (O3 sample) the intensity slightly decreased with widening in the FWHM. This can be attributed to either the enhancement of the film crystallinity, or more likely due to the film thickness as the thickness increased and decreased with the same pattern of the 002 peak intensity, Fig. 6.1(b). The well-known Scherrer equation [21] and Miller indices were used to compute the crystallite size and the lattice parameter, respectively (Table 6.1). The crystallite size increased with increasing oxygen partial pressure until O2, after which it decreased again. The lattice parameter c for the film obtained in vacuum is ~ 0.5334 nm which is greater than for bulk ZnO (0.5209 nm), and the lattice parameters c for the films obtained in oxygen (O1, O2 and O3) were almost equal to the lattice parameter c for bulk ZnO. This may be attributed to the excess of Zn atoms in the crystal lattice which were eliminated after introducing oxygen. The equation

$$\sigma = -2.33 \times 10^{11} \left(\frac{c_{film} - c_{bulk}}{c_{bulk}} \right)$$

was used to estimate the films stress [19] and the results are shown in Table 6.1. The film deposited in vacuum atmosphere was found to have a compressive stress, whereas those obtained in oxygen partial pressures were found to be almost stress-free films.

Table 6.1. Lattice parameters, crystallite size and roughness of the Eu doped ZnO PLD thin films deposited in different atmospheres.

Sample	FWHM (degree)	2 θ (degree)	Lattice parameters (c) (nm)	Interplanar spacing (d) (nm)	Crystallite size (D) (nm)	Stress (GPa)
Vacuum	1.13	33.56	0.5334	0.2667	8 \pm 1	-5.91
O1	0.53	34.44	0.5204	0.2601	16 \pm 1	0.22
O2	0.46	34.29	0.5213	0.2612	18 \pm 1	-0.18
O3	0.48	34.38	0.5210	0.2605	17 \pm 1	-0.04

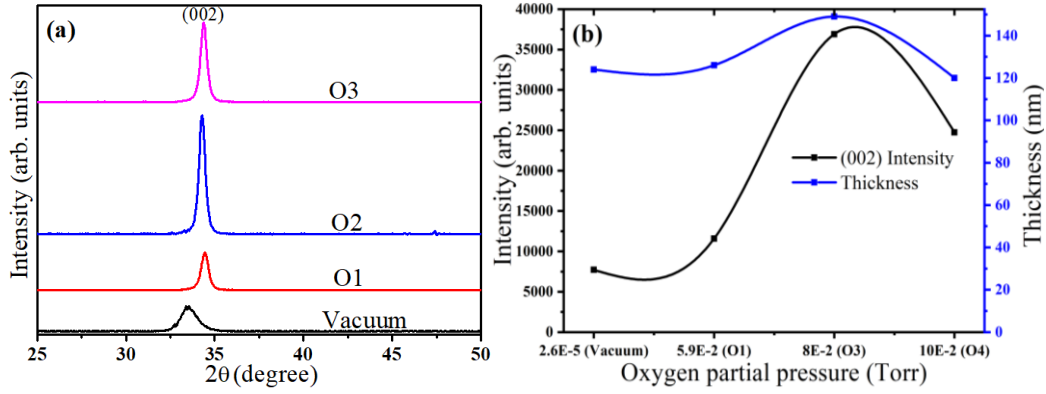


Fig. 6.1. (a) XRD patterns and (b) XRD 002 peak intensity and thickness of the Eu doped ZnO PLD thin films deposited in the different atmospheres.

Fig. 6.2 shows the SEM images and corresponding cross-sections of the Eu doped ZnO thin films deposited in the different atmospheres. The film deposited in the vacuum base pressure has a smooth surface with no clear particle boundaries. Introducing oxygen gas at the O1 partial pressure resulted in an irregular particles shape with identified boundaries. Increasing the oxygen partial pressure led to the formation of circular particles with well-defined boundaries. The changes in the particle morphology may be explained by the plasma plume dynamics. The plume (ablated particles) is comprised of ions, atoms, ZnO molecules and clusters. In vacuum atmosphere, the plume particles travel from the target to the substrate with their original kinetic energy and speed which are very high. When these particles reach the substrate, the probability of these particles, due to their high energy, to stick on the substrate surface is low as well as the possibility of sputtering off the previous existing material. Therefore, the film deposited in vacuum is smooth and have poor crystallinity as also observed in the XRD results (Fig. 6.1(a)). Introducing gas in the deposition chamber will cause the plume particles to collide with the gas molecules, so that their mean-free path and kinetic energy will be reduced. Consequently, the arriving adatoms on the substrate surface will have time to nucleate before the next adatom arrives, which may increase the deposition rate. Therefore, the films deposited in oxygen partial pressure favors growth of grains and led to better crystallinity [22]. The mean free path of the plasma plume particles (the ejected particles) was calculated using [23]:

$$\lambda = \frac{RT}{\sqrt{2}\pi d^2 N_A \rho}$$

where, R, d and N_A represents the gas law constant, collisional cross section and Avogadro's number, respectively. ρ is the gas pressure and T represents the substrate temperature (300 °C) around which the gas was present. The mean free path was found to be 11×10^{-5} m, 8.2×10^{-5} m and 6.6×10^{-5} m for the O1, O2 and O3 oxygen partial pressures. The average particle size

for the films obtained at the O2 and O3 partial pressures were about 40 nm and 45 nm, respectively. The film thickness increased with increasing the oxygen partial pressure up to O2 and then slightly decreased. The film deposited in vacuum usually lacks oxygen. Introducing oxygen will increase the adsorbed oxygen atoms per unit time on the surface, which promotes sufficient Zn-O atoms reaction on the surface and subsequently an increase in the growth rate. This may explain the increase on the film thickness with the initial increase in the oxygen partial pressures [24]. The decrease of the thickness for the film deposited in the O3 oxygen partial pressure is attributed to the reduction of the deposition rate as the result of the decrease in the mean-free path that was caused by the relatively high oxygen partial pressure.

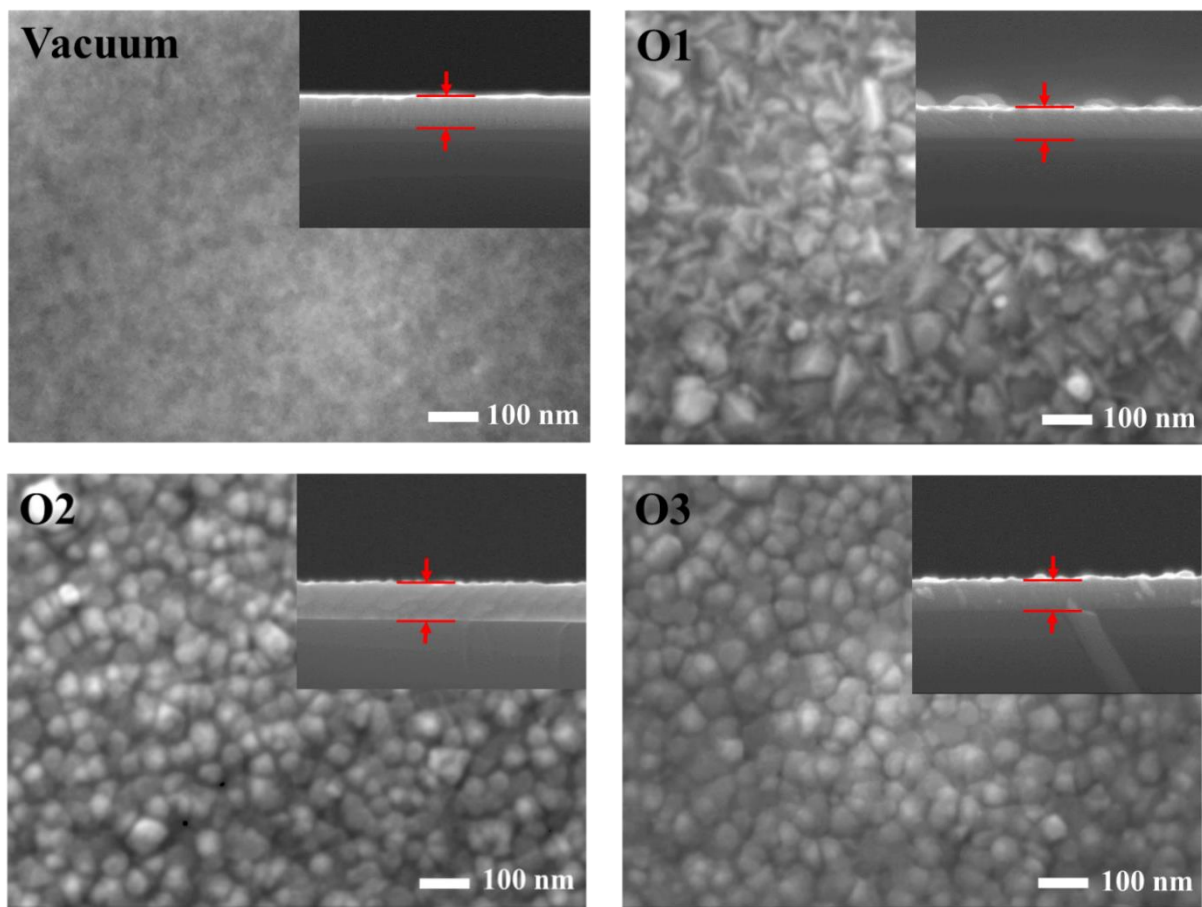


Fig. 6.2. SEM images of 3% Eu doped ZnO PLD films deposited in different atmospheres.

Fig. 6.3 displays 2D and their corresponding 3D AFM micrographs of the films deposited at the different atmospheres. The film obtained in vacuum comprised of small particles with an average size of about 32 nm, while the particle size for the films deposited in the oxygen partial pressure O1, O2 and O3 increased to about 57 nm, 51 nm and 62 nm, respectively as obtained from the AFM images. It was expected that the particle size would increase consistently with increasing oxygen partial pressure. However, the film obtained in the O1 partial pressure

exhibited bigger particles than the film obtained in the O2 partial pressure. This is attributed to the differences in their morphology as shown by the SEM images, where the film obtained in the O1 partial pressure showed irregular particles shape. The root mean square (RMS) roughness was 0.85 nm, 4.5 nm, 3.7 nm and 4.6 nm with increasing oxygen partial pressure from vacuum, O1, O2 and O3, respectively. The increase of the surface roughness can be ascribed to the particles growth [22].

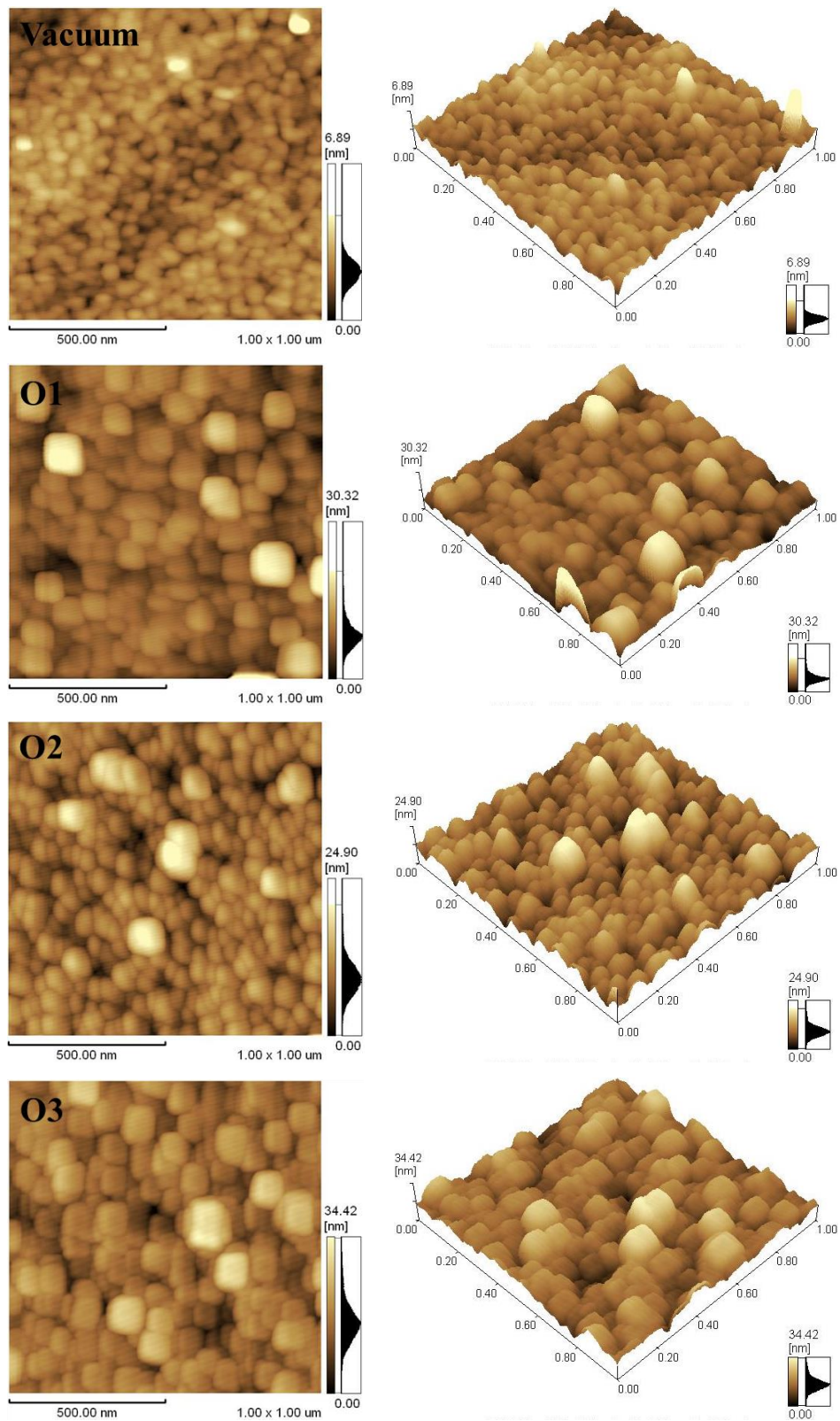


Fig. 6.3. AFM of the Eu doped ZnO PLD thin films deposited in different atmospheres.

6.3.2. Chemical analysis

Fig. 6.4 shows the high resolution XPS spectra of the Zn 2p level of the Eu^{3+} doped ZnO thin films obtained in different oxygen partial pressure (before and after 30 s of Ar^+ ion sputtering).

Two peaks attributed to the Zn 2p_{3/2} and Zn 2p_{1/2} doublet lines were detected at binding energies of 1044 eV and 1022 eV, respectively. The energy difference between the two lines was 23 eV. These values comfortably match the standard reference value of ZnO [18]. No metallic Zn could be detected, which is in agreement with the XRD measurements.

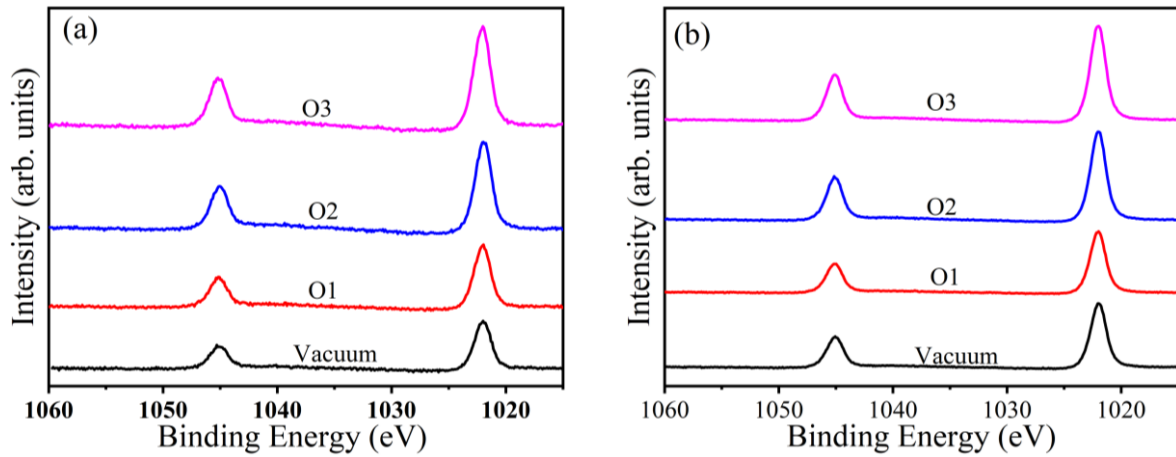


Fig. 6.4. High-resolution XPS spectra of Zn 2p core levels (a) before sputtering and (b) after sputtering of the Eu³⁺ doped ZnO PLD thin films deposited at different oxygen partial pressures.

Fig. 6.5 depicts the high resolution XPS spectra of the Eu 3d level for the films deposited in different oxygen partial pressure ((a) before and (b) after 30 s of Ar⁺ ion sputtering). Four peaks were detected at energy region between 1115 eV to 1180 eV for all the samples. Two peaks ascribed to the Eu 3d_{5/2} and 3d_{3/2} were detected at 1135.2 eV and 1165.0 eV, respectively. The binding energy difference between these two peaks was 29.8 eV. These values match the values corresponding to Eu³⁺ ions (trivalent state) in the ZnO host as reported previously [25]. Two other peaks associated with the divalent state (Eu²⁺) of Eu ions were also detected at the lower binding energy side of the Eu³⁺. The presence of the divalent together with the trivalent oxidation states of Eu indicated that the incorporation of Eu occurred in an oxidative environment [14]. Of interest is that the peaks associated with trivalent state of Eu³⁺ in ZnO have increased after sputtering, while the peaks associated with the divalent Eu²⁺ in ZnO have almost diminished. This indicates that most of the Eu²⁺ ions were present on the films surface along with surface contaminations. In our previous work, Eu doped ZnO spin coating thin films, the Eu²⁺ on the surface was associated with the adventitious EuF that formed during handling and air exposure [23]. The components of the Eu²⁺ ions may represent the Eu³⁺ ions that occupied the Zn²⁺ sites, whereas the Eu³⁺ components could represent the Eu³⁺ ions in interstitial sites or lattice sites leaving to charge imbalance. This argument may be supported by the fact that XRD exhibited the formation of pure ZnO as determined for all the films.

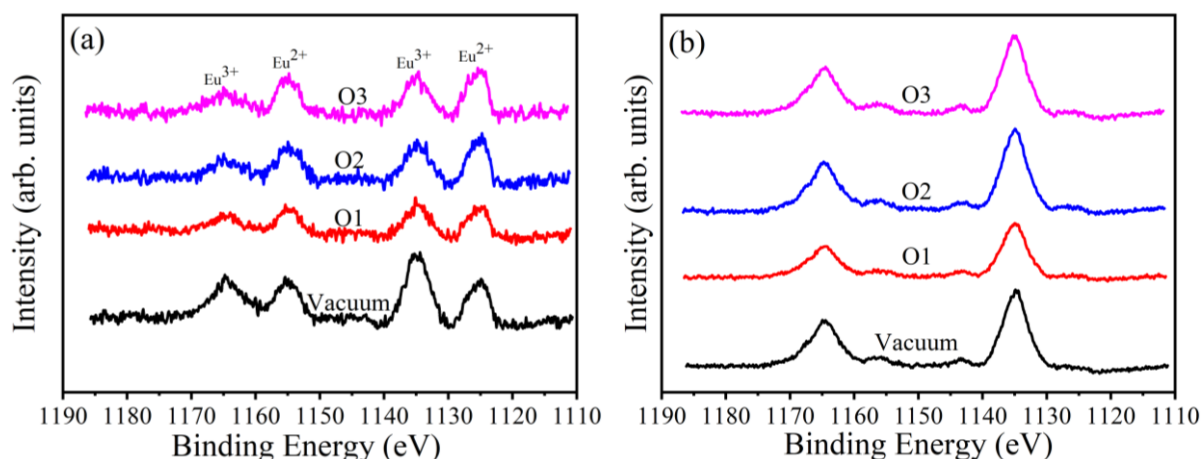


Fig. 6.5. High-resolution XPS spectra of Eu^{3+} 3d peaks (a) before sputtering and (b) after sputtering of the Eu^{3+} doped ZnO PLD thin films deposited at different oxygen partial pressures.

XPS high resolution spectra of the O 1s core level of the Eu^{3+} doped ZnO PLD thin films obtained in different oxygen partial pressures are shown in Fig. 6.6, before and after Ar^+ ion sputtering for 30s. The O 1s peak was deconvoluted into three components as indicated with different colours namely magenta, cyan and blue, centred at binding energy levels at 530.6 eV, 532.0 eV and 532.9 eV, respectively. The O 1s components were well identified in previous works [26, 27, 28] as follow; the magenta band (O_1) was attributed to the fully oxidized oxygen atoms in the Zn-O-Zn coordinates, the cyan band (O_2) was ascribed to the oxygen ions in deficient regions such as oxygen related defects and hydroxyl group, and the blue band (O_3) was always associated with the loosely bonded species on the surface (contaminations) such as atmospheric carbon and CO_2 . The O_2 and O_3 bands areas were higher for all the films before sputtering, and they were significantly reduced after sputtering. The increase of the O_1 peak area % and reduction in O_2 and O_3 peak area % indicated towards less defects and less loosely bonded species in the bulk of the material. This signify that most of the defects and surface contaminations were present on the surface. Although the XPS spectra of the Eu3d level confirmed the presence of Eu^{3+} in the film surface and bulk (in addition, Eu^{3+} is associated with the Eu_2O_3) while no peak related to the Eu_2O_3 could be detected. This is correlating with XRD results and support the argument of the successful substitution of Zn^{2+} ion by Eu^{3+} in the ZnO matrix. The details (peaks position and area) about the O 1s components are listed in Table 6.2.

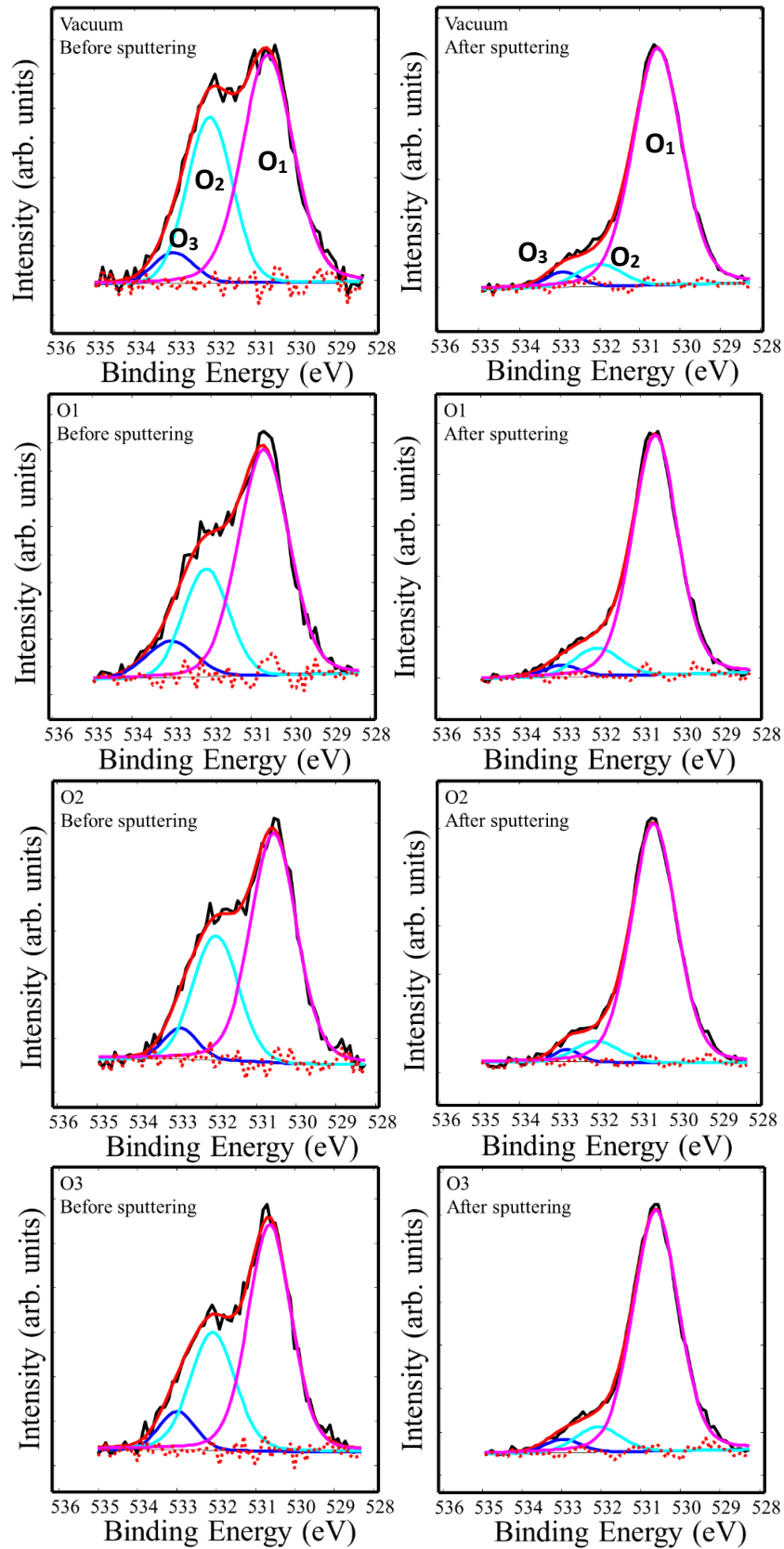


Fig. 6.6. The O 1s spectra of the Eu^{3+} doped ZnO PLD thin film deposited in different oxygen partial pressures.

Table 6.2. Peak positions and areas of the O1s de-convoluted components of the Eu³⁺ doped ZnO PLD thin films deposited in different oxygen partial pressures.

Sample	O 1s components	Peak position (eV)	Area% (before sputtering)	Area% (after sputtering)
Vacuum	Magenta O ₁	530.6	59	89
	Cyan O ₂	532.0	35	7
	Blue O ₃	532.9	6	4
O1	Magenta O ₁	530.6	65	88
	Cyan O ₂	532.0	26	9
	Blue O ₃	532.9	9	3
O2	Magenta O ₁	530.6	63	90
	Cyan O ₂	532.0	31	7
	Blue O ₃	532.9	6	3
O3	Magenta O ₁	530.6	60	88
	Cyan O ₂	532.0	32	8
	Blue O ₃	532.9	8	4

6.3.3. Luminescence analysis

Fig. 6.7 depicts the PL spectra of the films deposited in different atmospheres, excited at 325 nm using a He-Cd laser. The films exhibited a broad range of emissions including: ultra-violet (UV) emission at ~ 379 nm, deep level emission (DLE) across the visible region from ~ 450 nm to 700 nm, as well as characteristic emission of Eu³⁺ peak at ~ 616 nm protruding from the deep level emission for the films obtained in the oxygen atmospheres (O1, O2 and O3). The origin of the UV emission of ZnO is attributed to the near band to band (exciton) (NBE) transitions [29]. The deep level emissions are usually ascribed to the ZnO native defects such as: oxygen vacancies (V_o), zinc vacancies (V_{Zn}), oxygen interstitials (O_i) and zinc interstitials (Zn_i) [30, 31, 32]. The blue-green emission has been attributed mainly to be due to V_o [33] and the orange-red emission has been explained by the transition between Zn_i and O_i [34]. With the increase in oxygen pressure less V_o and more O_i are expected as seen from the trends in emission as function of oxygen pressure as indicated with the green and red arrows in Fig. 6.7 (b). The Eu³⁺ peak is due to the ⁵D₀-⁷F₂ transition of the 4f configuration [35]. The highest UV emission intensity was recorded for the film deposited in vacuum atmosphere, whereas the lowest UV intensity recorded for the films deposited in the oxygen atmospheres (O1, O2 and

O3). Since the UV emission is due to the free exciton recombination, creation of defects in the ZnO crystal lattice and subsequent deterioration of the film crystallinity both can contribute to the reduction of the UV emission intensity. However, in this case, XRD results showed an enhancement of the films crystallinity. Deep level emission indicated no more defects were created for the films obtained in the oxygen atmospheres (O1, O2 and O3). Therefore, neither defects nor crystallinity deterioration may be responsible for the reduction of the UV emission. The Eu^{3+} characteristic emission increased with increasing the oxygen partial pressure from O1, O2 to O3. Presumably, the reduction of the UV emission intensity maybe due to the fact that the excitation energy is shared between the exciton emission, deep level emission and the Eu^{3+} emission [36], with the excitonic emission transferring some of its energy to the Eu ions. It was also previously found that a decrease in defects led to a decrease in Eu^{3+} emission due to the lack of energy transfer from the conduction band to the Eu^{3+} ions [37].

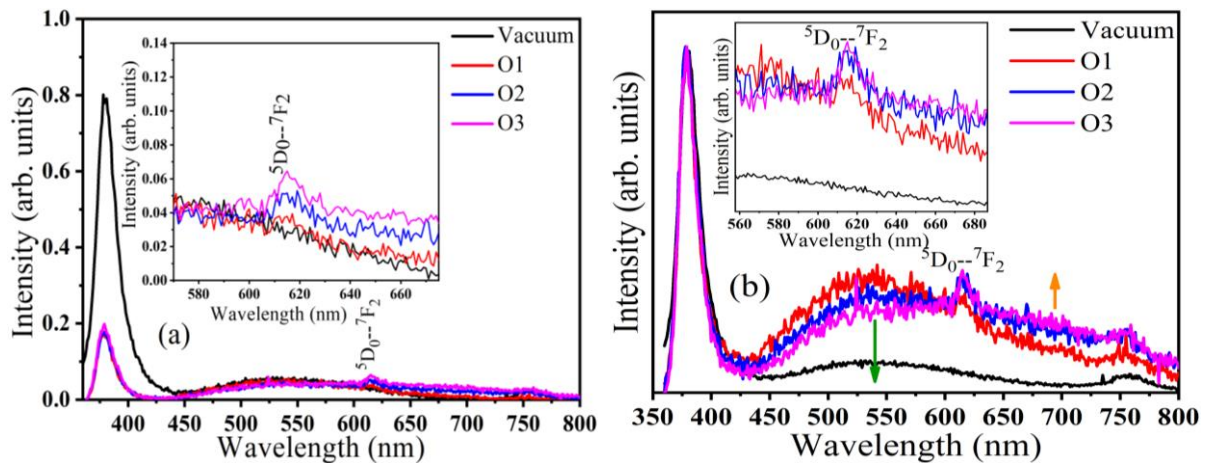


Fig. 6.7. (a) PL spectra of the Eu doped ZnO thin films deposited at different atmospheres, the inset is zoomed in for the region from 570 nm to 675 nm and (b) the normalized PL with respect to the NBE emission with an enlargement of the 560 to 680 region as inset.

Fig. 6.8 shows the excitation and emission spectra of the films obtained in different atmospheres. Fig. 6.8(a) is the excitation spectra of the films while monitoring the dominant Eu^{3+} peak excited at ~ 616 nm. The excitation spectrum of the film obtained in vacuum exhibited only a step absorption at ~ 380 nm all the way down until 230 nm. This step absorption is assigned to the ZnO optical band gap. Three other absorption peaks appeared for the oxygen atmosphere films, narrow peaks at ~ 464 nm, 394 nm and a broad peak centred at ~ 288 nm. The absorption peaks at ~ 464 nm and 394 nm are assigned to the ${}^7\text{F}_0 - {}^5\text{L}_6$ and ${}^7\text{F}_0 - {}^5\text{D}_2$ transitions, respectively. The absorption line around 288 nm is due to the charge transfer from O to Eu^{3+} [38], and its intensity increased with increasing the oxygen partial pressure.

This indicated an increase in the charge transfer with increasing the oxygen partial pressure. The charge transfer peak around 288 nm lies within the absorption range of the ZnO band gap and overlap with the excitation wavelength at 325 nm (Fig. 6.7). This might confirm the above-mentioned argument that the excitation energy was shared between UV emission, DLE and Eu^{3+} emission through a charge transfer mechanism (Fig. 6.7). The PL spectra for resonant excitation at 464 nm for the films are shown in Fig. 6.8(b). The film deposited in vacuum did not exhibit any characteristic emission of Eu^{3+} . The films deposited in oxygen atmospheres (O1, O2 and O3) exhibited a typical characteristic of Eu^{3+} lines at 536 nm, 578 nm, 595 nm, 616 nm, 656 nm and 707 nm, which correspond to the 4f – 4f transitions: ${}^5\text{D}_1 - {}^7\text{F}_0$, ${}^5\text{D}_0 - {}^7\text{F}_J$ ($J= 0, 1, 2, 3$ and 4), respectively [39, 4]. The Eu^{3+} emission when the films were excited at 464 nm increased with increasing oxygen partial pressures until O2 and then decreased for the film obtained at O3. The decrease for the O3 oxygen pressure is probably due to the decrease in the film thickness as found by the SEM cross-section (plotted in Fig. 6.1(b)). Fig. 6.8(c) displays the PL spectra of the films excited at 288 nm. The vacuum sample exhibited broad emission centred at ~ 585 nm, which is commonly associated with ZnO intrinsic defects. The samples obtained in the oxygen atmospheres (O1, O2 and O3) exhibited a characteristic emission of Eu^{3+} of the 4f – 4f transitions, with an intense peak at ~ 616 nm as well as small peaks at ~ 578 nm, 595 nm, 656 nm and 707 nm. The intensity of the Eu^{3+} emission when the samples were excited at 288 nm has increased with increasing the oxygen partial pressure, which is consistent with the broad absorption peak of the charge transfer in Fig. 6.8(a). The differences between the Eu^{3+} emission when the films were excited at 288 nm and at 464 nm, may be due to the fact that Eu^{3+} ions were excited via charge/energy transfer when the excitation wavelength was 288 nm. Interestingly, the film obtained in vacuum atmosphere did not exhibit any Eu^{3+} characteristic emission when excited at different wavelengths. This can be attributed to different reasons including (I) absence of trivalent (Eu^{3+}) oxidation state of Eu due to the lack of oxidation environment, (II) absence of oxygen related defects that promote charge transfer from O^{2-} ions to Eu ions sites, and (III) structure and morphology-related reasons such as creation of defects, which formed non-radiative recombination that quench the Eu^{3+} emission, and presence of internal compressive stress that affect the Eu ions symmetry, which also quench the luminescence of the Eu^{3+} . However, XPS revealed that trivalent (Eu^{3+}) oxidation state of Eu and oxygen related defects are present in all the samples including the sample obtained in vacuum and the sample obtained in vacuum did not show Eu^{3+} emission even when excited resonantly at 464 nm. Therefore, the first (I) and second (II) arguments are likely not true. Hence, the third (III) argument is likely true since it is supported by XRD and

SEM, where the film deposited in vacuum showed high value of internal compressive stress and a very smooth surface.

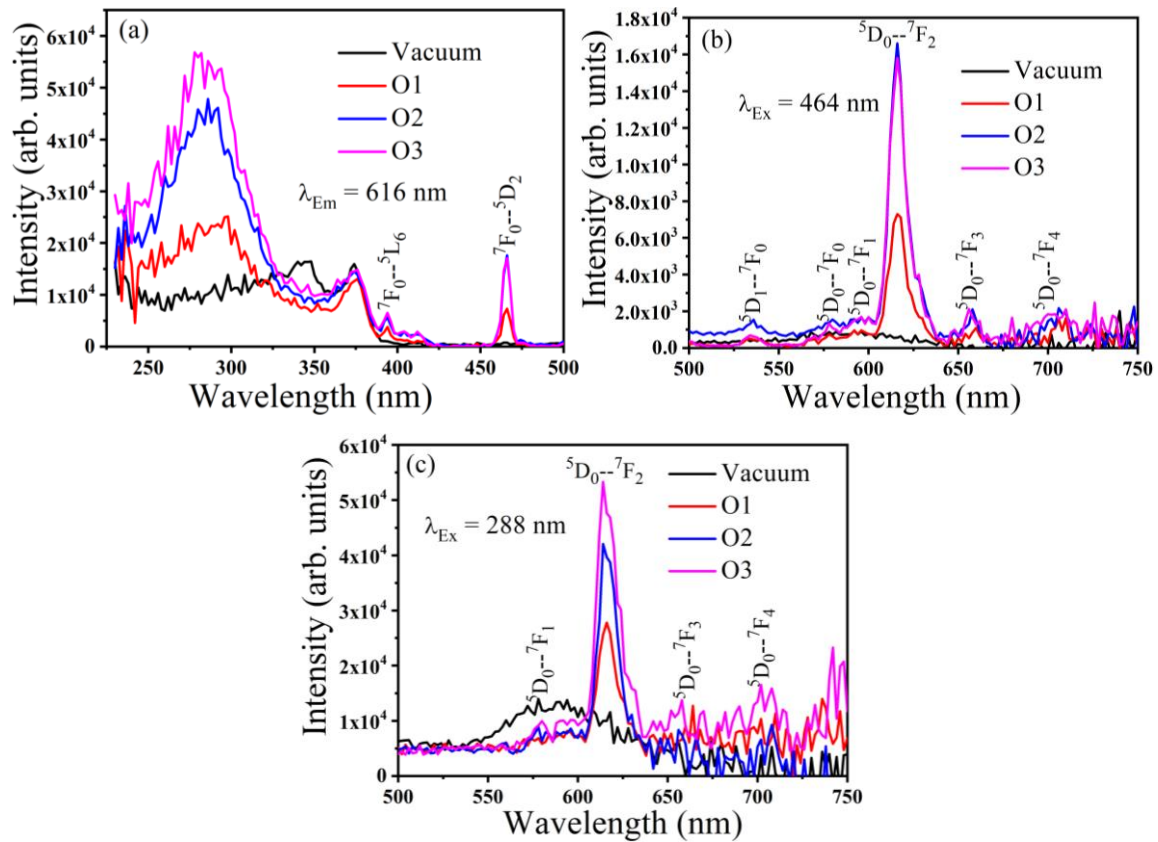


Fig. 6.8. (a) Excitation spectra and (b & c) emission spectra of 3% Eu doped ZnO films deposited in different atmospheres.

CL of the films deposited in different atmospheres is depicted in Fig. 6.9(a). The film obtained in vacuum did not exhibit any CL, which is similar to its counterpart PL when excited at 464 nm. The films obtained in oxygen atmospheres exhibited the characteristic emission of Eu^{3+} that corresponded to the $4f-4f$ transitions as marked in the graph. The electron beam possesses enough energy (above the ZnO band gap) to excite all luminescent centres including ZnO defects, band to band emission and Eu^{3+} centres. However, in this case CL spectra showed the characteristic emission of Eu^{3+} with no ZnO native emission to be observed, which is different to the PL spectra excited above the ZnO band gap at 325 nm He-Cd laser. The electron beam excites luminescence centres in two ways, direct impact excitation by hot electrons or indirect impact excitation by generating electron-hole pairs that transfers their energy nonradiatively to the Eu^{3+} centres [40]. Due to the absence of ZnO native emissions, donors and acceptors defects as well as exciton bonds may have been involved in the generation of the electron-hole pairs and nonradiatively transferred their energy to the Eu^{3+} $4f$ centres, and hence indirect impact excitation may be the dominant excitation mechanisms for the CL. The form of the CL spectra

are slightly different to the PL spectra when the films were excited at 464 nm. This difference can be attributed to the excitation mechanisms [41], where the electron beam energy (2000 eV) was enormously higher than the photon energy with wavelength of 464 nm (2.67 eV): the penetration depth of the electron beam is $\sim 0.09 \mu\text{m}$ and for the photons is $\sim 0.2 - 0.5 \mu\text{m}$ [42], so photons with wavelength of 464 nm excite the luminescent centres resonantly (directly) whereas incident electrons excite the luminescent centres either via direct or indirect impact excitation/ ionization [43]. The CL intensity of the characteristic emission Eu^{3+} increased with increasing the oxygen partial pressure until O2 and then decreased at O3. This decrease may be attributed to the reduction of thin film thickness as revealed by SEM cross-section results. The intensity evolution as a function of oxygen partial pressures of the films obtained in different oxygen partial pressures when the films were excited by different mechanisms is shown in Fig. 6.9(b). The CL intensity spectra showed a similar pattern to the PL intensity of the films when resonantly excited at 464 nm, whereas the PL intensity of the films excited at 288 nm kept increasing as a function of oxygen partial pressure. This may indicate that the electron beam has directly impact excited the luminescence centres, which is in contradiction to the aforementioned assumption that indirect impact excitation was the dominant mechanism for CL. The CL intensity evolution vs oxygen partial pressure is slightly different to the PL intensity evolution when the films are excited at 464 nm. Therefore, might be both direct and indirect impact excitation mechanisms were responsible for the CL excitation. Since the PL intensity of the films excited at 288 nm kept increasing with increasing the oxygen partial pressure, some defect-mediated excitation such as energy/charge transfer may have taken place.

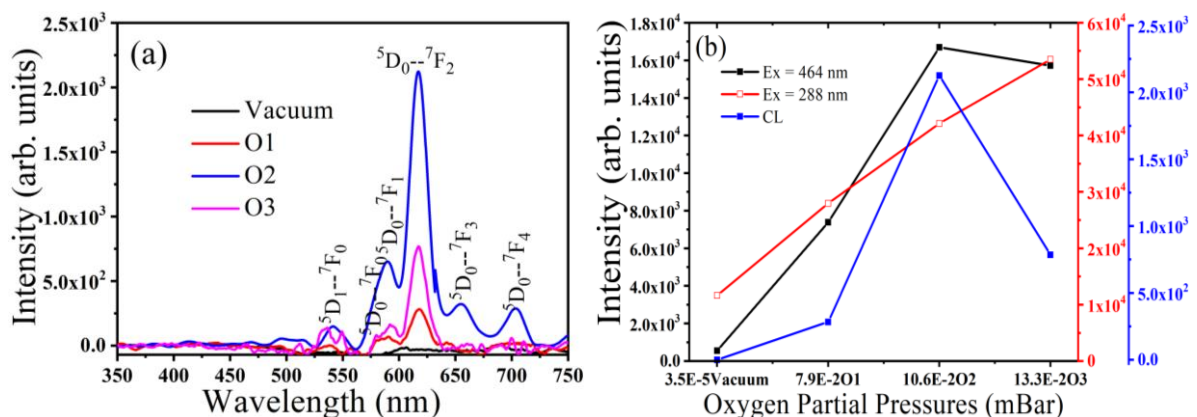


Fig. 6.9. (a) CL spectra and (b) intensities of the Eu^{3+} characteristic emission as a function of oxygen partial pressures of the Eu (3 mol %) doped ZnO PLD thin films deposited in different atmospheres.

6.3.4. Current-voltage measurements

In order to determine if any rectification can be obtained, IV measurements were done. Fig. 6.10 shows the I-V characteristics on the forward and reverse bias of the p-Si/ZnO:Eu³⁺ (deposited in different oxygen atmospheres) heterojunctions with 150 nm thick Al contacts on both sides. Al/p-Si and Al/n-type ZnO contacts always form ohmic contacts [44, 45, 46]. Therefore, any rectification characteristic is more likely coming from the heterojunctions. All the heterojunctions exhibited a diode-like behaviour with a turn-on voltage of about 10 V. The slope of the I-V curve became more positive for the O₂ oxygen atmosphere sample, which indicated better rectification ratio and reduction in the series resistance. In the reverse bias, the samples showed a leakage current, which was higher for the sample obtained in the vacuum atmosphere. The leakage current decreased for the samples obtained in oxygen atmospheres. These results confirmed that the oxygen atmosphere played a significant role in the rectification behaviour of the p-Si/ZnO:Eu³⁺ heterojunctions. The diode current depends on the variation of the carrier concentration, recombination of majority carriers in the pn-junction and small minority diffusion current in the pn materials interface or both. ZnO native defects such as excess zinc-related defects play a significant role in the electrical properties of ZnO. In particular, oxygen vacancies (V_O) are the most suspected defects to contribute in the free-carrier concentration, conductivity and the electron mobility of the n-type ZnO. Hence, introducing oxygen may help to fill these oxygen deficiencies, and may lead to reduction of the free carrier concentration, which increased the width of the depletion region in the interface between the np-junctions, and finally resulted in better rectification ratio and lower leakage current [47]. The rectification ratio and the leakage current were improved with an increase on the film thickness and deteriorated with the decrease on the thickness. Therefore, the film thickness plays a key role in the electrical properties of the pn-junction.

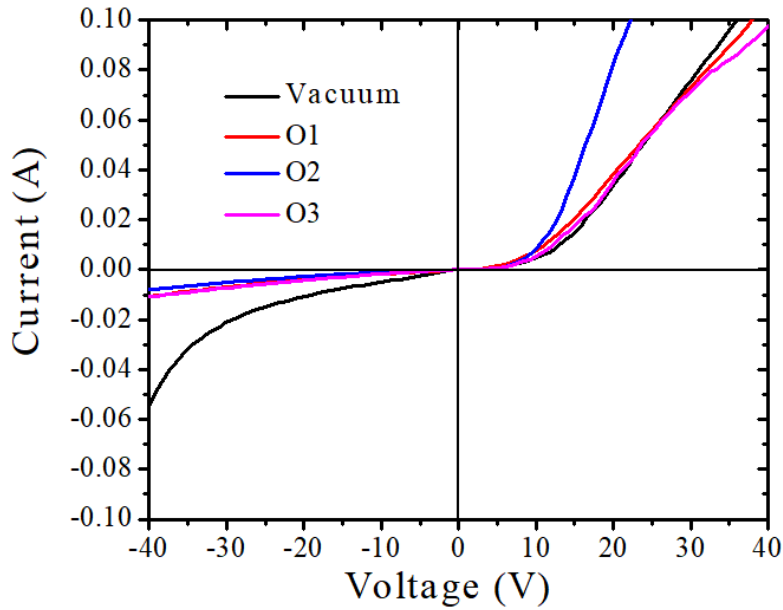


Fig. 6.10. I-V characteristics of the n-ZnO:Eu³⁺/p-type Si heterojunctions for the n-ZnO:Eu³⁺ deposited in different oxygen atmospheres.

6.4. Conclusion

Eu doped ZnO films were successfully deposited on p-type Si substrates by PLD. The effect of oxygen partial pressures on the films' structure, morphology, electrical and luminescence properties of the films were investigated. The variation of the oxygen partial pressure led to two factors that play a critical role on the films final properties: (1) The initial increase in the oxygen partial pressure increased the deposition rate, which resulted in improving the films crystallinity and increasing the films thickness. Consequently, the film morphology was improved and the electrical and the luminescence properties enhanced. (2) A reduction in the mean free path of the plume particles (adatoms) with a further increase in the oxygen partial pressure, especially at the higher oxygen pressure (at O3), resulted in particles not reaching the substrate and a decrease in the growth rate, which reduced the film thickness and therefore the rectification ratio and the luminescence intensity were reduced. Charge transfer from O²⁻ to Eu³⁺ ions was found to take place and the charge transfer rate increased with increasing the oxygen partial pressure, which enhanced the PL of the characteristic emission of the Eu³⁺. The film's structure (internal stress) and morphology were found to play a vital role in the luminescence properties of the Eu³⁺ doped ZnO PLD thin films. The film deposited at 8 x 10⁻² Torr oxygen pressure (O2) showed the best crystallinity, morphology, luminescence intensity and better diode rectification behavior. These PLD films are very promising as a red emissive layer in optoelectronics devices such as light emitting diodes (LEDs) and flat panel displays (FPDs).

6.5. References

- [1] D. Aryanto, W. N. Jannah, Masturi, T. Sudiro, A. S. Wismogroho, P. Sebayang, Sugianto and P. Marwoto, Preparation and structural characterization of ZnO thin films by sol-gel method, *J. Phys.: Conf. Ser.* **817** (2017) 012025. doi:10.1088/1742-6596/817/1/012025.
- [2] R. Swapna, T. SrinivasaReddy, K. Venkateswarlu and M. C. Santhosh Kumar, Effect of Post-Annealing on the Properties of Eu Doped ZnO Nano Thin Films, *Procedia Materials Science* **10** (2015) 723 – 729. <https://doi.org/10.1016/j.mspro.2015.06.085>.
- [3] K. Suzuki, K. Murayama and N. Tanaka, Enhanced luminescence in Eu-doped ZnO nanocrystalline films, *Appl. Phys. Lett.* **107** (2015) 031902. <http://dx.doi.org/10.1063/1.4926986>.
- [4] X. Zeng, J. Yuan and L. Zhang, Synthesis and Photoluminescent Properties of Rare Earth Doped ZnO Hierarchical Microspheres, *J. Phys. Chem. C* **112** (2008) 3503-3508. doi: 10.1021/jp0768118.
- [5] L. Yang, J. Dong, Y. She, Z. Jiang, L. Zhang and H. Yu, Self-purification construction of interstitial O in the neighbor of Eu 3+ ions to act as energy transfer bridge, *Appl. Phys. Lett.* **104** (2014) 033109. doi: 10.1063/1.4863083.
- [6] S. M. Ahmed, P. Szymanski, L. M. El-Nadi and M. A. El-Sayed, Energy-Transfer Efficiency in Eu-Doped ZnO Thin Films: The Effects of Oxidative Annealing on the Dynamics and the Intermediate Defect States, *ACS Appl. Mater. Interfaces* **6** (2014) 1765–1772. doi: 10.1021/am404662k.
- [7] S. A. M. Lima, M. R. Davolos, W. G. Quirino, C. Legnani and M. Cremona, Low-voltage electroluminescence of europium in zinc oxide thin films, *Appl. Phys. Lett.* **90** (2007) 023503. doi: 10.1063/1.2431566.
- [8] Y. Haj-Hmeidi, R. Röder, D. Cammi and C. Ronning, Electroluminescence of intrashell transitions in Eu doped single ZnO nanowire, *Nanotechnology* **30(9)** (2019) 095201. <https://doi.org/10.1088/1361-6528/aaf82c>.
- [9] M. Huang, S. Wang, G. Wan, X. Zhang, Y. Zhang, K. Ou and L. Yi, Effect of co-doped Tb³⁺ ions on electroluminescence of ZnO:Eu³⁺ LED, *J. Mater. Sci. Mater. Electron* **29(9)** (2018) 7213-7219. <http://doi.org/10.1007/s10854-018-8709-9>.

- [10] V. Craciun, J. Elders, J. G. E. Gardeniers and Ian W. Boyd, Characteristics of high quality ZnO thin films deposited by pulsed laser deposition, *Appl. Phys. Lett.* **65(23)** (1994) 2963-2965. <https://doi.org/10.1063/1.112478>.
- [11] A. K. Kunti, K. C. Sekhar, M. Pereira, M. J. M. Gomes and S. K. Sharma, Oxygen partial pressure induced effects on the microstructure and the luminescence properties of pulsed laser deposited TiO₂ thin films, *AIP Adv.* **7** (2017) 015021. doi: 10.1063/1.4973721.
- [12] J. W. Kim, H. S.g Kang, J. H. Kim, S. Y. Lee, J. K. Lee and M. Nastasi, Variation of structural, electrical, and optical properties of Zn 1 – x Mg x O thin films, *J. Appl. Phys.* **100** (2006) 033701. doi: 10.1063/1.2219153.
- [13] E. H. H. Hasabeldaim, O. M. Ntwaeaborwa, R. E. Kroon, E. Coetsee and H. C. Swart, Photoluminescence and cathodoluminescence of spin coated ZnO films with different concentration of Eu³⁺ ions, *Vacuum* **169** (2019) 108889. <https://doi.org/10.1016/j.vacuum.2019.108889>.
- [14] V. Kumar, Vijay Kumar, S. Som, M. M. Duvenhage, O. M. Ntwaeaborwa and H. C. Swart, Effect of Eu doping on the photoluminescence properties of ZnO nanophosphorsforredemissionapplications, *Appl. Surf. Sci.* **308** (2014) 419–430. <http://dx.doi.org/10.1016/j.apsusc.2014.04.192>.
- [15] S. M. Ahmed, P. Szymanski, L. M. El-Nadi and M. A. El-Sayed, Energy-Transfer Efficiency in Eu-Doped ZnO Thin Films: The Effects of Oxidative Annealing on the Dynamics and the Intermediate Defect States, *ACS Appl. Mater. Interfaces* **3** (2014) 1765-1772. doi:10.1021/am404662k.
- [16] R. N. Aljawfi, M. J. Alam, F. Rahman, S. Ahmad, A. Shahee and S. Kumar, Impact of annealing on the structural and optical properties of ZnO nanoparticles and tracing the formation of clusters via DFT calculation, *Arab. J. Chem.* **In press.** (2018). <https://doi.org/10.1016/j.arabjc.2018.04.006>.
- [17] L. P. Etcheverry, W. H. Flores, D. L. D. Silva and E. C. Moreira, Annealing Effects on the Structural and Optical Properties of ZnO Nanostructures, *Mater. Res.* **21** (2018) 0936. doi: <http://dx.doi.org/10.1590/1980-5373-MR-2017-0936>.
- [18] J.F. Moulder, Handbook of X-ray Photoelectron Spectroscopy: a Reference Book of Standard Spectra for Identification and Interpretation of XPS Data, Chicago: Physical Electronics, Perkin-Elmer Corporation,1995.

- [19] E. Muchuweni, T. S. Sathiaraj and H. Nyakoty, Synthesis and characterization of zinc oxide thin films for optoelectronic applications, *Heliyon* **3** (2017) e00285. doi:10.1016/j.heliyon.2017.e00285.
- [20] M. H. Aslana, A.Y. Oral, E. Mensur, A. Gul and E. Basaran, Preparation of c-axis-oriented zinc-oxide thin films and the study of their microstructure and optical properties, *Sol. Energy Mater. Sol. Cells* **82** (2004) 543–552. doi:10.1016/j.solmat.2003.06.016.
- [21] R. E. (Ted) Kroon, Nanoscience and the Scherrer equation versus the ‘Scherrer–Gottingen equation’, *S Afr J Sci.* **5/6** (2013) 109. <http://dx.doi.org/10.1590/sajs.2013/a0019>.
- [22] A. K. Kunti, K. C. Sekhar, Mario Pereira, M. J. M. Gomes and S. K. Sharma, Oxygen partial pressure induced effects on the microstructure and the luminescence properties of pulsed laser deposited TiO₂ thin films, *AIP Adv.* **7** (2017) 015021. doi:10.1063/1.4973721.
- [23] E. Hasabeldaim, O. M. Ntwaeaborwa, R. E. Kroon, D. E. Motaung, E. Coetsee and H. C. Swart, Effect of PLD growth atmosphere on the physical properties of ZnO:Zn thin films, *Opt. Mater.* **74** (2017) 76-85. <https://doi.org/10.1016/j.optmat.2017.04.061>.
- [24] P. J. Cao, W. J. Liu, F. Jia, Y. X. Zeng, D. L. Zhu and Y. M. Lu, "Effect of O₂ partial pressure on optical and electrical properties in Al doped ZnO thin films," *mater technol*, vol. 29:5, pp. 275-280. DOI 10.1179/1753555714Y.0000000149, 2014.
- [25] E. J. Cho, S. J. Oh, S. Imada, S. Suga, T. Suzuki, T. Kasuya, Origin of the high-binding-energy structure in the 3d core-level spectra of divalent Eu compounds, *Phys. Rev. B* **51** (1995) 10146. <https://doi.org/10.1103/PhysRevB.51.10146>, 1995.
- [26] V. Kumar, H. C. Swart, S. Som, Vijay Kumar, A. Yousif, A. Pandey, S. K. K. Shaat and O. M. Ntwaeaborwa, The role of growth atmosphere on the structural and optical quality of defect free ZnO films for strong ultraviolet emission, *Laser Phys.* **24** (2014) 105704. doi:10.1088/1054-660x/24/10/105704.
- [27] E. H. H. Hasabeldaim, O. M. Ntwaeaborwa, R. E. Kroon, E. Coetsee, and H. C. Swart, Enhanced green luminescence from ZnO nanorods, *J. Vac. Sci. Technol. B* **37** (2019) 011201; doi: 10.1116/1.5052543.
- [28] V. Kumar, H. C. Swart, O. M. Ntwaeaborwa, R. E. Kroon, J. J. Terblans, S. K. K. Shaat, A. Yousif and M. M. Duvenhage, Origin of the red emission in zinc oxide nanophosphors, *Mater. Lett.* **101** (2013) 57–60; doi:10.1016/j.matlet.2013.03.073.

- [29] Y. M. Lu, X. P. Li, P. J. Cao, S. C. Su, F. Jia, S. Han, W. J. Liu, D. L. Zhu and X. C. Ma, Study of Ultraviolet Emission Spectra in ZnO Thin Films, *Journal of Spectroscopy*, **2013** (2012) 1-7. <http://dx.doi.org/10.1155/2013/797232>.
- [30] D. Thapa, J. Huso, J. L. Morrison, C. D. Corolewski, M. D. McCluskey and L. Bergman, Achieving highly-enhanced UV photoluminescence and its origin in ZnO nanocrystalline films, *Opt. Mater.* **58** (2016) 382-389. <https://doi.org/10.1016/j.optmat.2016.05.008>.
- [31] A. Janotti and C. G. Van de Walle, Oxygen vacancies in ZnO, *Appl. Phys. Lett* **87** (2005) 122102. doi: 10.1063/1.2053360.
- [32] A. Travlos, N. Boukos, C. Chandrinou, H. S. Kwack and L. S. Dang, Zinc and oxygen vacancies in ZnO nanorods, *J. Appl. Phys* **106** (2009) 104307. doi: 10.1063/1.3259413.
- [33] V. Kumar, O. M. Ntwaeaborwa, T. Soga, V. Dutta and H. C. Swart, Rare earth doped zinc oxide nanophosphor powder: A future material for solid state lighting and solar cell, *ACS Photonics* **4(11)** (2017) 2613-2637.
- [34] V. Kumar, H. C. Swart, O. M. Ntwaeaborwa, R. E. Kroon, J. J. Terblans, S. S. K. Shaat, A. Yousif and M. M. Duvenhage, Origin of the red emission in zinc oxide nanoparticles, *Mater. Lett.* **101** (2013) 57-60. doi:10.1016/j.matlet.2013.03.073.
- [35] A. Ishizumi, Structural and luminescence properties of Eu-doped ZnO nanorods fabricated by microemulsion method, *Appl. Phys. Lett* **86** (2005) 253106. <https://doi.org/10.1063/1.1952576>.
- [36] H. Akazawa and H. Shinjima, Energy transfer and dissipation processes studied using photoluminescence of Eu³⁺ ions doped in epitaxial ZnO films, *Thin Solid Films* **616** (2016) 204-212. <http://dx.doi.org/10.1016/j.tsf.2016.08.029>.
- [37] V. Kumar, O. M. Ntwaeaborwa and H. C. Swart, Effect of oxygen partial pressure during pulsed laser deposition on the emission of Eu doped ZnO thin films, *Physica B: Condensed Matter* **574** (2019) 411713.
- [38] J. Huang, S. Liu, B. Gao, T. Jiang, Y. Zhao, S. Liu, L. Kuang and X. Xu, Synthesis and Optical Properties of Eu³⁺ Doped ZnO nanoparticles used for white light emitting diodes, *J. Nanosci. Nanotechnol.* **14** (2014) 3052–3055. doi:10.1166/jnn.2014.8620.
- [39] N. S. Hussain, Y. P. Reddy and S. Buddhudu, luminescence properties of Eu³⁺ doped ZnO-B₂O₃-SiO₂ glasses, *Spectrosc. Lett.* **35(2)** (2002) 275-283. <http://dx.doi.org/10.1081/SL-120003812>.

- [40] W. M. Jadwisienczak, H. J. Lozykowski, A. Xu, and B. Patel, Visible emission from ZnO doped with rare-earth ions, *J. Electron. Mater* **31** (2002) 776-784. doi: 10.1007/s11664-002-0235-z.
- [41] S. Cuffe, C. Labbé, B. Dierre, J. Cardin, L. Khomenkova, F. Fabbri, T. Sekiguchi and R. Rizk, Cathodoluminescence and photoluminescence comparative study of erbium-doped silicon-rich silicon oxide, *J Nanophotonics*. **5** (2011) 051504-051516. doi: 10.1117/1.3549701 · Source: OAI.
- [42] E. Hasabeldaim, O. M. Ntwaeaborwa, R. E. Kroon, and H. C. Swart, Surface analysis and cathodoluminescence degradation of undoped ZnO and ZnO:Zn phosphors, *J. Vac. Sci. Technol. B* **34** (2016) 041221. doi: 10.1116/1.4953561.
- [43] L. Ozawa, Cathodoluminescence and photoluminescence: theories and practical applications, Boca Raton, London and New York: CRC Press., 2007.
- [44] H. S. Yang, Y. Li, D. P. Norton, K. Ip, S. J. Pearton, Soohwan Jang and F. Ren, Low-resistance ohmic contacts to p - Zn Mg O grown by pulsed-laser deposition, *Appl. Phys. Lett.* **83** (2005) 192103. doi: 10.1063/1.1925309.
- [45] S. J. Ikhmayies, N. M. Abu El-Haija and R. N. Ahmad-Bitar, A comparison between different ohmic contacts for ZnO thin films, *J. Semicond* **36** (2015) 033005. doi: 10.1088/1674-4926/36/3/033005.
- [46] C. M. Polley, W. R. Clarke and M. Y. Simmons, Comparison of nickel silicide and aluminium ohmic contact metallizations for low-temperature quantum transport measurements, *Nanoscale Res. Lett.* **6** (2011) 538. doi:10.1186/1556-276x-6-538.
- [47] T. Schultz, S. Vogt, P. Schlupp, H. von Wenckstern, N. Koch and M. Grundmann, Influence of Oxygen Deficiency on the Rectifying Behavior of Transparent-Semiconducting-Oxide–Metal Interfaces, *Phys. Rev. Appl* **9** (2018) 064001. doi: 10.1103/PhysRevApplied.9.064001.

Chapter 7

Pulsed laser deposition of a ZnO:Eu³⁺ thin film: study of the luminescence and surface state under electron beam irradiation

7.1. Introduction

Zinc oxide doped with trivalent europium ions (ZnO:Eu³⁺) is a promising red emitting material with a wide range of uses in applications including light emitting diodes (LEDs), flat panel displays (FPDs) [1], etc. Over the past few years extensive research has been focused on studying the fundamental properties of ZnO:Eu³⁺ in order to improve its luminescence efficiency. Despite the difficulties of obtaining sufficient energy transfer from ZnO to Eu³⁺ ions, studies have shown that obtaining bright red luminescence from Eu³⁺ ions incorporated in a ZnO host is possible by utilizing different growth methods and techniques [2]. Suzuki et al. [3] achieved bright red luminescence from ZnO:Eu³⁺ films fabricated by a microemulsion method and deposited using a spin coating technique. Bright red emission was seen even with the naked eye when the films were irradiated with an UV lamp at a wavelength of 365 nm. Therefore, ZnO:Eu³⁺ has potential applications as a red phosphor in field emission displays (FEDs), plasma display panels (PDPs), cathode ray tubes (CRTs) and other optoelectronic devices. Chemical, surface and luminescence stabilities are critical issues for any applicable material in optoelectronics devices. Electron beam irradiation has been used for decades in many aspects of scientific research studies, including imaging in the case of TEM and SEM, fabrication of thin films and nanostructures, patterning, etc [4, 5]. High energy electron beam irradiation is a powerful tool to investigate the material stability and its applicability. Due to the electron-material interaction, surface/bulk damage, chemical decomposition [6], atomic displacement [7], mass loss, etc. might occur during electron beam irradiation [8, 9], and hence, the luminescence properties of the examined material may be deteriorated. Due to the harsh conditions that an electron beam induces in the material's bulk or on the local surface, the material that is stable under electron beam irradiation might be stable at other operational conditions such as photon excitation and electric field excitation (electroluminescence). Demand for flat panel displays with high contrast ratio, light weight, low power consumption, wide angle of view, and longer lifetime have created opportunities for the development of new technologies. FEDs have gained considerable attention because of their potential to provide the above-mentioned properties [10]. One demand is that the phosphor must be stable under electron bombardment to be used in these displays. Organic-based optoelectronic devices have

shown short lifetime and low efficiency compared to crystalline semiconductor light emitters and weak resistance against environmental degradation [11]. Sulphide-based luminescent materials have shown poor chemical stability and they tend to desorb from the surface, form a non-luminescent layer on the surface, especially under electron beam irradiation, or releasing volatile gases such as SO₂ and H₂S during operation which are detrimental to the electron emitter tips of FED devices. Swart et al. and Holloway et al. have investigated the stability of ZnS under electron beam irradiation and found that electron stimulated surface chemical reactions (ESSCRs) led to the formation of a non-luminescent ZnO layer which significantly reduced the luminescence efficiency of the ZnS [12-14]. Due to the above-mentioned drawbacks of organic and sulphide-based luminescent materials, a research for an alternative efficient and stable luminescent material that can counter and compensate for these problems has been a critical research concern. Oxide-based materials were thought to have superior properties to overcome these challenges of organic and sulphide based materials. Yousif et al. [15, 16] studied the luminescence and chemical stability of Y₃(Al,Ga)₅O₁₂:Tb phosphor (powder and thin films) under electron beam irradiation. They found that an interleaved oxide layer formed during electron bombardment contributed to the superior stability of this phosphor compared to the sulphide-based materials. Swart et al. [17] studied the degradation of Y₂SiO₅:Ce³⁺, Gd₂O₂S:Tb³⁺ and SrAl₂O₄:Eu³⁺, Dy³⁺ pulsed laser deposited (PLD) thin films under electron beam irradiation. They observed the initial degradation of the cathodoluminescence (CL) intensity due to the formation of different interleaved oxide layers and then stabilization of the CL intensity. Generally, Y₂SiO₅:Ce³⁺ and SrAl₂O₄:Eu³⁺, Dy³⁺ exhibited better stability than the Gd₂O₂S:Tb³⁺ phosphor thin films. Hasabeldaim et al. studied the stability of the green luminescence of ZnO powder [10], thin film [18] and nanorods [19] under electron irradiation. They found that ZnO possessed good chemical and luminescence stability under electron beam irradiation. However, morphology modification such as coalescence of the particles, growth and thinning of the nanorods were found after electron bombardment. Therefore, it is worthwhile to study the luminescence of the red emission and surface state of ZnO:Eu³⁺ thin film deposited by PLD.

7.2. Experimental procedures

Firstly, Eu (3 mol%) doped ZnO powder was prepared by the solution combustion method as reported in [20, 21]. The ZnO powder was then post annealed at 950 °C in air for 2 h to improve its physical and optical properties. About 12 g of the final product was compressed in a 1-inch disk at about 12 tons for 2 h using a hydraulic press. The cylindrical pellet was sintered at 950

°C for 8 h, 1100 °C for 6 h and 1200 °C for 6 h in air using a Carbolite furnace at 5 °C/min rate of heating and cooling. This produced a very compact and ceramic-like hard pellet which was used as the target for PLD for the preparation of the films. It was inserted in a PLD chamber and held in a target holder that rotated at 10 degree/second to avoid laser pinning effects. A piece of intrinsic-type Si (100) substrate was cleaned using an ultrasonic bath in isopropanol, acetone, ethanol and distilled water and finally dried with nitrogen gas. It was mounted on a substrate holder 7 cm from the target (pellet). The PLD chamber was pumped down to a vacuum base pressure of about 2.3×10^{-5} Torr and high purity oxygen gas was then introduced to the chamber to a pressure of about 0.1 Torr. The substrate temperature was raised up to 300 °C with a ramping rate of about 5 °C/min and a Nd:YAG laser with wavelength of 266 nm was utilized for the target ablation and subsequent film deposition. The laser energy and ablated spot diameter were maintained at 30 mJ/pulse and 1.5 mm while the deposition process was continued for 75 min at 10 pulses/s. The sample deposited at 0.01 Torr will be referred to as the sample deposited at high O₂ pressure. Another sample was deposited at low oxygen partial pressure of about 0.02 Torr, and it was only subjected to chemical and photoluminescence characterizations by using XPS and a 325 nm He-Cd laser, respectively. This was to investigate the effect of oxygen pressure on the sample stoichiometry.

X-ray diffraction (XRD) was used to examine the crystal structure, using a Bruker D8 Advance diffractometer with Cu K α radiation ($\lambda = 0.154184$ nm). A JEOL scanning electron microscope (SEM) model JSM-7800F with electron beam voltage maintained at 5 kV was utilized for the morphology measurements. A Shimadzu SPM-9600 atomic force microscope (AFM) with commercial software was used to scan the sample surface as well as calculating the root mean square (RMS) roughness. A PHI 5000 Versaprobe system was used for the X-ray photoelectron spectroscopy (XPS) measurements using an Al K α X-Ray beam (100 μ m, 25 W and 15 kV). For depth profile measurements, an Ar⁺ ion beam (2 kV and 2 μ A) was used to sputter the sample by rastering over an area of 1 mm x 1 mm at a sputtering rate of about 15 nm/min. Photoluminescence (PL) measurements were conducted using a 325 nm He-Cd laser as excitation source and the photomultiplier tube (PMT) detector for recording the PL emission spectra. In addition, a FLS980 system (Edinburgh Instruments) was utilized to excite the sample at different wavelengths using a xenon lamp and to monitor the emission. For acquisition of the CL spectra and degradation studies, a PHI model 545 system and a USB2000 Ocean Optics spectrometer were used. The CL was excited by the same electron beam normally used for Auger electron spectroscopy measurements. The emitted light from the excited phosphor passed through a quartz port at 90° to the incident electron beam. A focus lens

connected to a fibre optic was used to relay the CL light to the Ocean Optics spectrometer. The CL emission spectra was measured during prolonged electron irradiation. The maximum intensity of the CL emission was plotted as function of electron dose. The electron beam voltage, current, current density and beam spot size were maintained at about 2 keV, 24 μ A, 2.12 mA/cm² and 1.2 mm, respectively. The vacuum was maintained near 2.7 x 10⁻⁸ Torr for all the measurements. The sample deposited at high O₂ pressure was subjected to electron beam irradiation for about 24 h (170 C/cm²) while recording the CL intensity.

7.3. Result and discussions

7.3.1. Structure and morphology analysis

Fig. 7.1 shows the XRD pattern of the bare Si (100) substrate, bulk ZnO (ICSD#:067849) and ZnO:Eu³⁺ thin film. Only one reflection was detected at $2\theta = 34.35^\circ$ for the ZnO:Eu³⁺ thin film, which was indexed as the (002) plane of the wurtzite structure of ZnO. This indicated the preferred orientation along the *c*-axis that was perpendicular to the substrate surface. No peaks for incidental impurities or Eu₂O₃ were detected. Also no peaks associated with the Eu₂O₃ phase were detected for the bulk of the film, with XPS for the 3 mol% Eu sample, which also confirmed the successful incorporation of the Eu ions in the ZnO host [20]. This was also for the case of spin coating thin films [20]. In case of the spin coated films traces of Eu²⁺ on the surface was associated with adventitious EuF on the surface due to handling of samples [21]. Scherrer's equation [22] and Miller indices were used to compute the crystallite size and lattice parameters; the values are presented in Table 7.1. The lattice parameters (*c*) and interplanar spacing (*d*) are slightly greater than the lattice parameters for bulk ZnO (*c* = 0.5207 nm) and the interplanar spacing (*d* = 0.2604 nm) [23]. This is due to the incorporation/ substitution of Eu³⁺ ions with a bigger ionic radius (0.095 nm) to Zn²⁺ ions with a smaller ionic radius (0.074 nm) [24]. The biaxial strain model was used to estimate the thin film stress [25]:

$$\sigma = -4.5 \times 10^{11} \left(\frac{d - d_0}{d_0} \right) \quad (1)$$

where *d* represents the plane spacing of the ZnO:Eu³⁺ thin film calculated from the (002) plane of the XRD pattern, and *d*₀ is the lattice parameter of bulk ZnO (0.2604 nm). The film was found to have a compressive stress (Table 7.1). The silicon substrate XRD reflection peaks at 2θ angles ~ 48°, 54° and 56° are due to the allowed 400 reflections from weak L β ₁, L β ₂ and L γ ₁ X-rays resulting from W, which can contaminate the Cu target of older X-ray sources.

Table 7.1. Lattice parameters, crystallite size, the calculated stress in the thin film, as well as the R_q/R_a roughness for undegraded and degraded samples.

Sample	c (nm)	d (nm)	Crystallite size (nm)	Stress (GPa)	Roughness (R_q/R_a) (nm)
Undegraded	0.5217	0.2608	18 ± 1	0.3	1.33
Degraded	-	-	-	-	1.37

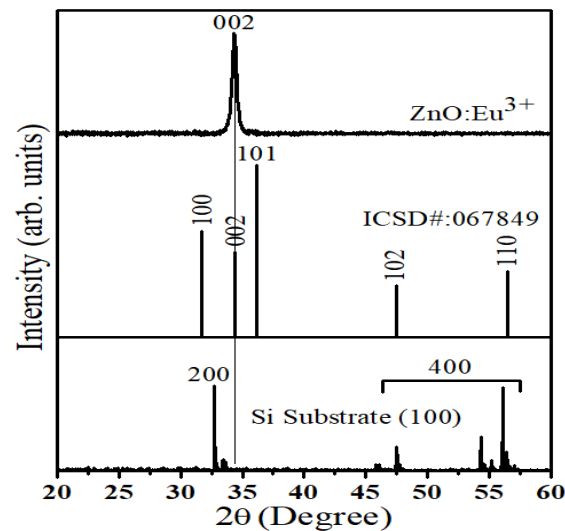


Fig. 7.1. XRD pattern of Si (100) substrate, bulk ZnO and the sample (ZnO:Eu^{3+} PLD thin film deposited at high O_2 pressure).

To examine the film's morphology, top-view and cross-sectional SEM images were captured at a high magnification and are displayed in Fig. 7.2. The film comprised of normally distributed small particles with an average size of about 47 nm, Fig. 7.2(a). The film thickness estimated from the cross-section was found to be ~ 115 nm. No cracks, voids, wrinkles or exfoliations were observed, which confirms that the film had good quality.

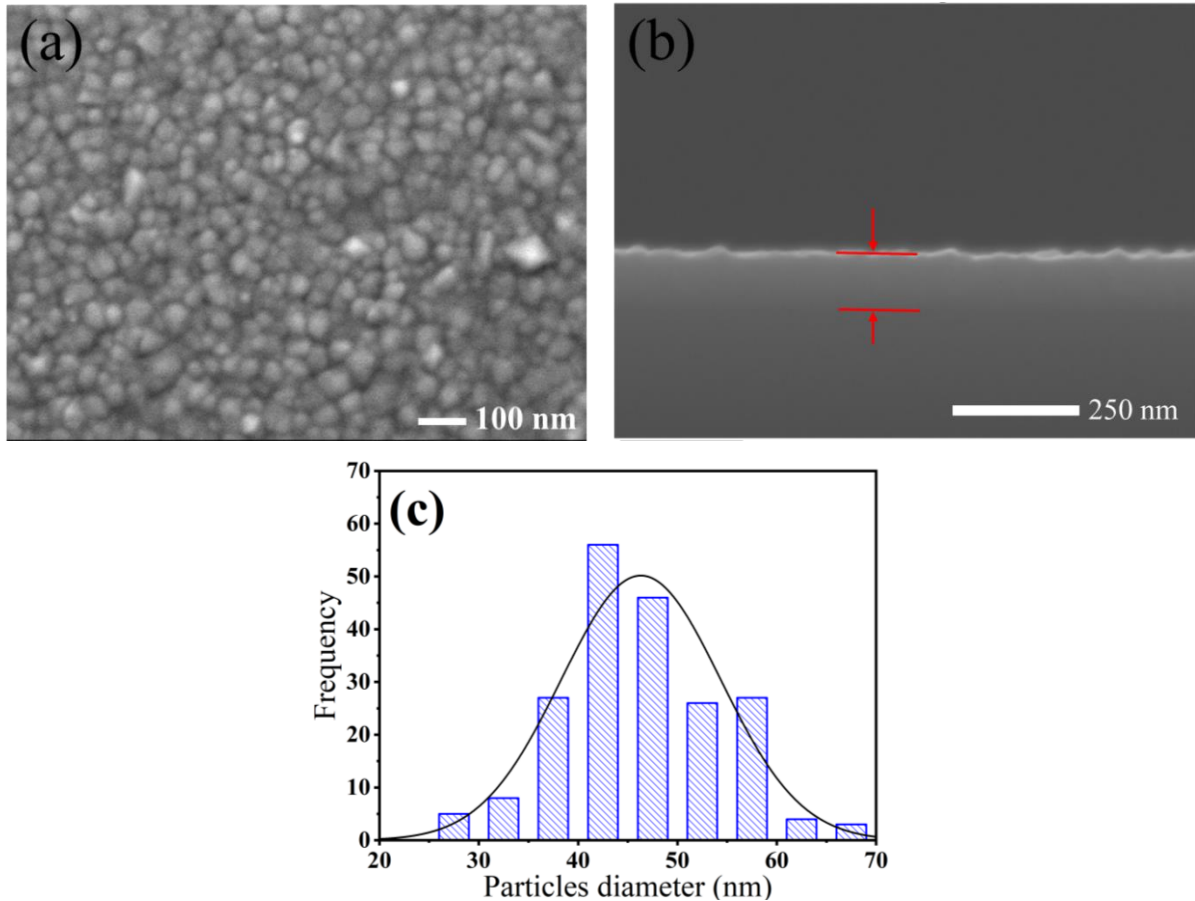


Fig. 7.2. (a) Top-view, (b) cross-sectional SEM images and (c) the histogram of the particle sizes distribution of the ZnO:Eu³⁺ PLD thin film deposited at high O₂ pressure.

Fig. 7.3(a) depicts the AFM micrographs (2D and 3D) of the film before and after the electron exposure (i.e. undegraded and degraded samples). The average particle size for the undegraded sample was estimated from the corresponding histogram and was found to be ~ 53 nm. The root mean square roughness (R_q) and the average roughness (R_a) for the undegraded sample were found to be 4.8 ± 0.2 nm and 3.6 ± 0.2 nm, respectively. The ratio R_q/R_a is indicative of the film's surface quality and high prospects of industrial applications. Statistical theory predicts that the R_q/R_a ratio should be 1.25 for useful surfaces, while experimental results give the value as 1.31 for most engineering surfaces [26]. The ratio for the undegraded sample was 1.33 which is close to the experimentally desired value. Electron beam irradiation is well-known to cause damage and modification on the specimen surface, so a good material is one that can maintain its properties and withstand such application treatments. Therefore, AFM was also performed for the degraded area and the images are shown in Fig. 7.3(b). Increases of the average particle size to about 63 nm and reduction in the average roughness to about 3.5 nm were observed after electron beam irradiation. The ratio R_q/R_a increased to $4.8/3.5 = 1.37$, which confirmed that the surface underwent a considerable modification due to the electron

beam irradiation. When energetic particles (in this case high energy electrons) impinge on a semiconductor surface, different and complicated phenomena takes place including generation of heat on the sample surface, sputtering, radiolysis, electrostatic charging, dehydration, knock-on (ballistic) displacement and hydrocarbon contamination [27]. Subsequently mass loss and creation of new defects could occur. Therefore the lattice/grain boundaries have to compensate by means of reconstruction/rearrangements of the atoms to minimize energy, hence the surface morphology and topography are altered. The electrostatic field of atomic nuclei cause the deflection of incident electrons, which promote knock-on (ballistic) damage. Energy transfer from the incident electrons to the specimen atoms play a critical role on the sputtering of atoms, atomic displacement and creation of defects in the crystal lattice. When the energy transfer magnitude is around several electron volts, it would be sufficient to sputter atoms from the specimen surface. If this energy transfer is in the order of magnitude of about tens of electron volts, atomic displacement and formation of defects in the crystal lattice can occur. The energy (E) transferred by an incident electron to an atomic nucleus (atomic mass number A) is given by [28].

$$E = E_{max} \sin^2 \left(\frac{\theta}{2} \right) \quad (2)$$

E_{max} is the maximum energy transfer to an atom and can be found from equation (3).

$$E_{max} = E_0 \frac{(1.02 + \frac{E_0}{10^6})}{465.7A} \quad (3)$$

E_0 represent the energy of the incident electron in eV, while θ is the angle of scattering. Clearly, E_{max} increases with the incident electron energy and is inversely proportional to the atomic mass number A . It is believed that radiolysis takes place in an oxide surface by means of the Knotek-Feibelman process [8]. The incident electron creates a neutral or positively charged oxygen atom due to the interatomic Auger relaxation from oxygen. The neutral or positively charged oxygen atom will be repelled by the surrounding metal ions and ejected into the vacuum level, leaving behind a vacancy and metal-rich surface with a pitted appearance [8]. In our previous reports, coalition and/or growth of particles was observed on undoped ZnO thin film after electron beam irradiation [18]. Growth and thinning of nanorods were also observed for our chemical bath deposited ZnO nanorods after prolonged electron beam irradiation and the morphology changes were attributed to migration and diffusion of the ZnO defects, formation of an interleaved non-luminescent ZnO layer and/or removal of the atomic hydrogen from the ZnO lattice [19]. In this case, different mechanisms may have contributed to the increase of the particles of the ZnO:Eu³⁺ PLD thin film. Defects may be created, migrate and

diffuse, as well as a non-luminescent interleaved layer might have formed and contributed to the particle growth.

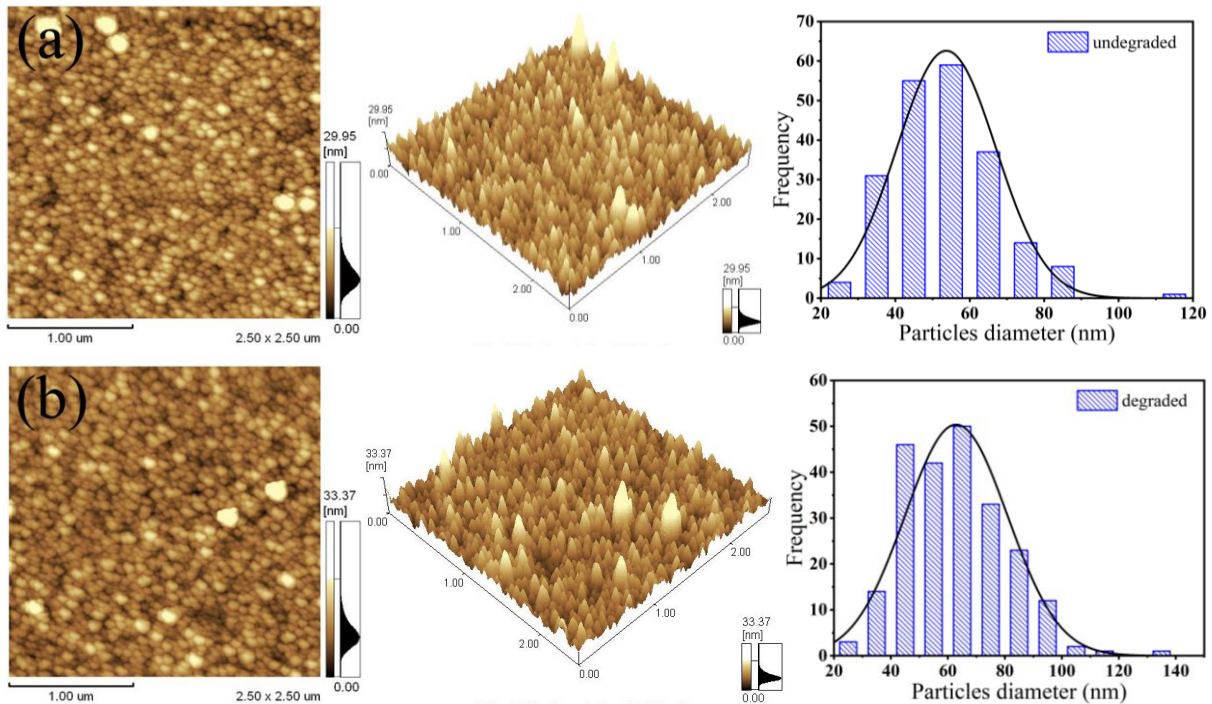


Fig. 7.3. 2D, 3D AFM images and the corresponding histograms of the particle size distribution of the ZnO:Eu³⁺ film deposited at high O₂ pressure (a) undegraded and (b) degraded areas of the film.

Fig. 7.4 shows the XPS high resolution spectra of the Zn 2p core level for the un-degraded and the degraded sample (before and after Ar⁺ ion sputtering). Zn 2p exhibited a doublet whose binding energies are at 1022.0 eV (2p_{3/2}) and 1045.0 eV (2p_{1/2}). The binding energy difference is 23 eV, which indicates the presence of Zn atoms in their Zn²⁺ oxidation state. No peaks associated with metallic Zn was observed [29].

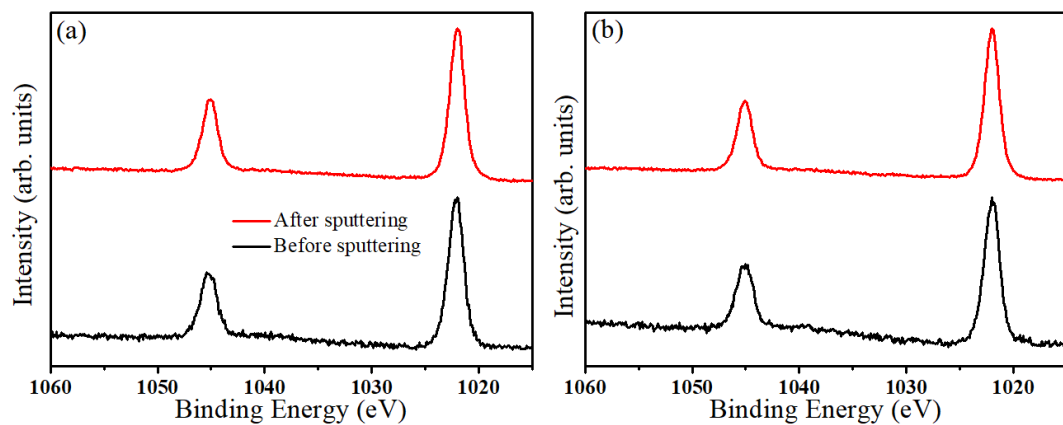


Fig. 7.4. High-resolution XPS spectra of Zn 2p core levels for (a) undegraded and (b) the degraded ZnO:Eu³⁺ PLD film (for the film obtained at high O₂ pressure).

Fig. 7.5 shows the XPS high resolution spectra of the Eu 3d levels for the un-degraded and the degraded samples. Four peaks at the energy region from 1115 eV to 1180 eV were detected. The dominant peaks at 1135.2 eV and 1165.0 eV with energy difference of 29.8 eV are due to the Eu 3d_{5/2} and 3d_{3/2}, respectively, and indicating the trivalent state of Eu³⁺ ions in the ZnO host [30]. The other two peaks at the lower binding energy side are attributed to the divalent oxidation state of Eu²⁺ ions. The Eu³⁺ peaks have increased after sputtering for both (un-degraded and the degraded) samples. This confirm that most of the Eu²⁺ ions were present on the surface along with the surface contamination. No considerable changes in the chemical states/composition of the film can be observed after electron beam irradiation (degradation).

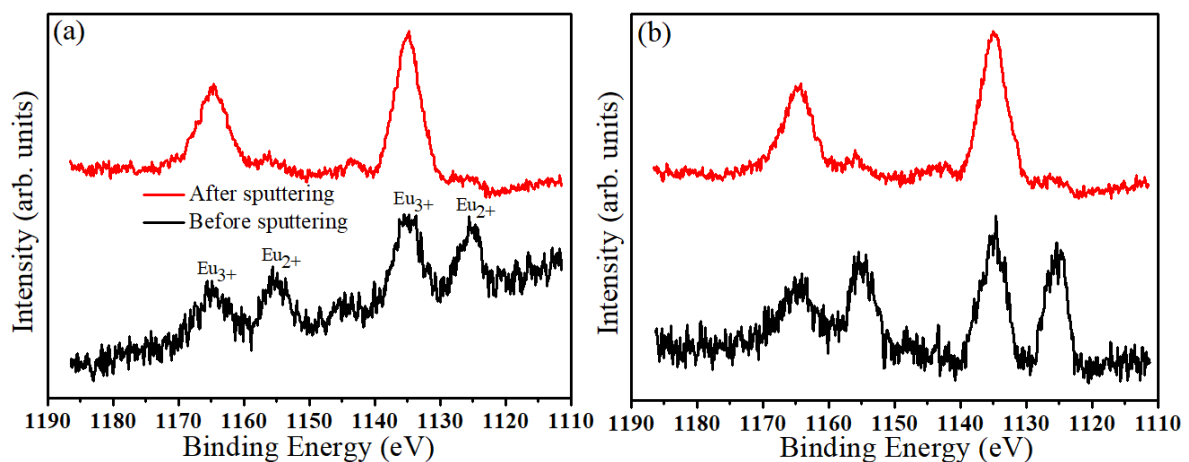


Fig. 7.5. (a and b) High-resolution XPS spectra of Eu 3d core levels for undegraded and the degraded ZnO:Eu³⁺ PLD film (for the film obtained at high O₂ pressure).

The XPS depth profile measurement of the ZnO:Eu³⁺ samples deposited at high and low O₂ pressure are shown in Fig. 7.6. In both the samples, the principal elements (Zn, O and the Eu dopant) were detected in addition to the C surface contamination, which was removed soon after the sputtering started. However, some C contaminant was also present at the Si/ZnO:Eu³⁺ interface layer. These may be due to handling/exposing of the Si substrate to air atmosphere before deposition and after cleaning. Any other traces of C, if any, in the layer itself might be due to the shadowing effect during Ar⁺ sputtering during depth profiling. The angle of the Ar⁺ sputtering ions and the direction of the XPS measurements is not the same and the measurements may contain small amounts of C that was not yet sputtered at that specific spot if rough surfaces are measured as in this case. The atomic concentration of Zn, O and Eu were about 32%, 63% and 2%, respectively, for the film deposited at high O₂ pressure. The atomic concentration of the principal elements for the film deposited at low O₂ pressure were about 54%, 41% and 3% for the Zn, O and Eu, respectively. It can be clearly seen that the film deposited at high O₂

pressure contained excess oxygen, while the film obtained at the low O_2 pressure lacks oxygen. The atomic concentration of the principal elements remained constant throughout the film depth during sputtering.

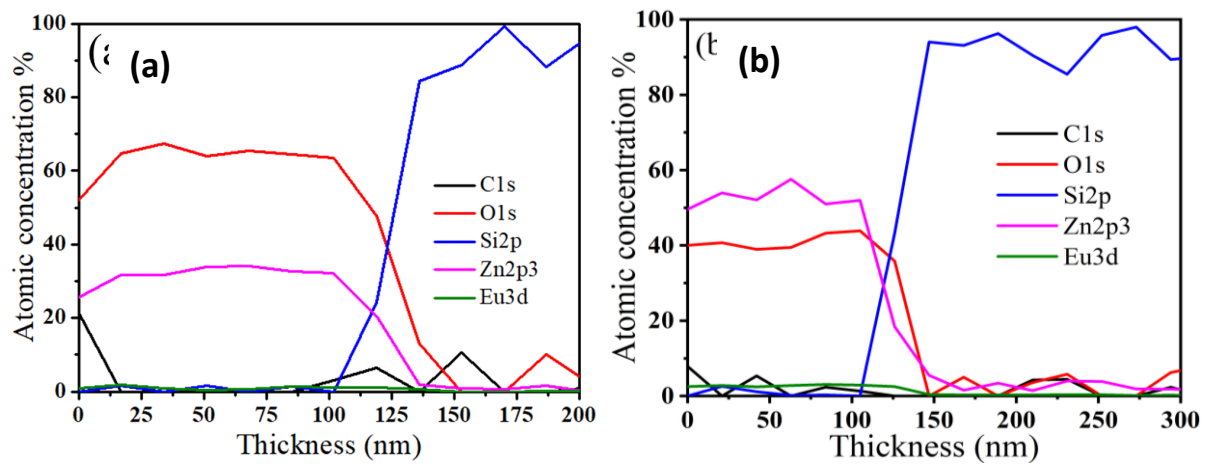


Fig. 7.6. XPS depth profiles for the $ZnO:Eu^{3+}$ PLD films (a) deposited at high O_2 pressure and (b) deposited at low O_2 pressure.

De-convoluted O 1s peaks for the $ZnO:Eu^{3+}$ PLD thin film obtained at low oxygen pressure (a) before and (b) after sputtering, high oxygen pressure (c) before and (d) after sputtering and the degraded spot (e) before and (f) after sputtering are shown in Fig. 7.7. The O 1s peak was de-convoluted by using the Gaussian-Lorentz function, and three components were found as marked as O1, O2 and O3. These components were always explained as follow: O1 is due to the O^{2-} ions in the Zn-O-Zn network of the wurtzite structure, O2 was ascribed to the O^{2-} in deficient regions such as oxygen related defects and hydroxile group, and O3 is due to the chemisorbed species and loosely species on the surface [31, 32]. No peaks associated with Eu_2O_3 phase were detected for the film bulk, which indicates a successful incorporation of the Eu ions in the ZnO host. The O2 and O3 components have decreased after the sputtering for both samples whereas O1 increased, which can be attributed to the removal of the surface contaminations. The decrease in O2 might be an indication of less defects in the bulk of the film with respect to the surface of the thin film. The O2 peak has increased for the film obtained in the high O_2 pressure, which indicated the formation of extra oxygen-related defects due to the increasing O_2 pressure. The O2 component has again slightly increased after electron beam irradiation (degradation). This imply that new defects were created during the electron beam irradiation. The details of the de-convoluted O 1s components are given in Table 7.2.

Table 7.2. Peak position and area of the O1s de-convoluted components of the ZnO:Eu³⁺ PLD thin films obtained at different O₂ pressure (un-degraded and the degraded area).

Sample	O 1s components	Peak position (eV)	Area% (before sputtering)	Area% (after sputtering)
Low O ₂ pressure	O1	530.62	68	85
	O2	531.88	22	10
	O3	532.61	10	5
High O ₂ pressure Un-degraded	O1	530.62	66	81
	O2	531.88	25	14
	O3	532.61	9	5
High O ₂ pressure Degraded	O1	530.62	63	80
	O2	531.88	27	15
	O3	532.61	10	5

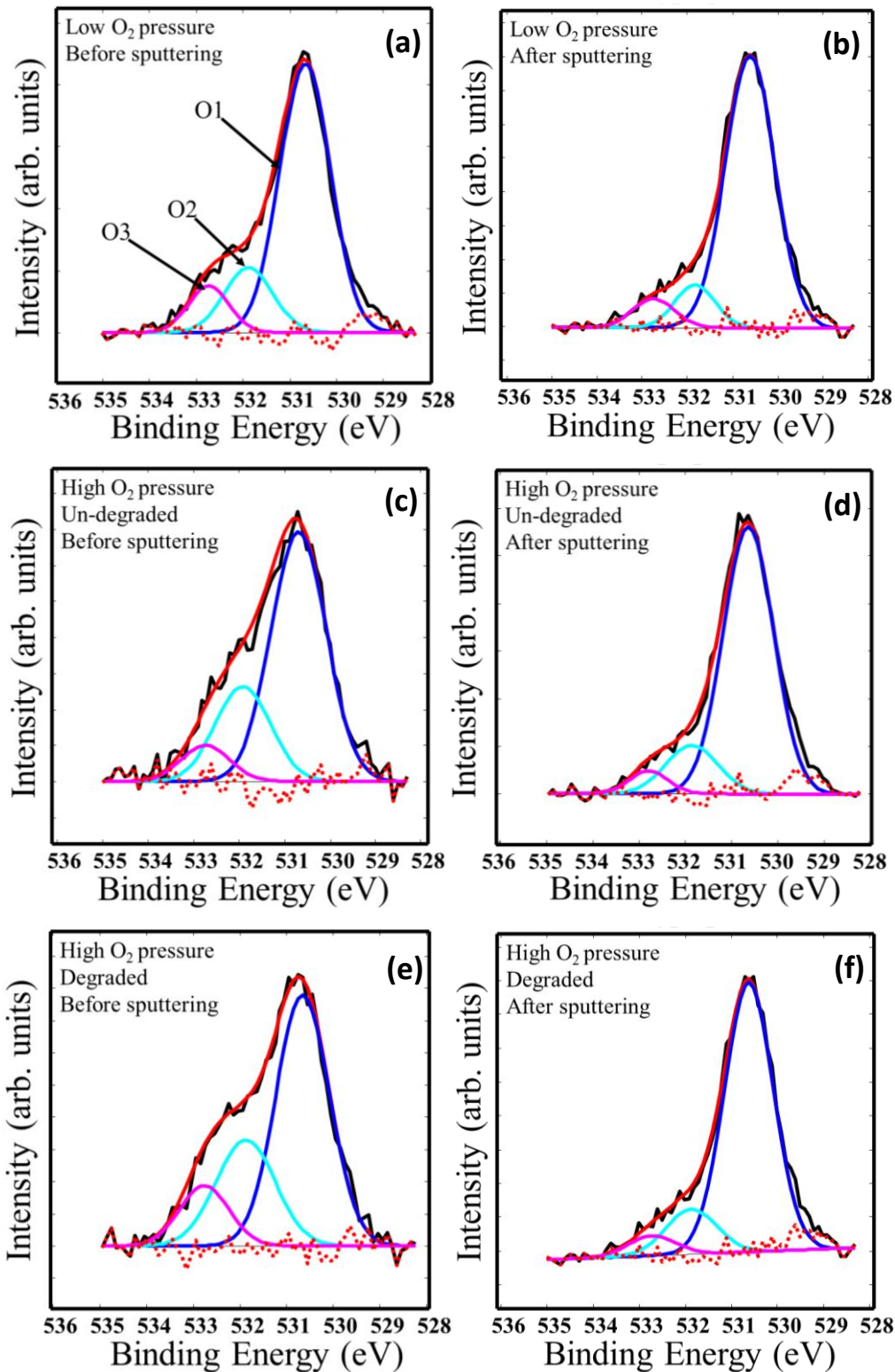


Fig. 7.7. De-convoluted O 1s peak for the ZnO:Eu³⁺ PLD thin film obtained at low oxygen pressure (a) before and (b) after sputtering, high oxygen pressure (c) before and (d) after sputtering and the degraded spot (e) before and (f) after sputtering as indicated.

7.3.2. Luminescence analysis

Fig. 7.8 demonstrates the room temperature PL of the ZnO:Eu³⁺ deposited in low and high O₂ pressure (a), as well as the CL spectra of the sample deposited in high O₂ pressure (b). The PL spectrum of the sample deposited at low O₂ pressure exhibited ultra violet (UV) emission at ~ 376 nm and broad visible emission centred at ~ 530 nm, the emission around 530 nm have frequently been attributed to the excess zinc related defects such as oxygen vacancies (V_O) of ZnO [33-35]. The PL spectrum for the sample obtained in high O₂ pressure reveals ultra-violet (UV) emission at 376 nm which is ascribed to the exciton recombination [36], broad visible deep level emissions (DLEs) centred at ~ 645 nm which originated from the oxygen-related defects such as oxygen interstitials (O_i) of ZnO [37] and the characteristic emission of Eu³⁺ ions due to the 4f – 4f intrashell transitions as indexed in the graph [38]. The simultaneous presence of UV, DLE and Eu³⁺ emissions for the sample obtained in high O₂ pressure could imply that either energy transfer from ZnO defect levels to Eu³⁺ levels took place and/or the excitation energy was shared between the defects and the Eu³⁺ ions. It was also previously found that a decrease in defects led to a decrease in Eu³⁺ emission due to the lack of energy transfer from the conduction band to the Eu³⁺ ions [39]. The CL spectrum for the sample deposited in high O₂ pressure showed only the unique characteristic emission of the Eu³⁺ ions at 536 nm, 565 nm, 592 nm, 617 nm, 657 nm and 701 nm. These peaks were indexed to the ⁵D₁ - ⁷F₀, ⁵D₀ - ⁷F_J (J = 0, 1, 2, 3 and 4) transitions, respectively [38]. No CL emission (neither ZnO native emission nor Eu³⁺ characteristic emission) was observed for the sample obtained in low O₂ pressure. Of interest, despite the fact that the excitation energy for both PL and CL was higher than the ZnO band gap, the 325 nm He-Cd laser excited free excitons, deep defect levels and the Eu³⁺ luminescence centres, whereas the CL (electrons) excited only the Eu³⁺ luminescence centres. This is mainly attributed to the differences in their excitation mechanisms such as CL electrons possessing a much higher energy (2 keV) than the PL photons. The photons penetrate the thin film deeper than the electrons [10]. The electrons may excited the film via the impact excitation/ionization mechanism similar to that of electroluminescence [40]. Tentatively, since the CL electrons have high enough energy to produce Auger electrons, the excited electrons of the luminescent centres in the crystal sites that should normally be involved in a radiative recombination with trapped holes and emit broad DLEs lights which might now be involved in the Auger de-excitation process.

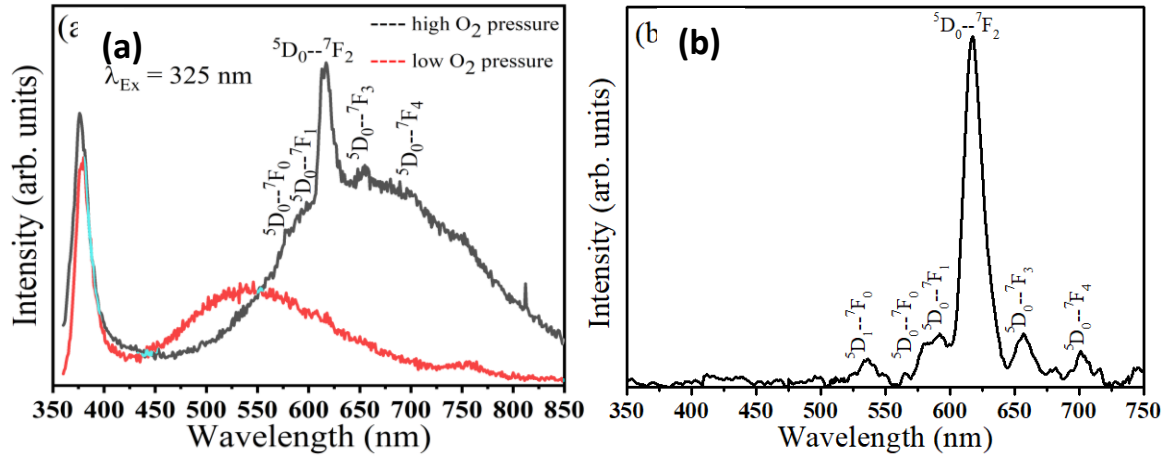


Fig. 7.8. (a) PL spectrum (excited at 325 nm using He-Cd laser) for the samples obtained at different O₂ pressures as indicated, and (b) CL spectrum (2 keV) of the ZnO:Eu³⁺ PLD thin film deposited at high O₂ pressure.

Fig. 7.9 depicts (a) the excitation spectrum recorded while monitoring the Eu³⁺ peak at 616 nm and (b) the PL spectra excited at 288 nm and 464 nm for the ZnO:Eu³⁺ PLD thin film. The excitation spectrum exhibited a clear absorption line at 464 nm indexed to the ⁷F₀ – ⁵D₂ 4f – 4f transition of Eu³⁺, while a weak excitation line near 394 nm indexed to the ⁷F₀ – ⁵L₆ transition is less clear. As the excitation wavelength decreased below around 375 nm there is the onset of host absorption of the ZnO, while at about 340 nm there is the additional onset of the charge transfer excitation band associated with Eu³⁺ ions. This strong broad peak centred at 288 nm is ascribed to electrons transferred from the oxygen 2p orbital to the empty 4f orbital of Eu³⁺ [41]. The PL spectra of the sample when excited at either 464 nm or 288 nm showed the characteristic emissions of the 4f – 4f transitions (labelled in the graph) of Eu³⁺ ions in ZnO [42]. The PL intensity was higher when the sample was excited at 288 nm compared to excitation at 464 nm, which indicate that the charge transfer excitation was more efficient than the direct excitation, as is generally the case. The weak excitation in the range 375 – 340 nm which occurs via the absorption of photons by the ZnO host suggests that there is not strong energy transfer from the host to the Eu³⁺ ions. No Eu²⁺ emission was observed. The rendering indices of the sample excited at different wavelengths, including the colour coordinates (x, y) and colour correlated temperature (CCT) are shown in Table 7.3, while the colour coordinates graph is shown in Fig. 7.10(b). Colour purity is defined as the degree to which a certain colour mixed with white or black colour. In our case, the colour purity of the red is the degree to which the red colour at ~ 616 nm mixed with other wavelengths of the electromagnetic spectrum. Therefore the equation [43]

$$\text{colour purity} = \frac{\sqrt{(x - x_i)^2 + (y - y_i)^2}}{\sqrt{(x_d - x_i)^2 + (y_d - y_i)^2}}$$

was used to estimate the colour purity of the sample excited with the xenon lamp as well as CL. In this equation (x, y) are the colour coordinates of the emission spectrum, (x_d, y_d) represent the colour coordinates of the dominant wavelength on the spectrum and (x_i, y_i) denote the colour coordinates for the illuminant point of the 1931 International Commission on Illumination (CIE) standard source. The sample emission lies within the red region with a considerable red colour purity.

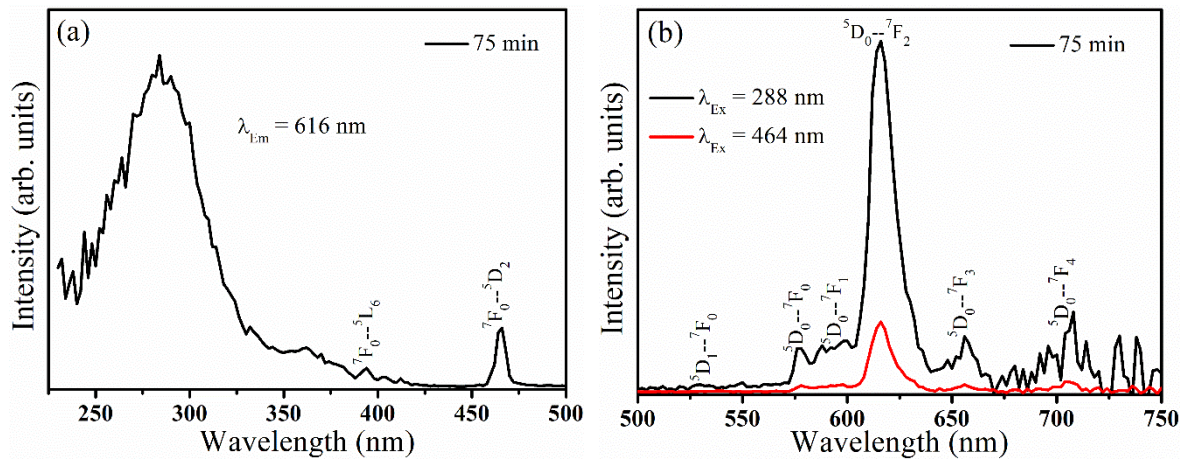


Fig. 7.9. Excitation spectrum (a) and PL spectra (b) of the ZnO:Eu³⁺ PLD thin film deposited at high O₂ pressure for a deposition time of 75 min.

Table 7.3. Rendering indexes (x, y) , CCT and colour purity of the film emission for different excitation sources (for the sample deposited at high O₂ pressure).

Excitation source	x	y	CCT (K)	Color purity (%)
Xenon lamp 288 nm	0.64	0.36	2228	90
Xenon lamp 464 nm	0.65	0.35	2561	92
CL before irradiation	0.58	0.36	1787	74
CL after irradiation	0.60	0.35	2012	79

Fig. 7.10(a) displays the CL intensity of the peak at 616 nm recorded while the sample was under continuous electron beam excitation (degradation). Also no Eu²⁺ emission was observed. The CL intensity initially increased slightly until $\sim 25 \text{ C/cm}^2$ and then stabilized afterwards. Atmospheric carbon is always present on a sample surface and it might suppress part of the CL emission. Atmospheric carbon is a very loosely bounded surface contamination that can be dissociated into volatile species by the electron beam irradiation due to the electron stimulated

surface chemical reaction (ESSCR) process [12]. Therefore, the initial increase in the CL intensity may be due to the removal of the surface contaminations (atmospheric carbon). Rougher surfaces possess a higher surface to volume ratio than the smoother surfaces, and the rougher sample usually emits with a higher intensity than the smoother surface. AFM analysis revealed that the sample became rougher after electron beam irradiation. Therefore, the increase in the sample roughness after irradiation may have also contributed to the initial CL intensity increase. CIE coordinates, CCT and colour purity of the CL spectra before and after degradation were calculated and are shown in Table 7.3. They slightly changed after degradation although they still appear within the red region. The colour purity of the sample was slightly improved after electron beam irradiation.

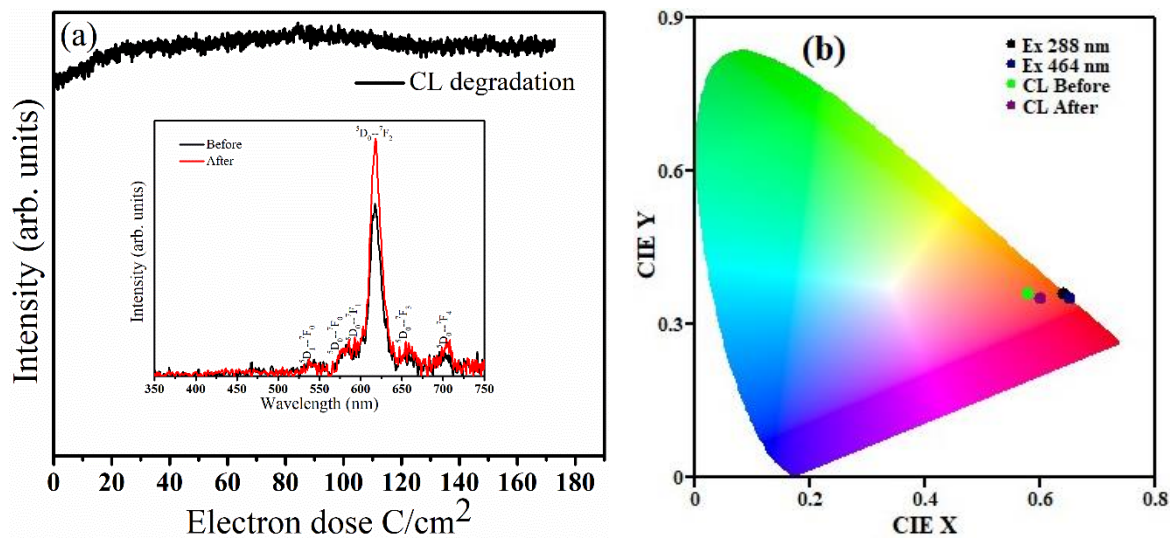


Fig. 7.10. (a) CL intensity degradation (the inset represents the CL spectra before and after degradation) and (b) CIE coordinates based on the excitation source and wavelength of the ZnO:Eu³⁺ PLD thin film deposited at high O₂ pressure.

7.4. Conclusion

ZnO:Eu³⁺ thin films with strong *c*-axis preferential orientation were prepared by the PLD technique. Successful incorporation of Eu ions into the ZnO host was confirmed by XRD and XPS analysis. Slight surface modification was observed as the result of electron beam irradiation (degradation). The sample emitted only 4f-4f characteristic emission of the Eu³⁺ ions when excited via the electron beam, although exciton and ZnO defect emissions were also observed for PL when the sample was excited by a He-Cd laser at 325 nm. The rendering index for CL emission was within the red area with reasonable red colour purity. The effect of electron beam irradiation on the CL spectra of the sample was also examined and slight changes in the CL spectra were seen after degradation. Despite some changes to the surface roughness

and the creation of new defects during electron beam irradiation, the luminescence of this sample was reasonably stable during the degradation study, which adds to the potential for ZnO:Eu³⁺ thin films to be used as an emissive red layer in optoelectronic applications.

7.5. References

- [1] L. Luo, F. Y. Huang, G. J. Guo, P. A. Tanner, J. Chen, Y. T. Tao, Jun Zhou, L. Y. Yuan, S. Y. Chen, Y. L. Chueh, H. H. Fan, K. F. Li, K. W. Cheah, Efficient Doping and Energy Transfer from ZnO to Eu³⁺ Ions in Eu³⁺-Doped ZnO Nanocrystals, *J. Nanosci. Nanotechnol.* **12** (2012) 2417–2423. doi:10.1166/jnn.2012.5779.
- [2] Y. Liu, W. Luo, R. Li, G. Liu, M. R. Antonio, X. Chen, Optical Spectroscopy of Eu³⁺ Doped ZnO Nanocrystals, *J. Phys. Chem. C* **112** (2008) 686-694. DOI: 10.1021/jp077001z.
- [3] K. Suzuki, K. Murayama, N. Tanaka, Enhanced luminescence in Eu-doped ZnO nanocrystalline films, *Appl. Phys. Lett.* **107** (2015) 031902. doi: 10.1063/1.4926986.
- [4] J. Andrés, E. Longo, A. F. Gouveia, J. P. C. Costa, L. Gracia, M. C. Oliveira¹, In situ Formation of Metal Nanoparticles through Electron Beam Irradiation: Modeling Real Materials from First-Principles Calculations, *J Material Sci Eng*, **7 (3)** (2018) 461. doi: 10.4172/2169-0022.1000461.
- [5] U. Henniges, M. Hasani, A. Potthast, G. Westman, T. Rosenau, Electron Beam Irradiation of Cellulosic Materials—Opportunities and Limitations, *Materials* **6** (2013) 1584-1598, doi:10.3390/ma6051584.
- [6] Y. Yang, L. Chen, D.-Y. Li, R.-B. Yi, J.-W. Mo, M.-H. Wu, G. Xu, Controllable reduction of graphene oxide by electron-beam irradiation, *RSC Adv.* **9** (2019) 3597, doi: 10.1039/c8ra06797j.
- [7] N. Jiang, Electron beam damage in oxides: a review, *Rep. Prog. Phys.* **79(1)** (2016) 016501. doi:10.1088/0034-4885/79/1/016501.
- [8] M. R. McCartney, D. J. Smith, Studies of electron irradiation and annealing effects on TiO₂ surfaces in ultrahigh vacuum using high resolution-electron microscopy, *Surf. Sci.* **250** (1991) 169-178. [https://doi.org/10.1016/0039-6028\(91\)90719-9](https://doi.org/10.1016/0039-6028(91)90719-9).
- [9] C. Xiao, Z. Li, H. Guthrey, J. Moseley, Y. Yang, S. Wozny, H. Moutinho, B. To, J. J. Berry, B. P. Gorman, Y. Yan, K. Zhu, M. M. Al-Jassim, Mechanisms of Electron-Beam-Induced Damage in Perovskite Thin Films Revealed by Cathodoluminescence

Spectroscopy, *J. Phys. Chem. C* **119(48)** (2015) 26904-26911.
doi:10.1021/acs.jpcc.5b09698.

- [10] E. Hasabeldaim, O. M. Ntwaeaborwa, R. E. Kroon, H. C. Swart, Surface analysis and cathodoluminescence degradation of undoped ZnO and ZnO:Zn phosphors, *J. Vac. Sci. Technol. B.* **34** (2016) 041221-8. doi.org/10.1116/1.4953561.
- [11] R. S. Cok , M. Meitl, R. Rotzoll, G. Melnik , A. Fecioru, A. J. Trindade, B. Raymond, S. Bonafede, D. Gomez, T. Moore, C. Prevatte, E. Radauscher, S. Goodwin, P. Hines, C. A. Bower, Inorganic light-emitting diode displays using micro-transfer printing, *J. Soc. Inf. Disp.* **25** (2017) 589-609. doi # 10.1002/jsid.610.
- [12] H. C. Swart, K. T. Hillie, Degradation of ZnS FED phosphors, *Surf. Interface Anal.* **30** (2000) 383–386, doi:10.1002/1096-9918(200008)30:1<383::aid-sia779>3.0.co;2-v.
- [13] P. H. Holloway, T. A. Trottier, J. Sebastian, S. Jones, X. M. Zhang, J. S. Bang, B. Abrams, W. J. Thomes, T. J. Kim, Degradation of field emission display phosphors, *J. Appl. Phys.* **88** (2000) 483, doi: 10.1063/1.373683.
- [14] H. C. Swart, A review on ZnS phosphor degradation, *phys. stat. sol. (c)* **9** (2004) 2354 – 2359, doi 10.1002/pssc.200404814.
- [15] A. Yousif, H. C. Swart, O. M. Ntwaeaborwa, Surface state of $Y_3(Al,Ga)_5O_{12}:Tb$ phosphor under electron beam bombardment, *Appl. Surf. Sci.* **258** (2012) 6495–6503, doi:10.1016/j.apsusc.2012.03.066.
- [16] A. Yousif, H. C. Swart, O. M. Ntwaeaborwa, Improved luminescence properties of pulsed laser deposited $Y_3(Al,Ga)_5O_{12}:Tb$ thin films by post deposition annealing, *J. Lumin* **143** (2013) 201–206, https://doi.org/10.1016/j.jlumin.2013.04.042.
- [17] H. C. Swart, E. Coetsee, J. J. Terblans, O. M. Ntwaeaborwa, P. D. Nsimama, F. B. Dejene, J. J. Dolo, Cathodoluminescence degradation of PLD thin films, *Appl. Phys A* **101** (2010) 633–638, DOI 10.1007/s00339-010-5915-6.
- [18] E. Hasabeldaim, O. M. Ntwaeaborwa, R. E. Kroon, V. Craciun, E. Coetsee, H. C. Swart, Surface characterization and cathodoluminescence degradation of ZnO thin films, *Appl. Surf. Sci.* **424** (2017) 412–420, http://dx.doi.org/10.1016/j.apsusc.2016.11.178.
- [19] E. H. H. Hasabeldaim, O. M. Ntwaeaborwa, R. E. Kroon, E. Coetsee, H. C. Swart, Cathodoluminescence degradation study of the green luminescence of ZnO nanorods, *Appl. Surf. Sci.* **484** (2010) 105-111. https://doi.org/10.1016/j.apsusc.2019.04.113.

- [20] V. Kumar, V. Kumar, S. Som, M. M. Duvenhage, O. M. Ntwaeaborwa, H. C. Swart, Effect of Eudoping on the photoluminescence properties of ZnO nanophosphors for red emission applications, *Appl. Surf. Sci.* **308** (2014) 419–430, <http://dx.doi.org/10.1016/j.apsusc.2014.04.192>.
- [21] E. H. H. Hasabeldaim, O. M. Ntwaeaborwa, R. E. Kroon, E. Coetsee, H. C. Swart, Photoluminescence and cathodoluminescence of spin coated ZnO films doped with up to 4 mol% Eu³⁺, *Vacuum* **169** (2019) 10888921 (13 pages), doi.org/10.1016/j.vacuum.2019.10888921.
- [22] R. E. Kroon, Nanoscience and the Scherrer equation versus the ‘Scherrer–Gottingen equation’, *S. Afr. J. Sci.* **109** (2013) 1-2, <http://dx.doi.org/10.1590/sajs.2013/a0019>.
- [23] H. Meskine, P. A. Mulheran, Simulation of reconstructions of the polar ZnO(0001) surfaces, *Phys. Rev. B* **84** (2011) 165430, [doi:10.1103/physrevb.84.165430](https://doi.org/10.1103/physrevb.84.165430).
- [24] O. M. Ntwaeaborwa, S. J. Mofokeng, V. Kumar, R. E. Kroon, Structural, optical and photoluminescence properties of Eu³⁺ doped ZnO nanoparticles, *Spectrochim. Acta A* **182** (2017) 42–49, <http://dx.doi.org/10.1016/j.saa.2017.03.067>.
- [25] G. Anil Kumar, M. V. Ramana Reddy, K. N. Reddy, Structural and Optical properties of ZnO thin films grown on various substrates by RF magnetron sputtering, *IOP Conf. Ser.: Mater. Sci. Eng.* **73** (2015) 012133. [doi:10.1088/1757-899X/73/1/012133](https://doi.org/10.1088/1757-899X/73/1/012133).
- [26] D. Raoufi, L. Eftekhari, Crystallography and morphology dependence of In₂O₃:Sn thin films on deposition rate, *Surf. Coat. Technol.* **274** (2015) 44–50, <https://doi.org/10.1016/j.surfcoat.2015.04.034>.
- [27] Y. Ding, K. C. Pradel, Z. L. Wang, In situ transmission electron microscopy observation of ZnO polar and non-polar surfaces structure evolution under electron beam irradiation, *J. Appl. Phys.* **119** (2016) 015305, <http://dx.doi.org/10.1063/1.4939618>.
- [28] R.F. Egerton, P. Li, M. Malac, Radiation damage in the TEM and SEM, *Micron* **35** (2004) 399–409, [doi: 10.1016/j.micron.2004.02.003](https://doi.org/10.1016/j.micron.2004.02.003).
- [29] J. F. Moulder, W. F. Strickle, P. E. Sobol, K. D. Bomben, Handbook of X-Ray spectroscopy, ULVAC-PHI, Inc, Chigasaki, 1995.
- [30] E. J. Cho, S.-J. Oh, S. Imada, S. Suga, T. Suzuki, T. Kasuya, Origin of the high-binding-energy structure in the 3d core-level spectra of divalent Eu compounds, *Phys. Rev. B* **51** (1995) 10146.

- [31] V. Kumar, H. C. Swart, O. M. Ntwaeaborwa, R. E. Kroon, J. J. Terblans, S. K. K. Shaat, A. Yousif, M. M. Duvenhage, Origin of the red emission in zinc oxide nanophosphors, *Mater. Lett.* **101** (2013) 57.
- [32] L. Armelao, G. Bottaro, M. Pascolini, M. Sessolo, E. Tondello, M. Bettinelli, A. Speghini, Structure-Luminescence Correlations in Europium-Doped Sol-Gel ZnO Nanopowders, *J. Phys. Chem. C* **112** (2008) 4049-4054.
- [33] F. H. Leiter, H. R. Alves, A. Hofstaetter, D. M. Hofmann, B. K. Meyer, The Oxygen Vacancy as the Origin of a Green Emission in Undoped ZnO, *phys. stat. sol. (B)* **226** (1) (2001) R4–R5, doi:10.1002/1521-3951(200107)226:13.0.co;2-f.
- [34] J. Cizek, J. Valenta, P. Hruska, O. Melikhova, I. Prochazka, M. Novotny, J. Bulır, Origin of green luminescence in hydrothermally grown ZnO single crystals, *Appl. Phys. Lett.* **106** (2015) 251902, <http://dx.doi.org/10.1063/1.4922944>.
- [35] E. H. H. Hasabeldaim, O. M. Ntwaeaborwa, R. E. Kroon, E. Coetsee, H. C. Swart, Enhanced green luminescence from ZnO nanorods, *J. Vac. Sci. Technol B* **37** (2019) 011201, <https://doi.org/10.1116/1.5052543>.
- [36] R. Amari, A. Mahroug, A. Boukhari, B. Deghfel, N. Selmi, Structural, Optical and Luminescence Properties of ZnO thin films prepared by Sol-Gel spin coating method: Effect of precursor concentration, *Chin. Phys. Lett.* **35** (2018) 016801, doi: 10.1088/0256-307X/35/1/016801.
- [37] P. A. Rodnyi, I. V. Khodyuk, Optical and Luminescence Properties of Zinc Oxide (review), *Opt. Spectrosc.* **111** (2011) 776–785, <https://doi.org/10.1134/S0030400X11>.
- [38] M. Zhong, G. Shan, Y. Li, G. Wang, Y. Liu, Synthesis and luminescence properties of Eu³⁺-doped ZnO nanocrystals by a hydrothermal process, *Mater. Chem. Phys.* **106** (2007) 305–309, doi:10.1016/j.matchemphys.2007.06.007.
- [39] V. Kumar, O. M. Ntwaeaborwa, H. C. Swart, Effect of oxygen partial pressure during pulsed laser deposition on the emission of Eu doped ZnO thin films, *Physica B* **576** (2020) 411713, doi:10.1016/j.physb.2019.411713.
- [40] S. Iwan, J. L. Zhao, S.T. Tan, S. Bambang, M. Hikam, H. M. Fan, X. W. Sun, Ion-dependent electroluminescence from trivalent rare-earthdopedn-ZnO/p-Si heterostructured light-emitting diodes, *Mat. Sci. Semicon. Proc.* **30** (2015) 263-266. <https://doi.org/10.1016/j.mssp.2014.09.048>.

- [41] E. Öztürk, E. Karacaoglu, The effect of ligand-to-Eu³⁺ charge-transfer transitions (LMCT) on the photoluminescence intensity of M₂SiO₄: Eu³⁺ (M = Ca, Zn) type phosphors, *Mat. Sci.-Poland* **36** (2018) 509-513, doi: 10.2478/msp-2018-0059.
- [42] X. Zeng, J. Yuan, L. Zhang, Synthesis and Photoluminescent Properties of Rare Earth Doped ZnO Hierarchical Microspheres, *J. Phys. Chem. C* **112** (2008) 3503-3508, doi: 10.1021/jp0768118.
- [43] X. Wang, Z. Zhao, Q. Wu, C. Wang, Q. Wang, L. Yanyan, Y. Wang, Structure, photoluminescence and abnormal thermal quenching behavior of Eu²⁺-doped Na₃Sc₂(PO₄)₃: a novel blue-emitting phosphor for n-UV LEDs, *J. Mater. Chem. C* **4** (2016) 8795, doi: 10.1039/c6tc01049k.

Chapter 8

Enhanced green luminescence from ZnO nanorods

8.1. Introduction

ZnO is a very attractive luminescent semiconductor material mainly due to its excellent properties which include a direct wide bandgap (3.37 eV) [1], large exciton binding energy (60 meV) [2], high electron mobility [3], high electron affinity (~ 4.7 eV) [4], high ionization potential (~ 7.82 eV) [5] and thermal and chemical stability [6]. These properties made ZnO a suitable material for use in different applications, in particular, optoelectronic devices such as transparent conductive electrodes (TCO) [5], emissive layers in light emitting diodes (LEDs) for ultraviolet (UV) emission [7], emissive phosphor layers in field emission display's (FEDs) [8], a window layer in heterojunction solar cells [9], etc. In addition, ZnO is a plentifully abundant chemical compound and can be prepared cost-effectively and easily [10]. Due to the relative open ZnO crystal structure, it offers plenty of sites to accumulate intrinsic defects and extrinsic dopants, as well as to store hydrogen. The native point defects in ZnO play an important role in its electrical and optical properties [11]. Theoretical studies suggested that oxygen vacancies (V_o) have a very low formation enthalpy and therefore they are easy to form in the ZnO crystal [12]. Hence, V_o are the most probable defects to contribute to the natural n-type [13] ZnO as well as the intense green emission around 500 nm that has always been observed in ZnO [14]. Hydrogen is an amphoteric impurity present in all kinds of metallic oxide materials and exhibits a distinctive behavior in ZnO [15].

Recent advances in ZnO nanostructures revealed that ZnO nanorods, nanotubes [6], nanocombs [16], nanowalls [17], nanosheets [18], nanoflowers [19] and nanobelts [16] have potential desirable properties in the field of optoelectronics. Due to their high surface-to-volume ratio, high crystalline quality, and quantum confinement effects [20], ZnO nanostructures can provide enhanced optical properties for different applications. Among these nanostructures, ZnO nanorods are considered as the best system to develop new devices with excellent performance [21]. Moreover, they can be grown on numerous substrates including polymers and they exhibit a low density of defects [22]. Furthermore, they can be interfaced between electrodes and act as a charge carrier pathway for sensors and dye sensitized solar cell applications [23].

Different techniques and methods have been utilized to produce ZnO nanorods and these include pulsed laser deposition [24], atomic layer deposition [25], chemical vapor deposition [26], vapor-liquid-solid growth [27] and the chemical bath technique (CBD). The CBD has

advantages such as low cost of production, ease of growth, controllability and the deposition of uniform well-aligned ZnO nanorods over large areas [28].

In this work, vertically-aligned ZnO nanorods were grown on p-type Si (100) substrates and then annealed in a reducing atmosphere for different times. Their structure, morphology and photoluminescence (PL) properties were studied in order to improve their crystallinity and morphology as well as to obtain tunable and enhanced PL.

8.2. Experimental

Vertically-aligned ZnO nanorods were grown on intrinsic (100) $\pm 0.5^\circ$ -oriented Si substrates. The 100 mm diameter substrates, with a thickness of $525 \pm 25 \mu\text{m}$ and resistivity of $> 2 \Omega \text{ m}$, were from Siltronic, Switzerland. The substrates were cut into smaller pieces of about 2 cm^2 and then sequentially cleaned using isopropanol, acetone, ethanol and distilled water in an ultrasonic bath. The sonication time was 5 min for each cleaning cycle. For the growth of the vertically-aligned ZnO nanorods, a thin seed layer of ZnO was required.

8.2.1. Deposition of ZnO seed layer

An equimolar ratio of zinc acetate dihydrate $[\text{Zn}(\text{CH}_3\text{COO})_2 \cdot 2\text{H}_2\text{O}]$ and monoethanolamine (MEA) ($\text{C}_2\text{H}_7\text{NO}$) was dissolved in 40 mL of high purity ethanol (99.99%) with a concentration of 0.2 mol. 1.7561 g of zinc acetate was dissolved in ethanol and kept under stirring, and the MEA was added drop wise in the zinc acetate solution. The mixture was stirred using a magnetic stirrer for 30 min until a homogeneous and transparent solution was obtained. The solution was aged for 24 h to form a colloidal gel. The gel was spin coated on the cleaned Si substrates at 3000 RPM for 30 s and then heated at 250°C for 10 min in air. The process from spin coating to the heating was repeated five times to obtain the desired thickness that varied between 70 and 80 nm. Finally, the thin layer-seeded substrates were annealed in air at 500°C for 1 h to improve the crystallinity and particle homogeneity.

8.2.2. Growth of the ZnO nanorods

An equimolar ratio of zinc nitrate hexahydrate $[\text{Zn}(\text{NO}_3)_2 \cdot 6\text{H}_2\text{O}]$ and hexamethylenetetramine (HMT) $[(\text{CH}_2)_6\text{N}_4]$ was separately mixed in 100 mL of distilled water with a concentration of 0.05 mol for each. The solutions were stirred for about 30 min at room temperature. The HMT solution was added to the zinc nitrate solution while the later was magnetically stirred, and the stirring continued for another 30 min. The beaker containing the final solution was immersed into a chemical bath at a temperature that was maintained at 90°C . The seeded substrate was then dipped into the zinc nitrate-HMT solution with the growth side facing downwards towards the bottom of the beaker, and the growth was continued for 4

h at the temperature of 90 °C. The substrate was removed and cleaned with distilled water to remove all the unwanted residuals and precipitates, and it was finally dried by carefully blowing with nitrogen on the surface. Finally, the samples were annealed in a reducing atmosphere (H₂:Ar with a ratio of 5:95) at 700 °C for 20, 30 and 50 min. The samples were ready for characterization. All chemical reagents used in this experiment were purchased from Sigma Aldrich and used without any further purification.

8.2.3. Characterization

For the structural analysis, a Bruker D8 Advance X-ray diffractometer (XRD) equipped with Cu K α X-ray generator providing an X-ray beam with a wavelength of 1.5406 Å was used. The Cu K α filament voltage and current were 40 kV and 40 mA, respectively. Atomic Force Microscopy (AFM) was used to obtain micrographs of the surface using the Shimadzu SPM – 9600 model. A JEOL secondary electron microscope (SEM) model JSM-7800F was utilized to examine the particle morphology. The electron beam voltage and the magnification order were maintained at 5 kV and X10 for all the samples, respectively. X-ray photoelectron spectroscopy (XPS) analysis was performed using a PHI 5000 scanning ESCA microprobe before and after 1 min of Ar⁺ ion beam sputtering (1 x 1 mm raster with a 7 nm/min sputter rate). A 100 μ m diameter monochromatic Al K α X-ray beam ($h\nu = 1486.6$ eV) generated by a 25 W, 15 kV electron beam was used to analyze the different binding energy peaks. If the pass energy was set to 11 eV, it gives an analyzer resolution of ≤ 0.5 eV. MULTIPACK version 9 software was utilized to analyze the spectra to identify the chemical compounds and their electronic states using Gaussian-Lorentz fits. A low energy Ar⁺ ion gun and low energy neutralizer electron gun were used to minimize charging on the surface. High resolution spectra of C1s, O1s and Zn2p was done using a hemispherical analyzer with the pass energy maintained at 11.8 eV for 10 cycles using 0.5 eV/step; the chamber pressure was maintained at 2.8×10^{-9} Torr during the acquisitions. Any charge correction was done by correcting the C-C bond at a binding energy of 284.6 eV. The PL data were recorded using a Cary Eclipse fluorescence spectrophotometer with a xenon lamp as the excitation source. The samples were excited at a wavelength of 325 nm. For the quantum efficiency and the decay measurements, an FLS980 spectrometer from Edinburgh Instruments was used. An integrating sphere was used for the quantum efficiency determination.

8.3. Results and discussion

8.3.1. Structure and morphology

The AFM images of (a) the Si(100) substrate, (b) the ZnO seed layer and (c) the ZnO nanorods before annealing are shown in Fig. 8.1. Figures 8.1 (a) – (c) show, respectively, the smooth Si

layer, the uniform ZnO seed layer, and the uniform ZnO nanorods. Figure 8.1(c) confirms that the ZnO nanorods have successfully grown uniformly on the seed layer. The average size of the seeds was 57 nm and of the as-grown nanorods 65 nm as determined from the AFM images.

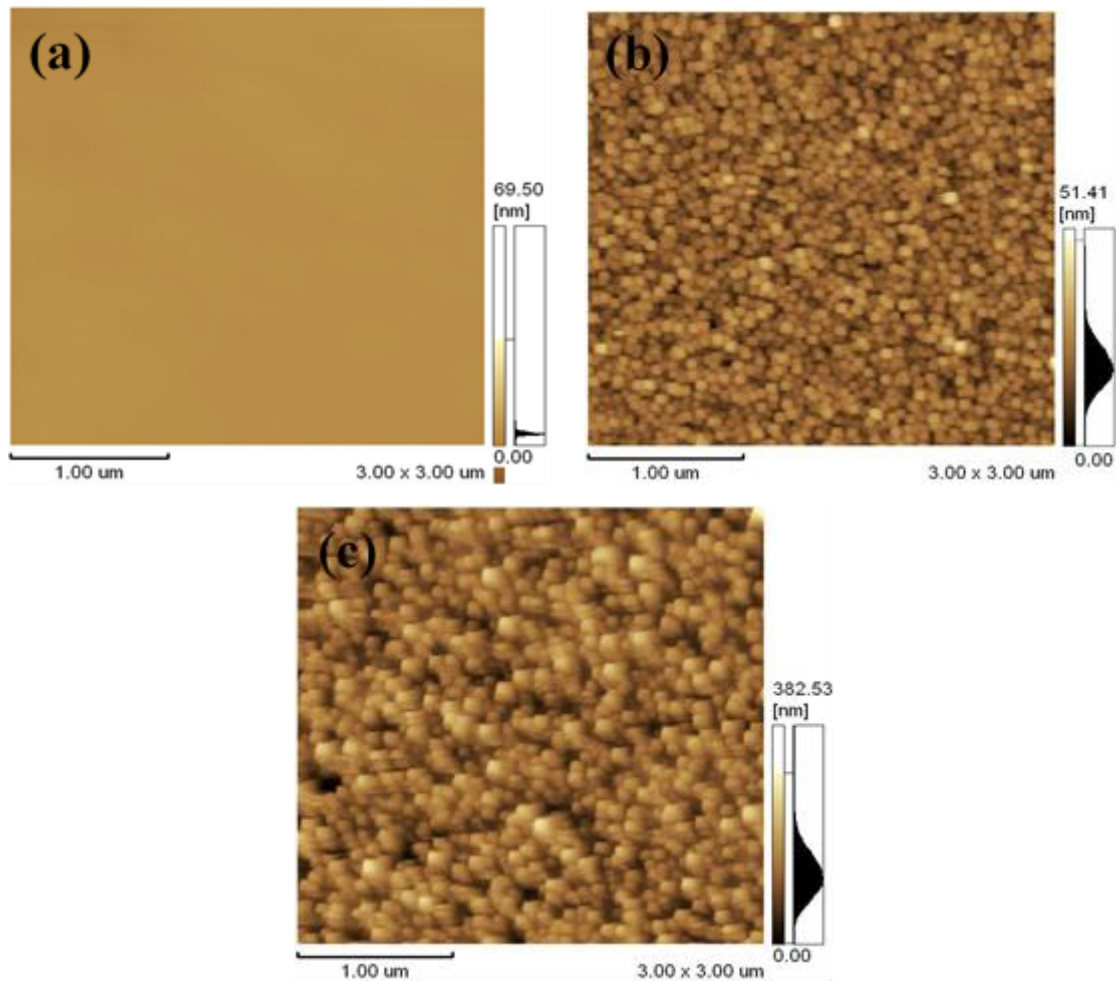


Fig. 8.1. AFM images of (a) the Si (100) substrate, (b) the ZnO seed layer, and (c) the ZnO nanorods before annealing.

Figure 8.2 displays the XRD patterns of the grown ZnO nanorods and annealed in a reducing atmosphere for different times. As can be seen, only one diffraction peak was detected around $2\theta \approx 34.8^\circ$ which was indexed as the (002) plane of the hexagonal structure of ZnO. This indicates successful growth of the ZnO nanorods in a wurtzite structure along the *c*-axis and perpendicular to the substrate surface. No extra peaks related to the hydroxyl (OH) groups, metal Zn or any other trace impurities, were observed. The (002) peak intensity first increased after annealing and then decreased with increasing annealing time. The weak (002) peak intensity for the longer annealing time indicates poor crystallinity. ZnO native defects normally play a critical role in the film crystallinity [20]. Therefore, since the ZnO nanorods were prepared by using a low-temperature chemical bath deposition (CBD) method, they might

contain excess oxygen defects as confirmed by the broad emission around 600 nm [Fig. 8.7.(a)], which was due to the oxygen related defect. That is why the (002) peak of the un-annealed sample has a lower intensity compared to the annealed sample.

After annealing in the reducing atmosphere for 20 min, some of the original oxygen-related defects were expected to be removed and therefore, the film's crystallinity improved and as a result the (002) peak intensity increased. Annealing in the reducing atmosphere containing H₂ however, which also created other hydrogen related defects in the ZnO lattice. Therefore, increasing the annealing time to 30 min resulted in a decrease in the (002) peak intensity again, which indicates that more defects were created in the ZnO lattice. Oxygen vacancies and hydrogen related defects are more likely to be created by annealing in the reducing atmosphere [29]. The (002) peak intensity substantially decreased when the annealing time was increased to 50 min, which confirms that the nanorods' degree of crystallinity was reduced when annealed for too long due to the chemical interactions caused by the creation of the defects. The (002) peak position slightly shifted to higher angles when increasing the annealing time. For more structural analysis, the well-known Sherrer's equation and Miller indices were used to calculate the crystallite size and the crystal parameters, respectively, and the results are shown in Table 8.1. The crystal parameter *c* and the planes spacing *d* decreased with increasing annealing time. The crystallite size increased with an increasing annealing time up to 30 min and then decreased upon further annealing.

Table 8.1. Crystal parameters (*c* and *d*), crystal size, and nanorods diameter of the ZnO nanorods annealed in a reducing atmosphere at 700 °C for different times.

Sample name	Crystal parameters		Crystallite size (D) (nm)	Nanorods diameter (nm)
	<i>c</i> (nm)	<i>d</i> (nm)		
Un-annealed	0.5153	0.2577	122 ± 1	50 ± 5
Annealed for 20 min	0.5153	0.2577	156 ± 1	220 ± 5
Annealed for 30 min	0.5149	0.2575	169 ± 1	250 ± 5
Annealed for 50 min	0.5142	0.2571	119 ± 1	Unidentifiable

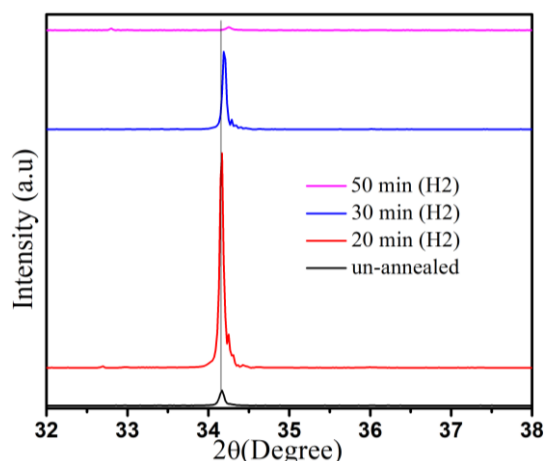


Fig. 8.2. XRD patterns of the un-annealed ZnO nanorods and annealed in a reducing atmosphere for different times.

Figure 8.3 shows the SEM images of the ZnO nanorods, [Fig. 8.3(a)] unannealed and [Figs. 8.3(b) – 3(d)] annealed in a reducing atmosphere for different times. The insets are the cross-sections of the corresponding samples. The images revealed that the vertically well-aligned ZnO nanorods were successfully grown. The unannealed sample contained very thin and dense nanorods with an average diameter and length of about 50 nm and 500 nm, respectively. Using the (002) peak, the Scherer's equation only gives the crystallite size along the c-axis, and therefore, the crystallite size of the as prepared nanorods sample is bigger than the rods diameter (Table 8.1); this confirms the crystallite preferential growth along the c-axis of the wurtzite structure. Annealing in a reducing atmosphere made the nanorods grow in size (diameter) with slightly reduced lengths. It is very clear that annealing in a reducing atmosphere under the flow of H₂/Ar gas helped the nanorods to grow closer together. This could be very similar to the growth of ZnO nanorods by the vapor-liquid-solid method [30, 31] where the Ar gas acts as a gas carrier. In this case, the Zn atoms and/or ZnO clusters are removed from some rods and may be conveyed to stick on and diffused into the nearby rods, while loosely bonded oxygen atoms could react with the H₂ and form H₂O which eventually evaporates. Following further annealing time, the nanorods alignment and even distribution was almost completely destroyed as can be seen in Fig. 8.3(d). The rod diameters of the rods are presented in Table 8.1.

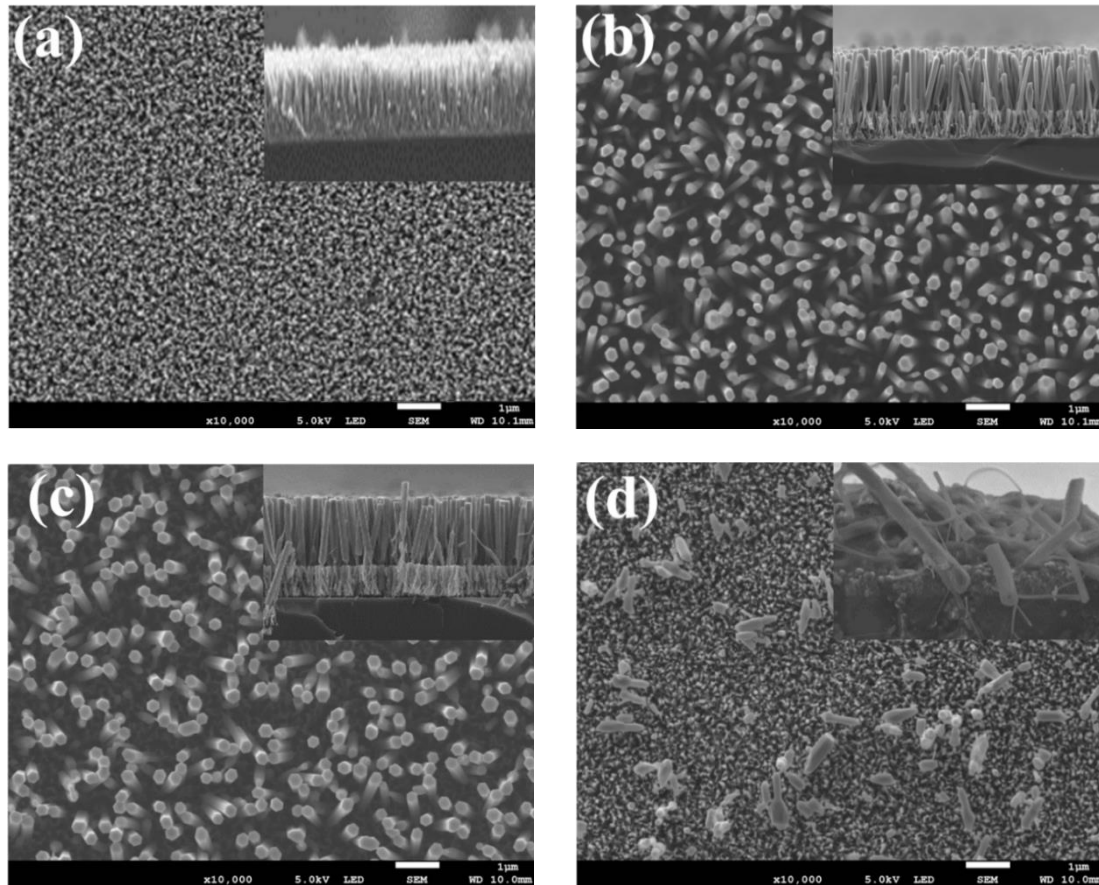


Fig. 8.3. SEM images of the ZnO nanorods annealed in reducing atmosphere at 700 °C for different times: (a) unannealed, (b) for 20 min, (c) for 30 min, and (d) for 50 min. The insets are the cross-sections of the films.

8.3.2. XPS analysis

Figure 8.4 shows the XPS high resolution spectra of the Zn 2p peak region (a) before and (b) after 1 min of sputtering using an Ar⁺ ion beam to remove the surface contaminations. There are two peaks (Zn-2p_{1/2} and Zn-2p_{3/2}) whose binding energies are 1022 eV and 1045 eV, respectively. The energy difference was 23 eV. These values are very close to the standard reference values of ZnO (Ref [32]) and indicated that all Zn atoms were fully oxidized and in their doubly ionized state (Zn²⁺). There was no change observed after Ar⁺ sputtering. No Zn metal was observed with binding energy of 1021.8 eV, which was consistent with the XRD results.

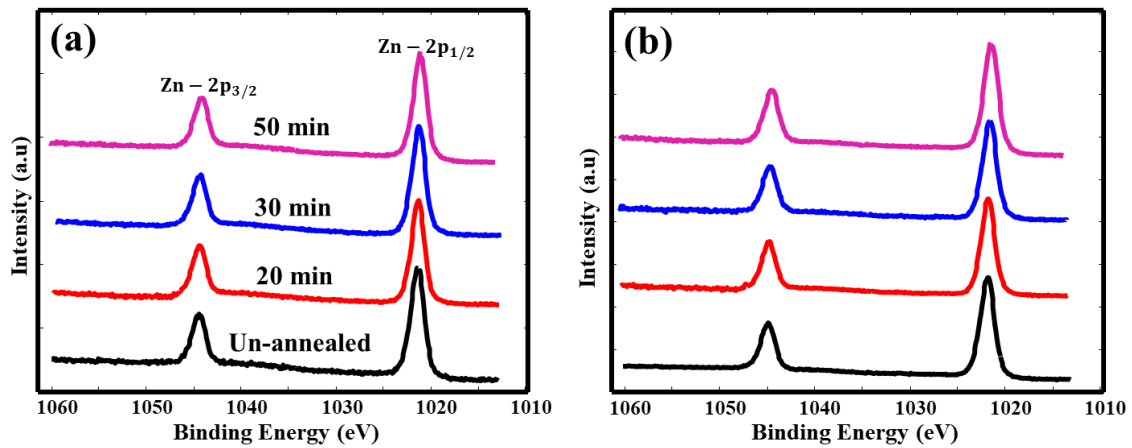


Fig. 8.4. High resolution XPS spectra of the Zn 2p core levels of the samples annealed in a reducing atmosphere for different times (a) before sputtering and (b) after sputtering for 1 min with Ar^+ ions.

The O 1s XPS spectra of the ZnO nanorods annealed in the reducing atmosphere for different times, measured before and after Ar^+ sputtering, were deconvoluted using MULTIPAK software as shown in Fig. 8.5. Kumar et al. [33, 34] deconvoluted the O 1s peak into three components. O1 is attributed to the O^{2-} ions in the wurtzite structure of ZnO, surrounded by Zn atoms that fully interacted with their nearest neighbors of O^{2-} ions. O2 is associated with the O^{2-} ions in the oxygen deficient regions in ZnO such as ZnOH and related defects, while O3 was ascribed to the loosely bonded species from the atmosphere such as CO_3 , H_2O and O_2 . O3 was detected before sputtering for all the samples and completely diminished after sputtering, due to the removal of the surface contaminations. The O2 peak was detected from all the samples before and after sputtering. After sputtering, the O2 peak area has increased with an increasing annealing time, and this was consistent with the PL measurements which indicated that more defects were created. However, although the O2 peak area for the film annealed for 50 min increased while the PL and XRD intensity decreased, due to the fact that XRD and PL are dependent not only on the amount of the defects present but also on the nanorods density, diameter, length and crystallinity. The O2 peak area is an indication of the defects relative to the fully oxidized Zn atoms (O1 peak); hence, more defects were present with respect to the fully oxidized Zn atoms in the sample annealed for 50 min. However, due to the destruction in crystallinity that the film experienced, as seen from the SEM image, [Fig. 8.3(d)], and the XRD pattern, the PL intensities decreased. Or otherwise complex defects such as ZnOH might be created in the structure which acted as non-radiative centers. The details of the binding energies and the peak areas of the deconvoluted O 1s peaks are given in Table 8.2.

Table 8.2. Binding energies of the deconvoluted peaks of the O 1s of the samples annealed in reducing atmosphere for different times, before and after sputtering.

Sample		Before sputtering		After sputtering	
		Peak position (V)	Area (%)	Peak position	Area (%)
Un-annealed	O1	530.3	78	530.3	85
	O2	531.7	16	531.7	15
	O3	532.6	6	—	—
Annealed for 20 min	O1	530.3	79	530.3	84
	O2	531.7	13	531.7	16
	O3	532.6	8	—	—
Annealed for 30 min	O1	530.3	72	530.3	80
	O2	531.7	24	531.7	20
	O3	532.6	4	—	—
Annealed for 50 min	O1	530.3	71	530.3	72
	O2	531.7	24	531.7	28
	O3	532.6	5	—	—

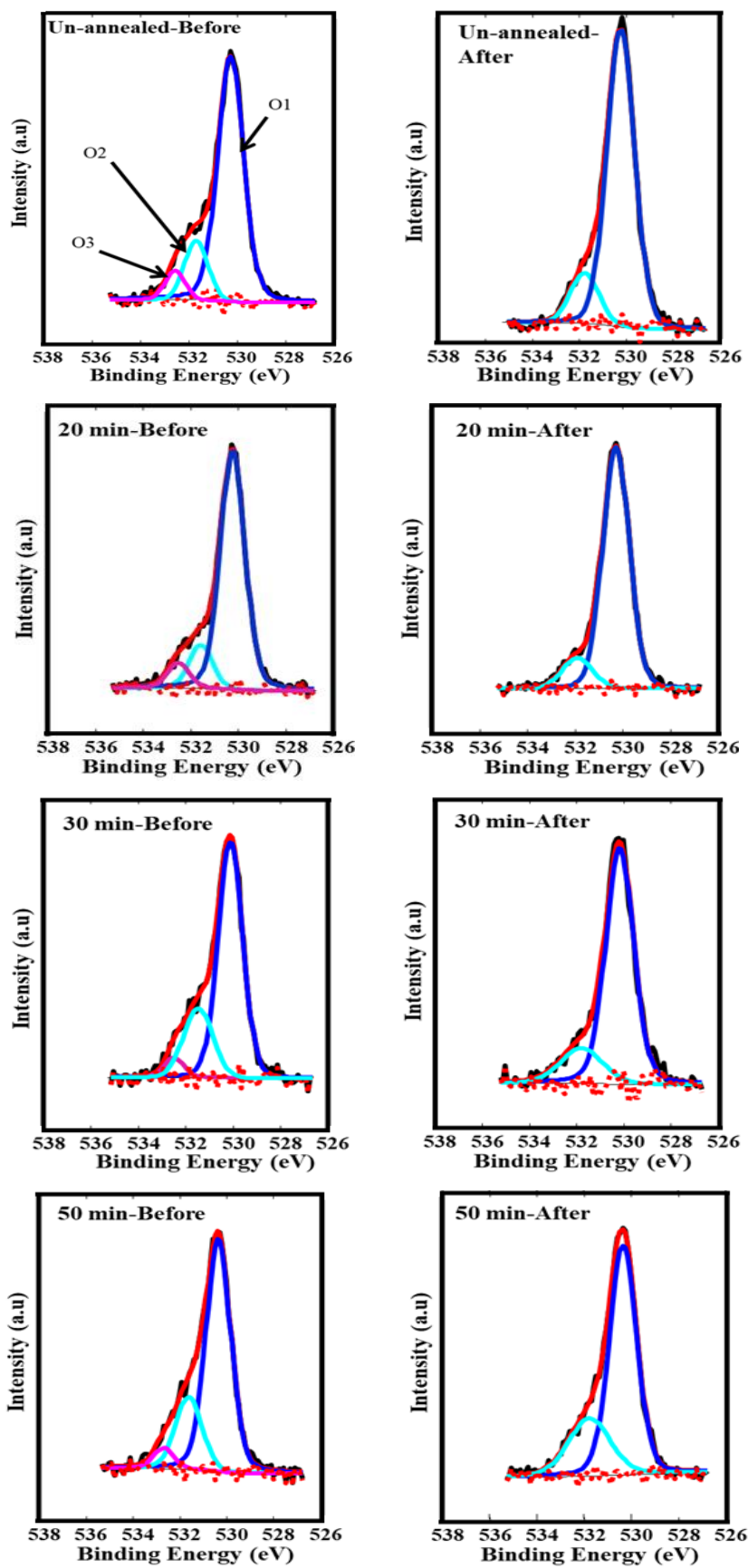


Fig. 8.5. Deconvoluted peak of the O 1s peak before and after sputtering of the samples annealed in a reducing atmosphere for different times.

8.3.3. Photoluminescence analysis

Figure 8.7 depicts the PL spectra of the unannealed ZnO nanorods and those annealed for different periods of time. ZnO has two distinct luminescence emissions: [35] band to band or excitonic emission which is at the ultraviolet region around 380 nm and the deep level emission over the visible region which is due to the native point defects in the ZnO crystals. The most prominent defects responsible for the visible emission of ZnO are doubly or singly ionized oxygen vacancies (V_o^{++}/V_o^+) [36], zinc interstitial (Zn_i), oxygen interstitial (O_i), and zinc vacancies (V_{Zn}) [37]. It has been reported that excess oxygen related defects (O_i and V_{Zn}) are responsible for the broad orange to red emission around 600 nm to 750 nm [38], while the Zn-excess related defects such as Zn_i , V_o^{++} and V_o^+ are responsible for the visible emission around blue (400 to 470 nm) and green (500 and 550 nm) [39, 40], respectively. The unannealed sample exhibited the band to band emission around 378 nm as well as the broad orange emission centred at 600 nm. The origin of the ultraviolet emission of ZnO is well documented. The orange emission around 600 nm is always observed for ZnO prepared via different methods such as combustion [38], sol-gel [37], co-precipitation [41] and low-temperature chemical aqueous growth, and it is thought to be due to the oxygen excess related defects that were created as a result of the excess oxygen atoms presented in the solution. With the hypothesis that the broad orange emission of ZnO was due to the oxygen excess related defects, annealing in a reducing atmosphere (H_2/Ar) would remove these defects and new kind of defects could be created. In particular, the Zn-excess related defects due to the removal of oxygen atoms would be expected, and the broad orange band should be eliminated while a new emission band could be created. Annealing in a reducing atmosphere raised a new green emission band centred at 500 nm [Fig. 8.7(a)], which was assumed to be due to the excess Zn-related defects. The intensity of the green emission increased with an increasing annealing time. The maximum intensity was recorded for the sample annealed for 30 min, and thereafter, the emission intensity has drastically decreased for further annealing time (50 min). It is very reasonable to conclude that increasing the annealing time in the reducing atmosphere has increased the Zn-excess related defects that were responsible for the broad green emission centred at 500 nm. The XPS data of Table 8.2 are in agreement since (for the after sputtering data) it shows an increase in the O2 peak area percentage related to oxygen deficiency, with increasing annealing time of 20 and 30 min. Nevertheless, according to the SEM results, the nanorods' diameters increased with an increasing annealing time and their density decreased with a further increase in the annealing times. Since the increase in the nanorods' diameter leads to a consumption of other nanorods, a decrease in the total surface area of the sample was

obtained. The decrease in the density might therefore increase the light scattering leading to an increase in the intensity. Furthermore, surface defects that might lead to luminescence quenching might also be reduced with lesser surface area. Therefore, the nanorods' morphologies (nanorods diameter and their density) could have played a significant role in the emission intensity. Consequently, the green emission has increased and reached its maximum for the sample annealed for 30 min and then dramatically decreased for the sample annealed for 50 min. The SEM image for the sample annealed for 50 min showed complete destruction of the uniform nanorods structure. It must also be pointed out that oxide materials are easily contaminated by hydrogen impurities mostly due to the strong bonding of the H atoms to an O atom [42]. Hydrogen impurities are suggested to have two kinds of donorlike states in ZnO: (i) interstitial hydrogen and (ii) substitutional H at an O site [42]. It may be speculated at this stage that during annealing in a hydrogen gas, the hydrogen diffused into the ZnO ([42]) and can complicate the defect emission in ZnO. At first, with a lower hydrogen concentration, the hydrogen may occupy the oxygen vacancies leading to a reduction in intensity of the oxygen vacancy emission and then with further diffusion leading to a higher concentrations of hydrogen in the ZnO that both filling the V_o (healing of V_o) and populating interstitial sites leading to nonradiative emissions and a decrease in PL intensity.

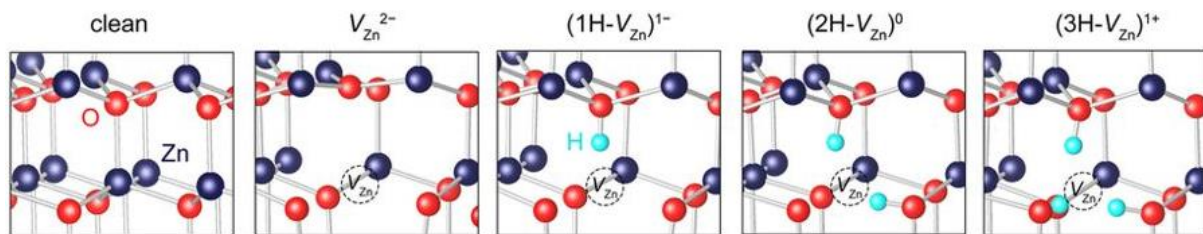


Fig. 8.6. Atomic structures of ZnO without defects, V_{Zn}^{2-} , $(1H-V_{Zn})^{1-}$, $(2H-V_{Zn})^0$, and $(3H-V_{Zn})^{1+}$ [Reproduced with permission from Y. Kang, H. N. Nahm, and S. Han, Sci. Rep. 6, 35148 (2016). Copyright 2013, Nature Publishing Group, licensed under a CC BY 4.0 license].

The concentration of a defect in the host material relies on the amount of available sites to form the defect and its defect formation energy that depends on growing or annealing conditions. Figure 8.6 gives an example where a V_{Zn} was formed. There are now four O sites available for the formation of O-H bonds as shown in Fig. 8.6 [43]. Figures are shown for $NH-V_{Zn}$ with $N = 1, 2$ and 3 . This one example clearly shows the effect of hydrogen on this specific defect distribution. Deng et al. [44] also showed that the migration of V_o has lower barriers in nanowires in comparison with their bulk counterparts and is found to be energetically favorable

in the direction from the bulk to the surface [44]. Their results imply a higher concentration of V_O at surface sites and also a relative ease of diffusion in the nanowires' structure. Changes in defect signatures while annealing at elevated temperatures in a hydrogen gas medium, as in this case, indicate that the relevant defects have become mobile and the interdiffusion of hydrogen has a severe effect on the defect distribution. Both the substitutional and interstitial forms of hydrogen have low formation energies in ZnO. However, hydrogen is only stable in ZnO up to $\sim 500^\circ\text{C}$ [12]. Even if the hydrogen defects are only stable up to $\sim 500^\circ\text{C}$, they will still play a major role in the defect redistribution when annealing in an H_2 atmosphere.

The insets in Fig. 8.7(a) are photographs taken by a digital camera for the samples annealed for 20 and 30 min. The emission of the samples annealed for 50 min was not detectable by the naked eye. Figure 8.7(b) shows the zoomed in region for the ultraviolet spectrum. The UV emission of the sample was almost brought to the noise level after annealing in a reducing atmosphere. This is due to the creation of more deep level defects that compete with and eventually suppressed the excitonic emission. To figure out the possible defects contributed in the green emission centred at 500 nm, the peak was fitted using the Gaussian function to determine the superposition of the peaks and the results are shown in Fig. 8.7(c). At least three peaks could be fitted around 465 nm, 510 nm and 550 nm. These peaks indicated that more than one kind of defect contributed to the green emission centred at 500 nm. The suggested defects responsible for the individual peaks are included within the spectra based on some reported research [45, 46, 47]. Figure 8.7(d) shows the photometric characteristic/color chromaticity for the sample annealed for 30 min. The color coordinates (X, Y) of the high intensity sample was calculated using the CIE 1931 software and were found as $X = 0.20$ and $Y = 0.39$. The color correlated temperature CCT was calculated via the McCamy equation and was found to be 8564 K for the high intensity sample.

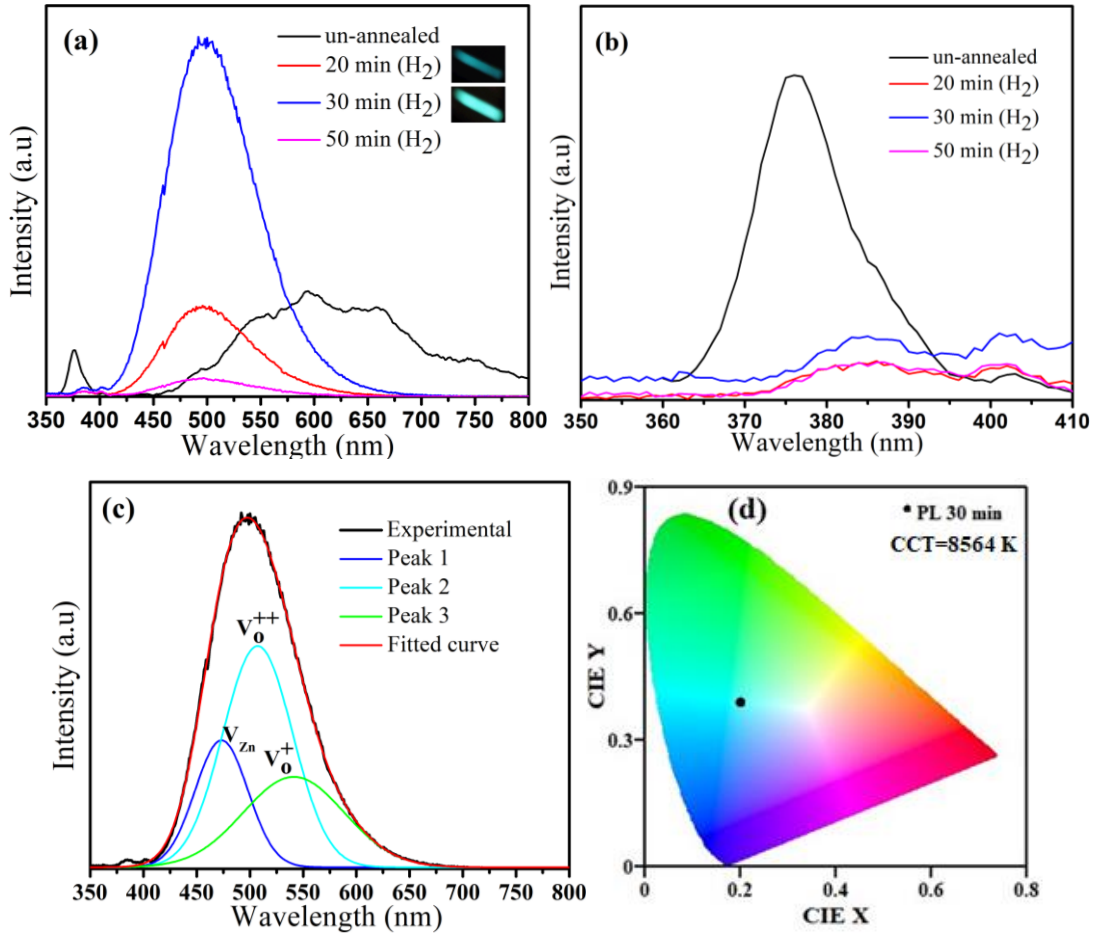


Fig. 8.7. (a) Photoluminescence spectra of the ZnO nanorods annealed in the reducing atmosphere at 700 °C for different time, (b) zoomed in spectra of the UV region, (c) deconvoluted peak of the sample annealed for 30 min and (d) CIE color coordinate of the sample annealed for 30 min.

The quantum yield (QY) has always been a matter of concern for any material that has to be used in optical applications. QY is defined as the ratio of the number of emitted photons (N^{em}) to the number of absorbed photons (N^{abs}) [41],

$$QY = N^{\text{em}}/N^{\text{abs}} \quad (8.1).$$

The QY was measured for the sample annealed for 30 min with the highest PL intensity. The sample and a standard (Benflect™) were excited at a wavelength of 325 nm and the results are shown in Fig. 8.8(a), with the intensity on a logarithmic scale. The continuous curve (red curve online) of the sample covered both the reflection (scatter) of the excitation light at 325 nm and the longer wavelength luminescence band near 500 nm. The black spectrum represents the reflection from the standard and the difference between it and the sample indicated the number of photons absorbed. The background obtained with the standard was scaled (green curve) and subtracted from the sample curve to obtain the number of emitted photons, and the QY was

calculated as 43 %. A similar measurement for excitation at 375 nm gave the QY as 37 %. The small peak on the background (green spectrum) near 615 nm was attributed to a tiny amount of Eu^{3+} -emitting phosphor contamination of the integrating sphere - due to the logarithmic intensity scale, its effect is negligible and it was not considered, although it may be noted that removing this peak in the background could only tend to increase the calculated number of emitted photons and therefore the QY.

The decay curve of the highest intensity sample was measured using a monochromatized xenon flash lamp with repetition rate of 100 Hz for excitation at the wavelength of 375 nm and emission at 504 nm and is presented in Fig. 8.8(b). The curve was well fitted to a triexponential decay using the following equation [48]:

$$I(t) = I_o + A_1 e^{-(t/\tau_1)} + A_2 e^{-(t/\tau_2)} + A_3 e^{-(t/\tau_3)} \quad (8.2),$$

where $I(t)$ is the intensity at a certain time t after excitation, I_o is the background and A_1 , A_2 and A_3 are the fitting amplitudes while τ_1 , τ_2 and τ_3 are the decay lifetime components. Using these parameters, the average lifetime (τ_{avg}) can be calculated by

$$\tau = \frac{A_1 \tau_1^2 + A_2 \tau_2^2 + A_3 \tau_3^2}{A_1 \tau_1 + A_2 \tau_2 + A_3 \tau_3} \quad (8.3)$$

The average lifetime (τ_{avg}) value for the sample annealed for 30 min was determined to be 11.58 μs . The triexponential function needed for the fit may be explained in terms of three different defects that contributed to the green emission at 500 nm. This assumption correlates very well with the deconvoluted PL peak of the sample, where three fitted peaks were found as shown in Fig. 8.7(c).

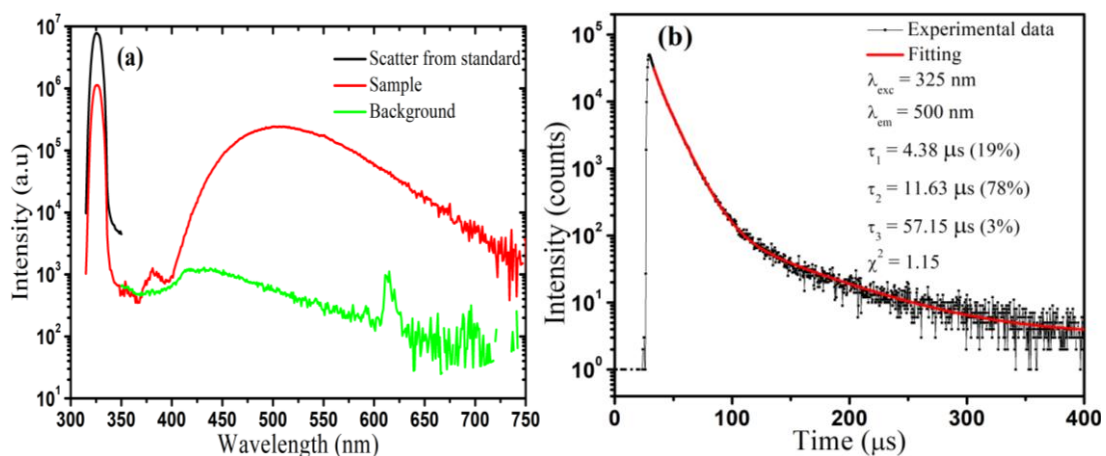


Fig. 8.8. (a) Data for quantum yield calculation and (b) decay curve of the sample annealed for 30 min.

8.4. Conclusions

Vertically aligned ZnO nanorods with *c*-axis orientation were successfully grown on a ZnO seed layer coated on an (100) Si substrate. The deconvoluted XPS peaks of the O 1s energy region indicated that defects related to the oxygen deficiencies were present in all the samples and played a significant role on the PL of the ZnO nanorods annealed in the reducing atmosphere at different times. The green emission centred at 500 nm with CIE coordinates ($X = 0.20$ and $Y = 0.39$) and high quantum yield (43%) was obtained from the samples annealed in a reducing atmosphere for 30 min. At least three kind of defects (V_o^+ , V_o^{++} , V_{Zn}) were found to contribute to the green emission centered at 500 nm. These emissions may be used in optoelectronic applications such as LEDs and FEDs.

8.5. References

- [1] D. Raouf, *J. Lumin.* **134**, 213 (2013).
- [2] H. D. Sun, T. Makino, Y. Segawa, M. Kawasaki and A. Ohtomo, *J. Appl. Phys.* **91**, 1993 (2002).
- [3] K. Alfaramawi, *Bull. Mater. Sci.* **37**, 1603 (2014).
- [4] C. Peter, S. Kasap, and A. Willoughby, *Zinc Oxide Material for electronic and optoelectronic device application* (John Wiley & Sons, Hoboken, New Jersey, 2011).
- [5] K. Ellmer, K. Andreas, and R. Bernd, *transparent Conductive Zinc Oxide: Basics and Applications in Thin Film* (Springer, New York, 2018).
- [6] N. A. Jayah, H. Yahaya, M. R. Mahmood, T. Terasako, K. Yasui and A. Hashim, *Nanoscale Res. Lett.* **10**, 7 (2015).
- [7] H. Huang, G. Fang, X. Mo, H. Long, L. Yuan, B. Dong, X. Meng, and X. Zhao, *IEEE Electron device letters* **30**, 1063 (2009).
- [8] R. D. Herrick, and J. L. Stickney, *J. Soc. Inf. Disp.* **6**, 149 (1998).
- [9] K. Ellimer, R. Wendt, and R. Cebulla, *Photovoltaic Specialists Conference*, Washington, DC, 13 – 17 May 1996.
- [10] Ü. Özgür, Ya. I. Alivov, C. Liu, A. Teke, M. A. Reshchikov, S. Doğan, V. Avrutin, S.-J. Cho, and H. Morkoç, *J. Appl. Phys.* **98**, 041301 (2005).
- [11] A. Janotti, C. G. Van de Walle, *J. Cryst. Growth* **287**, 58 (2006).
- [12] A. Janotti and C. G. Van de Walle, *Rep. Prog. Phys.* **72**, 126501 (2009).
- [13] T. Kun, S. L. Gu, J. D. Ye, S. M. Zhu, R. Zhang, Y. D. Zheng, *Chin. Phys. B* **26**, 047702 (2017).

- [14] J. Čížek, J. Valenta, P. Hruška, O. Melikhova, I. Procházka, M. Novotný, and J. Bulíř, *Appl. Phys. Lett.* **106**, 251902 (2015).
- [15] J. Lv, C. Li and J. J. BelBruno, *CrystEngComm* **28**, 5620 (2013).
- [16] Z. L. Wang, *J. Phys.: Condens. Matter* **16**, 829 (2004).
- [17] X. H. Zhang, Y. C. Liu, X. H. Wang, S. J. Chen, G. R. Wang, J. Y. Zhang, Y. M. Lu, D. Z. Shen and X. W. Fan, *J. Phys. Condens. Matter* **17**, 3035 (2005).
- [18] K. Chen, D. D. Thang, S. Ishii, R. P. Sugavaneshwa, and T. Nagao, *Opt. Mater. Express* **5** 353 (2015).
- [19] Z. S. Hu, F. Y. Hung, S. J. Chang and K. J. Chen, *Vacuum Nanoelectronics Conference (IVNC)*, Jeju, 9 – 13 July 2012.
- [20] E. Hasabeldaim, O. M. Ntwaeaborwa, R. E. Kroon, David E. Motaung, E. Coetseea, H. C. Swart, *Opt. Mater.* **74**, 76 (2017).
- [21] G. C. Yi, C. Wang and W. I. Park, *Semicond. Sci. Technol.* **20**, S22 (2005).
- [22] B. Weintraub, Y. Deng, and Z. L. Wang, *J. Phys. Chem. C* **111** 10162 (2007).
- [23] F. I. Lai, J. F. Yang, and S.Y. Kuo, *Materials* **8**, 8860 (2015).
- [24] Y. Ishikawa, Y. Shimizu, T. Sasaki and N. Koshizaki, *J. Colloid Interface Sci.* **300**, 612 (2006).
- [25] K. Jiao, X. Wu, C. Duan, D. Zhang, Y. Wang and Y. Chen, *Phys. Chem. Chem. Phys.* **17**, 4757 (2015).
- [26] D. S. Kanga et al., *J. Alloys Compd.* **509**, 5137 (2011).
- [27] C. Li, G. Fang, F. Su, G. Li, X. Wu and X. Zhao, *Nanotechnology* **17**, 3740 (2006).
- [28] D. Phromyothin, P. Phatbana, S. Jessadaluk, N. Khemasiri, R. Kowong, S. Vuttivong, S. Pornthreeraphat, C. Chananonwathorn, and M. Horphathum, *Mater. Today Proc.* **4**(5), pt. 2, 6326-6330 2017.
- [29] E. Hasabeldaim, O. M. Ntwaeaborwa, R. E. Kroon, E. Coetsee and H. C. Swart, *Proceedings of SAIP 2016*, Cape Town, 4-88 July 2016.
- [30] R. S. Wagner and W. C. Ellis, *Appl. Phys. Lett.* **4**, 89 (1964).
- [31] N.H. Alvi, Wasied ul Hassan, B. Farooq, O. Nur and M. Willander, *Mater. Lett.* **106**, 158 (2013).
- [32] J. F. Moulder, W. F. Strickle, P. E. Sobol and K. D. Bomben, *Handbook of X-Ray Photoelectron Spectroscopy* (Physical electronics, Eden Prairie, MN, 1995), p. 230.
- [33] V. Kumar, H. C. Swart, M. Gohain, Vijay Kumar, S. Som, B. C. B. Bezuindenhoudt and O. M. Ntwaeaborwa, *Ultrason. Sonochem.* **21**, 1549 (2014).

- [34] V. Kumar, Vijay Kumar, S. Som, L.P. Purohit, O.M. Ntwaeaborwa and H.C. Swart, *J. Alloys Compd.* **594**, 32 (2014).
- [35] P. A. Rodnyi and I. V. Khodyuk, *Opt. and Spectrosc.* **111**, 776 (2011).
- [36] K. M. Wong, S. M. Alay-e-Abbas, Yaoguo Fang, A. Shaukat, and Yong Lei, *Appl. Phys. Lett.* **95**, 183114 (2009).
- [37] E. Hasabeldaim, O. M. Ntwaeaborwa, R. E. Kroon, V. Craciun, E. Coetsee, H. C. Swart, *Appl. Surf. Sci.* **424**, 412 (2017).
- [38] V. Kumar, H. C. Swart, O. M. Ntwaeaborwa, R. E. Kroon, J. J. Terblans, S. K. K. Shaat, A. Yousif and M. M. Duvenhage, *Mater. Lett.* **101**, 57 (2013).
- [39] O. D. Jayakumar, V. Sudarsan, C. Sudakar, R. Naik, R. K. Vatsaa and A. K. Tyagi, *Scr. Mater* **62**, 662 (2010).
- [40] A. Travlos, N. Boukos, and C. Chandrinou, *Phys. Stat. Sol. B* **249**, 560 (2012).
- [41] O. M. Ntwaeaborwa, S. J. Mofokeng, V. Kumar and R. E. Kroon, *Spectrochim. Acta A* **182**, 42 (2017).
- [42] C. F. Windisch Jr, G. J. Exarhos, C. Yao, and L. Q. Wang, *J. Appl. Phys.* **101**, 123711 (2007).
- [43] Y. Kang, H. H. Nahm & S. Han, *Sci. Rep* **6**, 35148 (2016).
- [44] B. Deng, A. L. da Rosa, T. Frauenheim, J. P. Xiao, X. Q. Shi, R. Q. Zhang and M. A. Van Hoved, *Nanoscale* **20**, 11882 (2014).
- [45] J. W. cai, J. P. Xu, X. S. Zhang, X. P. Niu, T. Y. Xing, T. Ji and L. Li, *Optoelectron Lett* **8**, 4 (2012).
- [46] Y. Gong, T. Andelman, G. F. Neumark, S. O'Brien and I. L. Kuskovsky, *Nanoscale Res. Lett.* **2**, 297 (2007).
- [47] H. Zeng, G. Duan, Y. Li, S. Yang, X. Xu, and W. Cai, *Adv. Funct. Mater.* **20**, 561 (2010).
- [48] K. N. Kumar, R. Padma, L. Vijayalakshmi, J. S. M. Nithya and M. Kang, *J. Lumin.* **182**, 208 (2017).

Chapter 9

Cathodoluminescence degradation study of the green luminescence of ZnO nanorods

9.1. Introduction

Due to the relatively poor stability of sulfide based materials, as well as the degradation and low breakdown voltage of organic based material optoelectronic devices, developing new materials with good chemical stability that can compensate the weaknesses of sulfides and organic materials [1, 2] is a critical research issue. Oosthuizen et al. [3] and Swart et al. [4] have shown that ZnS phosphors formed ZnO on the surface during prolonged electron bombardment due to electron stimulated surface chemical reactions (ESSCRs) on the surface. The stability of ZnO as a light emitting material itself would therefore be a good choice to investigate for stability under electron bombardment.

Furthermore, metal oxide semiconductors are very important materials in electronic applications. In particular, wide band gap semiconductors such as ZnO, TiO₂, Ga₂O₃, SnO₂, etc. are prominent materials in the field of optoelectronics [5]. ZnO is established as a wide band gap (3.37 eV) metal oxide semiconductor having good properties such as large exciton binding energy (60 meV) [6] and chemical stability [7]. Moreover, ZnO can easily be grown in the form of different nanostructures [8], amongst which nanorod structures are well known to improve its optical and electrical quality. This is due to the high surface to volume ratio of the nanorods, which made it to be considered as the best system to understand the transport mechanism of 1D materials in order to develop high performing devices [9]. ZnO nanorods can be used in different applications including light emitters in light emitting diodes (LEDs), electrical pathway for electrodes in dye sensitized solar cells, solar cell applications due to its oxygen vacancies [10], and potentially for hydrogen storage. ZnO is a promising candidate as a green phosphor that can be used in the aforementioned applications due to its bright green emission originating from the native defects such as oxygen vacancies [11].

Green luminescence of ZnO has shown good stability under electron beam irradiation [12, 13]. However, the initial CL intensity degradation of the green emission when ZnO was irradiated with a beam of electrons, followed by subsequent recovery, is not understood yet and further investigation is needed. Atomic oxygen, atomic hydrogen [12], formation of non-luminescent ZnO layers and/or surface changes were suspected to be responsible from the initial degradation followed by subsequent recovery of the green luminescence of ZnO [14].

In this work, ZnO nanorods were prepared by the simple two-step method using spin coating in combination with the chemical bath deposition technique. The samples were annealed in a reducing atmosphere to obtain the bright green emission of ZnO. The degradation behavior of the ZnO nanorods during prolonged electron bombardment was investigated.

9.2. Experimental

ZnO nanorods was prepared via the previously described [15] two-step low temperature aqueous chemical growth method using chemical bath deposition. Briefly, a ZnO seed layer was deposited on a (100) oriented Si substrate using a spin coater. For the seed layer zinc acetate dihydrate was dissolved in 40 mL of high purity ethanol (99.9%) for a concentration of 0.2 mol/L. An equal molar concentration of monoethanolamine (0.2 mol/L) with volume of 0.483 mL was added into the zinc acetate solution dropwise and the mixture was stirred at room temperature for about 1 h until a clear solution was obtained. The solution was used to spin coat 5 layers on the Si substrate. The spin coating was done at 3000 RPM for 30 s for each layer and the sample was heated at 250 °C for 10 min in air after each layer. Finally the seeded layer substrate was annealed at 500 °C in air for 1 h. For the growth of the ZnO nanorods, a solution of zinc nitrate hexahydrate and hexaminetetramine (both with concentration of 0.05 mol/L) was prepared using deionized water and stirred at room temperature for about 1 h, and then placed in a chemical bath at a temperature of 90 °C. The substrate with the seed layer was dipped in the solution with the growth face down towards the bottom of the beaker and the growth continued for 4 h, after which the substrate was removed and washed with deionized water and dried by carefully blowing nitrogen gas over the surface. Finally, the sample was annealed in a reducing atmosphere (H₂:Ar with a ratio of 5:95) at 700 °C for 30 min.

A Cary Eclipse fluorescence spectrophotometer equipped with a xenon lamp was utilized for the photoluminescence (PL) measurements. The sample was excited with a wavelength of 325 nm. To study the degradation behavior of the sample, a PHI Auger electron spectroscope (AES) model 545 was used for the chemical composition and cathodoluminescence (CL) degradation study of the sample. The sample was subjected to electron beam irradiation for about 22 h. The electron beam working voltage, current and the current density were kept at 2 keV, 24 μA and 0.53 mA.cm⁻², respectively, and the irradiated area radius was found to be around 1.2 mm using a Faraday cup. The degradation (irradiation) experiments were performed in vacuum at a base pressure of 5.0 x 10⁻⁸ Torr and a back-filled oxygen atmosphere with an oxygen partial pressure of 5.5 x 10⁻⁸ Torr. Auger peak-to-peak heights (APPHs) and CL data were recorded simultaneously using the same electron beam. An Ocean Optics PC2000 spectrometer and OOI base 32 computer software were used for the CL data collection. The X-ray photoelectron

spectroscopy (XPS) measurements were carried out with a PHI 5000 Versaprobe-Scanning ESCA Microprobe. The measurements were carried out with a 100 μm monochromatic Al $K\alpha$ X-ray source with photon energy of 1486.6 eV generated at 25 W and 15 kV. High resolution spectra of the C 1s, O 1s and Zn 2p energy regions were collected with the hemispherical analyzer pass energy maintained at 11.8 eV for 10 cycles using 0.5 eV/step. The measurements were taken before and after 1 min of Ar^+ ion sputtering to remove the surface contamination, and this was done for both the original and degraded samples. The pressure during the acquisition was about 2.8×10^{-9} Torr. MULTIPAK software [16] was used for the deconvolution of the peaks. The morphology of the samples was characterized using a JEOL scanning electron microscopy (SEM) model JSM-7800F.

9.3. Results and discussions

Fig. 9.1 shows the SEM micrographs of the ZnO nanorods before and after electron beam irradiation. The changes induced by the electron beam irradiation on the ZnO nanorods morphology are clearly seen. The nanorods' density was substantially reduced after electron beam irradiation (degradation), while the hexagonal shape of the nanorods was slightly modified since there was a small groove in the nanorods as shown in Fig. 9.1(c). The upper half of the nanorods grew bigger while the lower half became thinner (Fig. 9.1(d)). The mechanisms in which the electron beam affects oxide surfaces and morphologies are very complicated phenomena. When high energy electrons impinged on the surface of an oxide, different processes may be involved, including: electrostatic charging, sputtering, heating, dehydration, radiolysis and knock-on displacement. These processes could create new defects via removal or diffusion of atoms/ions followed by reconstruction of the crystals and changes on the morphology [17]. Radiolysis occur through the Knotek-Feibelman mechanism, where an impinged electron beam creates an inner-shell vacancy on the metal site by removing oxygen atoms/ions [17]. This leads to a positively charged or neutral oxygen atom that can be repelled by the surrounding metal ions and eventually ejected into vacuum. This process leaves a metal (Zn)-rich surface with pitted morphology characteristics [18, 19]. Knock-on damages take place due to the deflection of the incident electrons via an electrostatic field of the atomic nuclei. At low energy transfer of several eV, normally the bottom atoms will be sputtered from the surface of the material. At higher energy transfer of tens of eV, atoms will be displaced and subsequently defects will be created in the crystals [20]. H atoms are always incorporated in ZnO during the growth and annealing process. They play a critical role in the stabilization of non-reconstructed surfaces. Due to the smaller size of the H atoms compared to Zn and O

atoms, they can gain much energy through collision with the incident electrons and therefore they are likely to be sputtered from the surface. It was demonstrated that H atoms can be released at 1.5 eV [21, 22]. Electron beam irradiation increases the local temperature on the surface which assist Zn atoms to oxidize, and hence new crystals grow on the surface [20]. All these mechanisms could contribute to the changes induced on the nanorods morphology such as the thinning of the lower half and the growth of the upper half. In another words, the thinning of the lower half and the growth of the upper half of the nanorods can be explained as follow: the incident electron beam creates an electric field and heats up the sample, as a result Zn atoms segregate and diffuse from the bottom to the top of the nanorods and then react with O atoms in the chamber and become oxidized, and eventually lead to the growth of the upper half and the thinning of the lower half. For the growth of the upper half of the nanorods, similar outgrowth was observed by Kalceff et al. [23] when he irradiated amorphous and crystalline SiO₂ with a high energy electron beam (30 kV). He observed an initial increase in the surface volume followed by a decrease in the volume after continuous irradiation of the amorphous SiO₂, while an outgrowth on the surface was also observed during irradiation of the crystalline SiO₂. These surface changes were attributed to the migration and diffusion of the defect species. The changes in our nanorods' morphology (the thinning of the lower half and the growth of the upper half) can be attributed to different reasons including: migration and diffusion of the ZnO defects, formation of an interleaved non-luminescent ZnO layer and/or removal of the atomic hydrogen from the ZnO lattice. Electron beam-induced surface change phenomena have been observed after degradation of different oxides. Hasabeldaim et al. [13] irradiated a ZnO thin film for about 24 h using an electron beam with energy of 2 keV and current of 10 μA and electron beam-induced surface change (coalition of particles) was observed during prolonged electron beam irradiation.

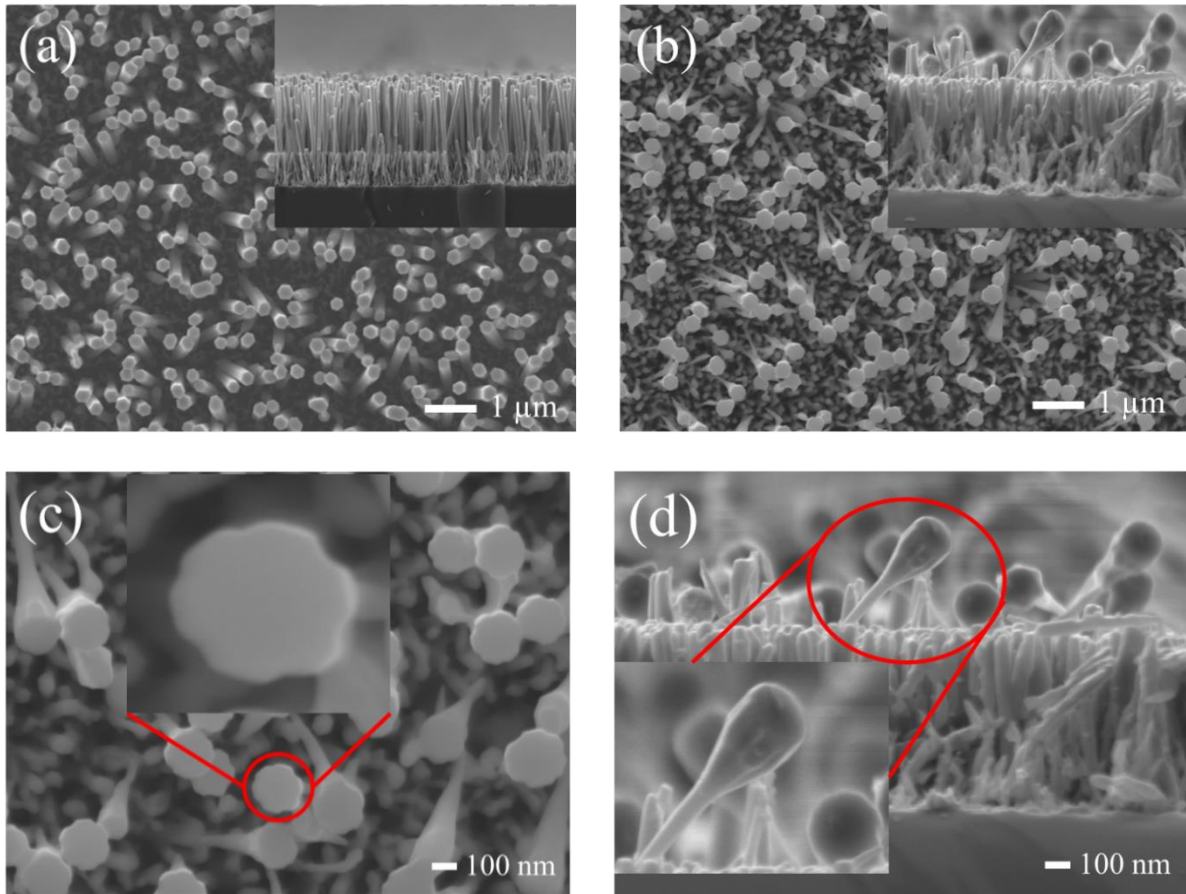


Fig. 9.1. SEM images of the ZnO nanorods annealed in reducing atmosphere for 30 min (a) before degradation and (b) after degradation, and (c and d) zoomed in images of the nanorods after degradation.

Fig. 9.2 shows the normalized CL and PL spectra of the ZnO nanorods. In both cases a broad single peak around 500 nm was observed. This emission is well known for ZnO fired in a reducing atmosphere and is attributed to the singly or doubly ionized oxygen vacancies [24]. Since the sample was annealed in reducing atmosphere, excess zinc-related defects such as oxygen vacancies, zinc interstitials and/or zinc antisites might be formed and therefore they might be responsible for the green emission. Generally, zinc antisites have higher formation energy than the oxygen vacancies and the zinc interstitials and they were not expected to form under near-equilibrium conditions [25]. Therefore, they are not expected to be involved in the broad green emission obtained from this sample. The slight difference between the PL and CL is due to the difference in their excitation mechanism. CL uses a high energy electron beam (2000 eV) which penetrates the material and produces secondary electrons that contribute to the host excitation, while PL uses low energy photons (3.8 eV) to excite the sample. The penetration depth of the photons are also deeper than the electrons in the ZnO as estimated in our previous work (0.09 μm for the electron beam and 0.2 – 0.5 μm for photons) [12]. The

commission international de l'Éclairage (CIE) coordinates of the sample based on the PL and CL data are shown in Fig. 9.2(b). The color coordinates and the color correlated temperatures were calculated using the well-known CIE 1931 diagram and the McCamy equation [26]. The results are shown in Table 9.1.

Table 9.1: The color coordinates and color correlated temperatures of the original sample for different excitation mechanisms.

Excitation mechanism	X	Y	CCT (K)
Photoluminescence	0.20	0.39	2464
Cathodoluminescence	0.21	0.44	3001

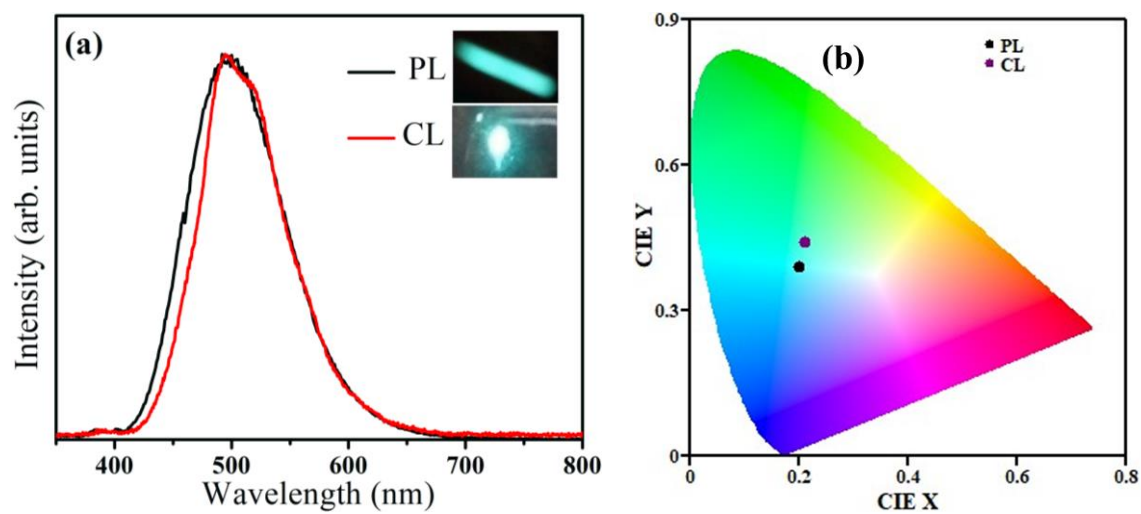


Fig. 9.2. (a) PL and CL of the ZnO nanorods (the insets are the PL and CL digital photographs of the sample) and (b) CIE color coordinates of the sample.

Fig. 9.3 shows the AES spectra of the sample before and after electron beam irradiation in vacuum and in an oxygen atmosphere. All the principal elements were detected, namely Zn peaks at the low energy level about (10 – 120 eV), Zn peaks at higher energy level (800 – 1050 eV) and O peaks around 513 eV. The peaks around 183 and 273 eV belong to the surface contaminations such as Cl and adventitious C, respectively. The surface contaminations were almost completely removed during electron beam irradiation in both cases (vacuum base pressure and oxygen partial pressure). In the case of the AES spectra recorded in vacuum, the principal elements (Zn and O) peak intensities have increased after degradation. This was due to the removal of the overlying contaminations, which reduced the inelastic scattering of the Auger electrons [3]. The increase on the Zn peaks intensity can also be attributed to the ejection of oxygen atoms from the specimen surface and the formation of a Zn-rich surface and new defects such as oxygen vacancies. Zn AES peak intensity at low energy (~ 10 – 120 eV)

increased more than those at ($\sim 800 - 1050$ eV). This is due to the fact that the low energy Auger electrons are much more surface sensitive because of their shallow escape depth [12]. In case of the AES spectra recorded in an oxygen atmosphere, the oxygen peak intensity has slightly increased, while the Zn peak intensity has slightly decreased. This may have resulted from the oxidation of the Zn atom/ions on the surface due to the oxygen atmosphere and the local temperature induced by the electron beam.

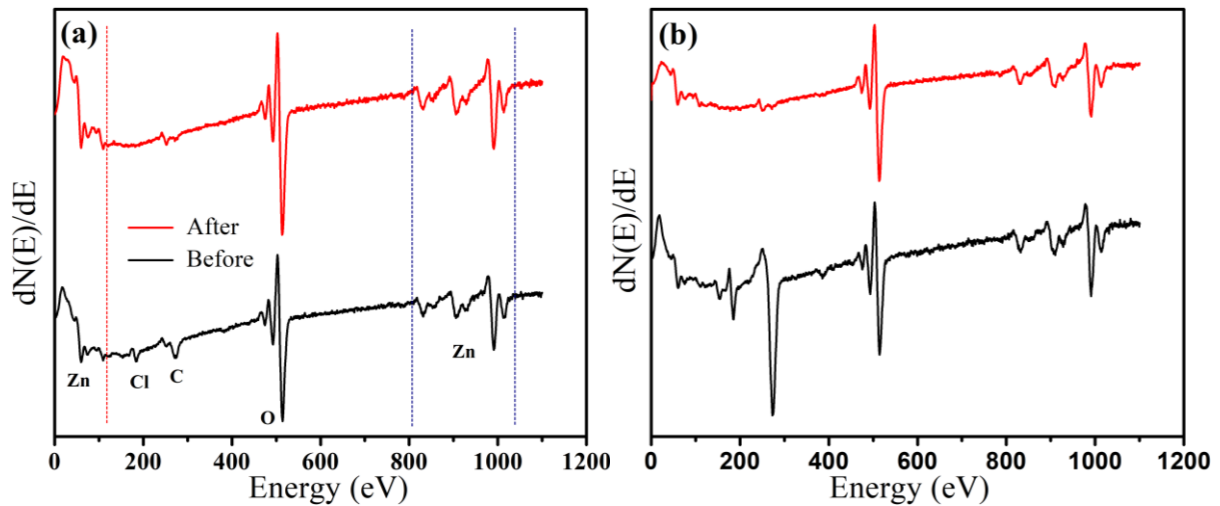


Fig. 9.3. Auger spectra of the ZnO nanorods before and after electron-beam irradiation in (a) vacuum with a base pressure of 5.0×10^{-8} Torr, and (b) backfilled with oxygen up to a pressure of 5.5×10^{-8} Torr.

To study the degradation behaviour of the sample under electron beam irradiation, the APPHs of the principal elements were monitored during electron dose exposure and the results are shown in Fig. 9.4 for the experiments performed in (a) vacuum and (b) oxygen. The C peak was reduced to about zero intensity level at the initial stage of the electron dose exposure. This indicated a complete removal of the C contaminating the sample surface, the mechanism being explained by the electron stimulated surface chemical reaction (ESSCR) model [27]. The C containing molecules on the surface dissociated into reactive C atoms as a result of the electron beam exposure, which eventually leave the chamber as volatile species. AES is a surface-sensitive technique; it characterizes only the top few layers of the sample [28]. The principal elements (Zn and O) were initially covered by the surface contaminations (C and Cl). During the removal of the surface contaminations the AES intensity of the principal elements increased slightly. For the vacuum-degraded sample, the APPHs intensities for the principal elements (Zn and O) have increased after the removal of surface contamination. Whereas in the case of oxygen-degraded sample, the oxygen peak intensity increased more relative to the Zn peak intensity compared to the oxygen peak intensity in vacuum. Zn APPHs peaks have also

increased initially and slightly decreased after electron dose of about 100 C/cm^2 . This can be attributed to the oxidation of Zn atoms/ions on the surface after the removal of the surface contamination.

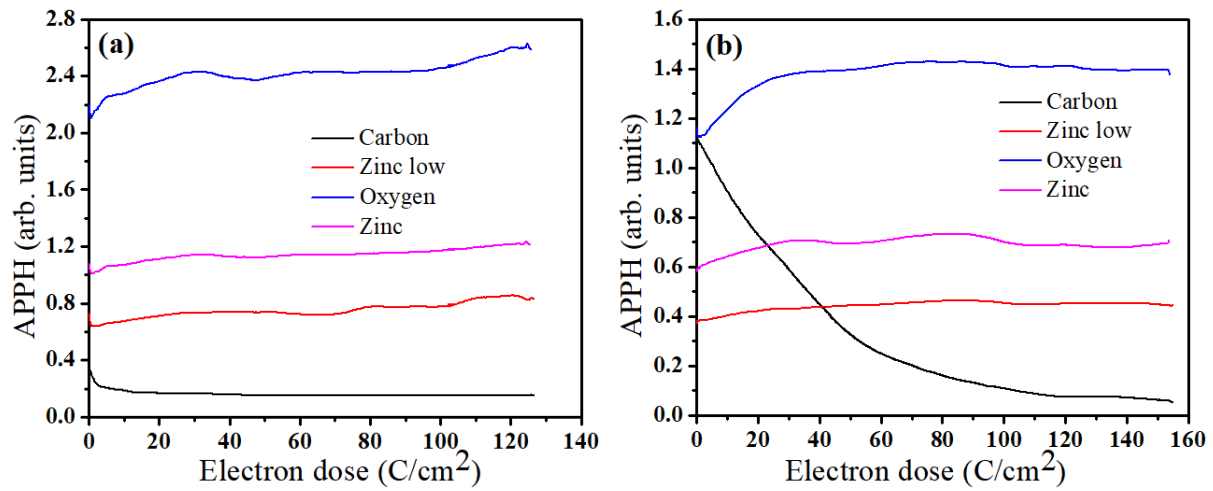


Fig. 9.4. Typical APPHs as a function of electron beam dose of the ZnO nanorods in (a) Vacuum with a base pressure of 5.0×10^{-8} Torr, and (b) backfilled with oxygen up to a pressure of 5.5×10^{-8} Torr.

Fig. 9.5 displays the CL intensity as a function of electron beam irradiation of the ZnO nanorods in (a) vacuum and (b) oxygen atmosphere. The CL intensity initially decreased as a function of electron beam irradiation dose. In vacuum it decreased to about 53% of its original intensity within about 121 C/cm^2 of electron dose, after which it stabilized (Fig. 9.5(a)). The initial rate of the CL degradation for the sample degraded in vacuum was estimated to be $\sim 0.44\%$ per C/cm^2 up to 100 C/cm^2 after which it stabilized. The initial degradation rate of the oxygen atmosphere sample was ~ 10 times higher up to 10 C/cm^2 after which it increased again and stabilized after 100 C/cm^2 to about 96% of the original intensity. This phenomenon has been observed for the degradation of phosphors and was attributed to the formation of an interleaved oxide layer which acted as a protective layer as well as reducing the CL intensity [29]. Yousif et al. [29] degraded $\text{Y}_3(\text{Al}, \text{Ga})_5\text{O}_{12}:\text{Tb}$ phosphor using electron beam irradiation. An exponential decrease of the CL intensity was attributed to a new oxide layer such as AlO_x , YO_x and $\text{Y}(\text{Al},\text{Ga})\text{O}_3$ which formed on the phosphor surface and acted as a protective layer while reducing the CL intensity. Swart et al. [30] and Trottier et al. [31] degraded ZnS based field emission display phosphors in different environments including vacuum, oxygen, hydrogen and water vapour. The CL intensity of the ZnS phosphor was severely degraded due to the formation of non-luminescent ZnO and/or ZnSO_4 layers and the removal of sulphur as the result of ESSCR. In our case, since our sample is ZnO and the emission arises from the native

defects of ZnO which are in a non-stoichiometric state, we suggest that some of the defects were removed and as a result a stoichiometric and non-luminescent ZnO layer may have been formed. For the degradation in the oxygen atmosphere shown in Fig. 9.5(b), the sample showed a different degradation behaviour than in the vacuum. The CL intensity rapidly decreased during the initial stage of the electron beam irradiation up to a dose of $\sim 10 \text{ C/cm}^2$, after which it increased until the electron dose was $\sim 100 \text{ C/cm}^2$ and then stabilized with further irradiation. The same behaviour was observed in degradation of ZnO powder and thin film in an oxygen atmosphere [12, 13]. An earlier report showed that atomic oxygen increases the CL yield of ZnO while atomic hydrogen decreases the yield [32]. Bylander [14] found that high surface recombination which was due to the change in the surface character was responsible for the initial rapid decrease of the CL intensity. Due to the fact that the sample was annealed in a hydrogen environment as well as the differences between the CL degradation of the sample in vacuum and in oxygen, one can speculate that either atomic oxygen or atomic hydrogen are responsible for the rapid initial degradation and/or the subsequent recovery of the CL in the case of the degradation in the oxygen. Since we postulated that the green luminescence was due to the excess Zn-related defects such as oxygen vacancies and zinc interstitials, introducing oxygen in the chamber while the sample was under electron beam irradiation could result in the passivation of such defects, with assistance of ESSCR. This could be the reason why the CL intensity substantially decreased during the initial irradiation. However, this argument cannot explain the subsequent recovery of the CL intensity. Hydrogen atoms play a prominent role in the optical and electrical properties of ZnO. They can easily diffuse into a ZnO matrix during the annealing process and occupy different sites such as oxygen vacancy or interstitial sites [33]. In both cases this may result in reducing the luminescence arising from these defects by forming non-radiative centres. Hydrogen atoms naturally have strong bonds with oxygen atoms. During degradation in an oxygen atmosphere with the assistance of ESSCR, atomic hydrogen in the sample possibly reacted with the oxygen in the chamber and formed $\text{H}_2\text{O/OH}$ groups which eventually left the sample and resulted in the reduction of the non-radiative centres, allowing the CL intensity to increase. No change in the shape of the CL spectra was observed before and after electron beam irradiation, for both cases of degradation in vacuum and in oxygen, indicating that the same type of defects was responsible for the luminescence.

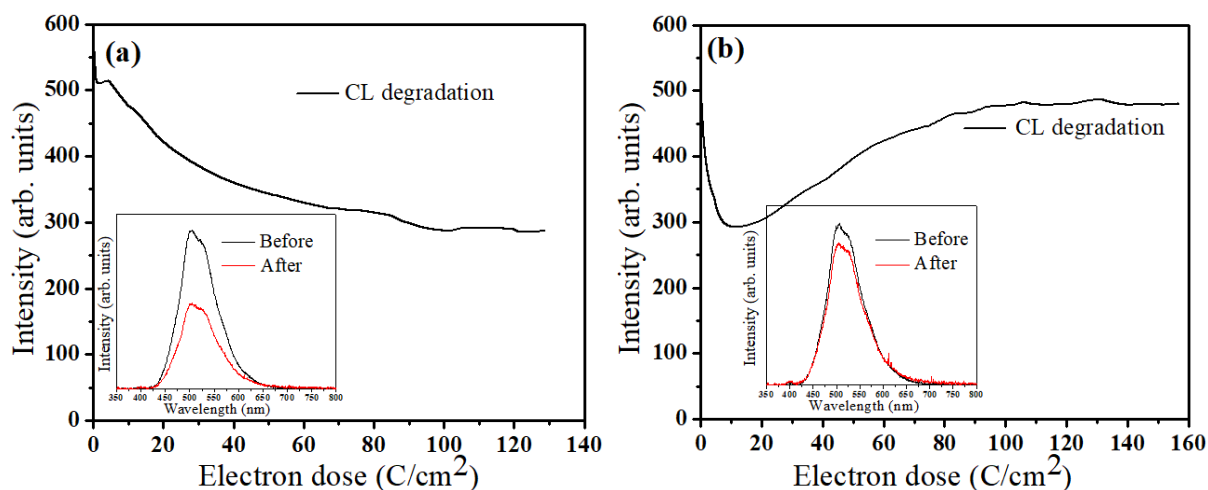


Fig. 9.5. CL intensity as a function of electron dose exposure of the ZnO nanostructure in (a) vacuum with base pressure of 5.0×10^{-8} Torr, and (b) backfilled with oxygen up to a pressure of 5.5×10^{-8} Torr (the insets are the CL spectra before and after degradations).

To assess the effect of the electron beam irradiation on the chemical state of the sample, XPS high resolution spectra of the Zn 2p peak region was measured for the original and the sample degraded in oxygen, before and after 1 min of sputtering using an Ar⁺ ion beam. The results are shown in Fig. 9.6. Two peaks with binding energies at 1022 eV and 1045 eV were detected and indexed to Zn 2p_{1/2} and Zn 2p_{3/2}, respectively. These values indicate that all Zn atoms were fully oxidized and in their doubly ionized state (Zn²⁺), based on the standard reference value of ZnO [34]. No Zn metal with binding energy of 1021.8 eV was observed.

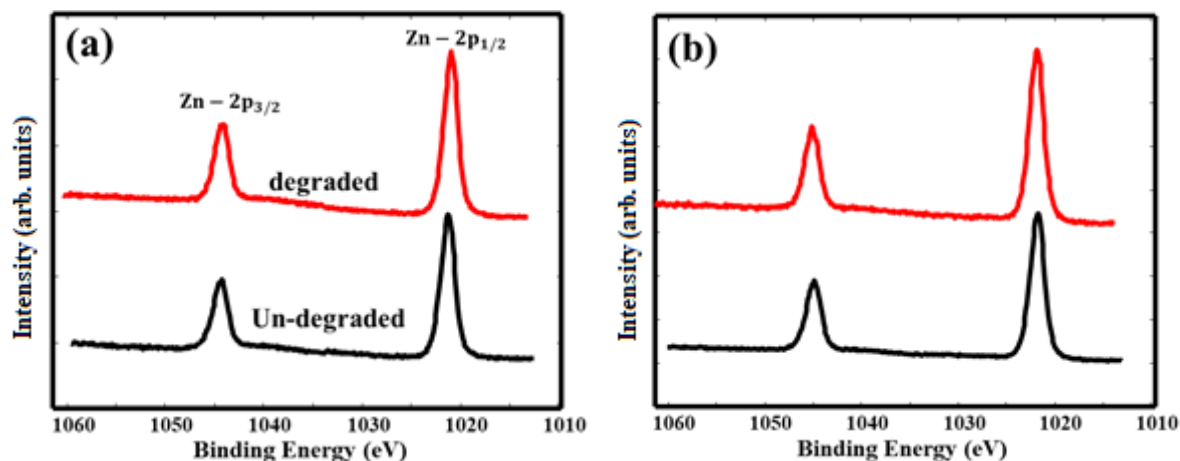


Fig. 9.6. High-resolution XPS spectra of the Zn 2p core levels of the original and degraded samples (a) before sputtering and (b) after sputtering for 1 min with Ar⁺ ions.

XPS high resolution spectra of the O 1s peak are shown in Fig. 9.7 for the original and degraded sample before and after 1 min of Ar⁺ ion sputtering. The O 1s peak was deconvoluted into three components (O1, O2 and O3) using MULTIPAK software. Kumar et al. [35, 36] previously

identified the three components of the O 1s peak. The component O1 is ascribed to the ionized oxygen atoms in the wurtzite ZnO, surrounded by the fully oxidized Zn atoms with their nearest O²⁻ ions. The component O2 is attributed to the O²⁻ ions in the oxygen deficient regions such as hydroxyl groups and defects, and O3 is due to the loosely bonded species on the surface which came from the atmosphere such as CO₃, CO₂, H₂O and O₂. The component O3 was only detected for both samples before sputtering and was not detected after the Ar⁺ ion sputtering. This is due to the fact that the surface contamination was removed from the surface during sputtering. The details (peaks positions and areas) for the O 1s components are given in Table 9.2. The O2 component peak area decreased after degradation in both cases, before and after Ar⁺ ion sputtering, while the O1 component area increased. These results are supportive of the CL degradation results, since the increase in the O1 component peak area can be explained by the removal of C on the surface and the possible formation of a thin stoichiometric and non-luminescent ZnO layer that was responsible for the initial decrease of the CL intensity, and which may have acted as a protective layer responsible for the CL stability for further electron dose. We speculate that the stoichiometric layer was a low defect layer with fully oxidized and ionized zinc and oxygen atoms (Zn=O) and hence there was little or no emission that arose from it. Since the O2 component was attributed to the hydroxyl groups complexes and hydrogen atoms were suspected to have diffused in our sample and formed non-radiative centres, the decrease in the O2 component area might explain the subsequent recovery after the initial decrease on the CL intensity in the case of degradation in the oxygen atmosphere (Fig. 9.5 (b)), while the presence of oxygen in the chamber during electron beam irradiation may have contributed to the hydrogen atoms leaving the sample by means of the already mentioned ESSCR model. The O/Zn ratios of the XPS peak areas were estimated for the original and the degraded sample before and after sputtering (Table 9.3), the O/Zn ratios have slightly increased in both cases before and after sputtering for the degraded samples. This result may also support the argument that Zn atoms diffused to the surface, react with oxygen atoms in the chamber and eventually oxidized due to the heat induced by the electron beam.

Table 9.2. Binding energies of the deconvoluted peaks of the O 1s of the original and degraded samples, before and after sputtering.

Sample	O 1s components	Peak position (eV)	Area % (Before sputtering)	Area % (After sputtering)
Original	O1	530.3	72	80
	O2	531.7	24	20
	O3	532.6	4	—
Degraded	O1	530.3	75	90
	O2	531.7	19	10
	O3	532.6	6	—

Table 9.3. O/Zn ratio of the original and degraded sample before and after sputtering.

Sample	O/Zn ratio	Before sputtering	After sputtering
Original	O/Zn	0.19	0.15
Degraded	O/Zn	0.22	0.16

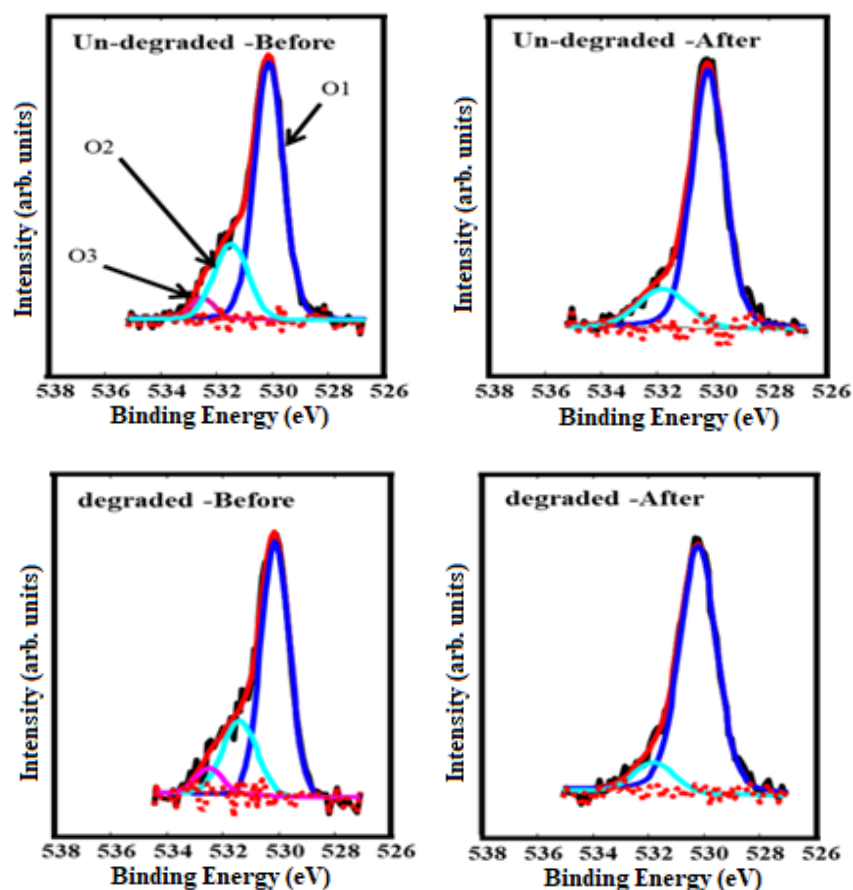


Fig. 9.7. Deconvolution of the O 1s peak before and after sputtering of the original and the degraded sample.

9.4. Conclusion

The effect of prolonged electron beam irradiation on the surface state and the intensity of the green CL emission at about 500 nm of ZnO nanorods was explored. The mechanisms behind the initial degradation and stability for further electron beam irradiation, and the subsequent recovery of the CL for the sample in an oxygen back-filled environment were investigated. The formation of a non-luminescent ZnO layer and surface morphology changes have been identified as important factors. Atomic oxygen is suggested to be responsible for the initial slump while the removal of the atomic hydrogen from the ZnO matrix is suggested to be responsible for the subsequent recovery of the green luminescence. Electron beam irradiation was found to induce changes of the nanorod morphology. This material may be useful for optoelectronic devices such as flat panel displays.

9.5. References

- [1] Y. Agrawal, G. Kedawat, P. Kumar, J. Dwivedi, V. N. Singh, R. K. Gupta and B. K. Gupta, High-performance stable field emission with ultralow turn on voltage from rGO Conformal Coated TiO₂ nanotubes 3D arrays, *Sci. Rep.* **5** (2015) 11612.
- [2] Y. Sun, W. Wang, H. Zhang, Q. Su, J. Wei, P. Liu, S. Chen, S. Zhang, High-performance quantum dot light-emitting diodes based on Al doped ZnO nanoparticles electron transport layer, *ACS Appl. Mater. Interfaces* **10** (22) (2018) 18902-18909.
- [3] L. Oosthuizen, H. C. Swart, P. E. Viljoen, P. H. Holloway, G. L. P. Berning, ZnS:Cu,Al,Au phosphor degradation under electron excitation, *Appl. Surf. Sci.* **120** (1997) 9-14.
- [4] H. C. Swart, J. S. Sebastian, T. A. Trottier, S. L. Jones, P. H. Holloway, Degradation of zinc sulfide phosphors under electron bombardment, *J. Vac. Sci. Technol. A* **14** (1996) 1697.
- [5] X. Yu, T. J. Marks, A. Facchetti, Metal oxides for optoelectronic applications, *Nat Mater.* **15** (2016) 383-396.
- [6] S. J. Pearton, F. Ren, Advances in ZnO-based materials for light emitting diodes, *Curr. Opin. Chem. Eng.* **3** (2014) 51-55.
- [7] P. Kajal, D. Pooja, N. Jaggi, Structural and optical properties of ZnO nanorods synthesized via template free approach, *Mater. Res. Express* **3** (2016) 065011.
- [8] A. B. Djurisi, A. M. C. Ng, X. Y. Chen, ZnO nanostructures for optoelectronics: Material properties and device applications, *Prog. Quantum Electron.* **34** (2010) 191-259.
- [9] G. C. Yi, C. Wang, W. I. Park, ZnO nanorods: synthesis, characterization and applications, *Semicond. Sci. Technol.* **20** (2005) S22-S34.
- [10] C. Bhakat, P. P. Singh, Zinc oxide nanorods: synthesis and its applications in solar cell, *International Journal of Modern Engineering Research (IJMER)* **2** (2012) 2452-2454.
- [11] Y. Hu, H. J. Chen, Origin of green luminescence of ZnO powders reacted with carbon black, *J. Appl. Phys.* **101** (2007) 124902.
- [12] E. Hasabeldaim, O. M. Ntwaeaborwa, R. E. Kroon, H. C. Swart, Surface analysis and cathodoluminescence degradation of undoped ZnO and ZnO:Zn phosphors, *J. Vac. Sci. Technol. B* **34** (2016) 041221.

- [13] E. Hasabeldaim, O.M. Ntwaeaborwa, R.E. Kroon, V. Craciun, E. Coetsee, H.C. Swart, Surface characterization and cathodoluminescence degradation of ZnO thin films, *Appl. Surf. Sci.* **424** (2017) 412-420.
- [14] E. G. Bylander, Surface effects on the low-energy cathodoluminescence of zinc oxide, *J. Appl. Phys.* **49** (3) (1978) 1188.
- [15] E. H. H. Hasabeldaim, O. M. Ntwaeaborwa, R. E. Kroon, E. Coetsee, H. C. Swart, Enhanced green luminescence from ZnO nanorods, *J. Vac. Sci. Technol. B* **37** (1) (2019) 011201.
- [16] MULTIPAK, version 9, Physical Electronics, Inc., Chanhassen, USA, 2006–2010.
- [17] Y. Ding, K. C. Pradel, Z. L. Wang, In situ transmission electron microscopy observation of ZnO polar and non-polar surfaces structure evolution under electron beam irradiation, *J. Appl. Phys.* **119** (2016) 015305.
- [18] M. R. McCartney, D. J. Smith, Studies of electron irradiation and annealing effects on TiO₂ surfaces in ultrahigh vacuum using high-resolution electron microscopy, *Surf. Sci.* **250** (1991) 169-178.
- [19] M. R. McCartney, P. A. Crozier, J. K. Weiss and D. J. Smith, Electron-beam-induced reactions at transition metal oxide surfaces, *vacuum*, **42** (1991) 301-308, 1991.
- [20] R. F. Egerton, P. Li, M. Malac, Radiation damage in the TEM and SEM, *Micron* **35** (2004) 399–409.
- [21] B. Dierre, X. Yuan, K. Ueda, T. Sekiguchi, Hydrogen released from bulk ZnO single crystals investigated by time-of-flight electron-stimulated desorption, *J. Appl. Phys.* **108** (2010) 104902.
- [22] D. Su, N. Jiang, J. C. H. Spence, F. He, W. T. Petuskey, On the dehydration mechanism of Mg(OH)₂ by a high-electron beam, *J. Appl. Phys.* **104** (2008) 063514.
- [23] M. A. Stevens Kalceff, M. R. Phillips, A. R. Moon, Electron irradiation-induced changes in the surface topography of silicon dioxide, *J. Appl. Phys.* **80**(8) (1996) 4308.
- [24] R. Bhaskar, A. R. Lakshmanan, M. Sundarrajan, T. Ravishan, M. T. Jose, N. Lakshminarayan, Mechanism of green luminescence in ZnO, *Indian J. Pure Appl. Phys.* **47** (2009) 772-774.
- [25] A. Janotti and C.G. Van De Walle, Fundamentals of zinc oxide as a semiconductor, *Rep. Prog. Phys.* **72** (2009) 126501.

- [26] J. Herná' ndez-Andre's, R. L. Lee, and J. Romero, Calculating correlated color temperatures across the entire gamut of daylight and skylight chromaticities, *Appl Opt.* **38** (1999) 5702-5709.
- [27] P. H. Holloway, T. A. Trottier, B. Abrams, C. Kondoleon, S. L. Jones, J. S. Sebastian, W. J. Thomes, H. C. Swart, Advances in field emission displays phosphors, *J. Vac. Sci. Technol. B* **17** (1999) 758-764.
- [28] H. C. Swart, E. Coetsee, J. J. Terblans, O. M. Ntwaeaborwa, P. D. Nsimama, F. B. Dejene, J. J. Dolo, Cathodoluminescence degradation of PLD thin films, *Appl. Phys. A Mater. Sci. Process.* **101** (2010) 633-638.
- [29] A. Yousif, H. C. Swart, O. M. Ntwaeaborwa, Surface state of $Y_3(Al,Ga)_5O_{12}:Tb$ phosphor under electron beam bombardment, *Appl. Surf. Sci.* **258** (2012) 6495-6503.
- [30] H. C. Swart and K. T. Hillie, Degradation of ZnS FED phosphors, *Surf. Interface Anal.* **30** (2000) 383-386.
- [31] T. A. Trottier, S. L. Jones, P. H. Holloway, Degradation of ZnS field-emission display phosphors during electron-beam bombardment, *J. Vac. Sci. Technol. A* **15(4)** (1997) 2349-2353.
- [32] W. B. Pennebaker, J. F. O' Hanlon, Low energy cathodoluminescence of ZnO: The ZnO plasma display, *J. Appl. Phys.* **45** (1974) 1315.
- [33] C. F. Windisch, G. J. Exarhos, C. Yao, L. Q. Wang, Raman study of the influence of hydrogen on defects in ZnO, *J. Appl. Phys.* **101** (2007) 123711.
- [34] J. F. Moulder, W. F. Strickle, P. E. Sobol, K. D. Bomben, Handbook of X-Ray Photoelectron Spectroscopy, ULVAC-PHI, Inc., Chigasaki , 1995.
- [35] V. Kumar, H. C. Swart, M. Gohain, Vijay Kumar, S. Som, B. C. B. Bezuindenhoudt, O. M. Ntwaeaborwa , Influence of ultrasonication times on the tunable colour emission of ZnO nanophosphors for lighting applications, *Ultrason. Sonochem.* **21** (2014) 1549.
- [36] V. Kumar, Vijay Kumar, S. Som, L. P. Purohit, O. M. Ntwaeaborwa, H. C. Swart, Role of swift heavy ions irradiation on the emission of boron doped ZnO thin films for near white light application, *J. Alloys Compd.* **594** (2014) 32.

Chapter 10

Summary and future work

This chapter gives is a summary of this research study as well as some suggestions for the future work that may be pursued.

10.1. Summary

This study was aimed at preparing Eu^{3+} doped ZnO thin films with different Eu^{3+} concentrations by using spin coating and PLD techniques, as well as preparing ZnO nanorods by using the chemical bath deposition technique. It was also intended to optimizing the red emission intensity for the Eu^{3+} doped ZnO films, and the green luminescence for the ZnO nanorods, and to investigate their structure, morphology and luminescence properties. The highest intensity red emitting samples were subjected to electron beam irradiations. Their surface, chemical states and luminescence stability under electron beam bombardment were investigated. In more detail:

Low concentrations (0.4, 0.6, 0.8 and 1 mol%) of Eu^{3+} doped ZnO thin films were fabricated by using the spin coating technique. Their structure, optical, morphology and photoluminescence (PL) properties were investigated. XRD and PL results confirmed the incorporation of the Eu^{3+} ions in the ZnO lattice. The film crystallinity was affected negatively as a result of increasing the Eu^{3+} concentration. The films were excited at different wavelengths using different excitation sources, and the energy/charge transfer taking place between ZnO and Eu^{3+} was discussed. The highest PL emission was recorded for the film doped with 0.6 mol% of Eu^{3+} after which quenching occurred. Judd-Ofelt analysis revealed that the local environment and in the vicinity of Eu^{3+} and their asymmetry plays a significant role in the PL emission. Crystallinity degradation, creation or reduction of defects and multipole-multipole interaction were found to be the major mechanisms for the concentration quenching.

Higher concentrations (1 to 4 mol%) of Eu^{3+} doped ZnO spin coating films were also prepared. The film thickness increased slightly compared to the previous films. Orientation along the c-axis for the films was confirmed by XRD measurements. No peaks associated with Eu_2O_3 or $\text{Zn}(\text{OH})_2$ were observed which indicated a successful incorporation and dispersion of Eu^{3+} ions in the ZnO matrix. Both divalent (Eu^{2+}) and trivalent (Eu^{3+}) ions were present in the samples as revealed by XPS measurements. PL and CL of the films were studied. 4f-4f transitions lines were observed. Charge transfer from O^{2-} to Eu^{3+} and energy transfer from ZnO defects to Eu^{3+} were investigated. The electron beam excited the luminescent centres via direct or indirect impact excitation, and therefore emission from 4f-4f transitions of Eu^{3+} ions in ZnO were

detected without other emission from ZnO native defects. The film with the highest luminescence intensity (3 mol% of Eu^{3+} ions) was subjected to electron beam irradiation for about 22 h. The surface, chemical and luminescence properties of the film was found to be very stable under electron beam irradiation.

A ceramic pellet made of 3 mol% Eu^{3+} doped ZnO powder that was synthesized using the composition method, was ablated in different oxygen atmosphere by using PLD to deposit the films on p-type Si substrates. Oxygen atmosphere (partial pressure) was found to play a critical role in the film crystallinity, morphology, luminescence and electrical properties. These properties were improved with increasing oxygen partial pressure to some extent after which they deteriorated. PL revealed that the charge transfer rate was proportionally increased with increasing oxygen partial pressure. Impact excitation was found to be the major mechanism in CL, CL emission associated with 4f-4f transition of Eu^{3+} was observed with no emission due to the ZnO native defects. This suggest that the electron beam excited the luminescence centres through either direct impact excitation, or indirect impact excitation by generating electron-hole pairs which transferred their energy non-radiative to the Eu^{3+} centres.

Oxygen atmosphere, deposition time and target-substrate distance were optimized in order to achieve the highest possible PL and CL intensity. The stability of the surface, chemical and luminescence properties of this sample under electron beam irradiation was investigated. A slight increase on the CL intensity at the initial degradation, minor growth of the film particles and creation of defects were observed during electron beam irradiation. However, the film was generally stable under electron beam irradiation.

Vertically aligned ZnO nanorods with *c*-axis orientation were successfully grown on a ZnO seed layer coated on a (100) Si substrate. High quantum efficiency of about 43% of the green emission centred at 500 nm was obtained after annealing in reducing atmosphere for different times. The deconvoluted XPS peaks of the O 1s energy region indicated that defects related to the oxygen deficiencies were present in all the samples and played a significant role on the PL of the ZnO nanorods. At least three kind of defects (V_o^+ , V_o^{++} , V_{Zn}) were found to be involved in the green emission centred at 500 nm.

The effect of prolonged electron beam irradiation on the surface state and the intensity of the green CL emission at about 500 nm of the ZnO nanorods was explored. The mechanisms behind the initial degradation and stability for further electron beam irradiation, and the subsequent recovery of the CL for the sample in an oxygen back-filled environment were investigated. The formation of a non-luminescent ZnO layer and the surface morphology changes have been identified as important factors. Atomic oxygen was suggested to be

responsible for the initial decrease while the removal of the atomic hydrogen from the ZnO matrix was suggested to be responsible for the subsequent recovery of the green luminescence. Electron beam irradiation was found to induce changes of the nanorod morphology. These emissions may be used in optoelectronic applications such as LEDs and FEDs.

10.2. Future work

Red emission of the 4f-4f transitions of Eu^{3+} ions in a ZnO host was obtained from spin coating and PLD thin films. The electron beam excitation mechanism was found to be similar to electroluminescence as an impact excitation mechanism. Efficient green luminescence was obtained from ZnO nanorods. These films and nanostructures were found to be stable under electron beam irradiation. Therefore, further work maybe needed to evaluate the application of these films in optoelectronic applications such as LEDs and FPDs by:

- Improving the luminescence and electrical properties of the Eu doped ZnO thin films obtained by spin coating and PLD techniques.
- Studying the effect of different deposition, spin coating and post annealing conditions on the luminescence and electrical properties of these thin films.
- Depositing the films on different substrates and study their electrical properties and the possibility of achieving electroluminescence for LEDs.
- Doping with different rare earth ions to achieve a wider spectrum of wavelengths for a full-colour FPD, and study their stability under prolonged electron beam irradiation.
- Implementation of the ZnO nanorods as a green LED by developing the proper electrical contacts on it.
- Implementing the ZnO nanorods annealed in reducing atmosphere in dye sensitized and perovskite solar cells.

Appendix

Publications

The following publications have resulted from this thesis:

- E. Hasabeldaim, O. M. Ntwaeaborwa, R. E. Kroon and H. C. Swart, Structural, optical and photoluminescence properties of Eu doped ZnO thin films prepared by spin coating, *J. Mol. Struct*, **1192** (2019) 105-114. <https://doi.org/10.1016/j.molstruc.2019.04.128>.
- E. Hasabeldaim, O. M. Ntwaeaborwa, R. E. Kroon, E. Coetsee and H. C. Swart, Enhanced green luminescence from ZnO nanorods, *J. Vac. Sci. Technol. B*, **37** (2019) 011201. <https://doi.org/10.1116/1.5052543>
- E. Hasabeldaim, O. M. Ntwaeaborwa, R. E. Kroon, E. Coetsee and H. C. Swart, Cathodoluminescence degradation study of the green luminescence of ZnO nanorods, *Appl. Surf. Sci.* **484** (2019) 105–111. <https://doi.org/10.1016/j.apsusc.2019.04.113>
- E. Hasabeldaim, O. M. Ntwaeaborwa, R. E. Kroon, E. Coetsee and H. C. Swart, Photoluminescence and cathodoluminescence of spin coated ZnO films doped with Eu³⁺ up to 4 mol%, *Vacuum*, 169 (2019) 10888921 (13 pages). <https://doi.org/10.1016/j.vacuum.2019.108889>
- E.H.H. Hasabeldaim, O.M. Ntwaeaborwa, R.E. Kroon, E. Coetsee, H.C. Swart, Luminescence properties of Eu doped ZnO PLD thin films: the effect of oxygen partial pressure, *Superlattices and Microstructures*, revised, Ref: SM_2019_1684, 14 November 2019.
- E. Hasabeldaim, O. M. Ntwaeaborwa, R. E. Kroon, E. Coetsee and H. C. Swart, Pulsed laser deposition of a ZnO:Eu³⁺ thin film: study of the luminescence and surface state under electron beam irradiation, *Appl. Surf. Sci.* **502** (2019) 144281. <https://doi.org/10.1016/j.apsusc.2019.144281>

Presentations at national and international conferences/workshops

- 7th South African Conference on Photonic Materials, 27-31th Mar 2017, Amanzi Private Game Reserve, South Africa.
- 10th African Laser Centre Student Workshop, 30th November-2nd December 2017, STIAS, Stellenbosch, South Africa.
- 63th Annual Conference of the SA Institute of Physics, 25-29th June 2018, University of the Free State, South Africa.
- 11th African Laser Centre Student Workshop, 22-24th November 2018, STIAS, Stellenbosch, South Africa.
- 8th South African Conference on Photonic Materials, 6-10th May 2019, Kariega Game Reserve, South Africa.
- Spring school on solar energy and photosynthesis, 23-27 Sep 2019, University of Pretoria, South Africa.